

Lehrstuhl E 15  
Institut für Astro-Teilchenphysik  
Fakultät für Physik  
Technische Universität München  
Prof. Dr. Franz von Feilitzsch

**High Efficiency Purification of Liquid Scintillators  
for the Solar Neutrino Experiment Borexino**

Ludwig Stefan Niedermeier

Vollständiger Abdruck der von der Fakultät für Physik der Technischen Universität München zur Erlangung des akademischen Grades eines

Doktors der Naturwissenschaften

genehmigten Dissertation.

Vorsitzender:

Univ.-Prof. Dr. W. Weise

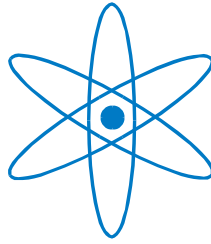
Prüfer der Dissertation:

1. Univ.-Prof. Dr. F. von Feilitzsch
2. Univ.-Prof. Dr. K. Schreckenback

Die Dissertation wurde am 22.12.2004 bei der Technischen Universität München eingereicht und durch die Fakultät für Physik am 31.01.2005 angenommen.



# PHYSIK-DEPARTMENT



## High Efficiency Purification of Liquid Scintillators for the Solar Neutrino Experiment Borexino

Dissertation

von

Ludwig Stefan Niedermeier



TECHNISCHE UNIVERSITÄT  
MÜNCHEN



# Contents

<b>Introduction</b>	1
<b>1. Solar Neutrinos</b>	2
1.1. The Standard Solar Model	2
1.2. Neutrino Oscillations	5
1.3. Solar Neutrino Experiments	9
1.3.1. Radiochemical Experiments	10
1.3.2. Water Cherenkov Detectors	11
1.3.3. Scintillation Detectors	13
1.4. Answers and Open Questions	15
1.5. Future Experiments	16
<b>2. The Experiment Borexino and its Prototype CTF</b>	17
2.1. Motivation and Future Possibilities	17
2.2. Detector Equipment	22
2.2.1. Liquid Handling	22
2.2.2. The Borexino Detector	23
2.3. Background	24
2.3.1. Radioactive Metal Isotopes and Radon	25
2.3.2. Further Radioactive Isotopes	27
2.3.3. Muon Induced Radioactivity	27
2.4. The Counting Test Facility	28
2.4.1. The CTF Detector	29
2.4.2. Test Campaign CTF1	29
2.4.3. Test Campaign CTF2	30
2.4.4. Test Campaign CTF3	30
2.4.5. Current Status	32
<b>3. The Module-0</b>	34
3.1. System Description	34
3.1.1. Components	36
3.1.2. Safety Issues	39
3.1.3. Surroundings	41
3.1.4. Construction and Development	42
3.2. Cleaning of the System	44
3.3. Radon Emanation Measurements	45
3.3.1. Motivation	45
3.3.2. Methods	45
3.3.3. Results	47
3.3.4. Conclusions	49
3.3.5. $^{220}\text{Rn}$ Emanation	49
3.4. Particulate Counting	50
3.4.1. Motivation	50
3.4.2. Method	50
3.4.3. Results	51
<b>4. Silica Gel Chromatography</b>	54
4.1. Theoretical Considerations	54
4.1.1. Static Model	54
4.1.2. Dynamic Model	56

4.1.3. Loop Purification Mode	57
4.1.4. Batch Purification Mode	58
4.1.5. Comparison	59
4.2. Laboratory Experiments	61
4.2.1. Liquid Scintillator Loading	61
4.2.2. Activity Detection and Analysis Methods	62
4.2.3. Free Enthalpy Determination	71
4.2.4. Laboratory Batch Purification Test	73
4.2.5. Purification Efficiency Limitation	76
4.3. Experiments with CTF3	79
4.3.1. CTF3 Loop Purification Test	79
4.3.2. CTF3 Batch Purification Test	86
4.4. Conclusion	88
<b>5. Adsorption on Surfaces</b>	90
5.1. Motivation	90
5.2. Experiments	90
5.2.1. Adsorption on Teflon and Glass (combined)	90
5.2.2. Adsorption on Stainless Steel	91
5.2.3. Adsorption on Glass	93
<b>6. Water Extraction</b>	94
6.1. Realisation Possibilities	94
6.2. The Borexino Water Extraction Plant	94
6.3. Experiments with CTF3	96
6.3.1. Test Set-up	96
6.3.2. First Test Phase	97
6.3.3. Second Test Phase	99
<b>Conclusion</b>	102
<b>Appendices</b>	i
A. Piping & Instrumentation Drawing of Module-0 and the CTF Inner Vessel	i
B. Scintillator Solvents	iii
C. Operation Procedures of Module-0	iv
C.I. Operation of Module-0 Safety Valves	iv
C.II. Transferring of Liquids	iv
C.III. Mixing of Scintillator	v
C.IV. Volumetric Loading of the CTF Inner Vessel	vi
C.V. Volumetric Unloading of the CTF Inner Vessel	vii
C.VI. Silica Gel Chromatography	viii
C.VII. Nitrogen Extraction	ix
C.VIII. Water Extraction	xi
C.IX. Liquid Supply to the Skid on the CTF Tank	xi
D. Recommended Alarm Set Points in Module-0	xii
<b>Tables &amp; Diagrams</b>	
<b>Bibliography</b>	
<b>Acknowledgement</b>	

# Introduction

The liquid scintillation experiment Borexino aims at a determination of the solar  ${}^7\text{Be}$  neutrino rate as well as at the observation of anti-neutrinos from supernovae, solar and geological sources. A low background rate is crucial for the success of such low counting rate experiments.

The Counting Test Facility, a prototype of this experiment, has been constructed for background examinations, mainly concerning the radiopurity of the liquid scintillator. The examination of scintillator purification methods constitutes the main goal of this thesis and aims at reaching the required activity level.

In this context, a liquid handling and purification system for both the CTF and the Borexino detector had to be installed at the experimental site, the Laboratori Nazionali del Gran Sasso in Italy. The functionality and radiopurity of this system had to be tested in order to further carry out various scintillator purification tests with the CTF detector. These tests, concerning a silica gel chromatography column and a water extraction plant, are illustrated in this thesis, together with interpretations of the observed effects. Based on the results of this so-called CTF3 testing campaign, well determined after a data taking period of two years, the status of the Borexino experiment can be evaluated.

The potential of the purification systems installed on-site – this thesis focuses on the silica gel chromatography plant – can be estimated by the development of a theoretic model, aiming at applicable purification methods. Small-scale laboratory tests have helped to experimentally confirm the assumptions and to determine important parameters of the model. On this basis, a simulation of the silica gel chromatography process supposed to be applied on the Borexino scintillator can clarify its potential with respect to necessary extensions of the plant.

# 1. Solar Neutrinos

Looking at all neutrinos that are destined to cross the earth on their way through the infinity of space, the sun is by far responsible for the biggest part of them. Moreover, the solar neutrino flux remains reliably constant and its direction is well known; so solar neutrinos offer us an excellent possibility to study the characteristics and behaviour of the neutrino itself. As

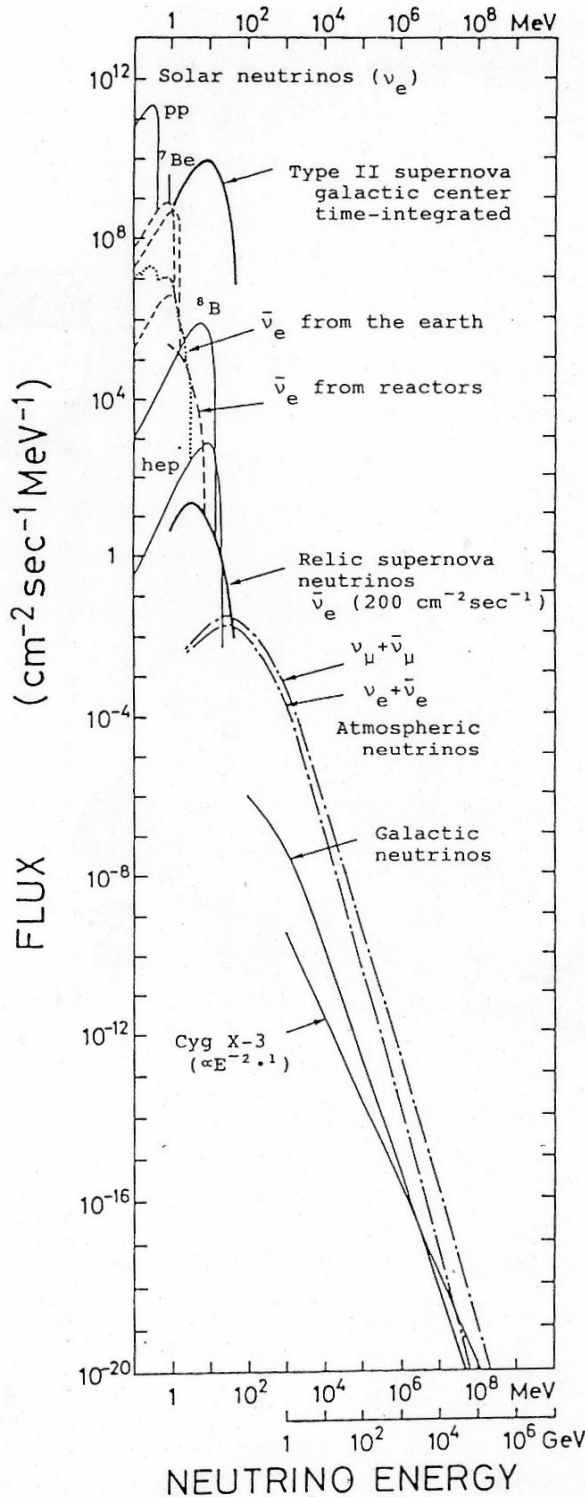


Diagram 1.1: Neutrino flux on the earth from different sources [Kos92]

neutrinos interact with matter at ultra low rates, of course it is not easy to detect them. But once done that, neutrino spectroscopy can serve as a unique method to look into regions, where no other kind of radiation is able to escape from in an undisturbed way. Like this, we hope to get further information about supernovae, far galaxies, but also on the composition of the earth. Diagram 1.1 shows the neutrino flux of many different sources and their energy ranges. The production of atmospheric neutrinos and reactor neutrinos is – like the solar neutrino flux – quite well understood and additionally helps to understand the nature of the neutrino.

## 1.1. The Standard Solar Model

The study of neutrino properties on the sun as neutrino source requires a sufficient knowledge of the solar structure itself. Fortunately, this is the case. The sun consists of concentrically distributed gas, mostly hydrogen, held together by gravitation. On the other hand, the thermodynamic gas pressure prevents it from collapsing. Now, we know that the sun loses energy by radiation, which normally would cause the gas to cool down and to contract more and more in order to maintain the pressure. In this case, the sun would never have been able to assume a stable state over the time period it has been existing for. But as with further contraction the gas temperature inside the sun increases, from a certain point on the thermal energy of the hydrogen nuclei is able to override the Coulomb barrier between two protons, so that nuclear reactions become possible. They are able to provide a lot of heat, to compensate the

radiation losses of a star over a very long time period and thus to stabilise the sun in its current state. There, hydrogen actually gets fused to helium. The solar neutrinos arise from these fusion reactions, illustrated in Diagram 1.2.

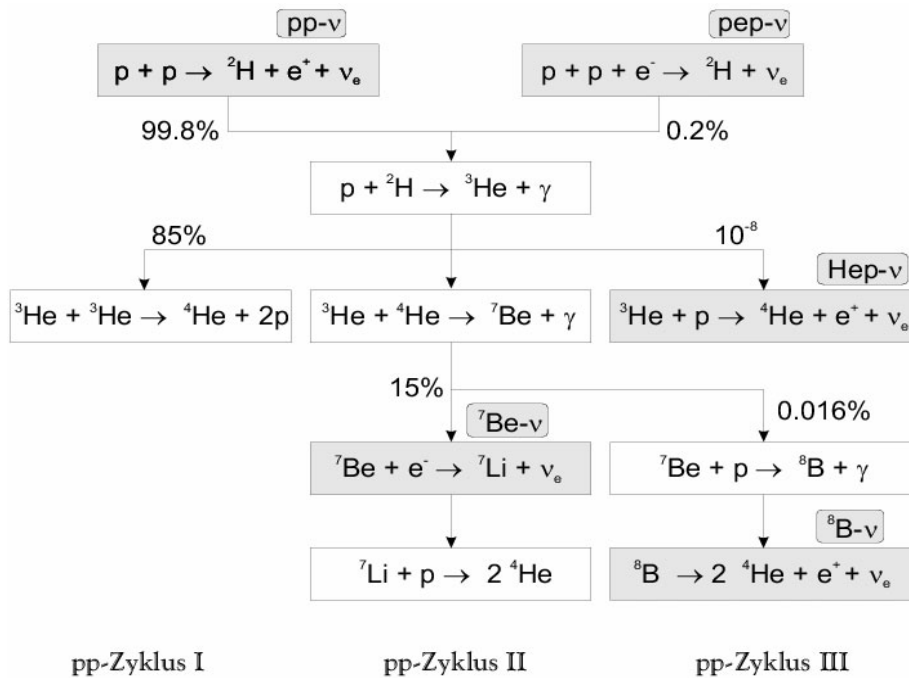


Diagram 1.2: The pp-cycle reactions of the helium fusion in the sun, together with the emitted neutrinos. The sum reaction is  $4 {}^1\text{H}^+ + 2e^- \rightarrow {}^4\text{He}^{2+} + 2\nu_e + 26,73 \text{ MeV}$ .

In particular, a quantitative neutrino flux determination requires the knowledge of the sun temperature, up to  $\sim 1.5 \cdot 10^7 \text{ K}$  in the core, its density profile and the cross sections of the nuclear reactions. A detailed description of the standard solar model can be found in [Bah89] and [Bah01], where also the Table 1.3 has been taken from. The rate of the main reaction, the pp-fusion, is very well settled by the value of the photonic, solar energy radiation. These photons travel  $10^5$  years to leave the dense matter of the sun, whereas neutrinos take about 10 minutes only; but normally the sun, as a light star, is assumed not to change significantly within  $10^5$  years, so that both fluxes refer to equal solar states when arriving on earth. Not mentioned in the above diagram is the so-called CNO fusion cycle, fusing helium out of hydrogen via a chain of nuclear reactions involving C, N and O atoms. The rate of this cycle – normally suppressed – gets especially enhanced at higher temperatures; and indeed, the easiest way to induce changes on the solar model consists in a variation of the sun temperature. As the probabilities of the different fusion reactions – generating neutrinos of different energy – depend diversely on the temperature, their rates get diversely modified in the case of a temperature change. That would indeed question the prerequisites of the solar neutrino rates in a relevant way. A comparison of the standard solar model, in particular of its density profile, to seismological measurements shows an excellent agreement with a discrepancy smaller than 1% [Bah01].

neutrino branch	neutrino flux $\Phi_\nu$ in $\text{cm}^{-2}\text{s}^{-1}$	average energy $E_\nu$ in MeV	maximal energy $E_{\nu, \text{max}}$ in MeV
pp	$(5.95 \pm 0.06) 10^{10}$	0.2668	0.423
${}^7\text{Be}$	$(4.77 \pm 0.48) 10^9$	0.863 (0.386)	0.863 (0.386)
${}^8\text{B}$	$(5.05^{+1.01}_{-0.81}) 10^6$	$6.735 \pm 0.036$	$\approx 15$
pep	$(1.40 \pm 0.02) 10^8$	1.445	1.445
hep	$9.3 \cdot 10^3$	9.628	18.778
${}^{13}\text{N}$	$(5.48^{+1.15}_{-0.93}) 10^8$	0.7063	$1.1982 \pm 0.0003$
${}^{15}\text{O}$	$(4.80^{+1.20}_{-0.91}) 10^8$	0.9964	$1.7317 \pm 0.0005$
${}^{17}\text{F}$	$(5.63 \pm 1.41) 10^6$	0.9977	$1.7364 \pm 0.0003$

Table 1.3: Energy and flux of solar neutrinos according to [Bah01]. The first five lines belong to the pp-cycle, shown in Diagram 1.2. The last three lines arise from the CNO cycle, where C, N and O atoms catalyse the fusion from H to He. The lines with equal average and maximal energies are mono-energetic,  ${}^7\text{Be}$  causes two of such lines.

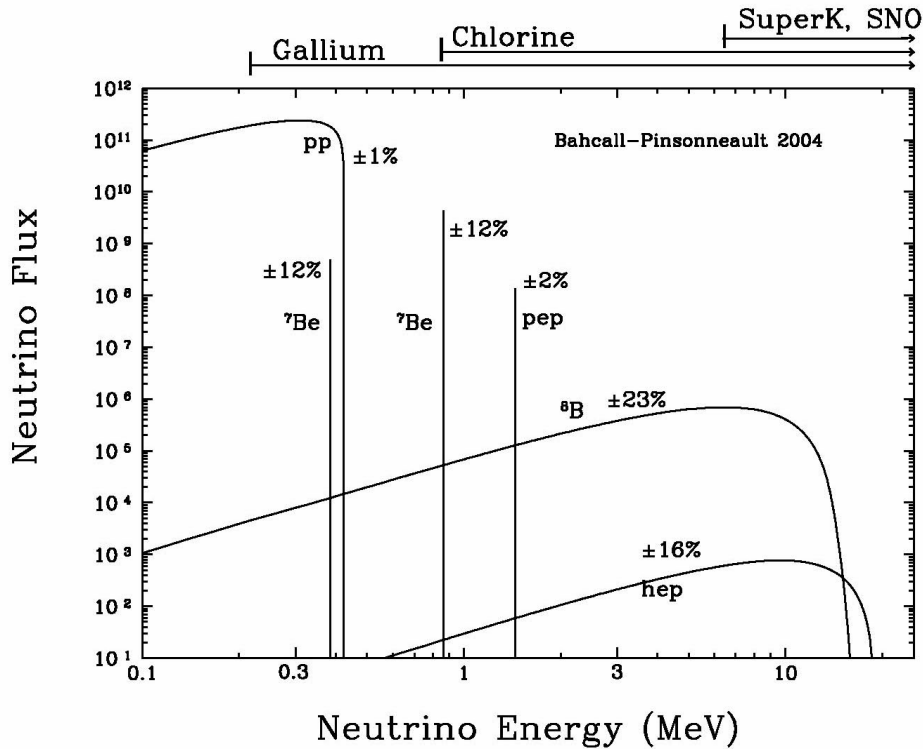


Diagram 1.4: Solar neutrino spectrum and according uncertainties, compared to the thresholds of some neutrino experiments [Bah04]

The reaction cross sections generally arise from the strong interaction theory and have partially been confirmed by experiments, like the LUNA experiment at the Gran Sasso laboratory measures the cross section of the reaction  ${}^3\text{He}({}^3\text{He}, 2p){}^4\text{He}$  in the relevant energy range.

Of course, some uncertainties remain also here; but the standard solar model and the nuclear reaction cross sections, sufficiently known to be considered as presumptions, have generally been used to examine the behaviour of the neutrino. The according solar neutrino experiments are described in the following paragraphs.

## 1.2. Neutrino Oscillations

According to quantum theory, each neutrino is described by a linear combination of elements of a defined basis. The basis can be expressed by a certain number of defined states, each of them perpendicular to each other. In neutrino physics, two different bases are usually introduced: the weak interaction basis, described by the canonical eigenstates  $\nu_e, \nu_\mu, \nu_\tau$ , and the vacuum propagation basis, described by the canonical eigenstates  $\nu_1, \nu_2, \nu_3$ . In order to examine neutrino propagation in matter, a third basis has to be introduced, in dependence on the matter density.

The number of active, i.e. weakly interacting, neutrino states has been experimentally determined to three [Gro00]. Hence, further states could only arise from sterile neutrinos – not interacting but oscillating –, but up to now there is no clear indication for the existence of this type of neutrino. In the following, we assume the number of neutrino states to three.

In this case, a unitary 3x3 matrix  $U$  – yielding three free parameters – describes the transition between the two bases. This transition corresponds to three subsequent rotations by different phase angles  $\theta_{12}, \theta_{13}, \theta_{23}$  between  $0^\circ$  and  $90^\circ$ , like illustrated in the calculation below. There,  $\theta_{12}$  describes the rotation between the  $\nu_1, \nu_2$ -system and the  $\nu_e, \nu_\mu$ -system, and so on. The rotation matrices have to be multiplied by another unitary matrix  $V$  containing three further parameters  $\alpha, \beta, \delta$  in order to account for CP violating processes, i.e. processes yielding different probabilities for transitions between neutrinos (e.g.  $\nu_e \rightarrow \nu_1$ ) compared to transitions between anti-neutrinos (e.g.  $\bar{\nu}_e \rightarrow \bar{\nu}_1$ ). If the neutrino is a dirac particle, whose left-handed state especially interacts with matter and whose right-handed state with anti-matter, only one CP violating phase is allowed ( $\delta \neq 0, \alpha = \beta = 0$ ). In case of a majorana neutrino, where neutrino and anti-neutrino are identical, all three CP violating parameters remain free.

$$\begin{aligned}
 U &= U_{23} \cdot V \cdot U_{13} \cdot U_{12} = \\
 &= \begin{pmatrix} 1 & 0 & 0 \\ 0 & \cos \theta_{23} & \sin \theta_{23} \\ 0 & -\sin \theta_{23} & \cos \theta_{23} \end{pmatrix} \cdot \begin{pmatrix} e^{i\delta} & 0 & 0 \\ 0 & e^{i\alpha} & 0 \\ 0 & 0 & e^{i\beta} \end{pmatrix} \cdot \begin{pmatrix} \cos \theta_{13} & 0 & \sin \theta_{13} \\ 0 & 1 & 0 \\ -\sin \theta_{13} & 0 & \cos \theta_{13} \end{pmatrix} \cdot \begin{pmatrix} \cos \theta_{12} & \sin \theta_{12} & 0 \\ -\sin \theta_{12} & \cos \theta_{12} & 0 \\ 0 & 0 & 1 \end{pmatrix} = \\
 &= \begin{pmatrix} c_{13}c_{12}e^{i\delta} & c_{13}s_{12}e^{i\delta} & s_{13}e^{i\delta} \\ -s_{12}c_{23} - c_{12}s_{13}s_{23} & c_{12}c_{23} - s_{12}s_{13}s_{23} & c_{13}s_{23} \\ s_{12}s_{23} - c_{12}s_{13}c_{23} & -c_{12}s_{23} - s_{12}s_{13}c_{23} & c_{13}c_{23} \end{pmatrix} \quad \text{with} \quad \begin{aligned} s_{ij} &= \sin \theta_{ij} \\ c_{ij} &= \cos \theta_{ij} \end{aligned}
 \end{aligned}$$

$$\text{whereby} \quad |v_\alpha\rangle = \begin{pmatrix} \nu_e \\ \nu_\mu \\ \nu_\tau \end{pmatrix} = U \begin{pmatrix} \nu_1 \\ \nu_2 \\ \nu_3 \end{pmatrix} = U |v_n\rangle \quad \text{or} \quad |v_n\rangle = \begin{pmatrix} \nu_1 \\ \nu_2 \\ \nu_3 \end{pmatrix} = U^{-1} \begin{pmatrix} \nu_e \\ \nu_\mu \\ \nu_\tau \end{pmatrix} = U^{-1} |v_\alpha\rangle$$

The latter equation shows how to transform a neutrino, produced in a weak interaction, into a vector of the vacuum propagation basis  $\nu_1, \nu_2, \nu_3$ , whereby  $U^{-1} = U^\dagger$ . The next step consists in an examination how these vacuum states intend to propagate in vacuum. Hereby, we can remember the temporary behaviour of any wave vector, deriving from the Heisenberg equation:

$$i \frac{\partial}{\partial t} |v_n\rangle = H |v_n\rangle \quad \Rightarrow \quad |v_n(t)\rangle = e^{-iHt} |v_n\rangle$$

The matrix  $H$  is the Hamilton operator, consisting of a kinematical propagation part  $H_{\text{kin}}$  and a dynamic interaction part  $H_{\text{dyn}}$ .  $H_{\text{kin}}$  can be expressed by  $E_{\nu_n} = \sqrt{p^2 + m_n^2} \approx p + m_n^2/2p \approx p + m_n^2$ , with the momentum  $p$  and the mass  $m_n$  of the neutrino state  $\nu_n$ .  $H_{\text{dyn}}$  can be split into the different kinds of interactions in which neutrinos participate. First, that is the neutral current interaction, equal for each neutrino state, implying  $H_{\text{NC}}$  to be a multiple of the identity matrix. Second, there is the charged current interaction, that depends on the lepton masses and thus implies different contributions to different neutrino flavours. Due to their energy range ( $E < m_\mu c^2 < m_\tau c^2$ ), solar neutrinos are able to only generate electrons, so that  $k_\mu$  and  $k_\tau$  vanish in this case. Third, some theory models beyond the standard model examine transitions between different neutrino flavours by new kinds of interactions, which would be expressed by an asymmetric matrix  $H_{\text{trans}}$ .

$$\begin{array}{ccc}
 & H & \\
 \swarrow & & \searrow \\
 H_{\text{kin}} & & H_{\text{dyn}} \\
 p \cdot \mathbb{I} + M/2E & & H_{\text{NC}} + H_{\text{CC}} + H_{\text{trans}} \\
 \left( \begin{array}{ccc} p & 0 & 0 \\ 0 & p & 0 \\ 0 & 0 & p \end{array} \right) + \frac{1}{2E} \left( \begin{array}{ccc} m_1^2 & 0 & 0 \\ 0 & m_2^2 & 0 \\ 0 & 0 & m_3^2 \end{array} \right) & & \left( \begin{array}{ccc} k_{\text{NC}} & 0 & 0 \\ 0 & k_{\text{NC}} & 0 \\ 0 & 0 & k_{\text{NC}} \end{array} \right) + \left( \begin{array}{ccc} k_e & 0 & 0 \\ 0 & k_\mu & 0 \\ 0 & 0 & k_\tau \end{array} \right) + \left( \begin{array}{ccc} 0 & \varepsilon_{e\mu} & \varepsilon_{e\tau} \\ 0 & 0 & \varepsilon_{\mu\tau} \\ 0 & 0 & 0 \end{array} \right)
 \end{array}$$

The two matrices proportional to the identity matrix do not lead to conversions between neutrino states, as they cause oscillations with equal frequencies for all neutrino states. In fact, if neglecting the mentioned non-standard models ( $H_{\text{trans}}=0$ ), there only remains the case  $H=M/2E+H_{\text{CC}}$  with  $k_\mu=k_\tau=0$  to consider. In the above notation, one has to be aware of the basis the different parts of  $H$  refer to. In particular,  $H_{\text{kin}}$  is diagonal in the basis of its eigenstates  $\nu_1, \nu_2, \nu_3$ , with the masses  $m_1, m_2, m_3$  as eigenvalues; whereas the interaction parts  $H_{\text{NC}}$  and  $H_{\text{CC}}$  are diagonal in the basis of the interaction eigenstates  $\nu_e, \nu_\mu, \nu_\tau$ . So, the above matrix expressions of  $H_{\text{kin}}$  and  $H_{\text{dyn}}$  refer to different bases – actually related to each other by the unitary transformation matrix  $U$  – and in particular they cannot be added like this, but only after a transformation of one of them into the basis of the other:

$$\begin{aligned}
 H &= \frac{1}{2E} \begin{pmatrix} m_1^2 & 0 & 0 \\ 0 & m_2^2 & 0 \\ 0 & 0 & m_3^2 \end{pmatrix} + U^{-1} \begin{pmatrix} k_e & 0 & 0 \\ 0 & 0 & 0 \\ 0 & 0 & 0 \end{pmatrix} U = \\
 &= \begin{pmatrix} m_1^2/2E + k_e c_{12}^2 c_{13}^2 & k_e c_{12} s_{12} c_{13}^2 & k_e s_{13} c_{12} c_{13} \\ k_e c_{12} s_{12} c_{13}^2 & m_2^2/2E + k_e s_{12}^2 c_{13}^2 & k_e s_{13} s_{12} c_{13} \\ k_e s_{13} c_{12} c_{13} & k_e s_{13} s_{12} c_{13} & m_3^2/2E + k_e s_{13}^2 \end{pmatrix}
 \end{aligned}$$

The resulting matrix contains the components responsible for the oscillation of solar neutrinos in matter as well as in vacuum. Knowing  $H$  and  $U$ , it is possible to calculate the different oscillation probabilities, i.e. the probabilities  $P(\nu_\alpha \rightarrow \nu_\beta)$  to detect a neutrino in the state  $\nu_\beta$  ( $= \nu_e, \nu_\mu$  or  $\nu_\tau$ ) that originally has been emitted in the state  $\nu_\alpha$  ( $= \nu_e, \nu_\mu$  or  $\nu_\tau$ ). During its propagation, oscillations between different neutrino states are generated by the matrix  $e^{-iHt}$ .

$$P(\nu_\alpha \rightarrow \nu_\beta) = \left| \langle \nu_\beta | \nu_\alpha(t) \rangle \right|^2 = \left| \langle \nu_\beta | U | \nu_n(t) \rangle \right|^2 = \left| \langle \nu_\beta | U e^{-iHt} | \nu_n \rangle \right|^2 = \left| \langle \nu_\beta | U e^{-iHt} U^{-1} | \nu_\alpha \rangle \right|^2$$

## Vacuum oscillations

In the vacuum case, corresponding to  $k_e=0$ , the Hamilton operator  $H$  – reduced to the kinetic part  $H_{\text{kin}}$  – is diagonal in the basis  $\nu_1, \nu_2, \nu_3$ , so that its eigenvalues  $m_n^2/2E$  imply the neutrino masses  $m_n$ . Assuming further the case of dirac neutrinos ( $\alpha=\beta=0$ ), the oscillation probabilities after a distance  $x \approx ct$  amount to

$$\begin{aligned}
 P(\nu_\alpha \rightarrow \nu_\beta) &= \sum_{k,j} U_{\alpha k} U_{k\beta}^{-1} U_{j\alpha}^{-1} U_{\beta j} e^{-i \frac{m_k^2 - m_j^2}{2E} x} = \\
 &= \underbrace{\delta_{\alpha\beta} - 4 \sum_{k>j} \text{Re}(U_{\alpha k} U_{k\beta}^{-1} U_{j\alpha}^{-1} U_{\beta j}) \left[ \sin \left[ \frac{m_k^2 - m_j^2}{4E} x \right] \right]^2}_{\text{CP-conserving}} - \underbrace{2 \sum_{k>j} \text{Im}(U_{\alpha k} U_{k\beta}^{-1} U_{j\alpha}^{-1} U_{\beta j}) \sin \left[ \frac{m_k^2 - m_j^2}{2E} x \right]}_{\text{CP-violating}}
 \end{aligned}$$

The survival probability of an electron-neutrino is

$$\begin{aligned}
 P(\nu_e \rightarrow \nu_e) &= 1 - \left[ \sin \left[ \frac{m_2^2 - m_1^2}{4E} x \right] \right]^2 2 \cos^4 \theta_{13} \sin^2 2\theta_{12} - \\
 &\quad - \left[ \left[ \sin \left[ \frac{m_3^2 - m_1^2}{4E} x \right] \right]^2 \cos^2 \theta_{12} + \left[ \sin \left[ \frac{m_3^2 - m_1^2}{4E} x \right] \right]^2 \sin^2 \theta_{12} \right] \sin^2 2\theta_{13} \\
 &\stackrel{\theta_{13}=0}{=} 1 - \left[ \sin \left[ \frac{m_2^2 - m_1^2}{4E} x \right] \right]^2 \sin^2 2\theta_{12}
 \end{aligned}$$

This already illustrates in the simplest two-dimensional case ( $\theta_{13}=0$ ), that a non-vanishing neutrino mass difference and a non-zero rotation angle are required to make the effect of neutrino flavour oscillations visible – otherwise one obtains  $P(\nu_\alpha \rightarrow \nu_\alpha)=1$  and  $P(\nu_\alpha \rightarrow \nu_\beta)=0$ . CP violating components ( $\delta \neq 0$ ) require all three rotation angles to be non-zero and only influence the oscillation probabilities  $P(\nu_\alpha \rightarrow \nu_\beta)$  between different flavours. Experimental determinations of these parameters will be described in 1.2.

## Matter oscillations

The influence of a matter distribution is represented by the constant  $k_e$  for the electron-like charged current interaction of neutrinos in a defined matter density  $\rho$ . In particular, the corresponding interaction is proportional to the electron density  $N_e$  and the Fermi constant  $G_F$ . Assuming one electron per two nucleons, the electro-weak interaction theory implies  $k_e = \pm \sqrt{2} G_F N_e = \pm \sqrt{2} G_F (\rho/2m_{\text{nucleon}})$ ; the negative sign has to be used in case of anti-neutrinos. As the matter term causes the matrix  $H$  to be asymmetric, the eigenvalues of  $H$  will now differ from the vacuum eigenvalues and lead to modified *effective neutrino masses*  $m_{1m}, m_{2m}, m_{3m}$ . At high electron densities  $N_e$ , it is even possible, that  $m_{1m}$  becomes bigger than  $m_{2m}$  or  $m_{3m}$ . For a determination of the  $m_{im}$ ,  $H$  can be diagonalised by the definition of a third basis  $\nu_{1m}, \nu_{2m}, \nu_{3m}$  for propagation in matter. The modified rotation angles  $\theta_{12m}, \theta_{13m}, \theta_{23m}$ , describing the transformation between this matter propagation basis and the weak interaction basis, are no new natural constants, but they will be – as said above – determined by the matter composition, the weak interaction theory and the vacuum rotation angles  $\theta_{12}, \theta_{13}, \theta_{23}$ . A quantitative calculation of all modified masses and rotation angles in the three-dimensional neutrino flavour space can be found in [Ohl00]. Using the modified parameters, the above calculation of the oscillation probabilities for the vacuum case can be directly applied on the matter case.

A consideration of the two-dimensional case – where the CP violation becomes impossible – is illustrated in [Schm97]. As in electron-like matter the  $\nu_\mu$ -interaction does not differ from the  $\nu_\tau$ -interaction, there is no direct matter oscillation between  $(\nu_2, \nu_3)$  and  $(\nu_{2m}, \nu_{3m})$ , so that the three-dimensional matter oscillation scenario can be split into two parallel two-dimensional scenarios  $(\nu_e, \nu_\mu) \leftrightarrow (\nu_{1m}, \nu_{2m})$  and  $(\nu_e, \nu_\tau) \leftrightarrow (\nu_{1m}, \nu_{3m})$ . In this case, the corresponding rotation angles in the two-dimensional neutrino flavour space amount to

$$\sin^2 2\theta_{12m, 2\text{-dim}} = \frac{\sin^2 2\theta_{12, 2\text{-dim}}}{\sqrt{\left(\frac{k_e}{m_2^2 - m_1^2} - \cos 2\theta_{12, 2\text{-dim}}\right)^2 + \sin^2 2\theta_{12, 2\text{-dim}}}}$$

$$\sin^2 2\theta_{13m, 2\text{-dim}} = \frac{\sin^2 2\theta_{13, 2\text{-dim}}}{\sqrt{\left(\frac{k_e}{m_3^2 - m_1^2} - \cos 2\theta_{13, 2\text{-dim}}\right)^2 + \sin^2 2\theta_{13, 2\text{-dim}}}}$$

$$\theta_{23m, 2\text{-dim}} = \theta_{23, 2\text{-dim}}$$

For  $k_e=0$  we especially obtain  $\theta_{ijm}=\theta_{ij}$ . The propagation of neutrinos in matter, maintaining the states  $\nu_{1m}, \nu_{2m}, \nu_{3m}$ , generates oscillations between the eigenstates of all other bases, in particular oscillations between the states  $\nu_e, \nu_\mu, \nu_\tau$  and between the states  $\nu_1, \nu_2, \nu_3$ . In this way, neutrinos entering a matter distribution begin to oscillate between the states  $\nu_1, \nu_2, \nu_3$  and will possibly have assumed a different flavour when leaving the matter again.

### *The MSW effect*

The so-called Mikheyev-Smirnov-Wolfenstein effect consists in a resonant neutrino flavour conversion inside a variable matter distribution in case of a corresponding non-zero vacuum mixing angle. Its influence on the solar neutrino flux is described in detail in [Schm97]. Looking at the approximation of  $P(\nu_e \rightarrow \nu_e)$  for  $\theta_{13}=0$  above – motivated, as the experiments really show  $\theta_{13}$  to be small – one can identify the amplitude of the oscillating probability  $P(\nu_e \rightarrow \nu_\mu)$  to  $\sin^2 2\theta_{12}$ . Of course, in matter one has to consider  $\sin^2 2\theta_{12m}$ , approximated well enough by the  $\sin^2 2\theta_{12m, 2\text{-dim}}$  above. This amplitude in case of  $k_e \rightarrow 0$  behaves like  $\sin^2 2\theta_{12m, 2\text{-dim}} \rightarrow \sin^2 2\theta_{12, 2\text{-dim}}$ , in case of  $k_e \rightarrow \infty$  like  $\sin^2 2\theta_{12m, 2\text{-dim}} \rightarrow 0$ , and especially in the *resonance case* of  $k_e = (m_2^2 - m_1^2) \cos 2\theta_{12m, 2\text{-dim}}$  like  $\sin^2 2\theta_{12m, 2\text{-dim}} = 1$ . The singularity of the resonance case consists in reaching a maximal oscillation amplitude at a certain electron density, independently of the vacuum mixing angle  $\theta_{12} \neq 0$ .

Now, in the special case of a neutrino traversing a decreasing electron density  $N_e$  – like a neutrino produced inside the sun and travelling outwards – it has also to cross a layer, where the electron density causes the resonance case, thus locally yielding the maximal oscillation probability of 1. [Schm97] shows that, if a neutrino of a certain vacuum state (e.g.  $\nu_1$ ) traverses this resonance layer adiabatically, – i.e. if the matter density changes slowly compared to the neutrino oscillation length – it gets converted into the other vacuum state ( $\nu_2$ ) in any case. [Kim93] determines the survival and conversion probability of the MSW effect, expressed in the weak interaction basis, to

$$P_{\text{MSW}}(\nu_e \rightarrow \nu_e) = \frac{1}{2}(1 + \cos 2\theta_{12m} \cos 2\theta_{12}) \quad \text{and} \quad P_{\text{MSW}}(\nu_e \rightarrow \nu_\mu) = \frac{1}{2}(1 - \cos 2\theta_{12m} \cos 2\theta_{12})$$

with  $\theta_{12m}$  being the mixing angle at the place of the neutrino production. However, the MSW effect requires two conditions; these are both an adiabatic neutrino translation and a sufficient

matter density to enable resonance. In particular, the first condition puts a lower limit and the second an upper limit on the energy of the neutrino, thus allowing the MSW effect in a certain energy range only. Diagram 1.5 shows that this energy range gets shifted by changing vacuum oscillation parameters, which are the neutrino mass difference  $D=m_2^2-m_1^2$  and the vacuum mixing angle  $\theta_{12}$ . Like this, the observation of a presence or absence of the MSW survival/conversion probabilities already implies constraints on the neutrino parameters. An assumption of the standard solar model together with the recent neutrino parameters indeed enables the MSW effect in the sun.

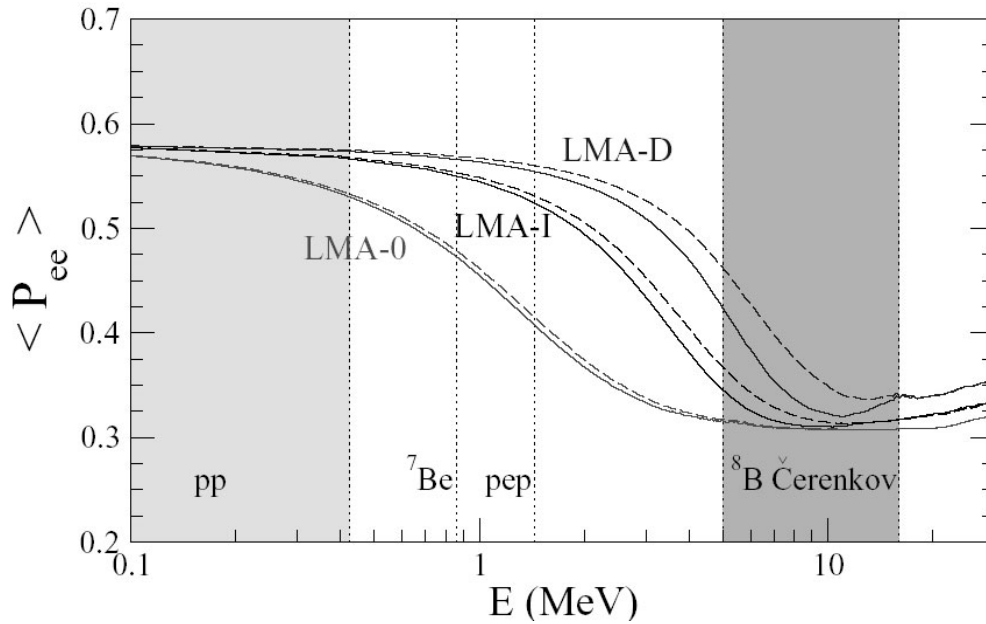


*Diagram 1.5:  $\nu_e$  survival possibility for different neutrino energies and different oscillation parameters (LMA-I, -0, -D). LMA-I corresponds to  $\Delta m^2=8.3 \cdot 10^{-5} eV^2$ ,  $\sin^2\theta=0.30$ . LMA-0 ( $\Delta m^2=1.4 \cdot 10^{-5} eV^2$ ,  $\sin^2\theta=0.30$ ) and LMA-D ( $\Delta m^2=8.3 \cdot 10^{-5} eV^2$ ,  $\sin^2\theta=0.70$ ) are solutions arising from the consideration of non-standard neutrino-matter interactions like flavour-changing or non-universal interactions. The MSW effect distinguishes between these different LMA solutions [Mir04a].*

Apart from this, anti-neutrinos in matter cannot be influenced by the MSW effect, because  $k_e < 0$  does not allow the resonance case.

In theoretical calculations of flavour resolved, solar neutrino fluxes on earth, both the vacuum oscillation on the way between sun and earth and the MSW effect inside the sun have to be accounted for. Additionally, matter oscillations inside the earth can lead to day-night-variations in the flux.

### 1.3. Solar Neutrino Experiments

During the past decades, the nature of the neutrino has been one of the most exciting questions in physics. A lot of effort has been put into neutrino detectors in order to reach a satisfying solution. Only huge target masses can rise the hope of provoking some neutrino reactions inside the detectors, whereby the next complicated task consists in the suppression of background events. The solar neutrino experiments are described in the following.

### 1.3.1. Radiochemical Experiments

Radiochemical experiments constituted the first approach to a non-standard behaviour of the neutrino. The chlorine experiment Homestake and the gallium experiments Gallex, GNO and SAGE first observed a solar neutrino flux significantly lower than the predicted one, in this way having motivated the recent neutrino experiments. Today, the radiochemical experiments have remained the only ones to confirm the neutrino oscillations in a sub-MeV energy range.

#### *Homestake*

In the year 1968, in order to confirm the thermonuclear fusion as source of solar energy, Homestake began to first detect solar neutrinos by the inverse beta decay  $^{37}\text{Cl} + \nu_e \rightarrow ^{37}\text{Ar} + e^-$ . The threshold of this reaction is at 814 keV, thus excluding the pp- and one line of the  $^7\text{Be}$ -neutrinos from the detection. The energy of the detected neutrinos, even if above the threshold, was not determined. The  $^{37}\text{Cl}$  was contained in 615 tons of a  $\text{C}_2\text{Cl}_4$  solution stored in the Homestake mine, USA, at a depth of 4200 m.w.e. After the solution was exposed to the solar neutrino flux for some months, the resulting  $^{37}\text{Ar}$  atoms were extracted with the help of helium gas, in order to determine their amount by the observation of the decay to  $^{37}\text{Cl}$  in proportional counters afterwards. As the rest energy of the  $\mu$  and  $\tau$  lepton exceed the solar neutrino energy, the inverse beta decay of  $^{37}\text{Cl}$  can only produce electrons, so that it is sensitive only to electron neutrinos. Hence, a  $\nu_e$  disappearance was observed. After 25 years of data taking, the result amounted to a neutrino rate of  $R_{\text{Homestake}} = (2.56 \pm 0.16(\text{stat.}) \pm 0.16(\text{sys.}))$  SNU [Dav98]. That roughly is one third of the predicted rate  $R_{\text{SSM}} = (7.6^{+1.3}_{-1.1})$  SNU [Bah01] by the standard solar model.

#### *Gallex, GNO and SAGE*

Motivated by the aim of covering the whole solar neutrino energy spectrum, these experiments detect neutrinos by the inverse beta decay  $^{71}\text{Ga} + \nu_e \rightarrow ^{71}\text{Ge} + e^-$ . With an energy threshold at 233 keV, that up to now is the only method to observe – even if only partially – the pp-neutrino flux. All other solar neutrinos contribute with their entire energy spectrum to the signal rates of these experiments. The neutrino energy however cannot be determined, and the experiments are sensitive to electron neutrinos only. The instable  $^{71}\text{Ge}$  atoms are extracted from the detector target in periods of  $\sim 1$  month, transformed to  $\text{GeH}_4$  gas, whose activity can be determined in proportional counters. Both experimental set-ups have been successfully tested by an exposure of the neutrino targets to a strong  $^{51}\text{Cr}$  source of a known neutrino production.

The experiment Gallex (1991-1997) and its follower GNO (1998-2003) detected solar neutrinos in a  $\text{GaCl}_3$  solution containing 30 tons of gallium at the Gran Sasso underground laboratory (3600 m.w.e.) in Italy. Hereby, GNO constituted an upgrade, improving the systematic error with respect to Gallex by an advanced technique concerning the  $^{71}\text{Ge}$  activity counting. The resulting neutrino rates are  $R_{\text{Gallex}} = (77.5 \pm 6.2(\text{stat.}) \pm 4.5(\text{sys.}))$  SNU,  $R_{\text{GNO}} = (62.9 \pm 5.4(\text{stat.}) \pm 2.5(\text{sys.}))$  SNU and the average  $R_{\text{Gallex+GNO}} = (69.3 \pm 4.1(\text{stat.}) \pm 3.6(\text{sys.}))$  SNU [Cat04]. They show a clear  $\nu_e$  disappearance compared to the full rate  $R_{\text{SSM}} = (129^{+8}_{-9})$  SNU [Bah98] according to the standard solar model.

The experiment SAGE, still operating, is located in the INR laboratory (4700 m.w.e.) at Baksan, Russia, using 60 tons of metallic gallium. The most recent result amounts to  $R_{\text{SAGE}} = (66.9 \pm 3.9(\text{stat.}) \pm 3.6(\text{sys.}))$  SNU [Gav01]. Compared to the above  $R_{\text{SSM}}$  value and in agreement with Gallex and GNO, it shows the same level of  $\nu_e$  disappearance.

The combined result of Gallex, GNO and SAGE amounts to  $68.1 \pm 3.75$  SNU [Cat04].

### 1.3.2. Water Cherenkov Detectors

The Cherenkov effect of fast electrons in water – scattered or emitted in neutrino driven processes – has turned out to provide a very practicable way of real-time neutrino detection. Large amounts of water can easily be procured, handled and purified, so that on the one hand a big target mass can compensate for the inferior detection capability of water compared to scintillators; and on the other hand the real-time detection offers superior information with respect to radiochemical methods. Leptons with a velocity above the speed of light in water cause a coherent shock wave of light, the Cherenkov radiation, detected by surrounding photomultipliers. The properties of the light signal allow to determine the event energy, the time, the flight direction and even to distinguish between electron and muon events. Background usually is suppressed by a comparatively high energy threshold in the MeV range, making these experiments aim for solar  $^8\text{B}$ , atmospheric and supernova neutrinos.

#### *Superkamiokande*

The Superkamiokande detector, as well as its forerunner, the smaller Kamiokande detector, is located in the Kamioka mine, Japan, at 2700 m.w.e. It contains 50000 tons of water, 22000 tons of which constitute the active detector volume (fiducial volume), and 11146 photomultipliers covering 40% of the entire steradian. The rest of the water volume surrounds the fiducial volume, shields it from exterior radiation and, particularly, acts as an active muon veto. In the detector, neutrinos can scatter on electrons by the charged current interaction  $\nu_\alpha + e^- \rightarrow \bar{\alpha} + \nu_e$  or the neutral current interaction  $\nu_\alpha + e^- \rightarrow \nu_\alpha + e^-$ , producing relativistic leptons, detectable by their Cherenkov light. Hereby, the CC cross section is higher by a factor of  $\approx 5.5$  than the NC cross section; and solar neutrinos can only generate electrons. For fast recoil leptons, corresponding to quite centric hit processes, the lepton energy and direction correspond more or less to those of the neutrino. In this way, comparing the direction signature of the scattered electrons to the sun position, the detector is able to discriminate solar neutrino events. A threshold of  $\sim 5$  MeV allows the detection of  $^8\text{B}$ - and hep-neutrinos only. During its first run from 1996 to 2001 (1496 days), Superkamiokande detected a solar  $^8\text{B}$  neutrino flux of  $(2.35 \pm 0.02(\text{stat.}) \pm 0.08(\text{sys.})) 10^6$  events/cm<sup>2</sup>·s, which are 14.5 events per day. The value corresponds to  $(40.6 \pm 0.4(\text{stat.})^{+1.4}_{-1.3}(\text{sys.}))\%$  of the predicted rate [Nak04]. As a real-time detector, Superkamiokande is moreover able to look for a day-night-asymmetry in the event rate, possibly caused by an additional matter oscillation effect in the earth. The result of the first run however is consistent with zero:  $A_{\text{DN}} = 2(R_{\text{day}} - R_{\text{night}})/(R_{\text{day}} + R_{\text{night}}) = 0.021 \pm 0.020(\text{stat.})^{+0.013}_{-0.012}(\text{sys.})$  [SK02].

Apart from solar neutrinos, a further contribution of the Superkamiokande experiment consists in the detection of atmospheric neutrinos in the GeV range. They are produced by cosmic radiation scatterings in the earth atmosphere with a ratio of  $(\nu_\mu + \bar{\nu}_\mu) / (\nu_e + \bar{\nu}_e) = 2$ . As, due the GeV energy range, the CC scattering of  $\nu_\mu$  on electrons is able to produce muons, and as these can be distinguished from electrons by the characteristics of their Cherenkov signal, the detector is able to distinguish  $\nu_e$ - and  $\nu_\mu$ - rates. In this way, in 1998 Superkamiokande discovered the neutrino oscillation scenario in the  $\nu_\mu$ - $\nu_\tau$ -sector. In the meantime, the range of  $\Delta m_{23}^2$  has been determined to  $[1.9 \cdot 10^{-3}; 3.0 \cdot 10^{-3}]$  eV<sup>2</sup> and the corresponding mixing angle to  $\sin^2 2\theta_{23} > 0.90$ , both by 90% of C.L. [SK04]. The result has additionally been confirmed by the accelerator experiment K2K.

Unfortunately, at the end of 2001 a big number of photomultipliers in Superkamiokande had broken unexpectedly. At the moment, a second run with a limited number of 5182 phototubes, covering 19%, is performed until 2005. The current data of this second run confirm the above results. The detector is planned to be fully reconstructed by 2006.

### *Sudbury Neutrino Observatory (SNO)*

The SNO detector in Sudbury, Canada, at a depth of 6000 m.w.e. contains 1000 tons of heavy water ( $D_2O$ ) in an acrylic vessel, shielded by 7000 tons of normal water. First, heavy water enables fast leptons to emit Cherenkov light just as normal water does. In this way, the detector can see CC and NC neutrino-electron scattering processes ( $\nu_\alpha + e^- \rightarrow \nu_\alpha + e^-$ ) like Superkamiokande. In particular, the SNO detector volume is not big enough to reach good statistics for atmospheric neutrinos. The more numerous solar neutrino events are recognized by their orientation to the sun position. Second, as main advantage of heavy water, neutrinos provoke two different reactions on deuterium: On the one hand, it can convert the neutron to a proton ( ${}^2D + \nu_e \rightarrow p + p + e^-$ ) by a charged current interaction, that in the energy range of solar neutrinos only is possible for electron neutrinos and that is recognised by the Cherenkov light of the electron. Here, the direction of the electrons after the reaction is differently distributed compared to the above electron scattering, thus allowing a distinction between these event groups by a fit. On the other hand, the neutrino can split neutron and proton ( ${}^2D + \nu_\alpha \rightarrow n + p + \nu_\alpha$ ) by a neutral current scattering, with an equal cross section for all neutrino flavours and distinguishable by the signature of the neutron. This gets thermalised and captured by deuterium, forming tritium and emitting a 6.25 MeV gamma. The gamma deposits its energy on electrons emitting Cherenkov light.

As the neutron capture cross section of deuterium is low and the signature of the gamma not particular, the experiment has been upgraded in 2001 with 2 tons of NaCl salt, containing the isotope  ${}^{35}Cl$  (phase II). Its advantages consist in a higher cross section for the reaction  ${}^{35}Cl + n \rightarrow {}^{36}Cl^* \rightarrow {}^{36}Cl + \gamma$ 's and a gamma cascade of 8.6 MeV in total, now clearly above the detector threshold. Recently, in a second upgrade, the salt was removed again and 40 strings of  ${}^3He$  proportional counters have been installed in order to independently observe neutrons by the reaction  $n + {}^3He \rightarrow p + {}^3H + 0.76MeV$  in the counters and to identify NC reactions event by event. Data taking of the new phase III is ongoing.

In particular, the detector is able to distinguish CC events – caused by  $\nu_e$  only – from NC events, caused by all flavours  $\nu_\alpha$  with equal probability, and thus to separately determine the  $\nu_e$  rate and the  $\nu_\mu + \nu_\tau$  rate. Moreover, the  $\nu_\alpha - e^-$  scattering rate (ES) – caused by a specifically weighted sum of all three flavours,  $6.5\nu_e + \nu_\mu + \nu_\tau$  – even provides a cross check of the two other rates, like Diagram 1.6 shows.

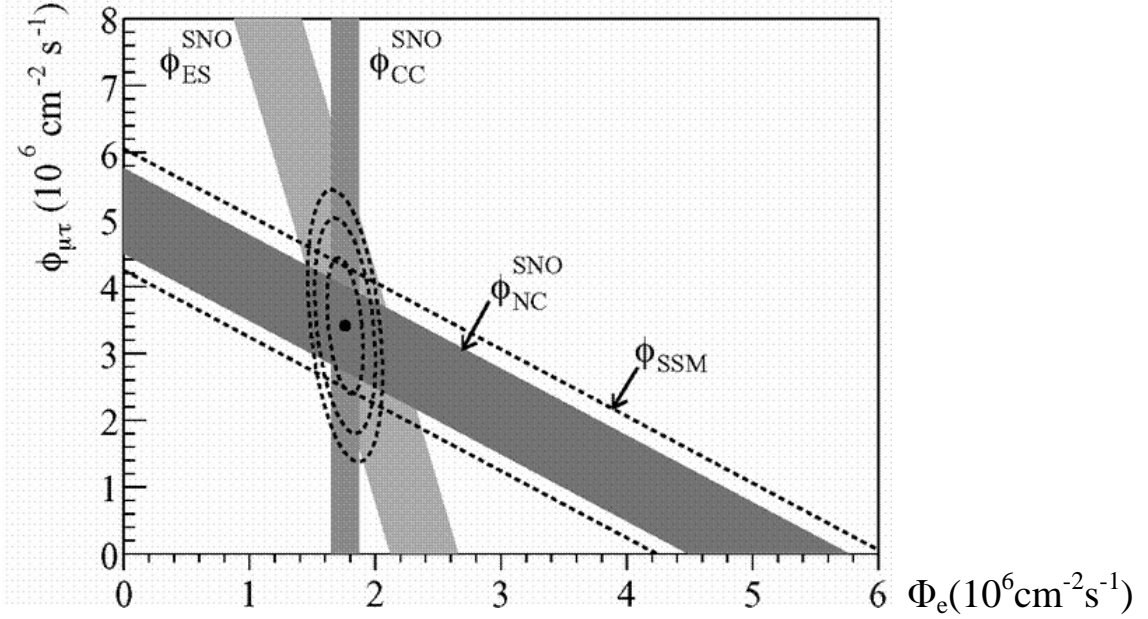


Diagram 1.6: Graphics of the SNO Phase I result (1999-2001).  $\Phi_{ES} = \Phi_e$  and  $\Phi_{CC} = 6.5\Phi_e + \Phi_\mu + \Phi_\tau$  determine the  $\Phi_e$  part and the  $\Phi_\mu + \Phi_\tau$  part of the total flux,  $\Phi_{SSM} = \Phi_{NC} = \Phi_e + \Phi_\mu + \Phi_\tau$  [Rob03].

In this way, SNO was able to prove solar neutrino oscillations, observing the first evidence for a  $\nu_\mu$  or  $\nu_\tau$  appearance during phase I. As the corresponding  $\Delta m^2$  was smaller than the one already observed by atmospheric neutrino oscillations ( $\nu_\mu \leftrightarrow \nu_\tau$ ) in Superkamionde, the solar neutrino oscillations were attributed to the ( $\nu_e \leftrightarrow \nu_\mu$ ) scenario. At that time, the SNO result implied to prefer a special region – the LMA region – among all the considered ones in the neutrino parameter space. Besides, SNO was – and still is – consistent with all other solar neutrino experiments, in particular with the neutrino-electron scattering rate of the Superkamiokande result. In the following, the LMA parameter region has been singled out as the only one and even further been constrained by phase II of SNO and by KamLand. The latest SNO phase II results are  $\Phi_{CC} = (1.59^{+0.08}_{-0.07}(\text{stat.})^{+0.06}_{-0.08}(\text{sys.}))10^6 \text{ cm}^{-2} \text{ s}^{-1}$ ,  $\Phi_{ES} = (2.21^{+0.31}_{-0.26}(\text{stat.}) \pm 0.10(\text{sys.}))10^6 \text{ cm}^{-2} \text{ s}^{-1}$  and  $\Phi_{NC} = (5.21 \pm 0.27(\text{stat.}) \pm 0.38(\text{sys.}))10^6 \text{ cm}^{-2} \text{ s}^{-1}$  [SNO04], in agreement with the above results of phase I. The NC event rate is further in agreement with solar models.

### 1.3.3. Scintillation Detectors

The real-time detection of low energy solar neutrinos still is an unsolved problem. Especially scintillation detectors can help out here, where photon emissions, generated by excited molecular states in special solid or liquid substances – the scintillators – make visible events down to the keV range. The experiment destined to solve this task principally is the liquid scintillation detector Borexino, being under preparation at the Gran Sasso Laboratory in Italy for about 10 years. The detection threshold of such a detector finally gets limited by radioactive or muon generated background. A detailed description of Borexino follows in Chapter 2.

The detection of reactor anti-neutrinos, simpler to realise because of the event signature, is however successfully performed by the KamLand experiment in Japan.

## KamLand

Even if not detecting solar neutrinos, KamLand is able to contribute to the solar neutrino oscillation problem in a relevant way by the observation of anti-neutrino oscillations in the  $(\bar{\nu}_e, \bar{\nu}_\mu)$ -sector. Here, it is important to mention that only in the case of CPT invariance the anti-neutrino sector is determined by the same parameter values as the neutrino sector. The scintillation detector KamLand in the Kamioka mine, Japan, measures anti-neutrinos from several surrounding nuclear reactors, very intense sources of anti-electron neutrinos produced in beta decays of neutron-rich fission fragments. It contains 1000 tons of liquid scintillator (80% dodecane, 20% pseudocumene), surrounded by 1900 phototubes and an active water Cherenkov muon veto detector. Anti-electron neutrinos interact mainly with protons – providing a higher cross section than electrons – by the inverse beta decay  $\bar{\nu}_e + p \rightarrow n + e^+$ ; the neutron gets thermalised and captured by another proton about 200 $\mu$ s later, emitting a 2.2 MeV gamma. These anti-neutrino events are discriminated by the coincidence of that gamma together with the  $e^+e^-$  annihilation, providing a detector threshold of 1.8 MeV.

Since KamLand has started to take data in 2002, it has been observing neutrino oscillations by a disappearance of anti-electron neutrinos. The expected neutrino rate is calculated with the single distances and neutrino fluxes of all surrounding nuclear reactors, even varying when reactors are turned on or off. The best fit of KamLand's data to neutrino oscillations yields  $\Delta m^2 = 8.3 \cdot 10^{-5} \text{eV}^2$ , considered as the  $\nu_e - \nu_\mu$  mass difference, and  $\sin^2 2\theta = 0.83$  for the corresponding mixing angle [Ara04]. The agreement with the results of all solar neutrino experiments – mainly SNO – is excellent, thus giving no indication for CPT violation. Assuming CPT invariance, KamLand provides a big quantitative improvement on the value of the mass difference, whereas the determination of the rotation angle is not influenced significantly (see Diagram 1.7).

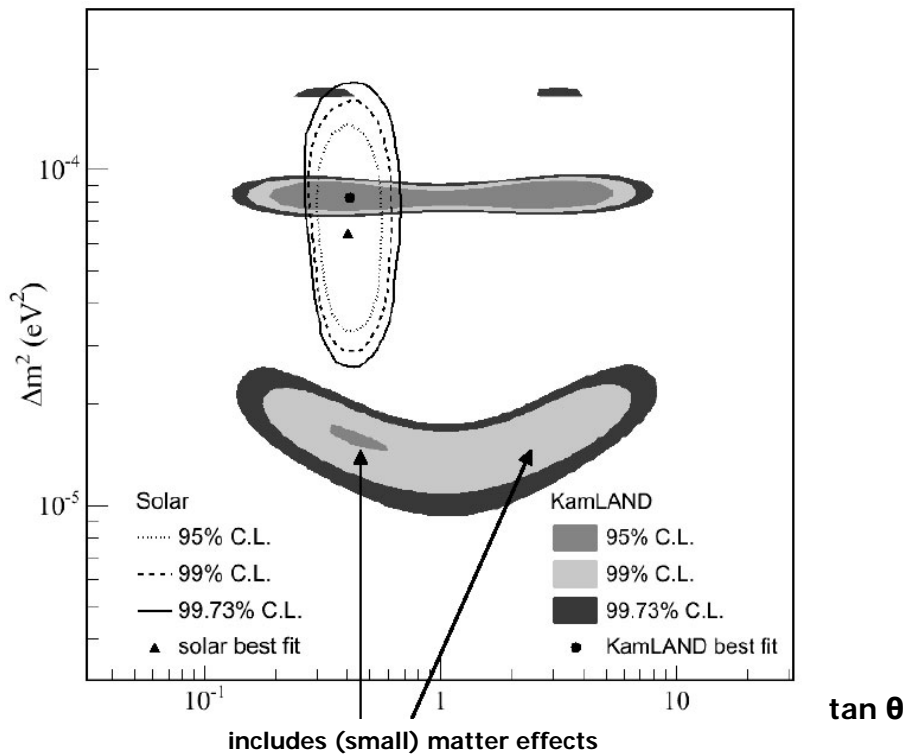


Diagram 1.7: Comparison of KamLand with the solar neutrino experiments' data (mainly SNO) in the  $(\nu_e, \nu_\mu)$  oscillation parameter space [Gra04]

Moreover, the detection of solar neutrinos in KamLand could be feasible – as KamLand has been constructed close to the Borexino detector design. However, the background rate in KamLand, mainly caused by  $^{222}\text{Rn}$  daughters, is currently too high, and an improvement of the scintillator radiopurity by some orders of magnitude would be necessary. KamLand might be aiming for that.

#### 1.4. Answers and Open Questions

The experiments described in the preceding paragraphs have determined a notable part of the neutrino parameters: non-zero mass differences and mixing angles. They have proven the existence of neutrino oscillations and reached a status that ten years ago still seemed far away. This progress mainly concerns

$$\begin{aligned}\Delta m^2_{12} &= [7.3; 9.4] \cdot 10^{-5} \text{eV}^2 \text{ at } 99\% \text{ C.L. [Gos04]} \\ \Delta m^2_{23} &= [1.9; 3.0] \cdot 10^{-3} \text{eV}^2 \text{ at } 90\% \text{ C.L. [SK04]} \\ \sin^2\theta_{12} &= [0.22; 0.36] \text{ at } 99\% \text{ C.L. [Gos04]} \\ \sin^2\theta_{23} &> 0.90 \text{ at } 90\% \text{ C.L. [SK04]}\end{aligned}$$

All considerations of solar neutrinos include the MSW effect, that influences the neutrino rate exiting from the sun. In particular, the MSW effect – and here the existence of matter oscillations – is confirmed by the solar neutrino experiments, which observe a survival possibility of  $P(\nu_e \rightarrow \nu_e) < 0.5$ . In case of no matter influence, only values  $P(\nu_e \rightarrow \nu_e)$  between 0.5 and 1 – in dependence on  $\sin^2\theta_{12}$  – would be able to result, arising from the average of the survival probability  $P(\nu_e \rightarrow \nu_e)$  over the variable  $x/E$ .

The values of the mixing parameters in the  $\nu_e$ - $\nu_\tau$ -sector still lack a direct measurement by an appearance experiment. The data of the Chooz-Experiment [Apo03], together with the latest Superkamiokande data yield the upper limit  $\sin^2\theta_{13} < 0.05$  at  $3\sigma$  bounds [Gos04]. As  $\theta_{13}$  seems close to zero, the  $\nu_e$ - $\nu_\tau$  oscillation often is neglected. The planned experiment Double-Chooz aims to improve the limit within some years (see 1.5). The according mass difference can be calculated by  $\Delta m^2_{13} = \Delta m^2_{12} + \Delta m^2_{23}$ . Here, the remaining problem consists in the unknown absolute mass values  $m_1, m_2, m_3$  – already the knowledge of one of them would be sufficient to calculate the others. At the moment, mainly cosmology arguments constrain the neutrino masses to less than  $\sim 1\text{eV}$ . Beta decay and double beta decay experiments try to reach a lower range but also real-time detectors like Borexino could improve this limit by observing travel time differences of the various neutrino flavours on the long way from a supernova to earth.

It is important to note, that all values of mixing angles depend on their specific definition, the parametrisation of the mixing matrix  $U$  (see 1.2). In particular, the elements of the matrix  $U$  get expressed in dependence on the parametrisation but the values themselves of these matrix elements are natural constants, independent of other definitions. Up to now, the experimental data has lead to the following approximation of  $U$  [Alt04]:

$$U = \begin{pmatrix} 0.84 & 0.54 & \approx 0.1 \\ -0.44 & 0.56 & 0.71 \\ 0.32 & -0.63 & 0.71 \end{pmatrix}$$

The CP violating parameters  $\alpha, \beta, \delta$  are completely undetermined up to now. As there is no indication for a CP violation in the neutrino sector, they get neglected in a big part of considerations. Even the original nature of the neutrino – dirac or majorana particle – is not

settled; let us remember that only majorana neutrinos imply the necessity of  $\alpha$  and  $\beta$ . A part of the Heidelberg-Moscow collaboration claims to have observed a neutrino-less double beta decay of  $^{76}\text{Ge}$  [Kla04], identifying the neutrino as majorana particle, but with a look on the results' impact on neutrino physics, a confirmation is missing to settle this observation.

So far, neutrino oscillations provide an excellent model to explain the discrepancy between the neutrino experiments' results and the expected neutrino rates without oscillations. On the other hand, it is important to question the oscillation parameters with respect to uncertainties in the assumptions. As already mentioned in 1.1, the standard solar model has mostly been confirmed by the helioseismology, i.e. by measurements of seismic modes in the sun matter [Bah01]. Furthermore, according to [Bur03], SNO and KamLand results prove the oscillation parameters concerning their robustness against fluctuations in the density profile of the sun.

However, a serious problem could arise from non-standard interactions. These could consist in transformations between different neutrino flavours by interaction with matter, like described by a non-zero matrix  $H_{\text{trans}}$  in Chapter 1.2. In particular, [Mir04a] shows that a non-standard scenario of this kind would enable two further pairs of  $(\Delta m^2_{12}, \theta_{12})$ , the so-called LMA-0 and LMA-D solutions (compare diagram 1.5), to agree with the whole experimental data set. In this case, more precise KamLand measurements would not resolve the ambiguity, yet, future solar neutrino experiments – like Borexino – could be able to rule out such non-standard scenarios with the help of the MSW effect on  $^7\text{Be}$  or  $^8\text{B}$  neutrinos.

Another parameter able to influence neutrino rates is the magnetic moment of the neutrino. In this way, neutrinos (in case of CPT invariance only dirac neutrinos) can be converted to anti-neutrinos by an interaction of the neutrino magnetic moment with the proton spin. The solar neutrino rate would decrease and solar anti-neutrinos would appear. KamLand, sensitive to anti-neutrinos by the inverse neutron decay, has observed the limit  $\Phi(\bar{\nu}_e) < 370 \text{cm}^{-2}\text{s}^{-1}$  at 90% C.L. [Egu04] in the region between 8.3 and 14.8 MeV. This yields an upper limit of a few  $10^{-12} \mu_B$  for the magnetic moment [Mir04b]. Astrophysical sources yield a limit of  $\mu_\nu < 10^{-12} \mu_B$ , depending however on supernova models. The solar neutrino experiment Borexino (see Chapter 2) will be able to provide a sensitivity to electron anti-neutrinos comparable to Kamland, but in a wider energy range, due to its distant location from nuclear reactors. Apart from that, as second type of a possible magnetic moment interaction, big magnetic fields can cause a helicity flip on solar neutrinos, turning them right-handed and making them invisible. In this way, a magnetic moment in the range of  $10^{-11} \mu_B$  would be able to account for the solar neutrino deficit; but the above limits exclude this case and settle the oscillation parameters in the context of a possible magnetic moment.

On the other side, assuming the neutrino oscillation parameters as settled, solar neutrino experiments can serve to specify parameters of the solar model, like thermonuclear fusion reaction rates. The Borexino experiment aims at a determination of the solar  $^7\text{Be}$  neutrino rate, that up to now shows a very large uncertainty. Its determination within a range of 10%, together with the luminosity of the sun, would allow a calculation of the solar pp reaction rate with an uncertainty of 1% only.

## 1.5. Future Experiments

### *Double-CHOOZ*

The mixing parameter of the electron- and tau-neutrino,  $\theta_{13}$ , has remained one of the most important questions in neutrino physics. The Chooz experiment has helped to settle the upper limit at  $\sin^2\theta_{13} < 0.05$  with  $3\sigma$  bounds [Gos04]. The future experiment Double-Chooz, envisioned at the same site in the north of France, aims to improve this limit with two

identical scintillation detectors, one at a distance of 150m and the other at 1050m from the core of a nuclear power reactor. The far detector is supposed to observe an anti-electron neutrino disappearance in comparison to the near one. Both detectors shall contain a 0.1% Gd loaded liquid scintillator in an acrylic vessel (12.67m<sup>3</sup>) as neutrino target, a surrounding scintillator volume in a second acrylic vessel (28.1m<sup>3</sup>) envisioned for the detection of gamma events, 500 photomultipliers, a non-scintillating buffer region (100m<sup>3</sup>) and a water Cherenkov muon veto (110m<sup>3</sup>). These different detector layers will form an onion structure similar to the Borexino detector design. According to [DCh04], the two detectors will start data taking in 2008 and are supposed to reach a sensitivity of 0.03 for  $\sin^2(2\theta_{13})$  in 2011.

### *LENA*

The LENA project (Low Energy Neutrino Astronomy, [Obe03b]) envisions a time resolved, large volume neutrino observatory. 50000 tons of liquid scintillator – up to now PXE is the most probable solution – at a low background site are supposed to be used as target. As scintillation detector, LENA will be adapted to low energy neutrino spectroscopy and perfectly complement to the water Cherenkov experiments carried out over the past years. Two places, both far away from nuclear power plants, are taken into account up to now; these are Pylos, Greece, where the detector can be placed in water down to 5000m below the sea level, and Pyhäsalmi, Finland, providing a mine at a depth of 4060 m.w.e. Due to its large volume, LENA will be a multi-purpose detector able to see neutrinos of different origins. Especially high statistics could be reached by solar neutrinos, leading to a precise determination of the different solar neutrino fluxes and other uncertain parameters concerning both the standard solar model, and the according nuclear reaction cross sections. A deeper insight into astrophysics could arise from supernova neutrinos, both galactic and relic ones. Here, the time resolved, flavour specific detection of galactic supernova neutrinos – due to flavour specific reaction channels – would reveal new details about both the supernova explosion mechanism, and the neutrino parameters, above all the still unknown absolute neutrino masses. LENA could be the first experiment detecting relic supernova neutrinos, thus providing important information about star formation processes in the early universe. Furthermore, an observation of geo-neutrinos would help to reveal information about the earth composition; a comparison to the data of the reactor neutrino experiment KamLAND could be useful as the abundance of radionuclides in the earth crust can vary at different places. Another interesting item would be the detection of atmospheric neutrinos in the range of 200MeV, aiming at an observation of the  $\bar{\nu}_e \leftrightarrow \bar{\nu}_\mu$  oscillation, due to the modified energy range with respect to the experiment SuperKamiokande. Accelerator neutrinos could be observed in the context of long baseline experiments, as the envisioned Pylos site is located off-axis concerning a beam from CERN to Gran Sasso. Finally, LENA would provide an excellent possibility to study the proton decay via the  $K^+$  channel, whose energy in water Cherenkov detectors is below the Cherenkov threshold. Practically, there would be no background due to the specific  $K^+$  decay signature. The detector would be sensitive to a proton life time at  $10^{34}$ – $10^{35}$  years, able to check the minimal SUSY SU(5) model that predicts a life time between  $10^{29}$  and  $10^{35}$  years. The actual best limit,  $2.3 \cdot 10^{33}$  years at 90% C.L., arises from SuperKamiokande [Jun04].

## 2. The Experiment Borexino and its Prototype CTF

The solar neutrino experiment Borexino has been envisioned since the mid of the 1990's in hall C of the Gran Sasso underground laboratory at a depth of 3600 meters of water equivalent. The first essential step comprised the construction of a prototype detector, the so-called Counting Test Facility (CTF, see 2.4), at the same location. Up to now, its task has consisted in the examination of background rates caused by external muons and impurities in detector materials, especially in the liquid scintillator itself. Recently, a new analysis of the CTF data has provided some limits concerning neutrino related parameters, as shown in 2.1. The Borexino detector however, nearly completed except for the liquid scintillator filling, is not yet taking data.

Borexino has been projected as liquid scintillator detector, with 300 tons of pseudocumene solvent plus 1.5g/l of the wavelength shifter PPO, surrounded by several layers of shielding liquid. The outer shielding layer has been constructed as water Cherenkov detector in order to provide an active muon veto. Events in the detector will cause photons of about 400nm in the scintillator, observable by 2214 spherically arranged photomultipliers. A detailed description of the detector can be found in [BOR02], or in paragraph 2.2. Neutrinos of all flavours are supposed to interact by neutral current (NC) elastic scattering processes on electrons ( $\nu_\alpha + e^- \rightarrow \nu_\alpha + e^-$ ), whereat the cross section for  $\nu_e$  compared to  $\nu_\mu, \nu_\tau$  is enhanced by a factor of  $\approx 6.5$  in the considered energy range because of the additional possibility of charged current (CC) interactions. Here, the  $\mu$ - or  $\tau$ -production by CC interactions of  $\nu_\mu$  or  $\nu_\tau$  is excluded due to the envisioned energy range (250keV~20MeV). The electrons involved in scattering processes will deposit their kinetic energy in the liquid scintillator. The generated light signal shall contain enough information to determine energy, position, shape and time of the event. Anti-neutrinos mainly interact with protons ( $\bar{\nu}_e + p \rightarrow n + e^+$ ), as the related cross section is higher by two orders of magnitude compared to electron scattering. The anti-neutrino signature consists in a time coincidence ( $\sim 200\mu\text{s}$ ) of an  $e^+e^-$ -annihilation and a 2.2 MeV gamma, emitted when the neutron will be thermalised and captured by a proton ( $n + p \rightarrow D + \gamma$ ). This shall provide an excellent background suppression also at low energies, an extraordinary advantage of scintillation detectors compared to water Cherenkov detectors. The anti-neutrino energy can be obtained by  $E = E_{\text{kin,positron}} + 2m_e c^2 + 0.78\text{MeV}$ , at which the sum  $E_{\text{kin,positron}} + 2m_e c^2$  is directly observable in the detector [BOR04]. The anti-neutrino detection threshold amounts to 1.8 MeV.

### 2.1. Motivation and Future Possibilities

Originally, the motivation for the Borexino detector consisted in the measurement of the solar  $^7\text{Be}$  neutrino rate in order to single out a specific neutrino parameter region in the  $(\Delta m^2_{12}, \theta_{12})$ -space. Even if this task has been completed meanwhile by other experiments, the ambitious goal of measuring the solar  $^7\text{Be}$  neutrino rate has remained unrealised. Apart from confirming the settled model of neutrino oscillations, it serves for astrophysical reasons, such as the accurate determination of stellar thermonuclear fusion rates. In particular, its determination within a range of 10% would allow a calculation of the solar pp reaction rate with an uncertainty of 1%. In the detector, the mono-energetic  $^7\text{Be}$  neutrino line at 863 keV implies a characteristic recoil electron spectra (see Diagram 2.1) with an integral rate of 33 events per day, taking into account the now known effect of neutrino oscillations. Nevertheless, further items in neutrinos physics have remained where Borexino could be able to contribute.

Looking at astrophysics, and here on the physics of the sun as the simplest possibility of examining a star from our restricted point of view, the easiest accessible value is that of its total photonic energy radiation. It implies a specific rate of pp-fusion reactions (compare Diagram 1.2), leading to a certain pp-neutrino flux. The value of the latter has not yet been measured directly. Of course, it should correspond to the photon flux, but as already mentioned in 1.1, photons travel about  $10^5$  years longer

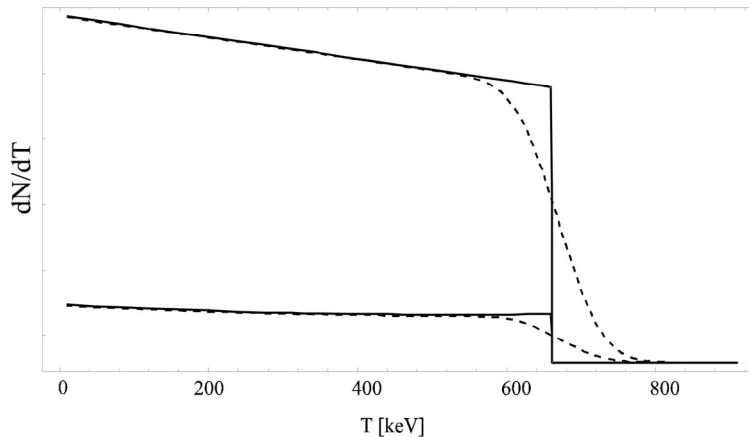


Diagram 2.1: Recoil electron spectra caused by the  ${}^7\text{Be}$  solar neutrino line at  $862\text{keV}$ . The maximal recoil energy is  $665\text{keV}$ . The dotted lines are modified according to the detector resolution. The upper curve shows the higher cross section for  $\nu_e$  (CC and NC) in contrast to  $\nu_\mu$  and  $\nu_\tau$  (lower line, only NC).

than neutrinos to traverse the dense matter of the sun until reaching its surface. So, the pp-neutrino rate could indeed reveal some news. Yet, it can hardly be detected by Borexino because of its low energy, as we will see later. Nevertheless, the so-called pep-neutrinos, a mono-energetic line at  $1445\text{keV}$  due to the fusion reaction  $p+e^-+p\rightarrow D+\nu_e$ , should be detectable; and as the branching ratio between the pp- and the pep-reaction is well known, it would lead to the requested pp-fusion rate. In particular, the pep-neutrino observation requires a good suppression of muon-induced  ${}^{11}\text{C}$  background. A background suppression in this energy range would additionally enable the detector to observe neutrinos produced in the CNO cycle, thus providing precious information to improve uncertain parameters of the standard solar model (see 2.3.3). In any case, both the pep- and the CNO neutrino rate, each of them expected to be at  $\approx 0.7$  events per day, could be used to check out non-standard energy mechanisms in the sun. In a larger context, thermonuclear CNO fusion rates can have an impact on models of heavy stars.

### Anti-neutrinos in Borexino

The possibility of detecting anti-neutrinos in Borexino has recently been destined to play a more important role in the period after SNO's and KamLand's revelations. One possibility arises from supernovae, emitting all kinds of neutrinos and anti-neutrinos. Anti-electron neutrinos can indeed easily be detected due to the bigger cross-section on protons and the unambiguous event signature. Moreover, (anti-)neutrino reactions on the numerous  ${}^{12}\text{C}$  nuclei in the scintillator offer more detection possibilities; NC and CC reactions involve both neutrinos and anti-neutrinos, and different event signatures provide good possibilities to distinguish all these channels and examine flavour oscillations, comparing NC and CC rates. A detailed description can be found in [Cad02a]. According to this source, a 10 kpc distant supernova would produce 79 events from  $\bar{\nu}_e$  captures on protons, only 5 from conventional electron scattering processes, but 27 from reactions on  ${}^{12}\text{C}$ , 21 of them due to neutral current scatterings of  $\nu_\mu$ ,  $\nu_\tau$ ,  $\bar{\nu}_\mu$ ,  $\bar{\nu}_\tau$ . Further 80 events per day should be caused by elastic neutrino scatterings on protons, observable at an energy threshold of  $\sim 200\text{keV}$  [Bea99]. Especially, the time delayed arrival of the mentioned  $\nu_\mu$ ,  $\nu_\tau$ ,  $\bar{\nu}_\mu$ ,  $\bar{\nu}_\tau$  compared to the  $\bar{\nu}_e$  signal would help to examine neutrino masses in the range above  $10\text{eV}$ .

Secondly, Borexino will be able to observe anti-neutrinos from nuclear power reactors. Especially the fact that the closest surrounding reactors are roughly at the same distance (~800 km) to Gran Sasso is advantageous: it defines a clear base line. The neutrino flux of all surrounding reactors – the power and distance of 42 reactors are reported in [Rot02] – implies 16 anti-neutrino events per year, including oscillations, and would allow to confirm the mixing parameters within three years at a  $4\sigma$  level. The blue line in Diagram 2.2 shows the expected spectrum.

Furthermore, Borexino can observe the so-called geo-neutrinos, anti-neutrinos emitted by the beta decay of natural radioactive isotopes in the earth crust. These isotopes, mainly  $^{238}\text{U}$  and  $^{232}\text{Th}$ , produce anti-neutrinos with an energy up to 3.5 MeV, corresponding to 2.7 MeV events in the detector (compare the red line in Diagram 2.2). As the reactor anti-neutrino flux can be calculated quite precisely, a quite obvious idea consists in subtracting the reactor events to determine geo-neutrino rates. The idea is actually being applied on the CTF data (CTF3, ~400 days). An upper limit for geo-neutrinos can be deduced, ~10 times higher than calculations according to earth crust models let assume [Ian04a]. Borexino is expected to observe about 10 geo-neutrino events per year. A second kind of geo-neutrinos could arise from a hypothetical earth reactor in the centre [Her92]. The actual, best limits derive from the CTF3 data and will be submitted.

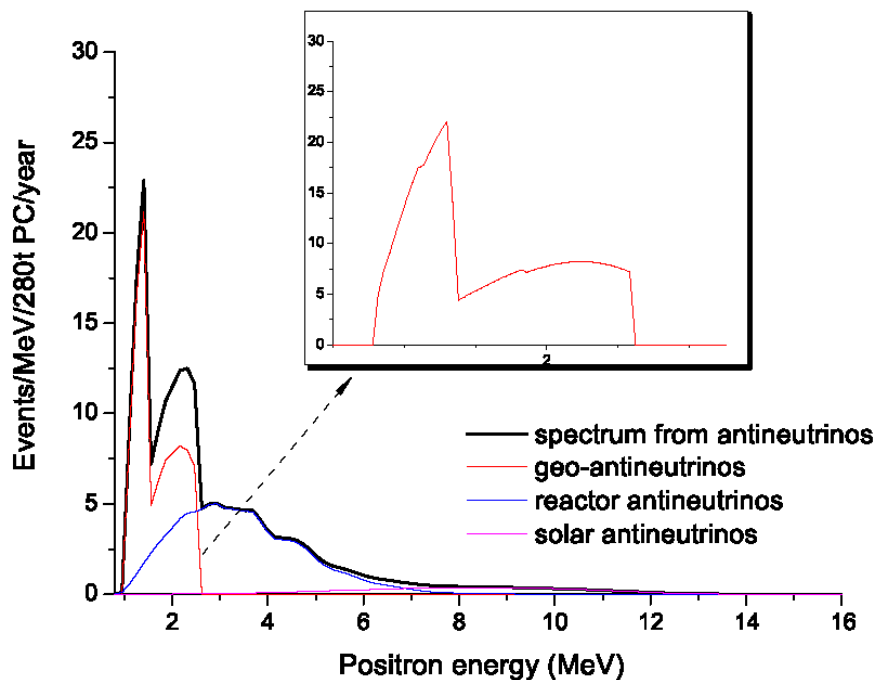


*Diagram 2.2: Calculated anti-neutrino spectra for Borexino [Ian04a]. The energy scale corresponds to the anti-neutrino energy minus 0.8 MeV. The geo-neutrino spectrum arises from calculations based on a model of the earth crust with uniformly distributed U and Th. The reactor spectrum is based on 42 reactors and includes neutrino oscillations. The solar spectrum uses the recent KamLand limit assuming the shape of an undistorted  $^8\text{B}$  neutrino spectrum.*

Finally, interactions related to a possible magnetic moment of neutrinos are able to add a further, comparatively small contribution to the anti-neutrino spectrum in Borexino, the solar anti-neutrinos. Up to now – as described in 1.4 – the KamLand detector provides the best restriction for the solar anti-neutrino flux (purple line in Diagram 2.2). The comparatively high reactor neutrino background at KamLand shifts the anti-neutrino detection threshold to 8.3 MeV. Borexino can be able to profit by its lower reactor background, setting its anti-

neutrino detection threshold at the end of the geo-neutrino spectrum at 3.5 MeV. This will provide better statistics. The data of CTF3 has already been used to derive the limits  $\Phi(\bar{\nu}_e) < 3 \cdot 10^5 \text{cm}^{-2} \text{s}^{-1}$  and  $\mu_\nu < 5.5 \cdot 10^{-10} \mu_B$  (90% C.L.) [BOR03a]. Borexino would be sensitive to the neutrino magnetic moment at a level of  $10^{-11} \mu_B$ , comparable to Kamland.

Another issue where CTF already contributes concerns the existence of so-called heavy neutrinos with a mass above  $2m_e$ . The bounds on the sum of the absolute neutrino masses, right in this range, are due to cosmological arguments. Now, considering only neutrino experiments, assuming that heavy neutrinos  $\nu_H$  would exist and that they would be emitted in the  ${}^8\text{B}$  decay in the sun, the decay  $\nu_H \rightarrow \nu_e + e^- + e^+$  should be observed. The CTF data has been used to set bounds on this decay. In consequence, concerning the neutrino mixing matrix  $U$  (compare 1.2), the limit  $|U_{eH}|^2 < 10^{-3} - 10^{-5}$  was derived for a heavy neutrino in the range from 1.1 to 12 MeV [BOR03b]. This limit is stronger by more than one order of magnitude than the limits obtained in previous reactor and accelerator experiments. Borexino should be able to further improve it.

### *Neutrino-less double beta decay*

According to the standard model, some nuclei decay by two beta decays at once, the so-called double beta decay. Their half-lives are comparatively high. Normally, this decay emits two neutrinos. But in the special case of majorana neutrinos, the “first” emitted neutrino, left-handed, could flip its helicity – by a small, non-zero possibility, as not exactly propagating with light speed – and immediately be reabsorbed, now acting as a right-handed anti-neutrino and inducing the second part of the double beta decay. In this procedure, no neutrino would be emitted to the outside. This decay channel would be recognisable by its energy spectra, a mono-energetic line at the end point of the normal double beta decay spectra. Compared to the conventional – already rare – double beta decay, the neutrino-less double beta decay – if existing – would be extremely suppressed and hardly detectable. Finally, a non-zero rate would among other things be sensitive to the square of  $|\sum U_{en}^2 m_n|$ , the so-called effective neutrino mass. Several experiments, Heidelberg-Moscow [Kla04] was one of them (compare 1.4), are trying to determine that. The CTF and Borexino provide a further possibility in this context.

In [Bel00], the idea of putting two different double beta decay sources in liquid scintillator was examined. It concerns a first phase CAMEO–I using 1kg of  ${}^{100}\text{Mo}$  in the CTF detector, providing a sensitivity down to 0.1–0.3 eV, and a second phase CAMEO–II able to reach 0.05–0.07 eV with 65kg of  ${}^{116}\text{Cd}$  in the CTF.  ${}^{116}\text{Cd}$  in Borexino (CAMEO–III) could reach 0.02 eV. Already CTF would be able to check the recent Heidelberg-Moscow result of 0.4 eV.

A further idea envisions to dissolve the double beta candidate  ${}^{150}\text{Nd}$  in the CTF scintillator. Calculations of unknown nuclear matrix elements by [Sta90] and [Fae98] suggest  ${}^{150}\text{Nd}$  as the most promising candidate for a respective experiment. Its half-life is ~60 times smaller than the one of germanium used in the Heidelberg-Moscow experiment. Further, the total decay energy of  ${}^{150}\text{Nd}$ , 3367 keV, is comparatively high, advantageous because of a lower background. The neodymium experiment aims at being sensitive to an effective neutrino mass of 10 meV, provided that neutrinos are majorana particles. After some pre-examinations it is considered to upgrade the CTF as double beta decay detector. Neodymium, containing 5.6% of  ${}^{150}\text{Nd}$ , is planned to be dissolved with a concentration of 1 g/l in PXE, the liquid scintillator used in the CTF2 campaign. Calculations show that one year of data taking with the CTF detector could reach a sensitivity to an effective neutrino mass of ~430 meV. A second phase of the neodymium experiment envisions to improve this sensitivity to ~70 meV, probing rigorously the claimed evidence by the Heidelberg-Moscow experiment and allowing

to test the case of an inverted neutrino mass scale after five years of data taking, by dissolving 5 kg of enriched  $^{150}\text{Nd}$  instead of normal neodymium.

## 2.2. Detector Equipment

### 2.2.1. Liquid Handling

The entirety of all equipment dedicated to the Borexino experiment consists of far more than only a single detector. Diagram 2.3 shows an overview of the Borexino area in hall C of the Laboratori Nazionali del Gran Sasso (LNGS). Aside, still in hall C, between the entrance and the storage area, the OPERA experiment is located.

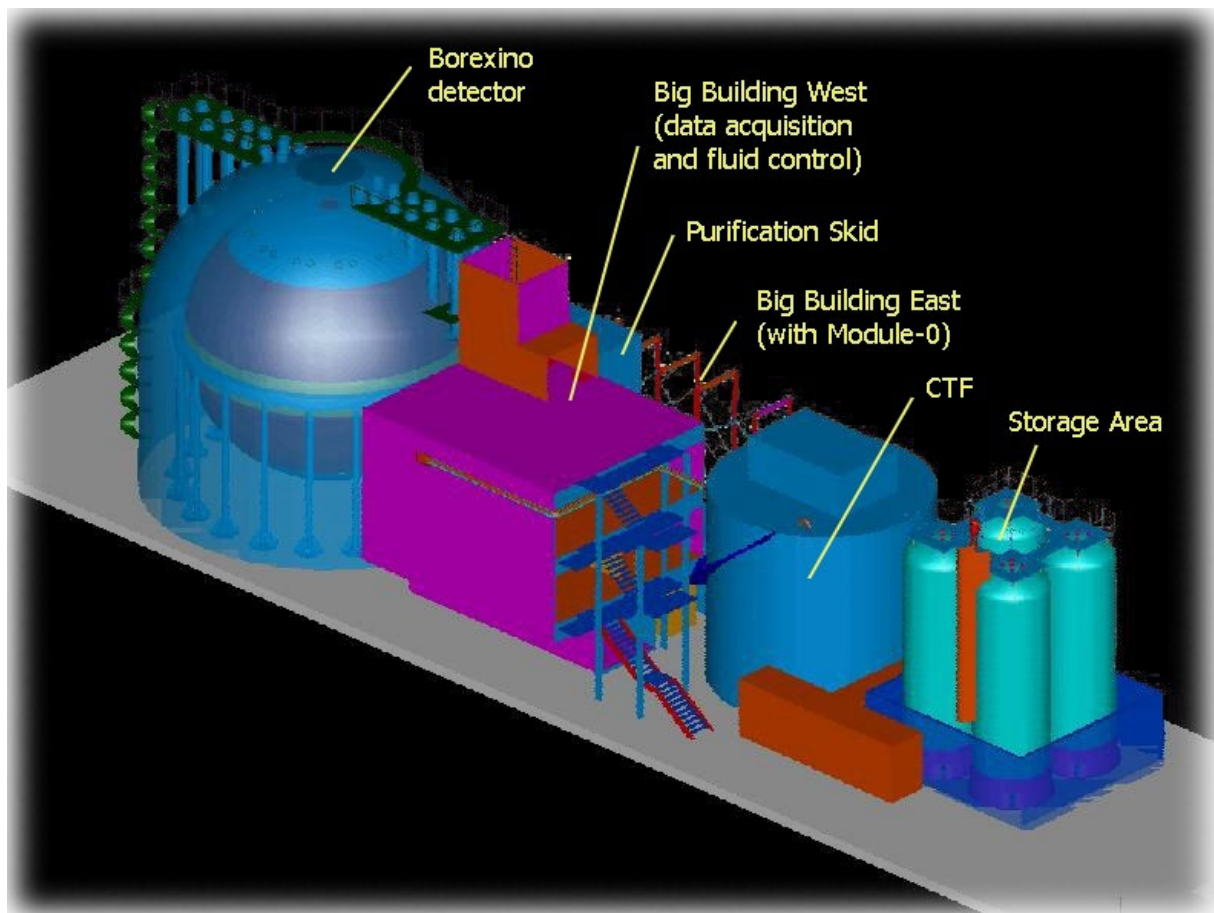


*Diagram 2.3: The Borexino area in hall C of the LNGS, Assergi, Italy*

The scintillator solvent pseudocumene (PC) arrives by trucks in hall C and can be stored in the four stainless steel tanks,  $100\text{m}^3$  each, of the Storage Area (SA). One of them – normally chosen to receive new PC – is able to perform nitrogen extraction. The PC can be moved by two nitrogen driven PTFE pumps from the SA to the so-called Interconnection System on the first floor of the Big Building East (BBE), from where it gets directed to the various plants; that are Module-0 (M0, see 3.), the Purification Skid (PS, see 5.) or the Filling Station (FS) of the Borexino detector. The CTF Inner Vessel and the wavelength shifter mixing plant (PPO Plant) are only accessible via Module-0. The water purification plant, located behind the CTF detector, and the nitrogen system, located outside the hall near the main entrance to hall C, are separately connected to the various subsystems. In particular, Module-0 and the Purification

Skid are scintillator purification plants, applying the methods of silica gel chromatography (see 4.) and nitrogen extraction, respectively water extraction (see 6.), distillation and also nitrogen extraction. Both, the scintillator purity – crucial to low counting rate experiments like Borexino – and other scintillator properties have been tested in the CTF detector in order to compare different scintillator samples and optimise purification. The Filling Station of Borexino and the Borexino detector itself – both being completed within these months – are meant to finally receive the purified scintillator.

## 2.2.2. The Borexino Detector

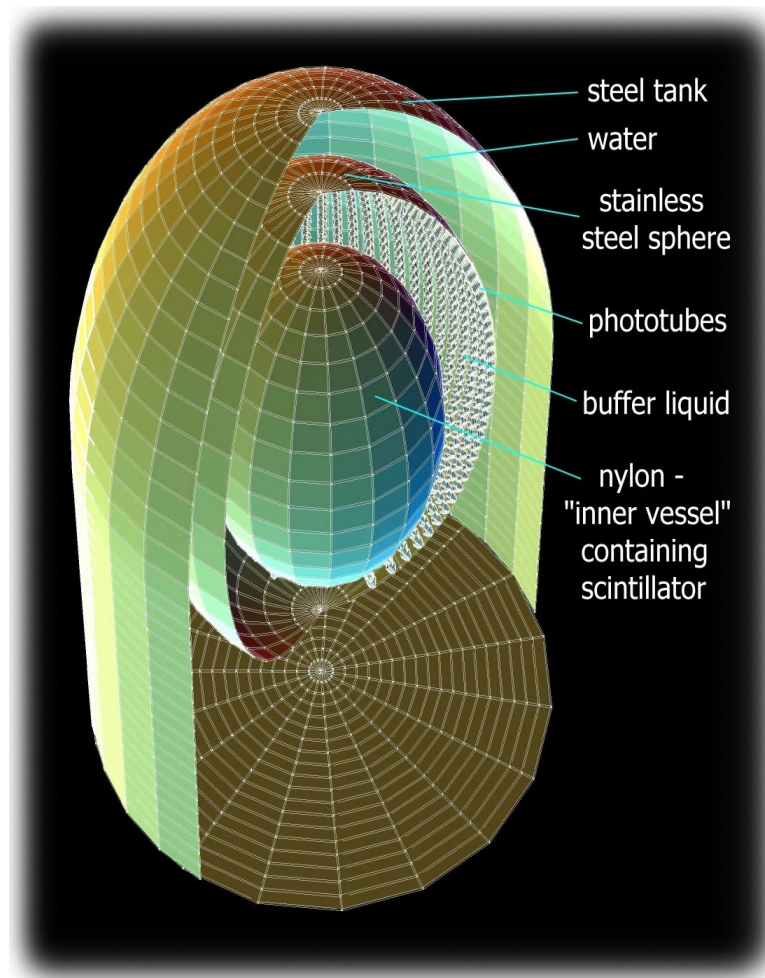


*Diagram 2.4: Configuration of the Borexino detector. Fiducial volume, shroud and muon veto PMT's are not displayed here.*

The Borexino detector shows a typical onion structure. The inner part, the so-called Inner Vessel (IV), a transparent nylon balloon of a thickness of  $125\mu\text{m}$ , is supposed to contain  $322\text{m}^3$  of scintillator, i.e. a pseudocumene (1,2,4-trimethylbenzene,  $\text{C}_9\text{H}_{12}$ ) solution containing  $1.5\text{g/l}$  of the wavelength shifter PPO (2,5-diphenyl oxazole,  $\text{C}_{15}\text{H}_{11}\text{NO}$ ) and with a density of  $0.89\text{kg/l}$ . However, only the inner region, defined by a  $3\text{m}$  radius, the so-called Fiducial Volume (FV,  $113\text{m}^3$ ), is intended to observe events considered neutrino candidates. The remaining volume of the vessel, at a radius from  $3\text{m}$  to  $4.25\text{m}$ , should help to understand and discriminate background events caused by detector materials like the nylon vessel itself. Outside the Inner Vessel, a further pseudocumene based solution constitutes the inner layer of shielding liquid, about  $1000\text{m}^3$  contained by a stainless steel sphere (SSS) of  $13.7\text{m}$  in diameter. The so-called “quencher” dimethyl

phthalate (DMP) will be dissolved in the buffer pseudocumene with a concentration of  $5\text{g/l}$  in order to prevent it from scintillating. Besides, the buoyancy force, too big to be carried by the tiny nylon vessel, makes it impossible to surround the Inner Vessel with water; whereas the density discrepancy caused by the different solvents PPO and DMP should be acceptable. Inside the buffer pseudocumene, at a distance of  $1\text{m}$  to the Inner Vessel, a second type of nylon vessel, called Outer Vessel or “Shroud”, and indeed acting as a barrier, is installed to prevent radioactive contaminants, mainly radon, from diffusing even closer to the heart of the detector. The fixing of the shroud, however, is not tight against pseudocumene. The stainless steel sphere – sealed tightly – is meant to contain the total amount of pseudocumene, taking

the whole buoyancy force compared to the water outside and, moreover, carrying 2214 phototubes (PMT's), spherically ordered and radially directed towards the interior. 1870 of them are equipped with aluminium light concentrators, making them focus on the Inner Vessel volume and covering a bigger steradian percentage with respect to the scintillator, namely 29.8% [Obe03a]. The rest of the PMT's remain without concentrators in order to watch Cherenkov radiation in the buffer pseudocumene and to contribute to the signature of muon events. Seven CCD cameras, also mounted on the SSS and equipped with electric bulbs, provide a possibility of optically looking inside the sphere in order to locate calibration sources and observe liquid filling processes. The SSS and its carriers are completely located inside a stainless steel tank, 18m in height and diameter, it is designed to contain, apart from the SSS,  $\sim 2500\text{m}^3$  of ultra-pure water. The water's main task, besides being a passive shield, is to provide an active muon veto covering the total steradian of the scintillator. Muons generate Cherenkov radiation inside the water, supposed to be reflected on a tyvec foil covering the whole inner tank surface, and finally detected by 208 photomultipliers mounted on the outer SSS surface and on the floor. 54 PMT's located on the floor should especially improve the signature of the muons in such a way to contain additional information about the muon track, thus upgrading the muon veto to a veritable muon detector. Finally, the Borexino detector is shielded from below by two steel plates, centrically ordered and of 8m·8m·10cm respectively 4m·4m·4cm in their size. The entirety of all passive shielding is directed against background radioactivity from detector materials, detector related equipment and the surrounding rocks.

All photomultipliers are individually connected to the data acquisition system (DAQ) via cables of equal length, containing both signal and high voltage. There, the signal is decoupled from the high voltage and provides time and charge of each single PMT pulse. This information gets on-line collected in a so-called *raw data file* and written to a hard disk. Later, the raw data file is processed off-line to sets of special parameters for each detector event, containing the event energy (proportional to the number of photoelectrons), the event position (determined by the time of flight of the photons to PMT's at various positions), the pulse shape (a time resolution of  $\sim 1\text{ns}$  allows to discriminate the slower decrease of an  $\alpha$ -decay pulse compared to other events), the event time and the contemporaneous response signature of the muon detector. In particular, the position reconstruction is designed to an accuracy of 15cm; and the  $\alpha$ - $\beta$ -discrimination should reach a precision of 99%. The parameter sets of all events, subsequently memorised on a hard disc, can be utilised for the final data analysis, the way how to later apply special parameter cuts and extract energy spectra, coincidences and particular reaction signatures.

### 2.3. Background

The suppression of background events is crucial in low counting rate experiments like Borexino. Difficulties mainly arise as electrons from neutrino scattering processes do not show any different signature compared to electrons from radioactive decays. The shapes of the energy spectra, a possible signature to recognise desired event groups of solar  $^7\text{Be}$ -, pep- and CNO-neutrinos, get wiped out by the scattering process and the detector resolution. Considering this, the total background rate should not exceed typical neutrino event rates, in case of pep- and CNO-neutrinos around  $\sim 1$  event per day. So, especially in the energy range below 1.5 MeV where solar pep- and CNO-neutrino events are expected to appear, and even more in the so-called "neutrino window" of the  $^7\text{Be}$  neutrino signal (250–800 keV), all possible radioactive decays must be taken into account. Unfortunately,  $\alpha$ -decays in scintillators are quenched, i.e. their visible energy amounts to only about a tenth of their decay energy, shifting most of them from  $\sim 5$  MeV to  $\sim 0.5$  MeV right into the neutrino window. The

$\alpha$ - $\beta$ -discrimination can filter them out mostly but not completely. The following paragraphs concentrate on radioactive background sources, mainly disturbing the low energy range. On the other hand, the detection of high energy events – as those caused by supernova neutrinos – quasi remains undisturbed, like also the anti-neutrino detection due to its coincidence signature.

### 2.3.1. Radioactive Metal Isotopes and Radon

Most radioactive isotopes to consider are heavy metals. With their extremely long half lives in the order of  $\geq 10^9$  years, the isotopes  $^{238}\text{U}$ ,  $^{232}\text{Th}$ ,  $^{40}\text{K}$ ,  $^{87}\text{Rb}$ ,  $^{113}\text{Cd}$ ,  $^{115}\text{In}$ ,  $^{138}\text{La}$  and  $^{176}\text{Lu}$  have survived since the formation of Earth and are present as impurities in a lot of materials and dust. So, apart from keeping dust out of the detector, it is required to pay main attention to the radiopurity of all equipment inside the detector; the closer to the Inner Vessel a part is, the higher the required purity. Except for the emanation of radon, metal impurities mainly stay in metals; and equipment like the stainless steel sphere, the photomultiplier housings and the light concentrators had to be checked very accurately. A lot of measurements were carried out in order to find materials with acceptable impurity concentrations.

The Inner Vessel and the scintillator itself, as organic compounds, naturally contain lower metal concentrations; but as they constitute the centre part of the detector, they also have to be the purest materials. The following table shows the requirements of the liquid scintillator.

Isotope	Half life	Required concentration [g/g] in the scintillator
$^{113}\text{Cd}$	$9,3 \cdot 10^{15}$	$2,8 \cdot 10^{-9}$
$^{115}\text{In}$	$4,4 \cdot 10^{14}$	$2,4 \cdot 10^{-12}$
$^{40}\text{K}$	$1,3 \cdot 10^9$	$7,8 \cdot 10^{-15}$
$^{138}\text{La}$	$1,1 \cdot 10^{11}$	$1,2 \cdot 10^{-12}$
$^{176}\text{Lu}$	$3,8 \cdot 10^{10}$	$3,7 \cdot 10^{-15}$
$^{87}\text{Rb}$	$4,7 \cdot 10^{10}$	$3,2 \cdot 10^{-14}$
$^{238}\text{U}$	$4,5 \cdot 10^9$	$2,3 \cdot 10^{-17}$
$^{232}\text{Th}$	$1,4 \cdot 10^{10}$	$5,8 \cdot 10^{-16}$

*Table 2.5: Scintillator purity requirements for Borexino corresponding to a background rate of  $1d^{-1}$  from 250-800 keV in 100 tons of scintillator. The daughter activity of the above isotopes is included, based on the assumption of equilibrated decay chains.  $\alpha$  decays are assumed to be discriminated with 95%. [Nef96]*

The PC and PPO obtainable at companies fulfil only a part of these limits. U, Th and K levels seem to be too high and require further purification.  $^{40}\text{K}$  with an isotopic abundance of  $1,2 \cdot 10^{-4}$  and a half-life of  $1,3 \cdot 10^9$  years deposits its decay energy below 1.5 MeV. During the first CTF phase, high  $^{40}\text{K}$  concentrations were discovered in some samples of the wavelength shifter PPO [Gol97]. However, water extraction – still one of Borexino’s purification options – seemed to extract  $^{40}\text{K}$  effectively. Looking on the other two critical elements, the decay chains of  $^{238}\text{U}$  and  $^{232}\text{Th}$  produce a wide spread of radioactive isotopes (see Figure 2.6), together emitting different kinds of radiation in a wide energy range, the reason that finally causes their acceptability in the scintillator to be lower than the others’.

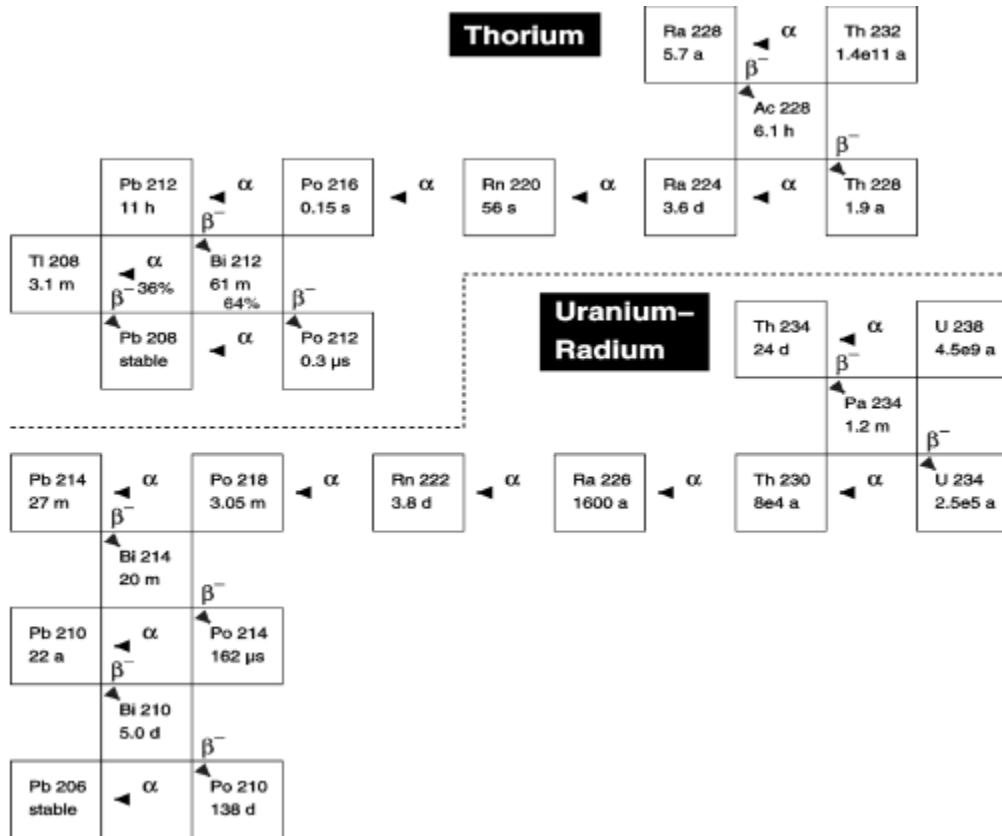


Figure 2.6: Decay chains of  $^{232}\text{Th}$  and  $^{238}\text{U}$

A possible decay equilibrium in both chains – forming in case of an undisturbed activity development in a closed system – gets broken at the element radon, a noble gas. As soon as it is produced, it can move around; but the even bigger problem is, that, indeed, radon atoms moving around can enter any poorly sealed volume, stick to any surface and dissolve in any liquid, able to contaminate whatever should have remained ultra-pure. First, the isotope  $^{220}\text{Rn}$  in the Th chain, called thoron, is harmless as it decays quite quickly to the stable  $^{208}\text{Pb}$ . Its decay chain contains a well recognisable  $^{212}\text{Bi}$ – $^{212}\text{Po}$  decay coincidence, utilised to deduce the activity of the lower part of the Th chain in the detector. This can be very useful in order to possibly subtract from the detector rate the constant activity caused by the long lived contaminants  $^{228}\text{Th}$  or  $^{232}\text{Th}$  – assured that  $^{220}\text{Rn}$  does *not* break the equilibrium. Now looking at the  $^{238}\text{U}$  chain, the  $^{222}\text{Rn}$  activity, unfortunately not disappearing quickly, turns out to be a bigger problem.  $^{222}\text{Rn}$  itself, continuously present in the air at an activity level of  $\sim 30\text{Bq/m}^3$ , would decay soon enough with a half-life of 3.8 days and even is well removable by nitrogen extraction. However, it forms the long lived  $^{210}\text{Pb}$  (22 years), that indeed emits a harmless 45 keV photon only, but maintains the activity of its decay daughters  $^{210}\text{Bi}$  and  $^{210}\text{Po}$  over a long time period. In effect, Borexino’s most serious background problem arises in this context. The  $\beta$  decay of  $^{210}\text{Bi}$  with its end point energy of 1.16 MeV and the  $\alpha$  decay of  $^{210}\text{Po}$ , in the liquid scintillator quenched from 5.4 to  $\sim 0.4$  MeV, deposit nearly their whole energy in the relevant range. Now, the decay coincidence of  $^{214}\text{Bi}$  and  $^{214}\text{Po}$  would help to reliably determine the  $^{222}\text{Rn}$  activity. However, during the last CTF background measurements, the main problem turned out to consist in a presence of  $^{210}\text{Bi}$  and  $^{210}\text{Po}$  activity only, without the corresponding  $^{222}\text{Rn}$  activity. This means that the  $^{222}\text{Rn}$  decay chain is broken at least one more time, possibly by the adsorption of the mentioned heavy metals on liquid handling surfaces or other effects. In particular, a pure liquid handling system can be contaminated by an unpurified scintillator and even a pure scintillator can be recontaminated by a liquid handling system. The entirety of this problem has to be solved in future; a purification of both the scintillator

and the liquid handling systems could help out. In this context, Chapters 4, 5 and 6 examine the surface adsorption problem as well as two effective purification methods.

### 2.3.2. Further Radioactive Isotopes

$^{85}\text{Kr}$ , a man-made fission product present in the air with an activity of  $1.1\text{Bq/m}^3$ , decays with a half-life of 10.72 years to the stable  $^{85}\text{Rb}$ . The  $\beta^-$  decay deposits 0.69 MeV in the detector, where in 0.43% of all cases the energy partially gets distributed on a coinciding gamma of 514 keV. This suppressed second branch helps to determine the  $^{85}\text{Kr}$  activity by the coincidence – even if providing very few events – and to subtract it statistically. Krypton can also be removed by nitrogen extraction in various plants, so that it should be possible to meet the requirements.

$^{39}\text{Ar}$ , arising from the effect of cosmic radiation on argon in the air, leads to a continuous activity of  $\sim 13\text{mBq/m}^3$ . It decays with a half life of 269 years to  $^{39}\text{K}$ , emitting a  $\beta^-$  of 0.57 MeV. As there is no special decay signature, the  $^{39}\text{Ar}$  activity has to be – and in fact can be – reduced by nitrogen extraction.

$^{14}\text{C}$ , formed by cosmic ray interactions with earth matter, showing a half-life of 5730 years and adjusting at an equilibrium ratio of  $^{14}\text{C}/^{12}\text{C} \approx 1.2 \cdot 10^{-12}$ , constitutes a qualitatively different kind of background source: as chemically equal to the  $^{12}\text{C}$  present in every scintillator molecule, it cannot be extracted by any purification method. So, there is no hope to avoid that its  $\beta$ -decay spectra with an endpoint of 156.5 keV imposes a lower threshold on the Borexino detector. In reality, the spectrum even gets smeared out by the detector resolution, so that the concentration of  $^{14}\text{C}$  influences the threshold. This  $^{14}\text{C}$  content depends among other things on the age of the oil selected for the pseudocumene production. The attempt to charge a company with importing oil from resources as old as possible lead to an excellent  $^{14}\text{C}/^{12}\text{C}$  ratio in the order of  $10^{-18}$  and a detection threshold around 250 keV. However, the solar pp-neutrino spectra and the second  $^7\text{Be}$ -line are below and remain undetectable.

$^7\text{Be}$ , produced by cosmic radiation on  $^{12}\text{C}$ , decays by electron capture with a half-life of 53 days and shows a 10% branch emitting a 478 keV gamma. In underground laboratories, screening the hadronic component of cosmic rays, it further can arise from muon-induced reactions (see 2.3.3), but with clearly lower rates. So, the  $^7\text{Be}$  activity gets enriched during the pseudocumene production process on the earth's surface and begins to decay underground. In the meantime, the scintillator, procured in the first half of 2002, has been stored long enough in hall C to have reduced the  $^7\text{Be}$  concentration to an excellent level.

### 2.3.3. Muon Induced Radioactivity

In the Gran Sasso underground laboratory, at a depth of 3600 m.w.e., muons appear with a rate of  $1.16\text{m}^{-2}\text{h}^{-1}$  – suppressed by a factor of  $10^6$  – and an average energy of 320 GeV. Direct muon signals are planned to be rejected by the muon veto in an effective way. However, muons can either themselves provoke nuclear reactions on the numerous  $^{12}\text{C}$  atoms in the scintillator or generate free neutrons in the rock material, able to enter the detector and cause nuclear reactions there. In both cases, unstable, light nuclei are permanently formed, causing background events by their subsequent decay in the detector.

	Isotope	Half life	$E_{\max}(\beta)$ in MeV	$E(\gamma)$ in MeV	counts/d in 100t, 0.25-0.8 MeV ( $\rightarrow {}^7\text{Be}-\nu$ )	counts/d in 100t, 0.8-1.4 MeV ( $\rightarrow \text{pep-}, \text{CNO-}\nu$ )
$\beta^-$	${}^{12}\text{B}$	0,02 s	13,4			
	${}^{11}\text{Be}$	13,81 s	11,5		$<4 \cdot 10^{-4}$	$<10^{-4}$
	${}^{10}\text{Be}$	$1,5 \cdot 10^6$ a	0,56			
	${}^{11}\text{Li}$	0,09 s	20,8			
	${}^9\text{Li}$	0,18 s	13,6		$<7 \cdot 10^{-4}$	$<10^{-3}$
	${}^8\text{Li}$	0,84 s	16,0		$2,5 \cdot 10^{-4}$	$8,0 \cdot 10^{-4}$
	${}^8\text{He}$	0,12 s	10,6		$<7 \cdot 10^{-4}$	$<10^{-3}$
	${}^6\text{He}$	0,81 s	3,5		0.04	0.07
$\beta^+$	${}^{11}\text{C}$	20,39 min	0,96		0	7.4
	${}^{10}\text{C}$	19,26 s	1,9	+0,72 in 98,53%	0	0
	${}^9\text{C}$	0,13 s	16,0		0	0
	${}^8\text{B}$	0,77 s	13,7		0	$3,3 \cdot 10^{-5}$
EC	${}^7\text{Be}$	53,3 d	-	0,478 in 10%	0.34	0

Table 2.7: Background caused by muon-induced radioactive nuclei [Goe01]

As long as their half lives are short ( $<1\text{s}$ ), the decays can be attributed unambiguously to the preceding muon events. Table 2.7 shows that even most nuclei cause negligible background rates in the interesting energy ranges. However, muon-induced  ${}^{11}\text{C}$  produces 7.4 events per day between 0.8 and 1.4 MeV, ten times the expected rates of pep- and CNO- neutrino events; moreover, the long half-life of 20 minutes does not allow to recognise a temporal correlation of these decays to the muon events. In order to solve this problem, i.e. to aim realistically at a pep- and CNO-neutrino detection, the muon veto design has been upgraded to allow a determination of the muon tracks. It is intended to set a locally confined, cylindrical veto around the track of each registered muon, long enough to identify an event localised inside this cylinder as muon-induced  ${}^{11}\text{C}$  decay – assuming that  ${}^{11}\text{C}$  nuclei do not move around by convection. The missing experimental proof of solar pep- and CNO-neutrinos attributes a special attention to this scope.

## 2.4. The Counting Test Facility

The Counting Test Facility (CTF), constructed in 1995, has successfully performed several important background measurements at the Borexino site – that means 20 meters from the Borexino detector – during three different test phases. Two options of liquid scintillators have been tested, in particular the solution PC with PPO and an alternative solution of PXE (phenyl-o-xylene,  $\text{C}_{16}\text{H}_{18}$ ) containing small concentrations of the wavelength shifters pTP (p-diphenylbenzene) and bis-MSB (1,4-bis-(2-methylstyryl)-benzene). The tests have mainly concerned the optical properties and the radiopurity of the scintillators, either in the raw state or after various purification methods. During the acquisition and analysis of the data, various techniques have been tested and developed in an effective way. Even the necessity of a muon detector in Borexino was examined with the help of CTF measurements during the first period [Nef96].

The liquid scintillator supply of the CTF Inner Vessel has ever since been provided by the liquid handling and purification system Module-0 (see Chapter 3), respectively its former system versions. Even now, as the entirety of all Borexino related liquid handling equipment seems extended by a whole order of magnitude, Module-0 has remained the only connection to the Inner Vessel of the CTF. The shielding liquid however is provided by a separate water

purification plant [Bal96], recently upgraded for the needs of the Borexino detector. Detailed descriptions of the CTF can be found in [Ali98a] and [BOR02].

#### 2.4.1. The CTF Detector

The CTF detector consists of a nylon Inner Vessel with a radius of 1m, containing a scintillator volume of 4.2m<sup>3</sup>, positioned in the middle of a 1000m<sup>3</sup> water tank. In particular, the Inner Vessel is able to carry the buoyancy force of the pseudocumene scintillator in water. 100 photomultipliers surround the Inner Vessel, mounted on an open steel structure inside the water tank. In 1999, before the CTF2 phase, CTF has been equipped with a Cherenkov muon veto, furnished with 16 further phototubes positioned on the floor of the tank. After the CTF2 phase, the Inner Vessel was replaced with an upgraded system of two nylon vessels, the inner containing scintillator and the outer – like the Shroud in Borexino – acting as diffusion barrier for radon atoms. Indeed, between 1997 and 2000 the CTF was out of work for several upgrade and repair works like those mentioned.

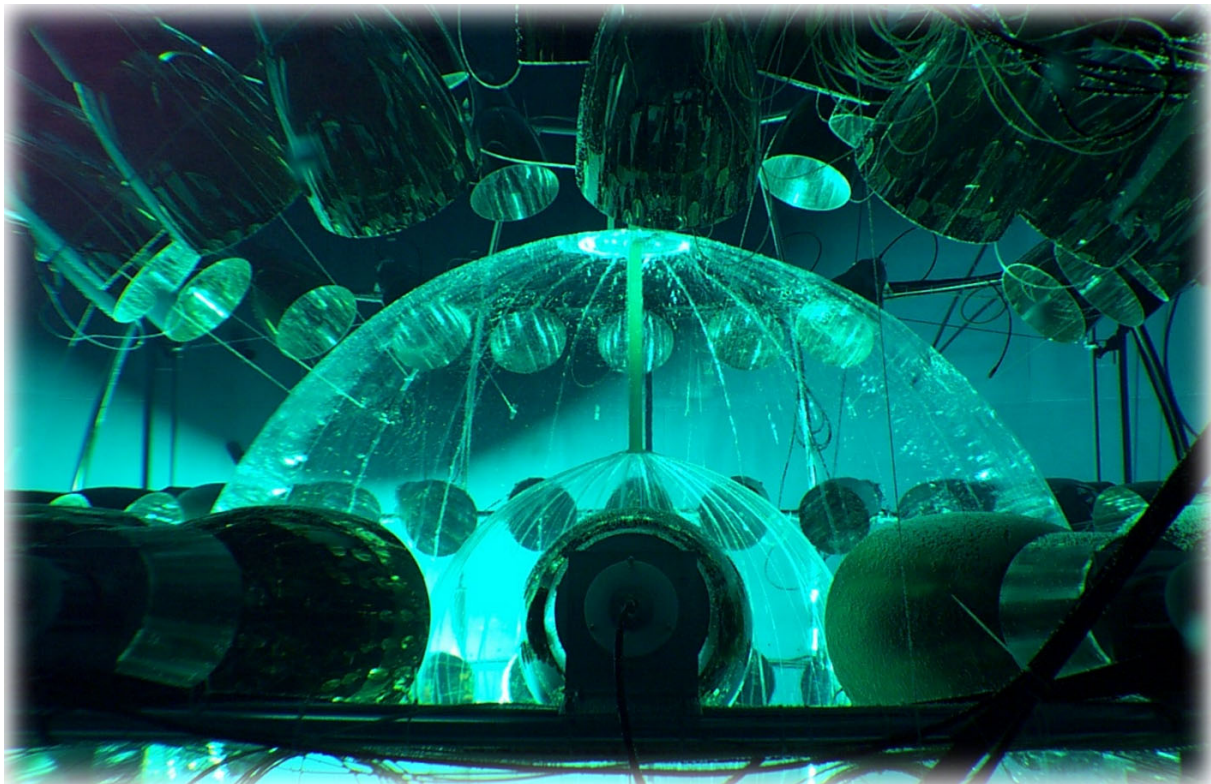


*Image 2.8: Interior of the CTF detector: Outer Vessel (“Shroud”), Inner Vessel and some of the surrounding phototubes, equipped with light concentrators. Water and scintillator are not distinguishable by colour here.*

#### 2.4.2. Test Campaign CTF1

The period CTF1 between February 1995 and January 1997 comprised first measurements with two different liquid scintillators (on base of PC and PXE), especially regarding optical properties, external and internal background determination and purification tests. The required liquid handling processes were carried out with a first temporary version of the Module-0 and an additional water extraction and distillation plant on top of the CTF tank. The latter still exists and once may be used for pre-purification steps. Module-0, in particular, was used for scintillator loading and unloading processes, mixing of PXE with pTP and bis-MSB, filtering,

silica gel purification, water extraction, and nitrogen extraction tests. At this, Module-0 was used to purify PXE, whereas PC was purified by the plant on top of the CTF tank. Module-0 operated successfully with the CTF, and the concept of ultra high vacuum tightness to minimise radon influx has shown to be effective.

In the PC scintillator, the CTF detected  $^{238}\text{U}$  daughters with a  $^{238}\text{U}$  equivalent of  $(3.5\pm 1.3)10^{-16}$  g/g and  $^{232}\text{Th}$  daughters with a  $^{232}\text{Th}$  equivalent of  $(4.4\pm 1.4)10^{-16}$  g/g [Ali98b]. The  $^{238}\text{U}$  and  $^{232}\text{Th}$  daughter activities were extracted by  $^{214}\text{BiPo}$  and  $^{212}\text{BiPo}$  coincidences. Data analyses are further explained in 4.3.1 within the example of the CTF3 campaign.

The PXE scintillator was purified inside Module-0 by silica gel chromatography, nitrogen extraction, filtering and water extraction. During several processes, the  $^{238}\text{U}$  equivalent decreased from  $(3.2\pm 1.6)10^{-14}$  g/g to less than  $10^{-17}$  g/g, and the  $^{232}\text{Th}$  equivalent from  $(2.7\pm 1.5)10^{-14}$  g/g to less than  $1.8\cdot 10^{-16}$  g/g. These concentrations were measured by neutron activation analysis (NAA) at the Technische Universität München, Germany [Hen99], because in the meantime the CTF detector has been shut down for the mentioned technical problems. The last concentrations detected with the CTF – before the last silica gel column and the last water extraction step – amount to  $(1.2\pm 0.1)10^{-15}$  g/g ( $^{238}\text{U}$  equivalent) and  $(1.7\pm 0.3)10^{-15}$  g/g ( $^{232}\text{Th}$  equivalent) [Goe01].

### 2.4.3. Test Campaign CTF2

An amount of  $5\text{m}^3$  of PXE scintillator was stored in the tank EPN of Module-0 after the end of the CTF1 campaign. Between May and October 2000, this scintillator was purified in Module-0 with  $\sim 40$  kg of silica gel (from the German company Merck, the same type as used during CTF1), purged with ultra-pure nitrogen and loaded into the CTF Inner Vessel in four batches of  $1\text{m}^3$  each.

Afterwards, the CTF detector determined a  $^{238}\text{U}$  equivalent of  $(1.7\pm 0.4)10^{-15}$  g/g and an upper limit of  $8\cdot 10^{-16}$  g/g regarding the  $^{232}\text{Th}$  equivalent. The  $^{238}\text{U}$  equivalent has been obtained by cutting out a group of unknown underground events by position reconstruction [Goe01]. Further calculations show that nitrogen extraction in the tank BTE of Module-0 reduced the activity of  $^{222}\text{Rn}$ , emanated out of silica gel, by a factor between 500 and 5000. In particular, the nitrogen extraction factor scales with the extraction time and the nitrogen flow rate until the purity level of the nitrogen is reached. In Module-0, at a nitrogen flow around  $20\text{m}^3/\text{h}$ , a reduction by the factor  $e$  was obtained in 40 – 60 minutes [Nie00].

[Goe01] further examines successfully the optical properties and the quality of the  $\alpha$ - $\beta$ -discrimination with the PXE scintillator. The aim of CTF2 generally consisted in proving the PXE scintillator as an adequate backup option for PC. Several advantages of the PXE scintillator compared to PC are even recognisable, starting from a lower danger level, i.e. a simpler handling, via the density close to that of water, the arising possibility of water as the only shielding liquid, and finally to a better shielding performance by the higher density of water compared to PC. However, certain reasons and motivations already stabilised during previous evaluations must have lead to a contrary decision.

### 2.4.4. Test Campaign CTF3

Between October 2001 and June 2002, 270 tons of the scintillator solvent PC have been procured at the company Enichem and the subsequent Polimeri Europa on Sardinia, Italy. This amount was delivered to the LNGS on trucks, in so-called Isotanks,  $19\text{m}^3$  each. Each batch was transferred to the Storage Area in hall C, from where smaller test batches were moved to Module-0. The CTF Inner Vessel was loaded with 3760kg ( $\approx 4.25\text{m}^3$ ) of scintillator from the Module-0 tank EPS. Later, in order to repeatedly examine  $^{14}\text{C}$  content and radiopurity of the raw PC, about 400 kg of CTF scintillator were exchanged three times with

new test batches (see Table 2.9). PPO was added in form of a concentrated PC-PPO solution, prepared and pre-purified in the water extraction plant on top of the CTF tank. A part of that concentrated solution was added to the initial 3760 kg of PC and later to the first 400 kg exchange batch.

Time	Loaded PC in kg	Used liquid handling components	$\alpha$ 's per day in 4.2m <sup>3</sup>	<sup>14</sup> C/ <sup>12</sup> C concentration
Nov 2001	3760	Isotank, SA, BTW, EPS	2000	(1.34±0.01)10 <sup>-18</sup>
Jan 2002	440	Isotank, BTE	6000	(2.6±0.2)10 <sup>-18</sup>
Apr 2002	440	Isotank, SA, BTE	2000	(4.4±0.2)10 <sup>-18</sup>
Jun 2002	405	Isotank, SA, PS, BTW	3000	(4.4±0.4)10 <sup>-18</sup>

Table 2.9: Batches of raw PC measured during the CTF3 period. The  $\alpha$ -activity most probably is due to <sup>210</sup>Po. EPS, BTW and BTE are Module-0 tanks, SA means Storage Area, PS Purification Skid.

Some purification tests concerning silica gel chromatography and water extraction have been carried out, briefly summarised in the following. A detailed description can be found in Chapters 4 and 6. The  $\alpha$  activity in the detector changing with the accomplished tests during the CTF3 campaign is shown in Diagram 2.10.

During the so-called *silica gel loop test* (see 4.3.1) in February 2002, the CTF scintillator has been circulated 6 times its volume via a chromatography column with 2.4kg of ultra-pure silica gel in Module-0. An integral flow of 23.8 tons of PC scintillator passed the silica gel column in 5.26 days at a flow rate of 190 kg/h. The major goal of the test was met as neither the silica gel nor the liquid handling system did contaminate the scintillator in an unexpected way. The activities of <sup>238</sup>U daughters, <sup>232</sup>Th daughters, and <sup>210</sup>Po were reduced by small factors around ~2.

The Purification Skid (PS), a neighbour building to BBE and also located in hall C, contains a water extraction and distillation system. Between March and May 2002 the CTF scintillator was purified by *water extraction*, using an adequate system inside the Purification Skid (see Chapter 6). Module-0 acted as interface module between the CTF and the Purification Skid, monitoring and controlling input and output flow rates. The main test run comprised 13 scintillator volume cycles. The first five cycles decreased the  $\alpha$  activity (<sup>210</sup>Po) from ~700 to ~120 counts/day, however in those following it remained constant. <sup>238</sup>U daughters and <sup>232</sup>Th daughters were reduced by small factors of ~2.

During the so-called *silica gel batch test* (see 4.3.2) in June 2002, the CTF scintillator was unloaded to the Module-0 tank EPS, purified by a chromatography column with 2.4kg of ultra-pure silica gel and finally reloaded from the Module-0 tanks BTW, BTE into the CTF Inner Vessel. The test did not fulfil its expectations as the  $\alpha$  activity increased from ~400 to ~1000 counts/day. <sup>238</sup>U daughters and <sup>232</sup>Th daughters were not significantly influenced. Possible reasons for the  $\alpha$  activity increase are discussed in 4.3.2.

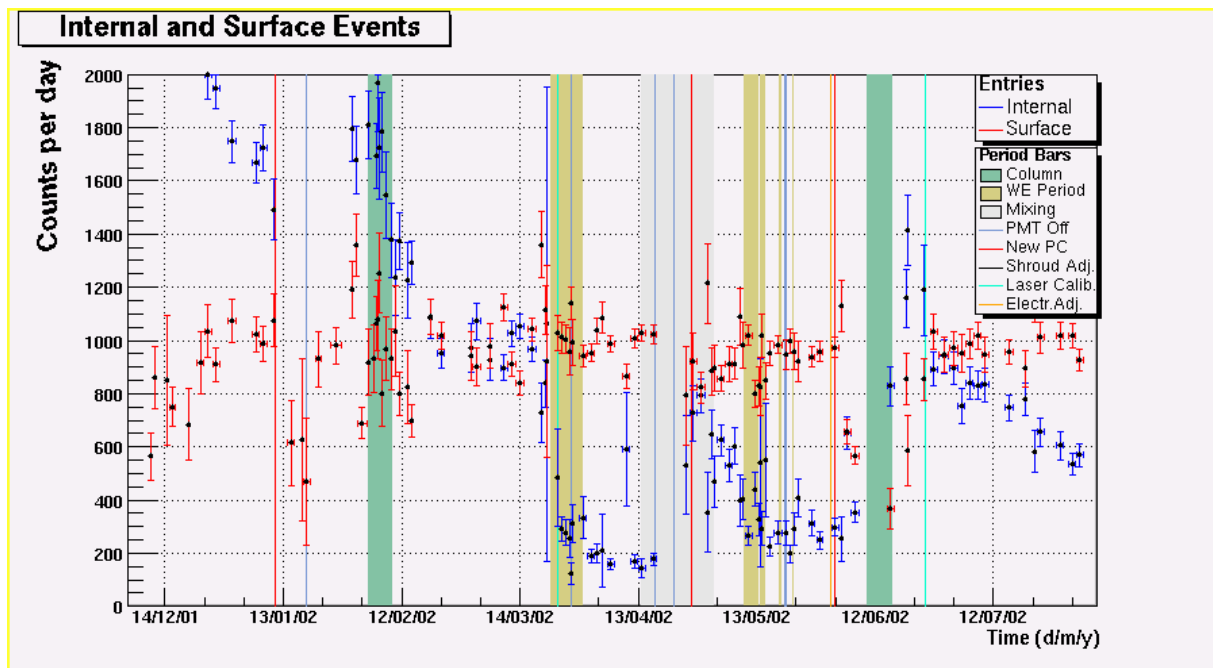


Diagram 2.10: Activity between 250 and 800 keV in the CTF detector during the CTF3 campaign [Mil04]. The red data points represent activity located at the nylon vessel, probably adsorbed on its surface or incorporated in the nylon. The blue data points show the scintillator activity. The events were separated by a radial data analysis using a Rayleigh Function. The vertical bars mark purification processes (1<sup>st</sup> green bar: silica gel loop test, 2<sup>nd</sup> green bar: silica gel batch test, brown bars: water extraction tests), scintillator circulation (mixing) and adjustments of some detector equipment. Especially the scintillator exchange processes (red lines), examining new PC batches, caused activity increases.

#### 2.4.5. Current Status

In August 2002, the CTF3 campaign ended abruptly with an accidental spill of about 50 litres of pseudocumene into the LNGS draining system. All activities in hall C involving pseudocumene were immediately suspended, two months later even all systems containing pseudocumene were sealed by the responsible authorities. The Borexino crisis finally culminated in May 2003 with the sequestration of the whole hall C, liberated again some weeks later. The seals on the afflicted liquid handling systems – Module-0 had remained free as not containing any PC at that time – were removed after a long wait in August 2004. However, pseudocumene actions are still suspended by the LNGS as long as works intended to improve environmental safety issues are going on. These concern repair works on the LNGS draining system as well as the sealing of the hall C floor with a pseudocumene resistant layer.

In the meanwhile – the only part taking advantage of this unlucky situation, and a certain piece of hope in the middle of a bunch of quasi-dead systems – the CTF detector, with its Inner Vessel volume sealed, has continued to acquire data over a long time period of two years, giving an indispensable insight into the development of different background event rates. Some of them, in fact, are only distinguishable due to the excellent statistics.

Now, the  $^{238}\text{U}$  equivalent in the scintillator can be specified to less than  $6.0 \cdot 10^{-16}$  g/g [Mil04] by  $^{214}\text{BiPo}$  coincidences. The  $^{232}\text{Th}$  equivalent has decreased from  $(6.8 \pm 2.0) 10^{-16}$  g/g [Mil04] after the silica gel batch test to less than  $3.1 \cdot 10^{-16}$  g/g (90% C.L.) [Ian04b] now; the latter value arises from  $^{212}\text{BiPo}$  coincidences, a radial cut on the Inner Vessel volume at  $r < 75\text{cm}$  to exclude nylon-related activity and a further z-axis cut at  $z > -40\text{cm}$  to exclude a slightly enhanced activity at the bottom that possibly is due to particulates or the vessel

flange. These U and Th related events however are negligible compared to the total rate, presumably dominated by  $^{210}\text{Pb}$  daughters. Other possible contaminants, not visible in the CTF, will be neglected as well in the following evaluation; and muon-induced background is small in the energy window between 250 and 800 keV (see Table 2.7). An  $\alpha$ - $\beta$ -discrimination and a temporal fit of the  $\alpha$ -decay ( $^{210}\text{Po}$  half life: 138 days) determine the current  $\alpha$  activity in the CTF – now clearly identified as  $^{210}\text{Po}$  – to  $\approx 50$  events/day and the  $\beta$  activity to  $\approx 40$  events/day [Mil04]. The energy range of the  $\beta$  activity however allows two possible contaminants,  $^{210}\text{Bi}$  and  $^{85}\text{Kr}$ . The latter has been determined via a gamma emitting decay channel to  $30 \pm 10$  events/day [Mil04] and is planned to be removed by nitrogen extraction with the help of the low-Ar-Kr  $\text{N}_2$  developed for this purpose. The  $^{210}\text{Bi}$  activity instead, amounting to the remaining  $10 \pm 10$  counts/day and observed to be constant, points to a present  $^{210}\text{Pb}$  contamination at the same level,  $10 \pm 10$  counts/day. One additionally expects a further decay of the  $^{210}\text{Po}$  activity towards this level. As the  $^{210}\text{Bi}$  activity, undistinguishable from neutrino events, is the most critical at this, two  $^{210}\text{Bi}$  decay spectra for different activities were simulated, illustrating the relation to the expected solar  $^7\text{Be}$  neutrino signal after 1000 days of data taking. Therefore, the current  $^{210}\text{Bi}$  activity in CTF of maximal 20 events/day was scaled up to 500 events/day respecting the volume ratio between the CTF Inner Vessel and the Borexino Fiducial Volume (see Diagram 2.11). In the following, a reduced  $^{210}\text{Bi}$  activity of 50 events/day was considered to illustrate a purification by a factor of 10 (see Diagram 2.12). In each case, the green curve shows the  $^{210}\text{Bi}$  spectra only, whereas the blue one constitutes its superposition with a simulated recoil electron spectra from solar  $^7\text{Be}$  neutrinos (compare Diagram 2.1), taking into account neutrino oscillations (33 events/day). Diagram 2.12 especially implies a realistic possibility to extract the solar  $^7\text{Be}$  neutrino signal out of the total rate in case of a contamination reduction by a factor of 10. Here, the isotope necessary to be reduced is  $^{210}\text{Pb}$ , as  $^{210}\text{Bi}$  decays within 5 days. An additional  $^{210}\text{Po}$  reduction would be helpful to save time in the order of some  $^{210}\text{Po}$  half-lives.

In this context, the purification of the isotopes  $^{210}\text{Pb}$  and  $^{210}\text{Po}$  is crucial for a successful accomplishment of the Borexino experiment. Chapters 4, 5 and 6 of this thesis are especially dedicated to the theory and praxis of this item. Chapter 3 describes a liquid handling and purification system at the Borexino detector site predestined to challenge this task.

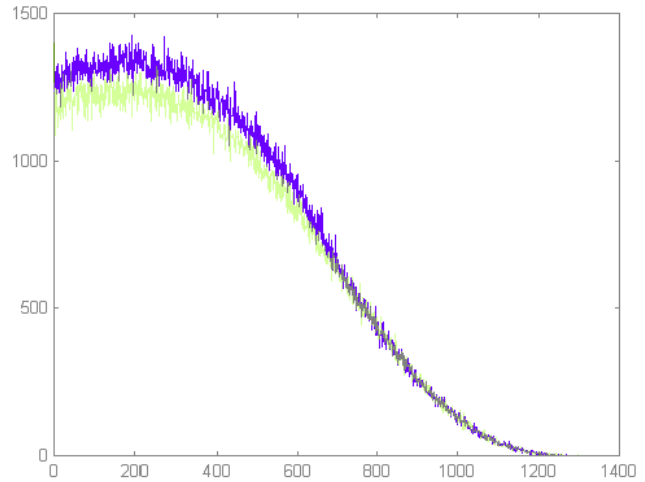


Diagram 2.11: Simulated energy spectra (event number over energy [keV]) in Borexino after 1000 days:  $^{210}\text{Bi}$ - $\beta$ 's with  $500d^{-1}$  +  $^7\text{Be}$ - $\nu$ 's with  $33d^{-1}$

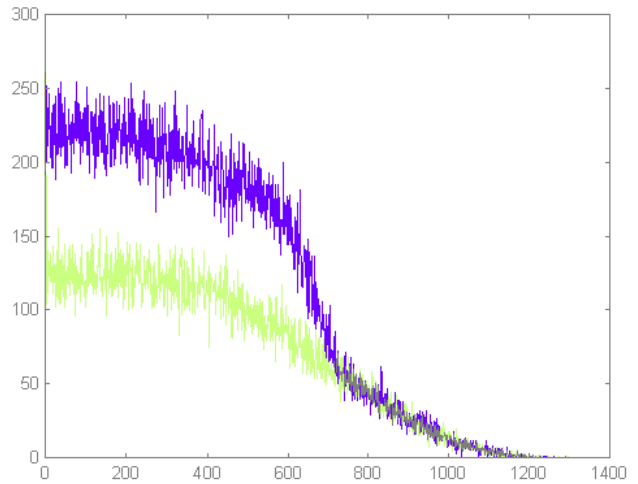


Diagram 2.12: Simulated energy spectra (event number over energy [keV]) in Borexino after 1000 days:  $^{210}\text{Bi}$ - $\beta$ 's with  $50d^{-1}$  +  $^7\text{Be}$ - $\nu$ 's with  $33d^{-1}$

## 3. The Module-0

This chapter aims to describe the so-called Module-0, a liquid handling system set up at the Borexino site by the Technische Universität München, and envisioned for scintillator purification. As explained in Chapter 2, the scintillator radiopurity is crucial for the experiment's success and, mainly concerning decay daughters of  $^{222}\text{Rn}$ , has to be further improved. At this, an indispensable requirement consists in an excellent purity state of the liquid handling and purification system itself. Therefore, the recent version of Module-0 has been constructed with ultra-pure and vacuum-tight equipment consisting of high quality materials only like stainless steel, teflon and nylon. The system has continuously been upgraded during the past years; among other things an effective purification unit has been installed to purify the liquid scintillator of Borexino. The following paragraphs summarise the design principles of Module-0, the equipment, its specifications, the safety aspects and some information about the development of the system since the first CTF tests in 1995. They should give an introduction to operating Module-0, whereas detailed information like procedures of specific operations can be found in the appendices. The chapter includes some experimental test results concerning the purity of the system, such as radon emanation measurements and particulate counting tests.

The main tasks of Module-0 consist in transferring, purifying and storing ultra-pure liquids, in particular deionised water and liquid scintillator for Borexino and the CTF. The following points summarise fundamental operations either envisioned or carried out during several tests with the CTF. In addition, Module-0 can be easily extended for future applications.

- Module-0 serves as liquid handling system of the CTF Inner Vessel. This comprises operations as receiving liquid scintillator from another plant in hall C, loading it into the CTF Inner Vessel and unloading it again (see C.4, C.5).
- Module-0 can be used for loading liquid scintillator into the Borexino Inner Vessel, thus being a back-up option of the Borexino Filling Station, the liquid handling plant envisioned for this job. The procedures would be similar to the ones applied to the CTF Inner Vessel.
- Module-0 contains a solid column purification system to purify liquid scintillators both for the CTF and Borexino (see C.6). The chromatography columns actually contain ultra-pure silica gel as adsorber material.
- Module-0 is able to perform nitrogen extraction and water extraction (see C.7, C.8).
- Module-0 interfaces two other Borexino liquid handling plants. These are a system responsible for the mixing of the scintillator solvent pseudocumene with the wavelength shifter PPO and another, smaller purification plant on top of the CTF tank (see C.9).

### 3.1. System Description

Module-0 is located inside the so-called Big Building East (BBE) in hall C of the Laboratori Nazionali del Gran Sasso (LNGS), Italy. Inside hall C, the BBE can be found between the CTF tank and the Borexino tank. The Module-0 equipment is installed on ground floor of the BBE, comprising several valve manifold systems, two pumps, three purification columns and four tanks. The so-called Interconnection System, interfacing the main liquid handling components of Borexino, as well as the wavelength shifter and quencher mixing systems, i.e.

the PPO System and the DMP System, are located on first and second floor of the BBE. The PPO system among other things comprises two transport tanks, that once belonged to Module-0. Figure 3.1 shows the location of the mentioned equipment inside the BBE.

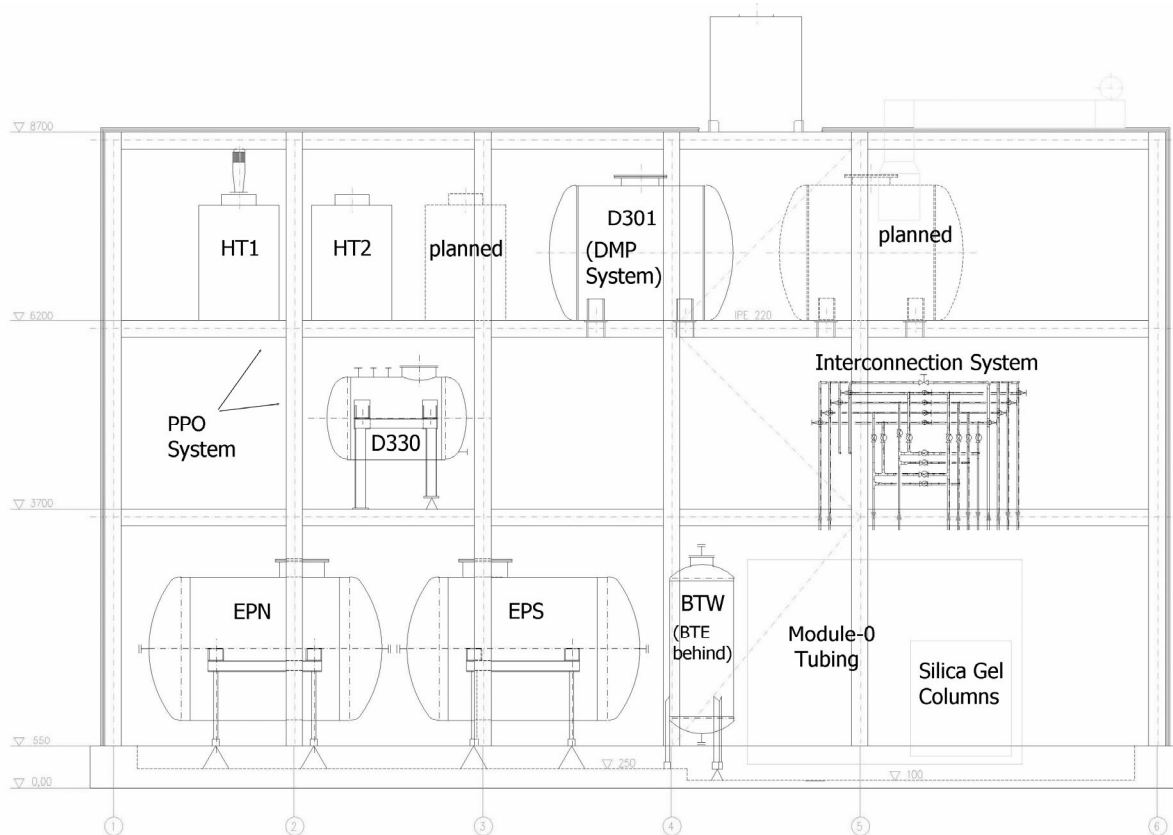


*Figure 3.1: Big Building East in Hall C, LNGS*

The following paragraphs describe different components of Module-0. The main connections between the Module-0 components and its adjacent systems are qualitatively shown in Figure 3.2. The system Module-0 itself however contains a by far larger quantity of entangled tube sections and junctions, sometimes appearing a bit weird at the first glance, but having every piece of tube in the right place after a more detailed contemplation (see Picture 3.4). The entire tubing is documented in the so-called Piping and Instrumentation Drawing (P&ID), a small version of which is shown in Appendix A. All abbreviations refer to this P&ID as well as to labels on the system itself and should help persons intending to operate Module-0.

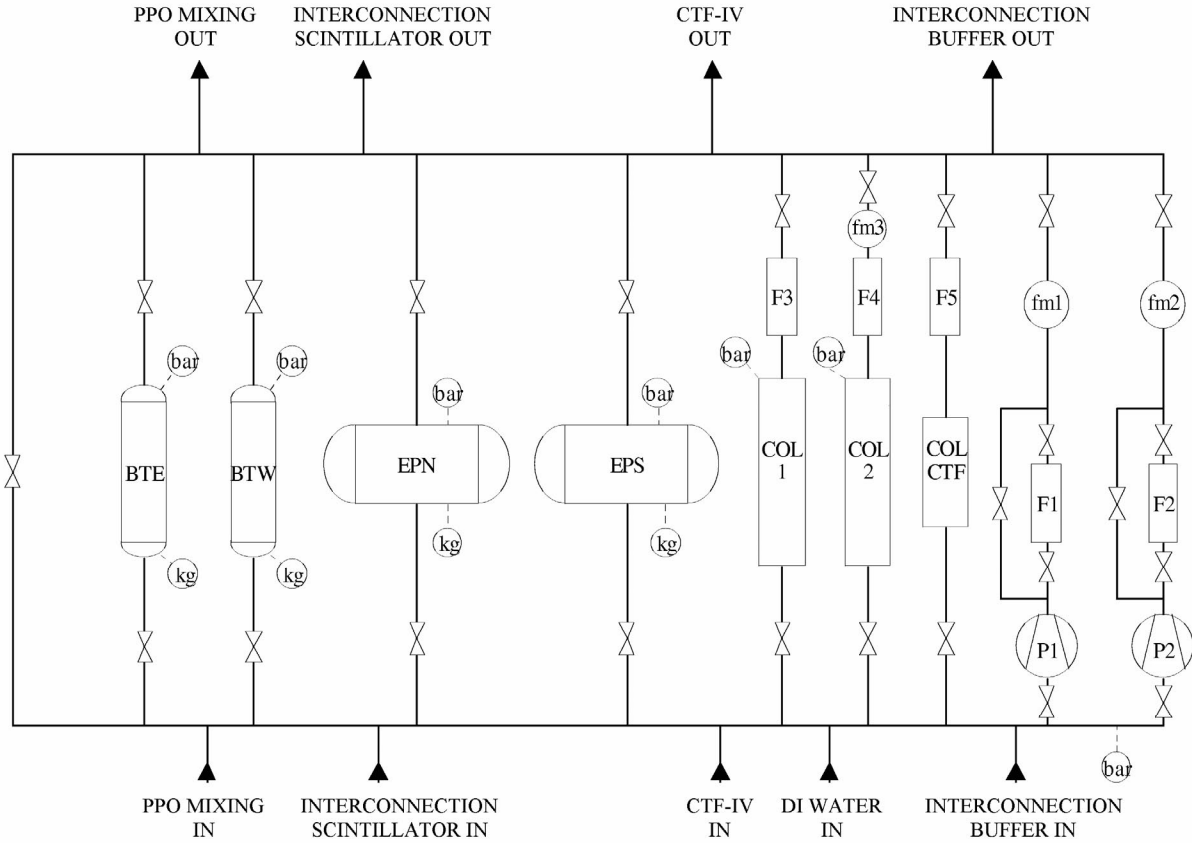


Figure 3.2: Block Diagram showing the main equipment of Module-0. BTE, BTW, EPN, EPS are tanks, 'bar' shows manometers, 'kg' shows load cells. F=filter, fm=flow meter, P=pump, COL=purification column.

### 3.1.1. Components

#### Nitrogen Supply

Liquid scintillator changes its optical properties and loses a part of the scintillation capability, when it comes in contact with oxygen. Exposition to air should further be avoided because of contamination with radon. Both problems are solved by using radon-free nitrogen as gas inside the vacuum tight system ('nitrogen blanket'). Dissolved radon or oxygen in the scintillator can be removed by nitrogen extraction in the tanks BTW and BTE.

On the other hand, nitrogen pressure is needed to supply the pumps of the system. For these reasons, since the CTF2 campaign, all Borexino-related subsystems like Module-0, are continuously supplied with ultra-pure nitrogen by a liquid nitrogen storage and purification plant, set up by the Max-Planck-Institut für Kernphysik, Heidelberg, and located near the entrance to hall C. Two different supply lines contain two nitrogen purity classes, namely Regular Nitrogen (RN<sub>2</sub>) and High Purity Nitrogen (HPN<sub>2</sub>). These purity classes are distinguishable by their <sup>222</sup>Rn content, which is ~0.1 mBq/m<sup>3</sup> in RN<sub>2</sub> and less than 1 μBq/m<sup>3</sup> in HPN<sub>2</sub>. Both types are gained by an evaporation of liquid nitrogen, whereby HPN<sub>2</sub> passes an additional charcoal column. During the past years, the CTF3 test results have led to the development of a third, superior nitrogen purity class, the low-Ar-Kr nitrogen (LAKN<sub>2</sub>). Its impurity concentrations shall be around ~15 ppb for Ar, ~0.05 ppt for Kr and ~1 μBq/m<sup>3</sup> for <sup>222</sup>Rn, in particular below the corresponding limits of 360 ppb, 0.14 ppt respectively 6.8 μBq/m<sup>3</sup> [Zuz04]. The LAKN<sub>2</sub> is planned to be supplied from the nitrogen plant in a third,

parallel line, up to now used for synthetic air. Module-0 is not connected to this line, can however be easily extended for that.

As the nitrogen plant provides a pressure between 7 and 16 bar, Module-0 is equipped with four pressure reducers (PR1-4, 'nitrogen panel') offering adjustable pressure levels down to one atmosphere. Here, RN<sub>2</sub> is directed to supply the pumps only, whereas HPN<sub>2</sub> is used for all other applications such as nitrogen extraction, tank blankets, purging of lines and chromatography columns. The flow of HPN<sub>2</sub> is monitored by a flow meter in the supply line.

### *Water Supply*

Deionised water is needed in numerous applications. It serves as exchange medium to unload scintillator from the CTF Inner Vessel (see Appendix A), it can be used for a possible water extraction process in batch mode (see also Appendix A) and, finally, it serves to purge tubes and other system components for cleaning purposes. Module-0 obtains ultra-pure water from a water purification system in hall C near the CTF tank. Here, the water is filtered, deionised and purged with nitrogen. The nitrogen extraction process mainly reduces the radon concentration. The water arrives at Module-0 with a pressure around 5 bar and a maximum flow rate at ~2m<sup>3</sup>/h. Some information can be found in [Bal96], the plant has however been upgraded since then.

### *Stainless Steel Tanks*

Module-0 possesses four electro-polished stainless steel tanks. Two of them, the so-called EP Tanks (EPN, EPS), contain a volume of 7.7m<sup>3</sup> each. They are certified to 4 bar overpressure (tested to 6 bar) by the Italian authority ISPESL and, due to their volume, among other things, able to perform complete volumetric scintillator loading and unloading processes of the CTF Inner Vessel. The two other tanks, called Buffer Tanks (BTE, BTW), contain a volume of 1.24m<sup>3</sup> each and mainly serve as process tanks. As they are not certified by an authority, the Italian law only permits overpressure until 0.48 bar. However, this regulation is not valid, if a tank contains liquid only and no gas volume. In this way, the Buffer Tanks are allowed to perform volumetric CTF loading and unloading processes like described in C.4, C.5. They are further equipped with nitrogen nozzles and spargers to remove gaseous contaminants from liquids by nitrogen extraction.

### *Upper and Lower Manifold*

The heart of Module-0 – the section where any liquid flow has to pass – consists of two manifolds facing each other, the upper and the lower manifold. All components like the Module-0 tanks, the chromatography columns, the Interconnection System and other related Borexino subsystems are connected to both the lower and the upper manifold. In particular, the upper manifold connects all the inlets, normally leading to the top of the containers, whereas the lower manifold connects the outlets at the bottom of the containers. The purpose of this topology is to provide a maximum flow path flexibility. Some bridges and two pumps connecting the two manifolds allow to move liquid from any outlet to any inlet, and between other connected components.

### *Teflon Pumps*

The two pumps (P1, P2, type Trebor Maxim 25) of Module-0 are diaphragm pumps driven by nitrogen pressure. They, like their connectors, consist of the two teflon types PTFE and PFA, assembled in a class 1000 clean room. As the connectors are insufficiently tight against

radon influx, both pumps are surrounded by an acrylic box, flushed with ultra-pure nitrogen to keep the radon concentration low. Liquids can be moved with a maximum flow rate of 32 l/min at 4.0 bar driving pressure and no back pressure, in direction from the lower to the upper manifold. The opposite direction is not blocked, however. At each pump, flow and pressure can be partially decoupled by a bypass, making the pump running more smoothly. The pump P1 is equipped with a pressure head (PH). The nitrogen support of the pump P2 is equipped with a pneumatic regulation valve (PV9), allowing to control the flux by a digital control system (DCS).

### *Tubes, Valves and Connectors*

All tubes, fittings and valves of Module-0 consist of electro-polished stainless steel (AISI 316L). They have been cleaned and packed according to SC11. All parts of probes in contact with liquid also consist of 316L stainless steel and are welded to the body. Especially there are no threaded connections. Rupture disks are selected following the same criteria. In order to assure tightness against radon, even in long term operations, only pipe connections with a leak rate below  $5 \cdot 10^{-11}$  bar·cm<sup>3</sup>/s have been used. This was achieved by orbital welding or VCR metal gasket connections. The VCR gaskets are of stainless steel, as some other kinds of metals do not resist pseudocumene. Gaskets in flanges are of teflon or nylon. All valves have a leak rate below  $4 \cdot 10^{-9}$  bar·cm<sup>3</sup>/s. Many of them are equipped with ¼ inch drain ports in order to allow cleaning, draining and sampling. The tube diameters in Module-0 are 28mm or 1 inch for the manifolds and liquid lines to tanks or adjacent plants, 18mm for side lines to the purification columns and 12mm for nitrogen lines and lines to the CTF Inner Vessel.

### *Chromatography Columns*

Two silica gel chromatography columns (COL1, COL2), the most delicate units in the Module-0 system, provide an excellent purification possibility for the scintillator of Borexino. The electro-polished stainless steel housings ('columns') are of rectangular shape, electro-polished inside and generally able to contain various adsorber materials. As in the past silica gel has turned out to be an excellent adsorber, each of the two columns has been filled with 30 kg of ultra-pure silica gel of the type 'Kromasil', provided by Eka Nobel, Sweden. The silica gel volumes are 129.7cm in length, 26.4cm in width, and 21.9cm in height, enclosed in two nylon filter papers with a pore size of 0.45µm. In particular, COL1 contains silica gel of a grain size of 20µm, delivered in February 2002 in a steel barrel, and COL2 is filled with silica gel of a grain size of 10µm, delivered in February 2001 in several cardboard barrels. Both chromatography columns are connected in parallel between the upper and lower manifold. Check valves at the column inlets avoid a back flow. A flow meter (FM3) serves to distinguish the single flow rates when operating the columns in parallel. A flexible ½ inch pipe can be installed between two spare connectors (C33 and C39) to operate the columns serially. Partially opening or closing adequate valves helps to separately adjust the pressure drop on each column. The columns' design pressure is 2.5 bar and their design flow, through each of them, 100 kg/h for pseudocumene.

A third chromatography column (COL3 or CTF-COL) connected in parallel serves for testing and is envisioned for pre-purification processes. This column was used during all CTF campaigns with exchanged batches of silica gel. In September 2002, 2.4 kg of new 'Kromasil' silica gel have been put in. This amount approximately arises from scaling the total 60 kg of silica gel in both big columns with the volume ratio between the CTF and Borexino Inner Vessels.

## *Filters*

Filters have been installed behind each pump and purification column in order to hold back dust and other particles. The filter cartridges consist of PTFE, offer a pore size of 0.05 or 0.1  $\mu\text{m}$ , a length of 10 inches and an effective surface of 7800  $\text{cm}^2$ . Their flow resistance should be negligible. However, if the flowing liquid is going to change between a hydrophilic and a hydrophobic medium – like from water to PC, the filter housing should be opened and the cartridge conditioned in isopropanol, otherwise the cartridge would block the flow. Also, nitrogen passes slowly through a wet cartridge. In case of the filters F1 and F2, such problems can be avoided by using the bypass.

## *Probes, Controls and DCS*

Important Module-0 system parameters are continuously measured and monitored by numerous probes. All values are reported via cables to a digital control system (DCS) located on the first floor of the Big Building West (BBW). This system has been envisioned to digitally control the major part of liquid handling processes related to the Borexino experiment – in which Module-0 is one of the very few sections controlled mainly manually. The DCS supplies several workstations distributed in hall C – among them one at Module-0 in the BBE – wherefrom expert operators are authorised to operate certain subsystems. Every DCS workstation is able to continuously monitor the parameters of all subsystems for any user, thus providing a maximum overview and safety.

The Module-0 probes show their values inside the Module-0 room in order to provide the fast and independent possibility of a manual system operation. In particular, Coriolis type flow meters (FM) measure flow and density of fluids; pressure probes (PP) monitor the pressure conditions in tanks, purification columns, and at some other positions. Load cells (MP) provide information about tank levels, whereas the properly calibrated values are available on the DCS monitors only. The load cell displays, located in a case near the Module-0 entrance, show values higher by factors of 5 to 6 for the Buffer Tanks and  $\approx 1.2$  for the EP Tanks. Furthermore, six manometers continuously monitor the pressure conditions at the Module-0 nitrogen panel and provide an analogue, independent safety option described in 3.1.2.

## *Gas Exhaust*

Harmful exhaust gases, normally nitrogen and pseudocumene vapour, are first collected by PTFE and PFA tubes in a Module-0 internal exhaust vessel of a volume of  $\sim 12$  litres. Small amounts of liquid can be caught here; an erroneous liquid flow inside the transparent teflon tubes can be recognised by eye. The exhaust vapour gets subsequently pipelined to a specific pseudocumene vapour exhaust system near the entrance of hall C, able to filter PC traces out of nitrogen.

### 3.1.2. Safety Issues

As pseudocumene, the liquid Module-0 is supposed to handle, is classified harmful and flammable – the fluid properties can be looked up in Appendix B – the safety of the liquid handling system Module-0 not only is an important item, it is even crucial concerning the operation permission for the system. A risk evaluation leads to the main danger consisting in a liquid spill caused either by a leak or by the breakage of a tank due to overpressure. In the following – assuming the worst case – electricity lightening can provoke a fire, especially as the flash point of pseudocumene is as low as  $45^\circ\text{C}$ . Escaping liquid releases at least harmful

vapours. Additionally, a leak in the nitrogen system can reduce the oxygen concentration in the air.

The Big Building East, containing the entire Module-0 equipment, provides the following safety installations:

- In case of leakage, a basin on the ground floor below the Module-0 equipment can hold 9.8m<sup>3</sup> of liquid. The entire BBE floor is sealed with a layer impermeable for pseudocumene.
- Foam glass inside the basin avoids high flames touching the tank surfaces in case of fire.
- A fire extinguishing system can distribute 'Inergen Gas' inside the BBE. It has to be manually started from outside, near the BBE front door.
- Temperature sensors in the BBE activate a siren when reaching 60°C.
- An oxygen monitor is located close to the upper manifold of Module-0. It is connected to a siren inside the BBE via the digital control system.
- No voltage inside the BBE exceeds 240V.
- A battery supplied emergency light automatically turns on in case of an electric power blackout.

Module-0 itself provides the following safety issues:

- Module-0 is a closed system, no liquid or vapour escapes into the air.
- The operating pressure is limited between 0 and 4 bar overpressure.
- All envisioned operations occur at ambient temperature, especially below the flash point of the handled liquids.
- The Module-0 devices are envisioned to be supplied by an Uninterruptible Power Supply (UPS), i.e. a system continuing the power supply in case of a blackout. This will prevent uncontrolled system reactions. If the UPS is out of order, the 'Module-0 safety valves' will automatically shut down Module-0 in case of a blackout.
- Safety against overpressure is provided by rupture disks. In particular, they break at 0.48 bar overpressure on BTE/BTW (RD9/10), and at 4.0 bar overpressure on EPN/EPS (RD8/11), or in the two high-purity nitrogen lines (RD1/2). Their uncertainty is at 10%.
- The outlets of the rupture disks on the tanks (RD8-11), possibly spilling liquid in case of a breakage, are connected to the so-called Blow Down System by stainless steel tubes. This is a system in hall C foreseen to contain and cool down hot liquid in the amount of several m<sup>3</sup>. The outlets of RD1 and RD2, as only dealing with nitrogen, are connected to the nitrogen exhaust vessel.
- A variable pressure control valve in the pump supply line (low purity nitrogen) cuts off the pump supply pressure, as soon as it becomes too high. It should be adjusted to 4.0 bar.
- The probes and controls in Module-0 provide a second level safety: Alarms can be configured in a flexible way via the digital control system and help to avoid dangerous system conditions. Appendix D shows the recommended values.
- An analogue pressure control system automatically shuts down the 'Module-0 safety valves' in case of erroneous pressure conditions in the nitrogen panel. These alarms can be set flexibly with the respective pressure manometers (PP1-5, PP12). Appendix D shows the recommended values.
- Module-0 safety valves: Pneumatic valves are installed in both nitrogen supply lines (PV1/2), at the bottom and top of the BT Tanks (PV5-8), and at the bottom of the EP Tanks (PV3/4). They will be closed either by an alarm case at the Module-0 nitrogen pressure controllers (PP1-5, PP12), or by pushing the red button 'Mod-0 Emergency

out', or by an according DCS output signal. This way, processes like pumping or pressurising that could cause danger are immediately stopped. In particular, such a shutdown overrules single DCS signals trying to operate the valves PV5-8. Detailed operation procedures can be found in C.1.

- Manual valves are installed at all Module-0 exit points. In dangerous situations, Module-0 can be isolated.
- Check valves are installed at the nitrogen distributors (CV1/2) to avoid an undesired back flow of liquid into the nitrogen system.
- Check valves at the purification column inlets (CV5/6) avoid a back flow in the chromatography columns that could break the column filters.
- Emergency shutdown: A red button labelled 'Mod-0 Emergency out' is installed outside the BBE near its front door. In case of emergency, that button can be pressed to immediately close the Module-0 safety valves. Liquid and gas flow will be stopped and the tanks isolated. However, other plants involved in current processes have to be shut down separately. In order to reopen the Module-0 safety valves, the button has to be pulled out again.

### *Alarms*

Module-0 provides two possibilities of configuring alarms. The first one refers to the pressure controllers at the nitrogen panel (PP1-5, PP12). Their alarm set points can be changed by opening the glass windows and adjusting the red pointers to a reasonable limit. If the pressure in one of the nitrogen lines reaches the respective limit, the pressure controller closes the Module-0 safety valves by an analogue electric signal. In this case, the control device near the nitrogen panel shows a red flash light referring to the activated manometer and starts a siren. The Module-0 safety valves can be reopened by pressing the "Reset" button. This acknowledges the alarm and ignores it in the following.

Apart from this, a second, more general possibility of configuring alarms is provided by the digital control system (DCS) of Borexino. It can be operated from several workstations in hall C, for instance from the one inside the BBE. The alarms can be set in a flexible way on each signal connected to the DCS. In an alarm case, the DCS sets off a red flashlight and a siren near the Module-0 equipment. The siren automatically goes out after 20 seconds. The flashlight remains on until the alarm is acknowledged on the DCS. Appendix D shows the standard set points of all Module-0 alarms. In particular situations it can however be useful to choose other values.

#### 3.1.3. Surroundings

Module-0 is one of several liquid handling components of the Borexino experiment. The other components can be reached in different ways. As said above, Module-0 is directly connected to the PPO Plant (via V4, V74), the CTF Inner Vessel (via V1, V87) and a plant on top of the CTF tank (via V1, V53, V80); indeed, it provides the connections to these modules from other liquid handling components. Three further components, the Purification Skid, the Storage Area, and the Filling Station can be reached via the so-called Interconnection System, situated on first floor of the BBE. This system basically consists of four main bus lines, divided into two scintillator lines (diameter 3/4") and two buffer lines (1"), one in both cases to be used in forward and one in backward direction (see Figure 3.3). The distinction between scintillator lines, referring to the scintillator for the Borexino Inner Vessel, and buffer lines, referring to the shielding pseudocumene, accounts for their different purity requirements. Module-0 provides one line to each Interconnection main bus, called 'Interconnection Scintillator in' (V79), 'Interconnection Buffer in' (V88), 'Interconnection Scintillator out' (V3)

and 'Interconnection Buffer out' (V83). The other plants are connected similarly. Two additional bridges between Module-0 and the Purification Skid help to operate these two plants in a serial mode. Apart from that, ultra-pure water from the water plant is available via V82 in the lower manifold.

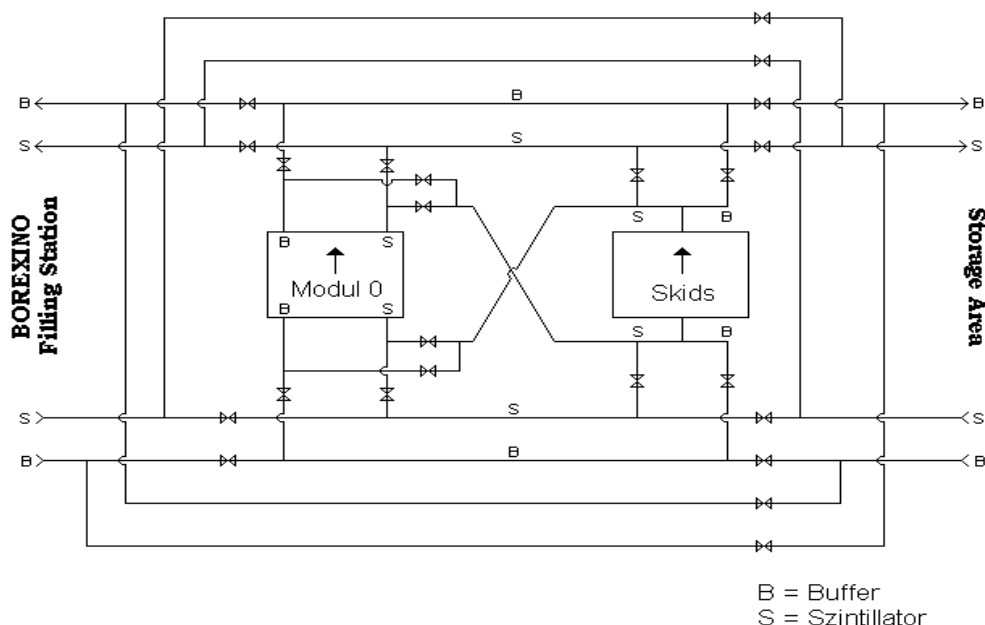


Figure 3.3: Sketch of the Interconnection System, providing the connections between Module-0 and other important liquid handling components of Borexino. 'Skids' means the Purification Skid.

### 3.1.4. Construction and Development

The design principles described above have been used since the very beginning of the Borexino experiment or the first CTF tests respectively in order to cope with similar tasks. The first version of the so-called Module-0 consisted in a preliminary system installed in 1995 to carry out fluid operations needed for the first scintillator tests with the CTF detector. That liquid handling system, mainly based on teflon material, performed, among other things, the scintillator preparation and loading process for CTF1 (compare 2.4.2). The system had to be removed from its location in autumn of 1998 due to the construction of the Big Building West.

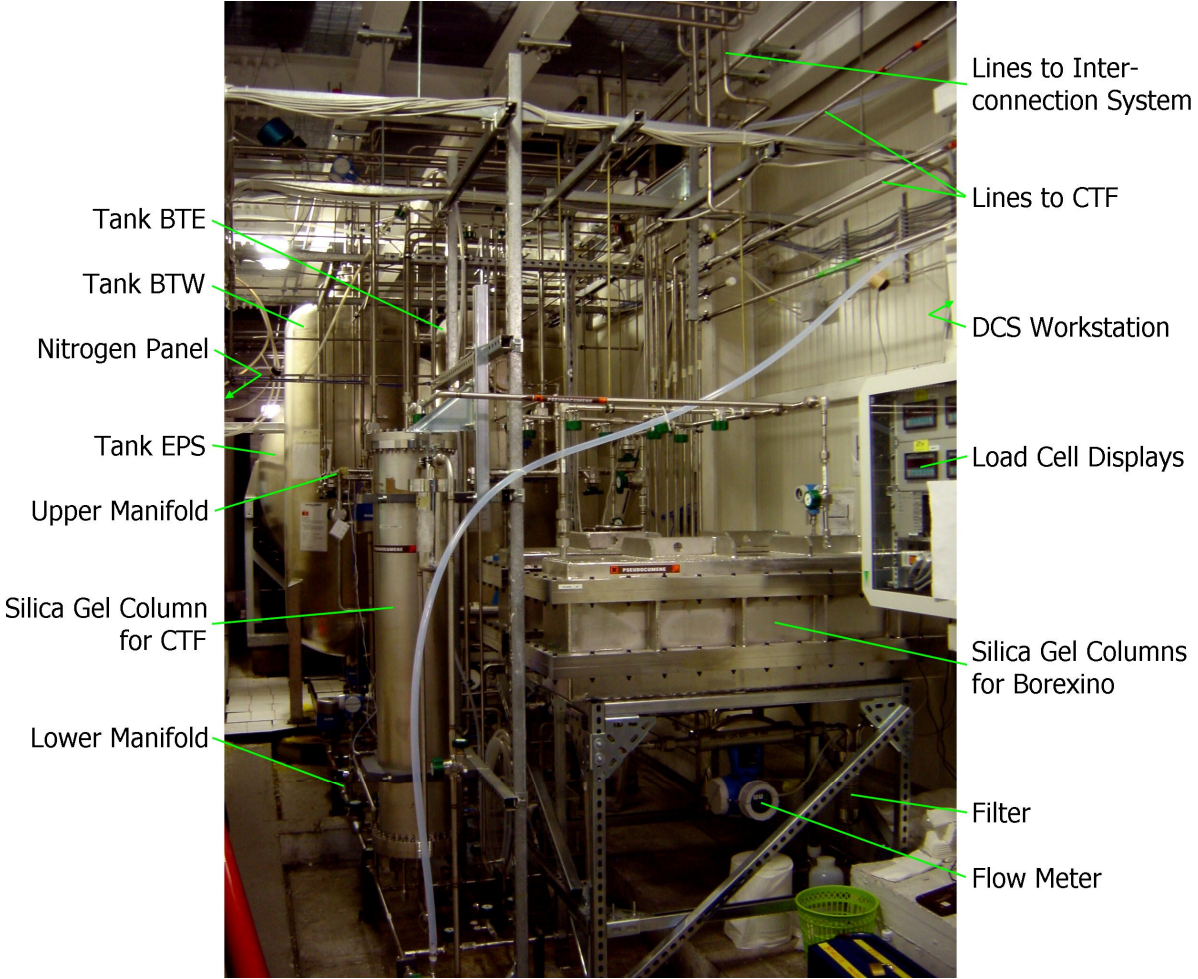
During the CTF1 campaign, Module-0 was responsible for the mixing of the scintillator solvent PC with the wavelength shifter PPO. It comprised three tanks of 2.2m<sup>3</sup> volume each, the so-called Hoover-Tanks (HT), where the mixing and purification of a concentrated PPO solution, the so-called 'Master Solution', was carried out. Before the filling of the CTF Inner Vessel, this Master Solution was added to an adequate amount of pseudocumene. In the following years, the idea of an 'in-line' scintillator mixing – during the scintillator filling process – has led to a change in the concept and to a separation between Module-0 and the scintillator mixing plant – a new PPO mixing plant has been constructed. Since then, Module-0 has only been used to add Master Solution batches to pseudocumene (see C.3).

The construction of the existing Module-0 version inside the BBE began in autumn of 1999. At that time, the idea of integrating a large scale silica gel chromatography system into the fluid handling system of Borexino was already present. Valves and tubes of the old Module-0 version, completely disassembled and cleaned inside a clean room, were reassembled

to manifolds and larger tubing sections, still inside the clean room. They were transported into hall C and connected by orbital welding inside the new BBE at the current Module-0 location. New pumps and the four Module-0 tanks were connected to the manifolds, new probes and controls were implemented. [Nie00] describes some more details about this work in context with the necessity to meet the purity requirements of the Borexino experiment. Between May and October 2000, the system, though not yet completed, was able to carry out the required operations for the CTF2 campaign (compare 2.4.3). During the summer of 2001, the construction works were concluded for the time being. The fluid handling part of the system was completed as far as possible, except for the two large purification columns.

During the CTF3 campaign, Module-0 was slightly upgraded to meet changing requirements. This mainly concerned the implementation of new probes and safety elements, and the connection to the DCS, worked out parallel to the CTF3 operations. In July 2002, the two large silica gel chromatography columns were finally installed after having been constructed and filled at the Technische Universität München. The old cylindrical column used until then has been kept in the system for CTF tests and pre-purification steps.

The Module-0 system is complete now; it has been inspected and permitted by the LNGS in 2003. Detailed documentation of set-up, components, specifications and important operation procedures is available at the LNGS. The purity of the system has been shown by radon emanation measurements (see 3.3), particulate counting tests (see 3.4), and the CTF3 tests (see 2.4.4) during the past years.



Picture 3.4: View of the Module-0 equipment from the entrance door, May 2003

Several blind VCR connectors included in the current design allow a future expansion of the system, like C57, C59, C62, C65, C85, C92, C99, C103 in the tank connection lines, as well as C40, C45 near the purification columns. Also the lines behind V2, V78 and V81 are currently not in use and open for future purposes.

### 3.2. Cleaning of the System

Each purification method – even the most effective process ever – is still restricted by the purity level of the purification system itself. Therefore, the cleaning of the liquid handling system Module-0 is crucial. This concerns macroscopic dust particles as well as single atoms sticking to surfaces. All these kinds of impurities generally threaten low level counting rate experiments because of the unavoidable presence of radioactive nuclides and substances. Dust particles and adhesive dirt rests can normally be dissolved and purged with organic solvents or detergent. A higher temperature improves the cleaning effect. Afterwards, the solvent or the detergent respectively has to be flushed out with deionised water. Atoms adsorbed on surfaces can often be removed with diluted acids, as they dissolve more easily at low pH values. An increased temperature or acid concentration improves also here the effect. It is important to apply the acid directly onto the surface, i.e. to remove rests of solvents – like pseudocumene – or other substances except water from the system before. This can be achieved by a detergent cleaning and a subsequent water flushing. Anyway, every cleaning solution should be flushed out of the system with deionised water immediately after its application. For example, a usual cleaning procedure consists of an initial flush with hot detergent, a subsequent flush with deionised water, a flush with hot, diluted nitric acid and a final, intensive flush with deionised water. Depending on the temperature, the nitric acid should not remain in contact with stainless steel for too long. Several similar cleaning procedures, described below, were applied on the different versions of Module-0 or on parts of it.

The first, temporary version of Module-0 was cleaned according to the following steps, before the CTF1 operations commenced in 1995:

- a hand cleaning of the BT Tanks by mechanical scrubbing with organic soap
- a flush with water to remove soap
- a flush with an organic solvent (e.g. gasoline) to remove organic films
- a flush with ethylene glycol in instances after the organic flush
- a flush with pure water
- a flush with a 10% nitric acid solution
- a final flush with deionised water from the water plant in hall C

At the beginning of the construction of the recent Module-0 version in 1999, the BT and EP Tanks were taken from the preceding version, maintaining their cleanliness level. The tank EPS was cleaned in 2000 with detergent and ultra-pure water before the beginning of the CTF2 campaign. In April 2002, the tank EPN was cleaned with the help of two teflon spray balls, using detergent, nitric acid (2%, 20°C, 4 hours) and ultra-pure water.

The piping of Module-0 was assembled with care and frequently flushed with pure argon to keep out radon and dust. Prior to the CTF2 operations, it was intensively flushed with ultra-pure water from the water plant in hall C.

In August 2002, as a consequence of the failure of the silica gel batch test, the BT Tanks and the piping were cleaned with detergent, nitric acid (3%, 60°C, 4 hours) and ultra-pure water. The cleaning process included the connections to the CTF Inner Vessel up to the valves V1CTFtop and V13CTFbottom. The connections from the manifolds to the EP Tanks however were not cleaned due to organisational problems. The cleaning process was

accomplished with the help of the so-called 'Cleaning Module', a system located in hall C and capable of circulating different types of detergents, diluted acids, organic solvents, and water around the various liquid handling components of Borexino. Since this cleaning, Module-0 has not been used again.

### 3.3. Radon Emanation Measurements

#### 3.3.1. Motivation

In the following, we consider the isotope  $^{222}\text{Rn}$  in the  $^{238}\text{U}$  chain, naturally produced by the U decay and thus present in the air at an activity level of about  $30\text{ Bq/m}^3$ . Close to earth – in caves or tunnels like the LNGS underground laboratory – the  $^{222}\text{Rn}$  activity can be higher by small factors around  $\sim 2$ .

Regarding the consequences in the context of Borexino,  $^{222}\text{Rn}$  itself decays quite quickly, being less harmful than its decay daughters – mainly  $^{210}\text{Pb}$ , that conserves the activity over a long time period (see Figure 2.6). Its daughters  $^{210}\text{Bi}$  and  $^{210}\text{Po}$  even deposit 59% ( $^{210}\text{Bi}$ ) and 100% ( $^{210}\text{Po}$ ) of their decay energy in the neutrino window between 250 and 800 keV. So, each  $^{210}\text{Pb}$  nucleus – product of a former  $^{222}\text{Rn}$  – will cause by its decay daughters  $1.35 \cdot 10^{-4}$  events per day in the neutrino window [Nef96]. One obtains that 1 mBq of  $^{222}\text{Rn}$ , decaying to 477  $^{210}\text{Pb}$  nuclei, will later cause 0.0646 disturbing events per day, implying that 320  $\text{m}^3$  of scintillator are allowed to stay in contact with a 1 mBq  $^{222}\text{Rn}$ -emanating tank for a *maximum of 44 hours* in order not to cause more than 1 event/day of  $^{210}\text{Pb}$  daughter activity between 250 and 800 keV in the 113  $\text{m}^3$  of Fiducial Volume.

With respect to the scintillator treatment before the experiment filling process, this number is completely unrealistic to fulfil. This, on the one hand, implies the necessity of an on-line purification method, going to be applied once the Inner Vessel of Borexino will be filled. But on the other hand – as the efficiency of on-line purification is not assured – it implies to have an eye on the radon influx from the very beginning and to keep it as low as possible.

Radon gets emanated by nearly all materials, as they normally contain traces of impurities, among others radioactive ones such as  $^{238}\text{U}$  and  $^{232}\text{Th}$  with all their decay daughters. In particular, radon – as a gas – is able to escape if it is produced by decays close to the material surface. This so-called *emanation* process takes place in all detector related parts – like liquid handling equipment – and is able to contaminate the scintillator in this way. Besides, it is obligatory to avoid small leaks to outside because of the radon contamination in the air. The verification of a low radon level in liquid handling systems can exclude both – leaks and impurity traces – and thus is an excellent indication for the purity state in general. Also dust or dirt normally contain a wide spread of different elements;  $^{238}\text{U}$  and  $^{232}\text{Th}$  concentrations in the earth crust have been determined to  $1.8 \cdot 10^{-6}$  and  $7.2 \cdot 10^{-6}$  [Mas82] and are visible for  $^{222}\text{Rn}$  emanation measurements.

In contrast, elements in the  $^{238}\text{U}$  chain below the isotope  $^{222}\text{Rn}$  cannot be detected in this way. Especially liquid handling equipment can be contaminated with radon daughters (Pb, Bi, Po) due to air contact during the installation phase and has to be purified afterwards (see Chapter 3.2).

#### 3.3.2. Methods

$^{222}\text{Rn}$  emanation has been examined by the group of the Max-Planck-Institut für Kernphysik, Heidelberg, Germany. Emanation rates out of many detector-related parts all over the Borexino experimental area have been measured. Various methods of extracting  $^{222}\text{Rn}$  out of

the considered volumes in order to determine its activity were applied. They are described in the following.

In case of the measurement of an empty tank volume, that volume was first purged ~10 times the volume with high-purity nitrogen in order to reset the inside radon activity to zero. Afterwards, the volume was tightly closed, leaving some nitrogen overpressure inside. The inner surface – especially dirt on it – emanates radon and generates an equilibrium of emanation and decay with a time constant of  $t_{1/2}=3.8\text{d}$  (see Figure 3.5). After a certain exposure time – at least one  $^{222}\text{Rn}$  half-life – a part of the overpressure gas was sampled, the contained radon extracted by adsorption on an ultra-cold charcoal filter and filled into a proportional counter. The measured  $^{222}\text{Rn}$  activities were extrapolated to their equilibrium values with knowledge of the exposure time. Measurements usually were repeated once at least.

The described extraction method can also be accomplished with water instead of nitrogen. As the water available at the Borexino site contains a higher  $^{222}\text{Rn}$  activity ( $\sim 1\text{ mBq/m}^3$ ) than the high-purity nitrogen ( $<1\text{ }\mu\text{Bq/m}^3$ ), the initial activity could not be reset to zero with this method. However, initial radon contamination in water decays towards an equilibrium activity corresponding to the emanation rate of its container. In this context, the considered tank was filled with water and left untouched for several weeks. Then, a part of the water ( $\approx 350$  litres) was sampled, the contained radon trapped in an ultra-cold adsorber and measured with a proportional counter. As water however contains  $^{226}\text{Ra}$ , generating  $^{222}\text{Rn}$ , this background activity had to be subtracted. The  $^{226}\text{Ra}$  related background was estimated to  $(1\pm 1)\text{ mBq per m}^3$  [Fre03].

Further  $^{222}\text{Rn}$  emanation rates were obtained with the CTF data, using  $^{214}\text{BiPo}$  coincidences (see 4.3.1). Therefore, the examined liquid handling part had to be filled with liquid scintillator and kept untouched for some  $^{222}\text{Rn}$  half lives in order to reach the emanation equilibrium – facing the same problem as prior to the described water measurement. Finally, the scintillator was loaded into the CTF Inner Vessel and the corresponding  $^{214}\text{BiPo}$  coincidence rise observed. The emanation equilibrium value was calculated by dint of the exposure time.

As the described preparation procedures take a time in the order of weeks, in several cases the necessity of a radon measurement collided with other experimental activities. In particular, it occurred that different substances, namely pseudocumene, water and nitrogen – all insoluble in each other – had remained in a tank for some reason but long enough to have reached an emanation equilibrium. Such situations provided further possibilities of radon emanation measurements by sampling the liquid phase at the bottom, i.e. pseudocumene or water. The emanation value of the whole tank could be calculated, accounting for the different phase volumes under consideration of the following points:

- The emanation rate into each phase was assumed to be proportional to the phase volume, although emanation is caused by the surface. Different surface-to-volume relations – resulting from the special tank shape and the exact location of the phase –

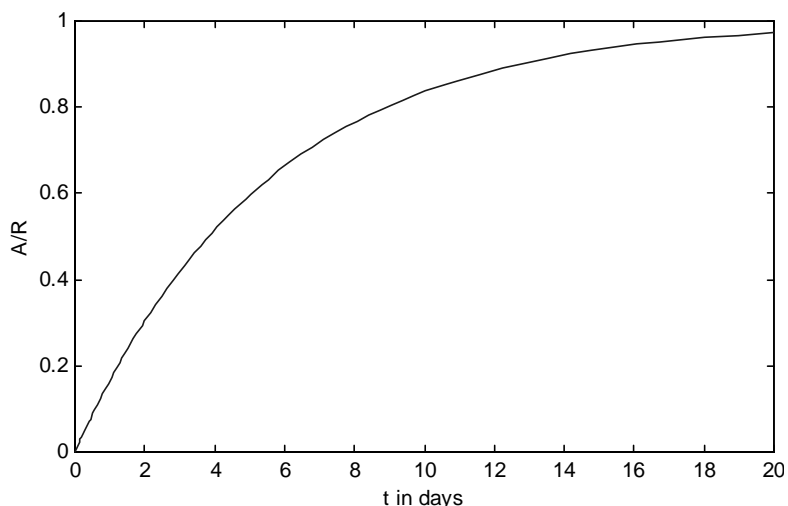


Figure 3.5:  $^{222}\text{Rn}$  activity progression caused by emanation. The activity is determined by  $A(t)=R(1-e^{-\lambda t})$ , whereby  $R$  is the emanation rate in  $\text{s}^{-1}$ .

were neglected, as this leads to a conservative consideration, like derived in the following.

- As soon as two phases mix, their radon concentrations behave according to the radon solubilities:  $S_{H_2O}=1.0$  (reference value),  $S_{N_2}=3.3$  [Woj96],  $S_{PC}=38$  [Zuz02]. In particular,  $N_2$  and PC accumulate a *higher* radon concentration than water.
- A solubility equilibrium between a liquid and a gas phase can continuously be assumed, according to examinations in [Zuz02].
- The solubility equilibrium between two liquid phases does *not* adjust, unless the two phases are mechanically mixed, or by conversion. Two liquid phases just statically touching mix only in the range of  $\sim 1\text{cm}$  by diffusion. Radon concentrations in different liquid phases of tank volumes do especially not equilibrate without a mechanical mixing. A confirmation of this presumption follows in 3.3.4.

Normally, water, PC, and nitrogen were together in a tank. In this case, it was assumed that PC equilibrated with the gaseous nitrogen, but not with the water at the bottom. So, if sampling the water, its activity was linearly extrapolated from the water volume to the tank volume. This interpretation is conservative, as contaminations caused by dust or dirt usually dominate at the bottom of a tank.

In case of only PC and nitrogen in a tank, the radon concentrations in both phases equilibrate with the ratio  $38/3.3 = 11.5$ . For equal PC and nitrogen volumes, the radon content of the sampled PC has to be multiplied by  $12.5/11.5$  in order to add the small radon contribution in nitrogen.

### 3.3.3. Results

Table 3.6 summarises all  $^{222}\text{Rn}$  emanation measurements performed on Module-0 related equipment. The results refer to equilibrium values.

Object	Date	Result	Preparation Method / Analysis
Tank EPN $V=7.7\text{m}^3$	Jan 2002	$65\pm 10$ mBq	Emanation into $6.6\text{m}^3$ of $\text{H}_2\text{O}$ , $1.1\text{m}^3$ of $\text{N}_2$ . Tank untouched for 5 weeks. $0.35\text{m}^3$ of $\text{H}_2\text{O}$ sampled and measured once. Counting rate in water $7.15\pm 0.59$ mBq/ $\text{m}^3$ . $1\pm 1$ mBq/ $\text{m}^3$ subtracted for $^{226}\text{Ra}$ in water. [Fre03]
Tank EPS $V=7.7\text{m}^3$	Nov 2001	[32;55] mBq	Emanation into $3.0\text{m}^3$ of $\text{H}_2\text{O}$ , $4.7\text{m}^3$ of PC. $\text{H}_2\text{O}$ was in EPS for 11d, PC for 22d. $3.8\text{m}^3$ of PC loaded into CTF, increase of $27\pm 0.8$ mBq [Mon02] detected. The loading process possibly induced a mixing between $\text{H}_2\text{O}$ and PC. A calculation assuming optimal mixing results in $33.4\pm 1.0$ mBq for the whole tank, assuming no mixing results in $53.6\pm 1.7$ mBq.
Tank EPS $V=7.7\text{m}^3$	Dec 2001	$76\pm 10$ mBq	Emanation into $6.6\text{m}^3$ of $\text{H}_2\text{O}$ , $0.85\text{m}^3$ of PC, $0.15\text{m}^3$ of $\text{N}_2$ . $\text{H}_2\text{O}$ and PC not mixed for 2 weeks. $0.35\text{m}^3$ of $\text{H}_2\text{O}$ sampled and measured once. Counting rate in water $10.9\pm 0.9$ mBq/ $\text{m}^3$ . $1\pm 1$ mBq/ $\text{m}^3$ subtracted for $^{226}\text{Ra}$ in water. [Sim02]
Tank EPS $V=7.7\text{m}^3$	Jan 2002	$77\pm 12$ mBq	Emanation into $5.2\text{m}^3$ of $\text{H}_2\text{O}$ , $0.9\text{m}^3$ of PC, $1.6\text{m}^3$ of $\text{N}_2$ . $0.35\text{m}^3$ of $\text{H}_2\text{O}$ sampled immediately after $\text{H}_2\text{O}$ -PC mixing loop. Counting rate in water only $1.9\pm 0.2$ mBq/ $\text{m}^3$ , because most Rn dissolved in PC. $1\pm 1$ mBq/ $\text{m}^3$ subtracted for $^{226}\text{Ra}$ in water. [Fre03]

Tank BTW V=1.24m <sup>3</sup>	Jan 2002	3.7±1.4 mBq	Emanation into 0.83m <sup>3</sup> of H <sub>2</sub> O, 0.35m <sup>3</sup> of PC, 0.10m <sup>3</sup> of N <sub>2</sub> . H <sub>2</sub> O and PC mixed 8 days before sampling of 0.35m <sup>3</sup> of H <sub>2</sub> O. That means: Water activity reset to ~0, then emanation during 8 days. Counting rate in water 2.98±0.41 mBq/m <sup>3</sup> . 1±1 mBq/m <sup>3</sup> subtracted for <sup>226</sup> Ra in water. [Fre03]
Tank BTW V=1.24m <sup>3</sup>	Jun 2002	2.0±0.5 mBq	Emanation into 0.50m <sup>3</sup> of PC, 0.74m <sup>3</sup> of N <sub>2</sub> . PC was in BTW for 3.2d. 0.46m <sup>3</sup> of PC loaded into CTF, <sup>214</sup> BiPo increase of 1.06±0.15 mBq [Mon02] observed. Background emanation rate of pipe Mod0↔CTF (0.35±0.11 mBq) subtracted.
Tank BTE V=1.24m <sup>3</sup>	Jan 2002	0.25±0.14 mBq	Emanation into 0.62m <sup>3</sup> of PC, 0.62m <sup>3</sup> of N <sub>2</sub> . PC was in BTW for 3 weeks. 0.46m <sup>3</sup> of PC loaded into CTF, <sup>214</sup> BiPo increase of 0.19±0.10 mBq [Mon02] observed. Volume of pipe Mod0↔CTF had separately been loaded.
Pipe Mod0-CTF top	Jan 2002	0.29±0.07 mBq	Emanation into PC. PC was in the pipe for 6 weeks. 25 kg of PC loaded into CTF, <sup>214</sup> BiPo increase of 0.29±0.07 mBq [Mon02] observed.
Pipe Mod0-CTF top	Feb 2002	0.41±0.09 mBq	Emanation into PC. PC was in the pipe for 2 weeks. 15 kg of PC loaded into CTF, <sup>214</sup> BiPo increase of 0.41±0.09 mBq [Mon02] observed.
Pipe loop Mod0-CTF	Feb 2002	0.9±0.3 mBq	Emanation into PC. PC was in the pipes for 4 days. CTF scintillator circulated via Module-0, <sup>214</sup> BiPo increase of 0.47±0.17mBq [Mon02] observed.
Pipe low pressure N <sub>2</sub> system	Mar 2000	< 0.088 mBq	Emanation into N <sub>2</sub> . N <sub>2</sub> evacuated and measured. C.L. at 90%. [Buc01]
Pressure head	Mar 2000	< 0.033 mBq	Emanation into N <sub>2</sub> . N <sub>2</sub> evacuated and measured. C.L. at 90%. [Buc01]
Silica gel for CTF1 (Merck)	1998	190±10 mBq/kg	Silica gel emanation measurement (63-200µm grain size, 60Å pore size). Emanation into N <sub>2</sub> . Emanation chamber evacuated. [Sch00]
Silica gel for CTF (Merck)	1998	207±10 mBq/kg	Silica gel emanation measurement (63-200µm grain size, 60Å pore size). Emanation into N <sub>2</sub> . Emanation chamber evacuated. [Sch00]
COL3 + Silica gel (Merck, CTF1)	1997	172±21 mBq/kg	Emanation into CTF1 scintillator (PXE) during circulation via purification column (COL3), loaded with 15kg of silica gel (63-200µm grain size, 60Å pore size). [Sch00]
Silica gel for CTF2 (Merck)	1999	320±30 mBq/kg	Calculation of silica gel emanation (63-200µm grain size, 60Å pore size). <sup>226</sup> Ra content measured with γ-spectroscopy. <sup>222</sup> Rn emanation calculated with use of the known activity ratio A( <sup>226</sup> Ra)/A( <sup>222</sup> Rn)=11.4±1.1 for this silica gel type. [Nie00]
Silica gel 'Kromasil'	Aug 2000	<1.2 mBq/kg	Silica gel sample of 45.5g (16µm average grain size, 60Å pore size). Emanation into N <sub>2</sub> . N <sub>2</sub> evacuated from emanation chamber at 120°C and measured. [Buc01]
COL3 + 2.4kg of 'Kromasil' (silica gel loop test)	Feb 2002	1.9±0.3 mBq	2.4kg of silica gel (10µm average grain size, 60Å pore size) was in purification column (COL3) for ~3 months. ~3 weeks before the test, the column was completely filled with PC. Emanation into PC. Then CTF scintillator was circulated via COL3 for 5 days. Fit to CTF data points during circulation (see 4.3.1)

COL1 steel housing	Jun 2002	0.59±0.05 mBq	Emanation into N <sub>2</sub> , N <sub>2</sub> evacuated. The result is the average of two measurements. [Fre03]
COL2 + 30kg of 'Kromasil' silica gel	Oct 2002	5.3±0.5 mBq	30kg of silica gel (10µm average grain size, 60Å pore size) in purification column COL2. Emanation into N <sub>2</sub> . N <sub>2</sub> overpressure released. The result is the average of two measurements. [Fre03]
COL1 + 30kg of 'Kromasil' silica gel	Dez 2002	4±2 mBq	30kg of silica gel (10µm average grain size, 60Å pore size) in purification column COL1. Emanation into N <sub>2</sub> . N <sub>2</sub> overpressure released. The result is the average of two measurements. [Fre03]
Silica gel 'Kromasil'	Dez 2002	0.13±0.05 mBq/kg	Calculation using the above values: Average of COL1, COL2 containing 30 kg of silica gel. Steel housing subtracted.

Table 3.6: <sup>222</sup>Rn emanation measurements with Module-0 equipment.

### 3.3.4. Conclusions

The radon emanation values of Module-0 related parts are in the same range as respective numbers of other Borexino liquid handling equipment. The Buffer-Tanks, tubes, and purification columns show low emanation rates in the range of some mBq. Especially the columns, containing 30 kg of ultra-pure silica gel, as confirmed by the above measurements, have been proven to be accurately installed in terms of tightness and radiopurity. Formerly, during the CTF1 and CTF2 campaigns, other types of silica gel caused emanation rates higher by 2 orders of magnitude. 30kg of the 'Kromasil' type, however, show the same emanation as stainless steel tanks with a volume of ~1m<sup>3</sup>. Only this fact allows the use of silica gel chromatography as purification method for the Borexino scintillator.

Silica gel does not hold back a considerable part of the emanated radon. With a view to the above CTF1 measurements, radon emanation out of silica gel into nitrogen (190±10 mBq/kg, 207±10 mBq/kg) does not show a significant difference compared to the emanation out of silica gel into flowing scintillator (172±21 mBq/kg). The CTF3 measurements do not contradict; the emanation out of 2.4kg of 'Kromasil' silica gel (0.32±0.17 mBq, derived from Table 3.6), as used in the silica gel loop purification test (4.3.1), is too low to allow a related statement – the major part of radon observed during this test (1.9±0.3 mBq) seems to be caused by the liquid handling parts themselves. The noble gas radon is not polar, and the presumably weak adsorption capability of silica gel for radon gets probably saturated by radon atoms from air contact.

The presumption that different radon concentrations in two adjacent, unmoved liquid phases do not equilibrate on small time scales has been confirmed by measurements with the tank EPS in Dec 2001 and Jan 2002 (Table 3.6). The first sample was taken after the tank had remained untouched for several weeks, whereat the result (76±10 mBq) was calculated using equal – not equilibrated by the solubilities – radon concentrations in PC and water. In particular, this does not differ from the second measurement (77±12 mBq), obtained after a mixing loop in the tank and the assumption of a perfect solubility equilibrium, with the radon concentration in PC 38 times higher than in water.

### 3.3.5. <sup>220</sup>Rn Emanation

<sup>220</sup>Rn, also called thoron, is a part of the <sup>232</sup>Th chain. It decays comparatively fast (half-life ≈12h for its total chain) to the stable nucleus <sup>208</sup>Pb. It especially does not produce any long

lived radioactive daughter. Therefore,  $^{220}\text{Rn}$  is not considered a dangerous contaminant. In CTF, it is observed by  $^{212}\text{BiPo}$  coincidences.

The emanation of  $^{220}\text{Rn}$  was observed during the silica gel loop test in February 2002 (see 4.3.1). This loop involved a purification column (COL3) with 2.4 kg of ‘Kromasil’ silica gel, some additional pipes, a teflon pump and a teflon filter in the Module-0, as well as the CTF loop pipes of about 50m in length, another teflon filter, and the Inner Vessel. In total, a constant  $^{212}\text{Bi}$  rate of  $60\pm 8$  counts/day [Dan02] was observed in the CTF detector during the described purification loop. After the loop, it decayed quickly, presumably with the mentioned half-life of  $\approx 12\text{h}$ . It can be considered as an equilibrium rate for the emanation of  $^{220}\text{Rn}$ .

The same effect was observed during the water extraction loop in March 2002, involving the CTF Inner Vessel, the CTF loop pipes, a teflon filter, some Module-0 pipes, two teflon pumps, and the whole water extraction and nitrogen stripping area in the Purification Skid. A  $^{220}\text{Rn}$  emanation equilibrium of  $29\pm 3$  counts/day [Dan02] was observed.

## 3.4. Particulate Counting

### 3.4.1. Motivation

Particulates are everywhere in the air – inside the Gran Sasso underground laboratory, their concentration, at least until the end of the CTF3 campaign, seemed even enriched due to ongoing construction works. Liquid handling parts can easily get contaminated with particulates during the installation phase – unless the work is done in a clean room, or the pipe and tank volumes are always kept closed. As the latter is difficult to realise, liquid handling systems have to be purified prior to their utilisation – normally with detergent and water (compare Chapter 3.2). Particulate counting tests are useful in order to prove the required cleanliness levels.

Dust in hall C of the LNGS contains a large variety of impurities. An estimation for the concentration of the radioactive isotope  $^{238}\text{U}$  in dust, arising from its concentration in the earth crust, amounts to  $\sim 1.8 \cdot 10^{-6}$  [Mas82]. With the restrictive limit for  $^{238}\text{U}$  in Table 2.5, this requires a particulate concentration in the liquid scintillator of  $< 1.3 \cdot 10^{-11}$  g/g. According to Table 2.5, all other isotopes result less restrictive.

Several water samples of different Module-0 tanks were taken prior to the CTF3 campaign in order to check the cleanliness level. A further goal consisted in an examination of the efficiency of the teflon filters. Therefore, different samples were taken before and after one of these filters in Module-0, furnished with a cartridge of a pore size at  $0.1\mu\text{m}$ .

### 3.4.2. Method

Water samples of 250g were taken from VCR ports in Module-0, either close to the lower manifold at a purging port of V71 or after the filter F1 at C29. The water, originally from the water plant in hall C, had been passed through one of the Module-0 tanks, EPN, EPS, BTE or BTW.

Small polyethylene bottles, having been cleaned and purged with deionised water, were opened in the Module-0 room and purged with high-purity nitrogen prior to the sampling process. During the water sampling, a slight nitrogen flow was directed horizontally above the bottle opening in order to prevent dust particles from entering. This turned out to be an improvement, whereas a nitrogen flow directed vertically to the bottle worsened the background dust. Blank measurements were performed by filling the bottles with deionised water in the chemical lab of the LNGS outside the tunnel, without using nitrogen flow.

After sampling, all bottles were closed and stored in a refrigerator. The particulate counting was performed in the chemical lab. The water samples were passed through different, new filter papers in order to hold back the particulates; each time the whole filtering apparatus had been flushed with deionised water. The filter papers were transferred onto a microscope with tweezers, where the particulates on the filters were counted and classified according to their diameter. The dust concentrations [g/g] with respect to the water amounts have been calculated afterwards, derived from the volume of the particulates of different size.

A general classification of liquids or gases containing particulates is provided by the US Military Standard 1246. The particulate concentrations in dependence on the particle diameter are defined in the following way for different purity classes. Curves of some purity classes are shown in the Diagrams 3.7.

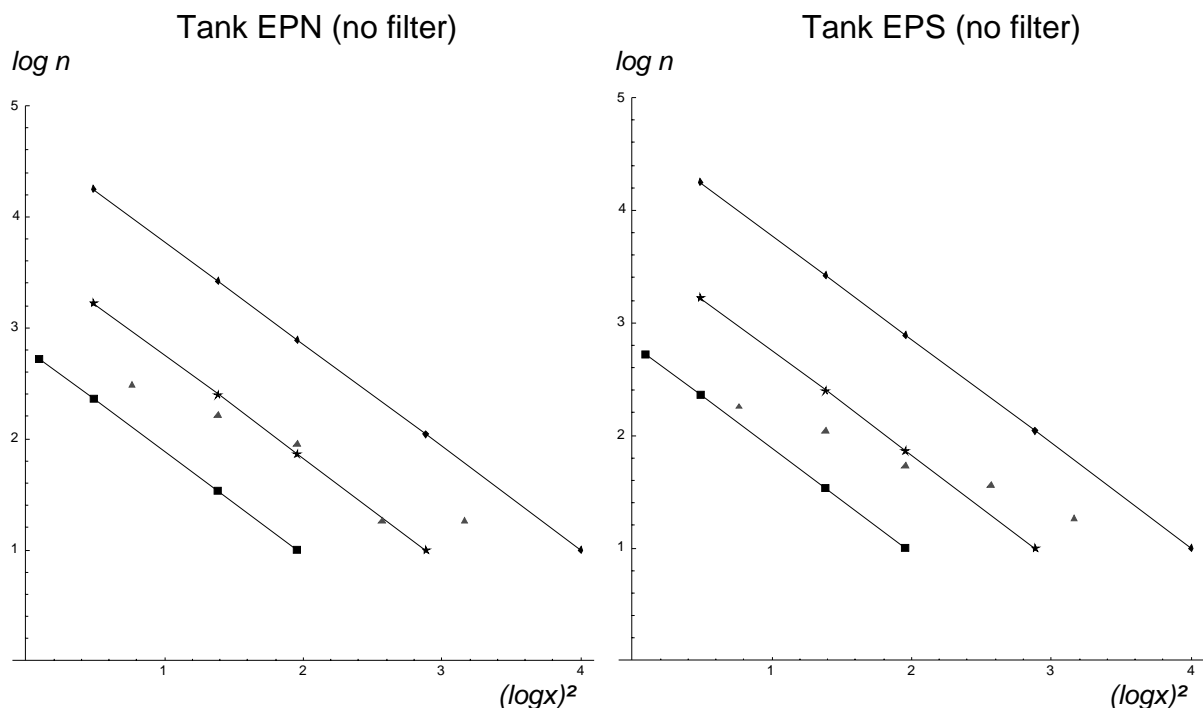
$$\log n = -0.925 ( (\log x)^2 - (\log c)^2 ) + 1$$

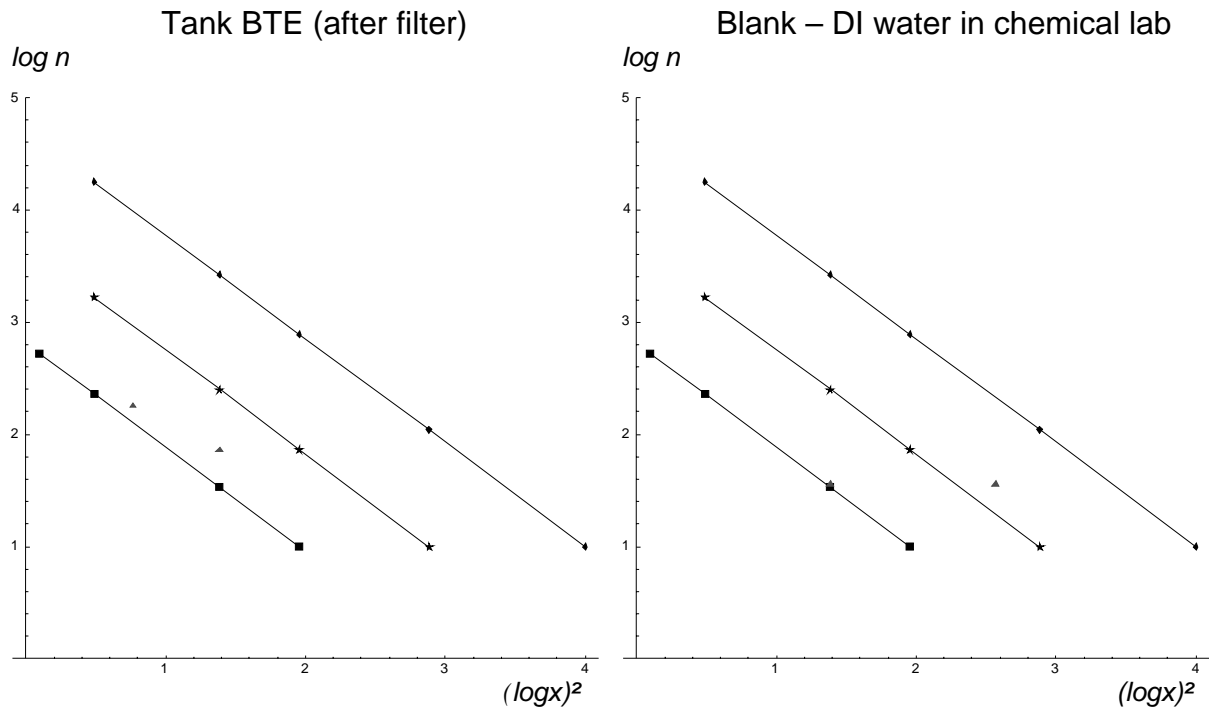
where

log	means the logarithm to the basis 10
x	the particle size in $\mu\text{m}$
c	the purity class number
n	the number of particulates per litre

### 3.4.3. Results

In the Diagrams 3.7, the experimental data (triangular points) is compared with lines of some purity classes. The upper line in each diagram corresponds to class 100, the one in the middle to class 50, and the lower one to class 25.





Diagrams 3.7: Particulate counting in Module-0 water samples

The tanks EPN and EPS, directly measured without a filter, show a level around class 50. The filter, according to the measurement with the tank BTE, seems to reduce the number of particulates. Table 3.8 specifies the particulate concentrations together with reference values of some purity classes.

Source	Particulate concentration
Blank	$(2.5 \pm 1.8) 10^{-9} \text{ g/g}$
EPN (no filter)	$(7.5 \pm 6.2) 10^{-9} \text{ g/g}$
EPS (no filter)	$(7.8 \pm 6.5) 10^{-9} \text{ g/g}$
BTE (with filter)	$(3.3 \pm 1.5) 10^{-10} \text{ g/g}$
class 200	$(6.2 \pm 0.5) 10^{-7} \text{ g/g}$
class 100	$(4.9 \pm 0.5) 10^{-8} \text{ g/g}$
class 50	$(3.6 \pm 0.6) 10^{-9} \text{ g/g}$
class 25	$(2.4 \pm 0.7) 10^{-10} \text{ g/g}$

Table 3.8: Particulate concentrations in water samples taken in Module-0, together with reference values of the US Military Standard 1246.

Although the uncertainties of the EPN and EPS results are high, some reliability arises as the two concentrations agree. They are above the concentration of the filtered sample, which was also taken underground at the Module-0 plant, thus indicating that the contamination in EPN and EPS is not due to background from the surroundings. This implies the necessity of filtering. The value of the filtered water roughly is one order of magnitude above  $1.3 \cdot 10^{-11} \text{ g/g}$ , the requirement of the Borexino scintillator mentioned in paragraph 3.4.1. However, as the blank value, arising from a measurement in the chemical lab, is even above the BTE measurement, this latter probably is strongly influenced by background particulates from the sampling process. Especially, the number of particulates bigger than  $10 \mu\text{m}$  is equal ( $n=4$ ) for the blank and the BTE measurement, whereas the number of smaller particulates is higher in

the BTE sample (n=10 compared to n=0). There, the sizes of the four bigger particulates account for the different concentration in Table 3.8. The high quantity of small particulates in the BTE sample indicates that these could be from the Module-0 water, or from the surrounding underground air. A background subtraction arising from this last consideration leaves a contamination of 10 particulates below 10 $\mu$ m in diameter (assumed average diameter: 6.3 $\mu$ m) and implies a concentration of  $(4.7\pm 1.5)10^{-11}$  g/g. This still differs from the requirement by a factor of  $\approx 4$ . The requirement is based on the conservative assumption of an equilibrated  $^{238}\text{U}$  chain with all its daughters present in dust. Most probably, the chain is broken somewhere (e.g.  $^{222}\text{Rn}$ ) and only the upper part contributes, thus increasing the required limit.

However, the BTE value, even if tried to be determined more exactly in the above paragraph, principally has to be considered an upper limit, as the background arising from the sampling process is undetermined. Also, the large uncertainties in the EPS and EPN values show that the obtained concentrations are at the detection limit.

In this way, the measurements show that the purity state of the examined water samples does not explicitly reach the required level; however, a sufficient purity of the system is possible or even probable, as the applied examination method turned out not to be sensitive enough. Apart from that, filtering is necessary.

## 4. Silica Gel Chromatography

With respect to the necessity of ultra low activity levels in liquid scintillators of low counting rate experiments – pointed out more than once in the course of the previous chapters –, this section presents and examines a promising method of purification, ready to be applied in the mentioned framework. Especially neutrino experiments, frequently constrained to work at ultra-pure levels due to the extremely weak interaction of the neutrino itself, may take advantage of the method described here, the silica gel chromatography.

The high requirements concerning the radiopurity of the pseudocumene liquid scintillator in the solar neutrino experiment Borexino call for further purification. As illustrated in part 2.3.1, mainly heavy metal impurities belonging to the  $^{238}\text{U}$  or  $^{232}\text{Th}$  chain and in particular the isotopes  $^{210}\text{Bi}$  and  $^{210}\text{Po}$ , apparently responsible for a big part of the remained background activity in the CTF detector after the CTF3 campaign, have to be considered (cf. 2.4.5). In this connection, the isotope  $^{210}\text{Pb}$ , even if not depositing its activity in the neutrino window, plays a key role as it conserves the dangerous activity of its daughters  $^{210}\text{Bi}$  and  $^{210}\text{Po}$  over a long time period. The examinations in the following paragraphs are motivated in this context.

### 4.1. Theoretical Considerations

An important goal approached in this thesis, the validity of existing theoretic models describing different application modes of silica gel chromatography processes, should be examined within the frame of related experiments during the past years. The respective models are summarised in the following paragraphs. In particular, the development of theoretic models for surface adsorption processes on silica gel in the context of liquid scintillator purification has commenced several years ago as documented in [Har97], [Gri00] and [Nie03].

#### 4.1.1. Static Model

The physical process responsible for the considered purification effect is based on an adsorption of impurities onto the silica gel surface. As the silica gel surface consists of polar OH groups, especially polar substances like metal atoms prefer to adsorb onto it. According to [Ung79], the density of adsorption sites on a silica gel surface amounts to  $4.6 \text{ nm}^{-2}$ . The porosity of silica gel leads to an outstanding surface to volume ratio, depending on the silica gel pore size and resulting in the adsorption site densities shown in Table 4.2.

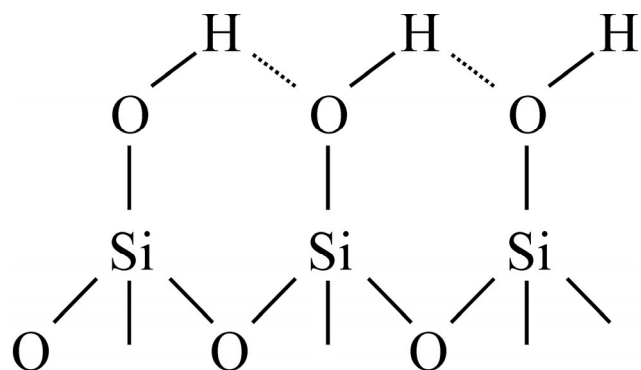


Figure 4.1: Surface of silica gel

pore size in Å	specific surface in m <sup>2</sup> /g	bulk density in g/cm <sup>3</sup>	adsorption site density in cm <sup>-3</sup>
60	527	0,40	9,7·10 <sup>20</sup>
100	305	0,50	7,0·10 <sup>20</sup>

Table 4.2: Some characteristics of the silica gel 'Kromasil' from Eka Nobel, Sweden, for different pore sizes. The intrinsic density of silica gel is 3,1 g/cm<sup>3</sup>.

In contact with air, water molecules adsorb on silica gel. These can be removed by heating it to 150–200°C for several hours (conditioning). An influence of this effect on the purification efficiency has not been noticed in a respective examination [Nie00]. This is not surprising, as a layer of water molecules should change neither the polar nature, nor the pH value ( $\approx 7$ ) of the silica gel surface. Apart from that, the mentioned adsorption prevents a flow of water or other polar liquids from crossing silica gel columns in an easy way.

A quantitative examination of the purification process – organic liquid scintillator being in contact with silica gel – can be derived from the assumption of an equilibrium between dissolved impurities in the scintillator and adsorbed ones on the silica gel surface. Diagram 4.3 illustrates the corresponding situation at the surface of a silica gel grain and in its pores. The grain sizes considered in this thesis are around 10–20  $\mu\text{m}$ , and the pore sizes of common silica gel samples are at 60 or 100Å.

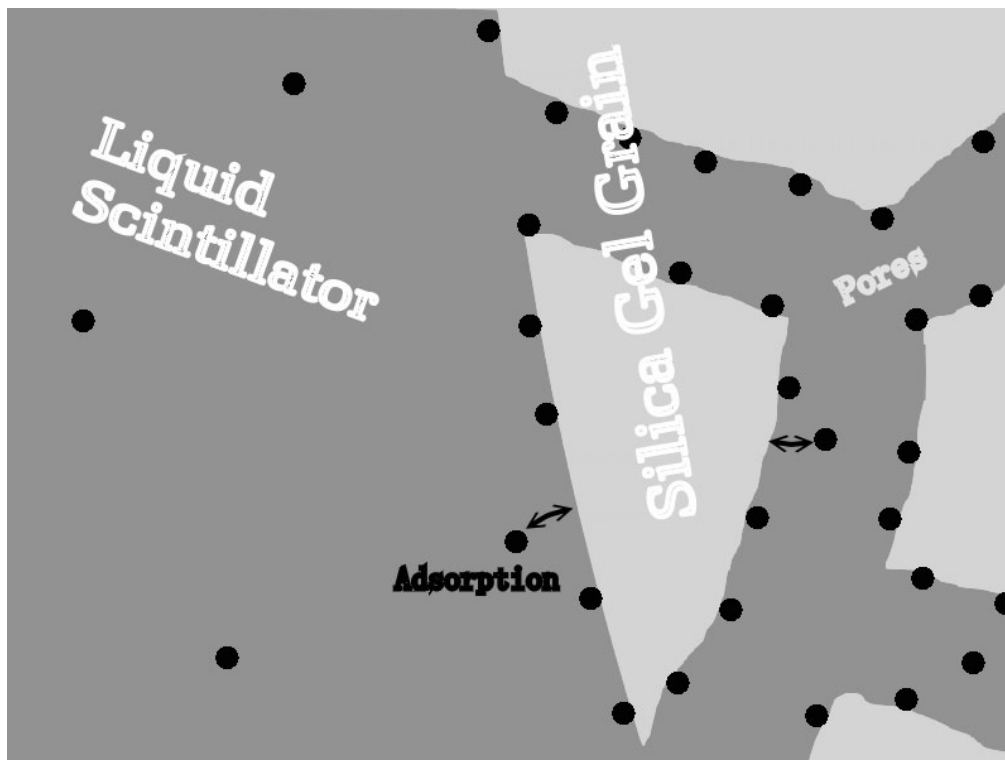


Diagram 4.3: Impurity adsorption on the silica gel surface in a sectional view of a silica gel grain and its pores

The equilibrium

$$k = \frac{c_{Y \text{ in SiGel}} \cdot c_{LS}}{c_{Y \text{ in LS}} \cdot c_{LS \text{ in SiGel}}}$$

quantifies the ratio of the impurity (Y) concentration in the silica gel and the impurity concentration in the liquid scintillator (LS). The other constants can be calculated with knowledge of the liquid scintillator density and the adsorption site density (see Table 4.2). For the silica gel type 'Kromasil' by Eka Nobel, Sweden, and pseudocumene scintillator one especially obtains  $c(\text{LS}) = 4.45 \cdot 10^{21} \text{cm}^{-3}$  and  $c(\text{LS in SiGel}) \approx c(\text{adsorption sites}) = 0.97 \cdot 10^{21} \text{cm}^{-3}$ .

The equation

$$\Delta G = - R T \ln(k)$$

relates  $k$  to the free enthalpy  $\Delta G$  in dependence on the temperature  $T$  and the gas constant  $R = 8.3145 \text{ J/mol}$ . It should be noticed, that  $\Delta G$  is a natural constant depending on solvent, silica gel and impurity type only, whereas  $k$  varies for different temperatures.

This model generally describes the static situation of a thermodynamic equilibrium in a volume of defined silica gel and scintillator amount. In order to comprehend a more complex, dynamic purification process, characterised by a liquid flow through a silica gel column, it has to be expanded.

#### 4.1.2. Dynamic Model

The essential expansion step relating the dynamics of a macroscopic purification process to the behaviour of the described microscopic equilibrium model consists in the definition of a time constant  $\tau$ , necessary to reach this equilibrium between the impurity concentrations in the liquid and on the silica gel surface.

In dependence on the flow velocity  $v$  of the liquid, the latter covers the distance  $x$  during the time  $\tau$ , as illustrated in Figure 4.4. The total column height  $h$  divided by  $x$  leads to the number of so-called *segments*, telling how many different equilibrium states the liquid can reach while passing through the silica gel. Now considering each single segment equilibrated after the time span  $\tau$ , the whole purification process in the column can be simulated by applying the  $\Delta G$ -equation on each *segment* and relating all segments subsequently. Hereby, the time a scintillator molecule takes to pass through the column should clearly be longer than  $\tau$  (whereby  $\tau \leq 50\text{s}$ , see 4.2.4), equivalent to the statement that this model only makes sense if the number of segments is bigger than 1.

Under this circumstance, the simulation shows that from the beginning the impurity concentration at the column inlet gets quite enhanced, whereas, forming a negative gradient along the column height axis, it remains low at the exit. In this way, the last column segments initially provide an excellent purity level for the liquid scintillator leaving the column. However, in the course of the purification process, the region of comparatively high contaminated silica gel segments expands towards the column exit, carrying the danger of comparatively high contaminated scintillator exiting the column from a certain time on. The happening of this phenomenon can be called *breakthrough*; and in specific purification procedures like the *batch purification mode* (4.1.4) it has to be avoided. These purification modes are explained in the following two paragraphs. An illustrative comparison can be found in 4.1.5.

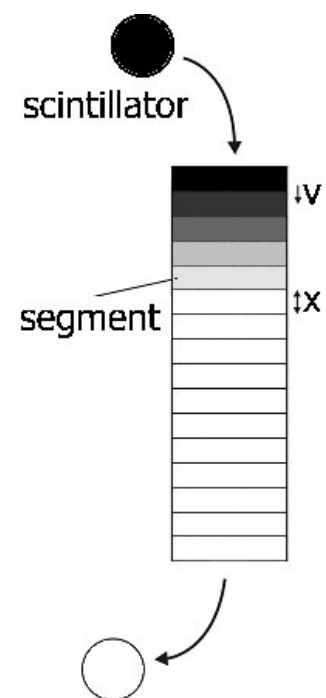
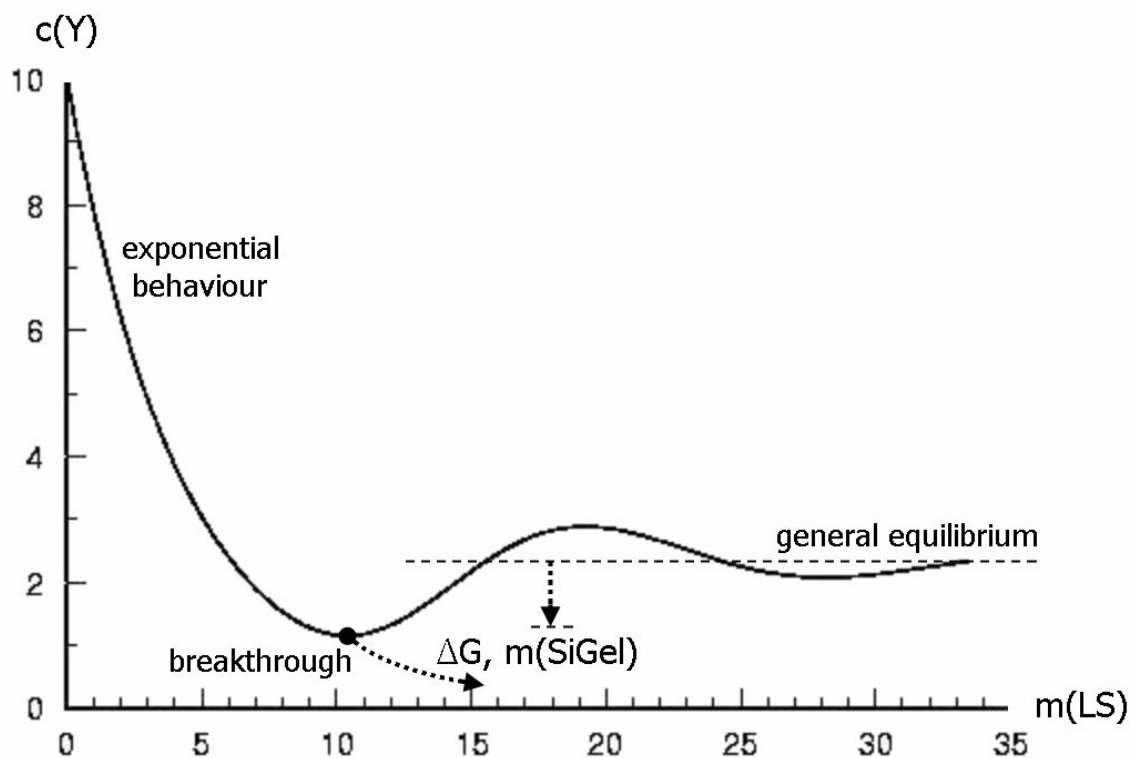


Figure 4.4:  
Segment model of a  
silica gel column

### 4.1.3. Loop Purification Mode

The characteristic of a loop purification process in the context of a silica gel column consists in the existence of only one liquid container, that contains the liquid to be purified, and where it has to be continuously returned to, each drop immediately after it exits the column. In other words, the liquid scintillator is continuously “looped” between its container and the silica gel column (see sketch in Diagram 4.8).

The continuous mixing of purified and unpurified scintillator implies that the impurity concentration in the scintillator can decrease only slowly and in a stetic way. According to the outlined simulation, this development is approximately exponential, until the silica gel column approaches the breakthrough point. From here on, the scintillator exits the column at a higher impurity concentration than the scintillator in the container has assumed; hence the impurity level in the container begins to rise. If the possibility of an on-line activity determination during the purification exists, it is advantageous to stop the process here, as according to the simulation, with a look on Diagram 4.5, the purity level in the container is never better than here. If the loop is continued, the concentrations in the scintillator and the silica gel equilibrate each other and, constituting a coupled system of two variable quantities, approach the general equilibrium state, determined by the free enthalpy  $\Delta G$  and the equations of paragraph 4.1.1, with a slight oscillation.



*Diagram 4.5: Qualitative development of the impurity concentration  $c(Y)$  with the mass of processed liquid scintillator. Increased parameters  $|\Delta G|$  and  $m(\text{SiGel})$  would cause the illustrated shifts of the breakthrough point and the equilibrium asymptotic. The numbers on the axes are arbitrary.*

Besides the illustrated purification progression, the two arrows in Diagram 4.5 intend to show, how important parameters can influence the situation. An enhanced absolute value of  $\Delta G$  and a higher quantity of silica gel would improve the purification effect by shifting the breakthrough to a higher amount of processed scintillator – and thus the corresponding impurity level to a better value – and by reaching a lower, final impurity concentration with

the general equilibrium. In particular,  $n$  times the amount of silica gel – as long as the flow rate is unchanged and homogeneous, but independent of the geometric shape of the column – delays the breakthrough by the factor  $n$ , improves the purification efficiency at the breakthrough point from  $f_{br}$  to  $(f_{br})^n$  and improves the factor at the final equilibrium from  $f$  to  $2(f-1)+1$ . A shorter equilibrium time  $\tau$  delays the breakthrough point and increases its purity level only slightly without influencing the general equilibrium concentration at the end.

#### 4.1.4. Batch Purification Mode

The batch purification mode avoids contact between purified and unpurified scintillator. A liquid scintillator *batch* passes through the column once and is afterwards collected in a second container. The purity state of this container is particularly crucial for the success of the purification and, as already mentioned in 2.2, a “breakthrough” of the silica gel column has to be avoided. The first point can be approached by an appropriate tank cleaning procedure as described in paragraph 3.2, whereas the second point usually requires a sufficient amount of silica gel, as all the other relevant parameters of the model normally are unchangeable.

Nevertheless, as the scintillator leaving the column possesses the excellent purity of the last column segment, is supposed to maintain this level and to only mix with scintillator of the same ultra-pure level, the batch purification is an extremely effective purification method as long as the above conditions are satisfied.

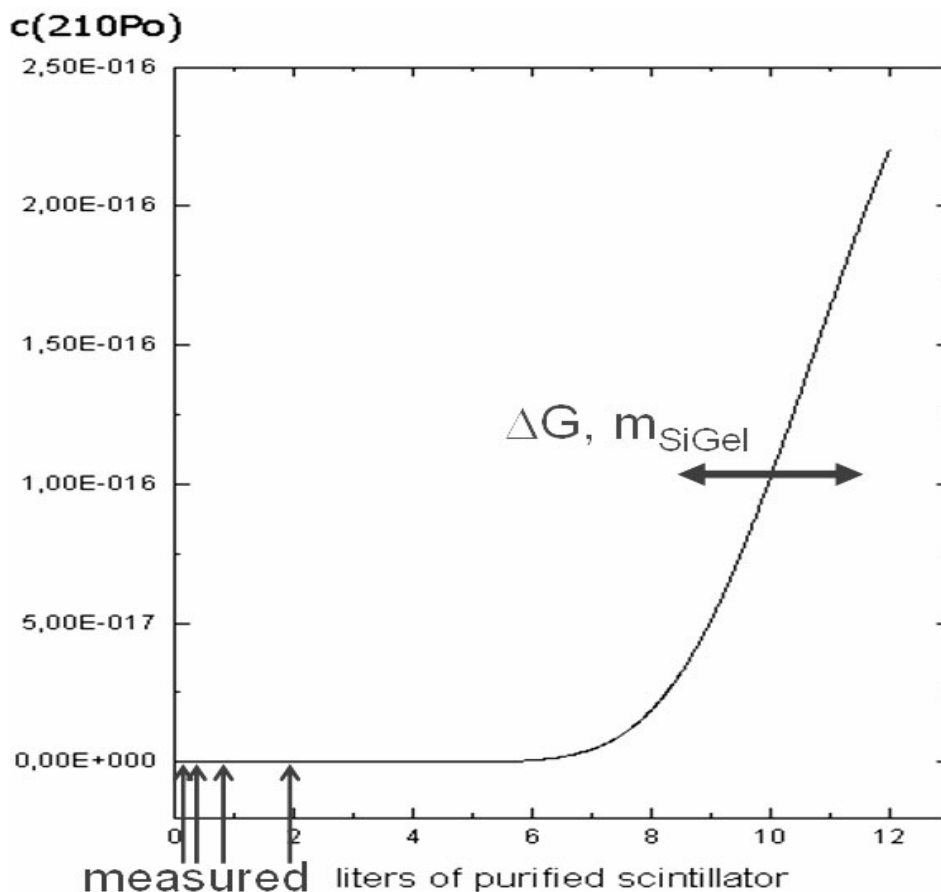


*Diagram 4.6: Impurity concentration ( $^{210}\text{Po}$ ) in the purified scintillator when leaving the column; simulated with the parameters of the batch test described in 4.2.4 and with  $\tau=10\text{s}$ . The rise gets shifted with  $\Delta G$  and  $m(\text{SiGel})$ .*

Diagram 4.6 illustrates this fact, as indeed the impurity concentration level of the purified scintillator exiting the column cannot properly be displayed on the linear scale. The plot has been generated with the parameters corresponding to the laboratory batch purification test described in paragraph 4.2.4, with the arrows at the bottom marking the tested range where the examined scintillator samples were taken – the range recommended to be used in future applications of this purification method. The over-dimensional rise of the curve is due to the breakthrough of the column and would be limited by the impurity concentration in the unpurified scintillator ( $3.2 \cdot 10^{-16} \text{g/g}$ ). It is shifted to the right in case of a higher absolute value of the free enthalpy  $\Delta G$  or a higher amount of silica gel.

The simulated purification factor – assuming no breakthrough – usually exceeds realisable orders and gets restricted by other sources of impurities (compare 4.2.5). Furthermore, it strongly depends on the number of column segments, directly adjustable by the flow rate. If possible, the flow should be chosen in such a way that it generates a higher number of segments than necessary according to the model, because experimental uncertainties may worsen the model prediction. Table 4.7 illustrates the behaviour of the purification factor in dependence on the segment number – and in fact on the equilibrium time constant  $\tau$  – with respect to the experimental parameters of paragraph 4.2.4.

$\tau$ in s	number of segments	purification factor
120	2	20
80	3	48
60	4	100
50	5	210
45	6	420
40	7	790
↓	↓	↓
20	14	$1.5 \cdot 10^5$
↓	↓	↓
1	282	$2.3 \cdot 10^{60}$
↓	↓	↓

*Table 4.7: Purification factors for different equilibrium time constants and segment numbers in the case of the batch purification experiment of paragraph 4.2.4 ( $^{210}\text{Po}$ )*

It is apparent that in many cases a certain number of segments leads to an experimentally unrealisable purification; especially the exact value of  $\tau$ , possibly in the order of 1s [Har99], cannot be determined easily. Even if the experimental parameters were tried to be chosen in a way to distinguish factors arising from equilibrium times  $\tau$  around 1s, the column segments would be very thin – here 0.18mm for  $\tau=1\text{s}$ , too thin to exclude a failure of the test due to uncertain geometrical conditions. A high flow rate could allow a determination of  $\tau$ , the resistance of finely granulated silica gel however is very high.

#### 4.1.5. Comparison

The results of the last two chapters undoubtedly imply that the batch mode is the more efficient one. It should be applied whenever possible. However, in certain conditions this may be impossible, especially huge experimental set-ups often provide only one liquid container. Another motivation for the loop mode can consist in a better control of the purification process. Sometimes, liquid scintillators in detector vessels can be observed during purification loops. This helps to identify a breakthrough as well as a different possible contamination of the scintillator by liquid handling equipment. Diagram 4.8 illustrates and compares the

behaviour during both purification modes, like already described in the previous two paragraphs.

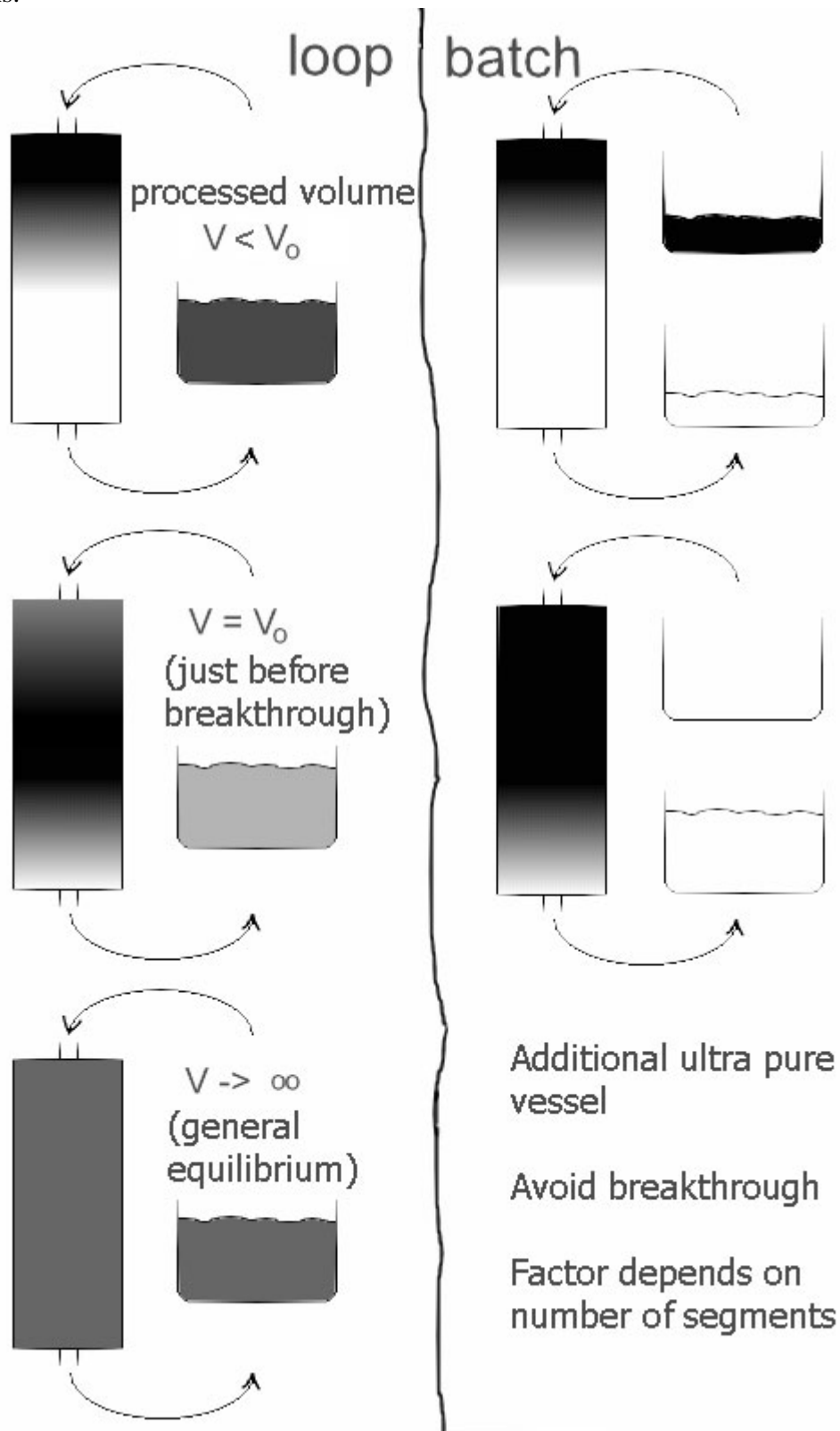


Diagram 4.8: Purification progression of loop mode and batch mode in comparison.  $V_0$  refers to the processed scintillator volume at the breakthrough.

## 4.2. Laboratory Experiments

The theoretic model described in the previous pages calls for an experimental confirmation. In the enlarged context of the solar experiment Borexino, where the technique of silica gel chromatography is supposed to be applied in future, the most fundamental assertion, the quantitative description of the adsorption equilibrium, as well as the most important point, the validity of the batch purification model, have to be checked. In particular, the first question, already examined with the heavy metals Bi and Po, needed to be extended to Pb, whereas the second question, the batch purification, has never successfully been tested.

### 4.2.1. Liquid Scintillator Loading

The relevant isotopes,  $^{210}\text{Pb}$ ,  $^{210}\text{Bi}$  and  $^{210}\text{Po}$ , get introduced into detector materials, like especially the liquid scintillator, by the  $^{222}\text{Rn}$  content in the air (see  $^{238}\text{U}$  chain in Figure 2.6). The respective concentrations, even if harmful in a large volume and low background detector, cannot be measured in small-scale laboratory set-ups. This requires the consideration of artificially contaminated samples. The most authentic way of testing purification methods in this context consists in the purification of a scintillator, which has been contaminated in a natural way by  $^{222}\text{Rn}$  in the air. Therefore,  $^{222}\text{Rn}$  atoms have been dissolved in liquid scintillator by circulating a  $^{222}\text{Rn}$  loaded air volume between an emanating  $^{226}\text{Ra}$  source and a pseudocumene batch, like shown in Diagram 4.9.

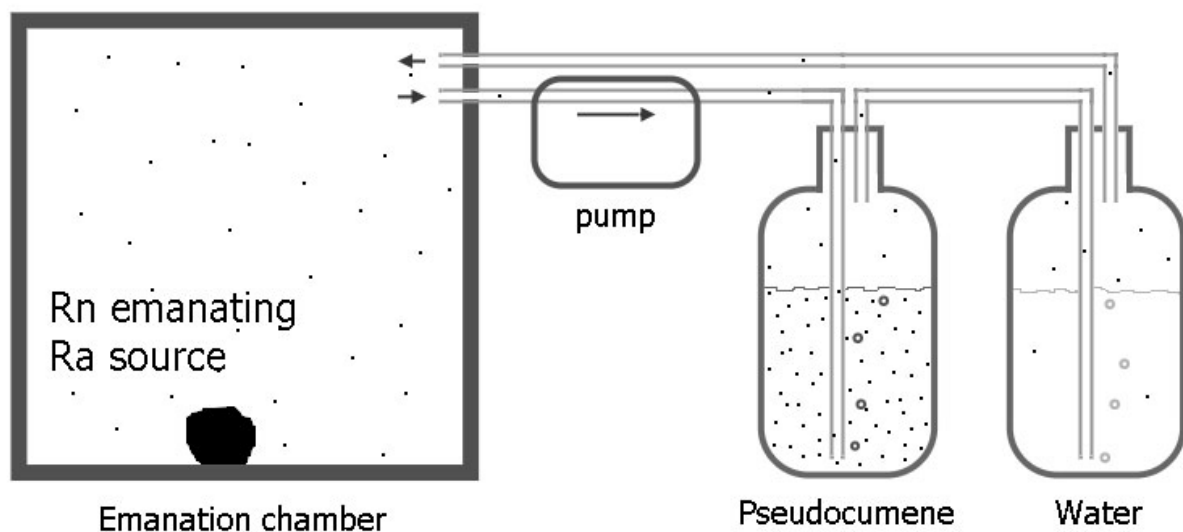


*Diagram 4.9: Sketch of the set-up used for the contamination of pseudocumene with radon at the PTB Braunschweig*

In particular, the emanation chamber of a  $\sim 2\text{MBq}$   $^{226}\text{Ra}$  source, situated at the PTB Braunschweig, Germany, was coupled to a bottle of 425.3g of pseudocumene for 36 days. The air was circulated in plastic tubes by a hose pump. The water bottle avoided an introduction of pseudocumene vapours into the emanation chamber. At the end, the pseudocumene amount was reduced to 398.0g, apparently by evaporation. The dose outside the bottle was determined to  $\sim 10\ \mu\text{Sv/h}$  directly at the bottle and to  $\sim 0.2\ \mu\text{Sv/h}$  at a distance of 1m. Afterwards, the scintillator was stored about a year prior to the experimentation, in order to have developed a sufficient activity of  $^{210}\text{Po}$ , the last isotope in the  $^{222}\text{Rn}$  decay chain.

## 4.2.2. Activity Detection and Analysis Methods

Purification effects on the loaded pseudocumene scintillator described above were quantitatively determined by activity measurements of unpurified and purified samples. These measurements were carried out in the underground laboratory of the Technische Universität München, Garching, at a shallow depth of 15 m.w.e. Two detectors were used, a scintillation detector for  $^{210}\text{Po}$  and  $^{210}\text{Bi}$  activity,  $\alpha$  and  $\beta$  events expected in the range below 1.2 MeV, and a high-purity germanium detector for  $^{210}\text{Pb}$  activity, recognisable by a 46.5 keV gamma line.

### *Scintillation Detector*

In this way, the  $^{210}\text{Bi}$  and  $^{210}\text{Po}$  detection took advantage of the circumstance that the according decay already takes place in a liquid scintillator and even provides an ideal energy range for this detection method. Small teflon boxes of  $\sim 70\text{cm}^3$  of volume, closed by a glass window and sealed with a silicon gasket, contained the liquid scintillator during the measurements. For each new scintillator sample, a box was cleaned with acetone, diluted nitric acid (10–65%, 20–60°C) and water. Pseudocumene samples of 28.0g, together with 42mg of the wavelength shifter PPO – the same scintillator as in Borexino – were filled into one of the teflon boxes for each examination. In order to guarantee a good light yield at a wavelength of  $\sim 380\text{nm}$ , a sufficient optical quality of the scintillator and an already reduced radon concentration, all scintillator samples in the teflon boxes were purged with nitrogen for at least half an hour. Two small inlets, closable by teflon caps, allowed this procedure. However, this forbade to fill the boxes completely with liquid scintillator. The glass window

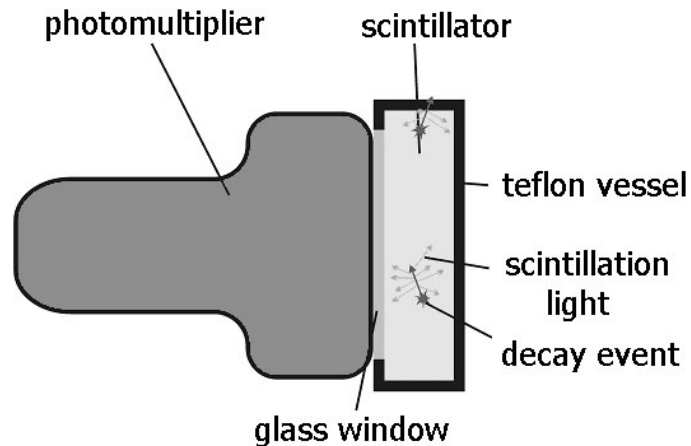


*Figure 4.10: PMT looking on liquid scintillator in a teflon sample box with glass window of the same size.*

of the teflon box was covered with a thin layer of silicon oil, in order to provide an optical coupling between the scintillator and a photomultiplier. The set-up, illustrated in Figure 4.10, prevents the scintillation light reflected on the teflon surface from escaping the sample box and allows a detection efficiency up to 1.

For the measurement, this equipment – arising from the necessity to shield it from further light sources – was entirely enclosed in a light tight steel housing of cylindrical shape and a volume of  $\sim 3$  litres. In order to reduce radon and oxygen around the teflon box, the housing was purged for 5–10 minutes with nitrogen before it was closed. Especially teflon material is not absolutely tight for gases like radon and oxygen. They still succeeded to diffuse into the box in the course of some weeks.

The steel housing with all the apparatus inside was brought into the underground laboratory and further shielded with 10 cm of lead from all sides. It provided two ducts for the high voltage and the signal cable. The first one was supplied with +1350 V, and the second one was directly connected to a transient recorder module, a type of digital oscilloscope, inserted in a computer. It provided a sample rate of 500 MHz at a voltage resolution of 10 bit. No NIM electronics, especially no amplifier, were used. The input impedance of the recorder module was  $50\ \Omega$ . The trigger was normally set at  $-62.5\ \text{mV}$ , cutting off the energy spectra

between 100 and 200 keV. The dead time was determined to 65 ms per event and subtracted after each measurement. The pulse length was about 50–100 ns.

The energy calibration, depending on the light yield of the scintillator, further on its oxygen content and on the time it had been in contact with air, was accomplished with a  $^{137}\text{Cs}$  source of  $\sim 10$  kBq. The according  $\beta$ -decay emits a further gamma of 662 keV that causes a Compton spectra by its scattering on electrons in the liquid scintillator. The end point of this spectra at 477 keV, smeared out with about  $\sim 50$  keV, provided a calibration with an according uncertainty, comparable to the energy resolution of a photomultiplier. Each sample was separately calibrated prior to the measurement; a pulse height of 100 mV corresponded to an event energy of 100–200 keV, depending on the light yield of the sample. With the existing energy resolution, a linear calibration was sufficient.

### *Analysis of $\alpha$ and $\beta$ events*

During the measurements, the photomultiplier pulses were saved in separate files and analysed afterwards. The energy of a signal was assumed to be proportional to the area of the corresponding charge pulse, the off-set was separately subtracted for each pulse. The Figures 4.11 and 4.12 compare the spectra of the contaminated scintillator before and after the silica gel batch purification test, described in 4.2.4.

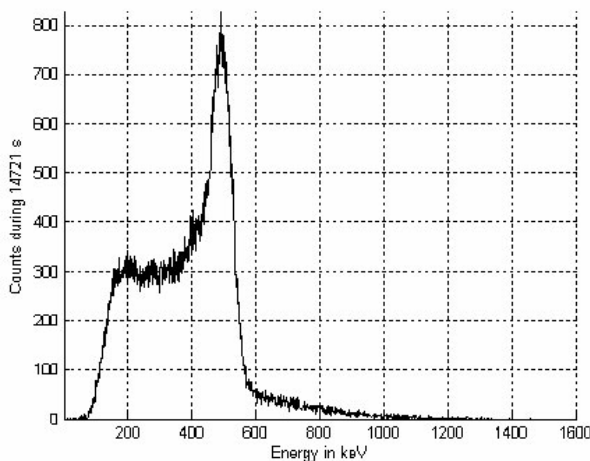


*Figure 4.11: Energy spectra of a contaminated scintillator sample. The  $\alpha$ -peak ( $^{210}\text{Po}$ ) and the  $\beta$ -spectra ( $^{210}\text{Bi}$ ) are superpositioned. The rate, with a look on the measurement time, is bigger by a factor  $\sim 100$  than the background rate in 4.12.*

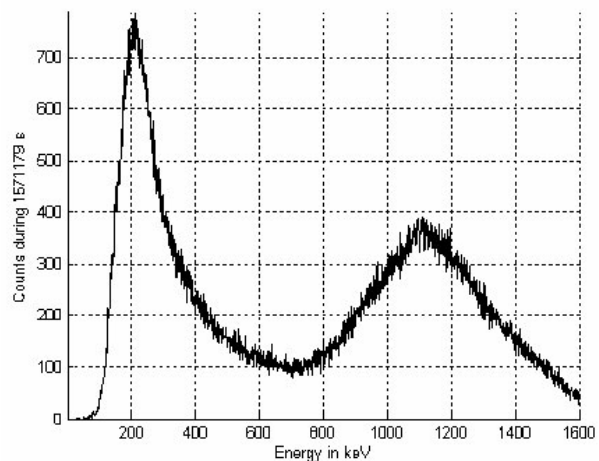


*Figure 4.12: Energy spectra of a purified scintillator sample. The spectra quasi is identical to a background spectra. The exponential decrease at low energies is due to gamma radiation from cosmic background. The broad peak around 1MeV is possibly caused by cosmic muons.*

In the spectra of the contaminated scintillator, the peak of the  $\alpha$  decay of  $^{210}\text{Po}$  ( $t_{1/2}=138.376\text{d}$ ) to the stable  $^{206}\text{Pb}$  is recognisable first. The energy of the peak, originally at 5.407 MeV, gets, as  $\alpha$  energies in liquid scintillators usually do, quenched to about 400–500 keV. The superpositioned spectra is due to the  $\beta$  decay of  $^{210}\text{Bi}$  ( $t_{1/2}=5.013\text{d}$ ) to  $^{210}\text{Po}$  with an end point at 1162.7 keV. The asymmetry in the  $\alpha$  peak – with respect to a higher rate on its left side – arises from the super-positioned  $\beta$  spectra, but also from the confined scintillator volume, shifting  $\alpha$  events at the edge of the sample to lower energies. The sample geometry (height  $\approx 8\text{mm}$ ) also distorts the  $\beta$  spectra in a way that low energy events are enhanced. Surface measurements in (5.3.1) showed that actually a big part of the activity adsorbed on the surface, enhancing these effects.

The spectra of the purified scintillator shows the usual, exponentially decreasing background of cosmic gamma rays. The further “peak” is possibly caused by cosmic muons, crossing the detector volume and depositing about 1MeV, whereby more energetic events get cut off by the upper threshold of the data acquisition. In fact, this spectra is not distinguishable by eye from a background spectra and an  $\alpha$  peak is not recognisable, already pointing to a good purification efficiency. So, concerning the spectra of the purified scintillator, the aim must now be focussed on deducing upper limits for the  $\alpha$  and  $\beta$  activities. Therefore, it is advantageous to consider the  $\alpha$ - $\beta$ -discrimination, illustrated in the following three-dimensional plots.

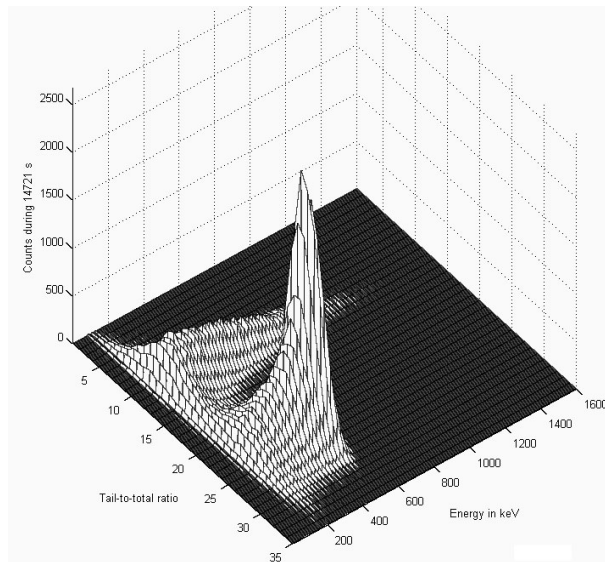


*Diagram 4.13: Energy-PSD spectra of a contaminated scintillator sample. The  $\alpha$ -peak ( $^{210}\text{Po}$ ) and the  $\beta$ -spectra ( $^{210}\text{Bi}$ ) are separated by the tail-to-total ratio of the single pulses. The energy binning is 20keV, the PSD binning is 1%.*

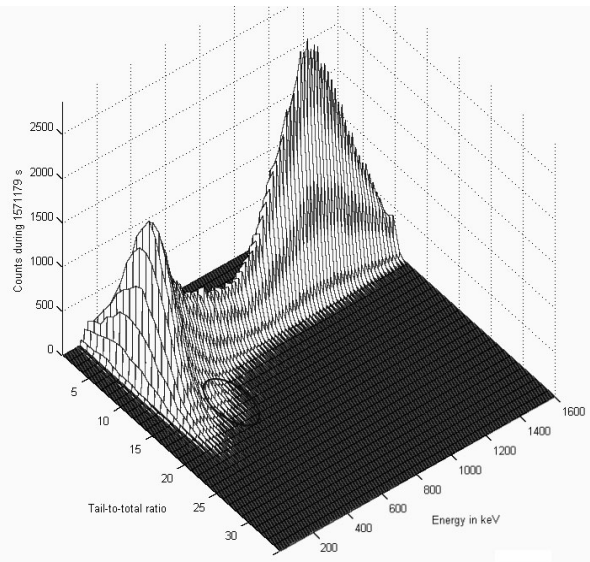


*Diagram 4.14: Energy-PSD spectra of a purified scintillator sample. The circle marks the applied discrimination parameters for  $^{210}\text{Po}$  events, explained in the following.  $\beta$ -like background events and  $\alpha$ 's from radon related activity cannot completely be separated here.*

The spectra of the contaminated scintillator shows very clearly how the tail-to-total ratio separates  $\alpha$ -like from  $\beta$ -like events. One can also see to which extent the  $\alpha$  peak, characterised by events with a higher tail-to-total ratio, is distorted to low energies, and further, how the discrimination quality decreases at these low energies – two inconvenient sources of uncertainties, examined within this chapter.

The spectra of the purified scintillator illustrates the  $\beta$  signature of all background events, also with a wider spread at low energies. Like in Diagram 4.12, there still is no  $\alpha$  peak recognisable.

In case of a clear  $\alpha$  peak, the spectra can be integrated over all energy values, and the activities of the  $\alpha$ -like peak and the  $\beta$ -like peak can be determined by two Gaussian fit curves, like illustrated in the plots 4.15. However, as long as the activity is too low, a fit is not feasible, and the activity has to be determined by an application of energy and pulse shape cuts.

The energy cut was applied at  $412\pm 97$  keV, corresponding to the average peak position and width determined by several contaminated scintillator samples. Hereby, the peak shift caused by a super-positioned  $\beta$  spectra had been accounted for, comparing samples with different amounts of  $^{210}\text{Bi}$  contamination. With respect to the mentioned  $\alpha$  peak distortion to

lower energies, the application of an energy cut changes the detector efficiency to values lower than 1. Its influence however vanishes in the behaviour of purification and adsorption factors. In particular, measurements supposed to refer to each other were always analysed in the same way.

The efficiency of a PSD window normally is above 90%, the problem here however consists in the determination of the cut parameters. Like already recognisable on the difference in the pulse shape spread of the  $\beta$ -like events in the Figures 4.13 and 4.14, the position and width of a PSD peak depends on the quality of the scintillator (see Diagram 4.15). The latter decreases with the oxygen amount the liquid scintillator has been exposed to, unavoidable during sampling and purification preparation procedures, so that especially in case of purified scintillator samples this quality is not optimal. A possible measure hereby is

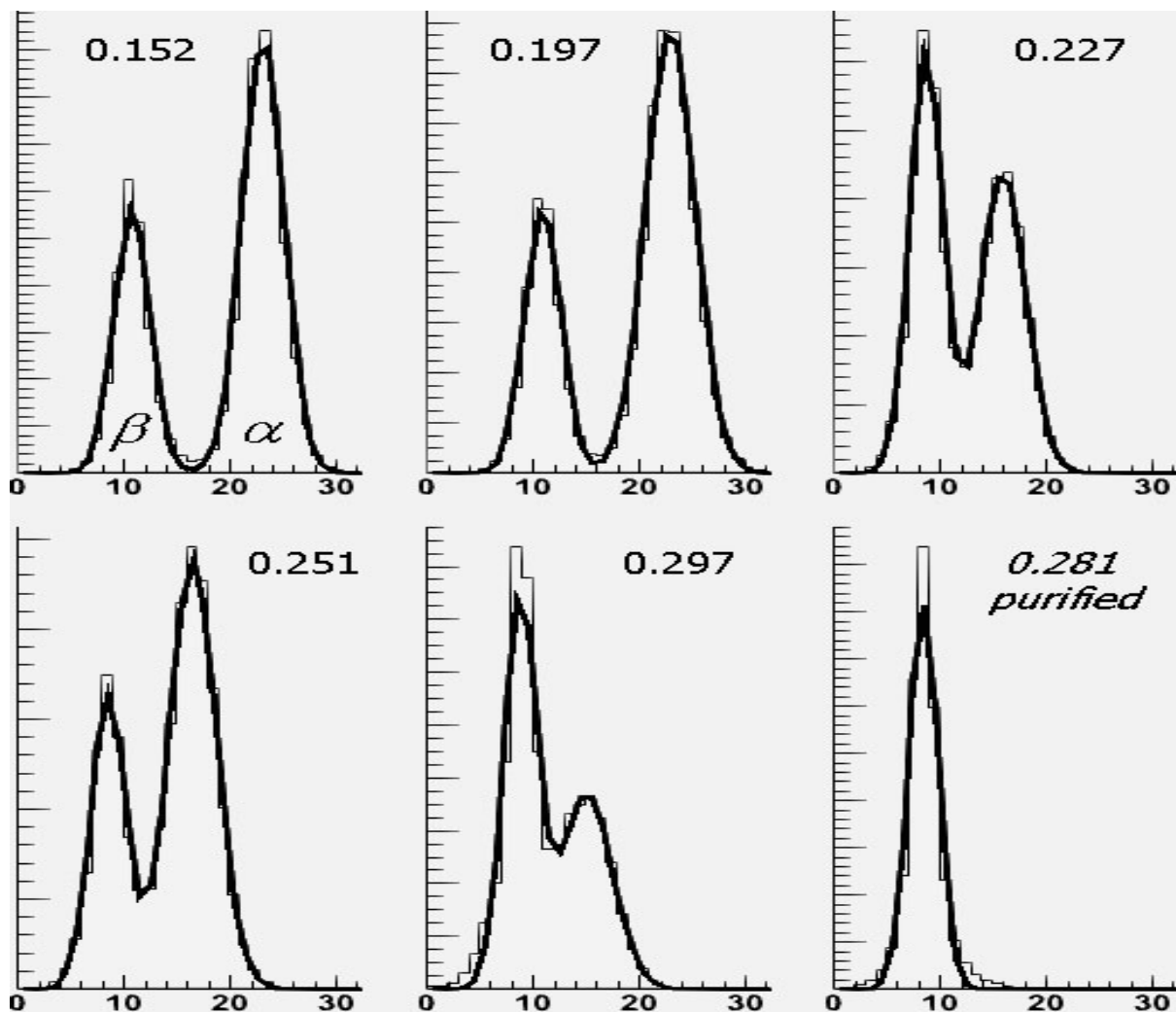


Diagram 4.15: Plots of the event number – the scale is meaningless – over the tail-to-total ratio (in %, binning: 1%) of five contaminated scintillator samples and a purified one, the latter arising from the scintillator after the batch purification test. The plot in the middle of the upper row is due to the sample considered in the Diagrams 4.11 and 4.13. The increasing energy calibration factor at the top of the plots represents a decreasing scintillator light yield.

The curves arise from fits with two Gaussians, used to determine the  $\alpha$ -like and  $\beta$ -like activities of the samples. In the last plot, the slight asymmetry of the data points compared to the fit curve indicates the presence of a small  $\alpha$ -like activity in the purified scintillator.

the light yield of the scintillator determined for each sample for energy calibration purposes. The following plots illustrate this dependence, referring to calibration factors, that were used to scale the area of the pulses to their energy in keV.

The energy integrated PSD spectra of five contaminated scintillator samples – with different  $\alpha$  and  $\beta$  beta activities which does not matter here – are compared regarding the positions of their  $\alpha$  and  $\beta$  peaks. They show, ordered by the explained, increasing energy calibration constant, a decreasing pulse shape discrimination quality with a decreasing light yield of the scintillator. To understand this behaviour is of particular importance, as the tail-to-total range of  $\alpha$ -like events in the sixth plot, the one of the purified scintillator sample, has to be fixed. Table 4.16 contains the peak position values extracted from the above plots.

energy calibration factor	maximum of $\beta$ -like events	minimum between $\alpha$ -like and $\beta$ -like	maximum of $\alpha$ -like events
0.152	10	16	23
0.197	10	16	22
0.227	8	12	16
0.251	8	11	16
0.297	8	11	15

*Table 4.16: Tail-to-total ratios [%] of pulse shape discrimination analyses at different energy calibration factors with respect to the plots in 4.15. The calibration factors increase with a decreasing scintillator light yield.*

Obviously, the position of the  $\alpha$  peak jumps at one point but remains rather constant in the ranges below and above. Hence, in case of the purified scintillator sample, with a calibration factor of 0.281, the maximum of the  $\alpha$  peak should be at a tail-to-total ratio between 15% and 16%. In particular, the PSD window determining the upper  $\alpha$  activity limit of the purified scintillator after the batch purification test was chosen to [13%, 20%], significantly beginning below the supposed  $\alpha$  peak maximum but above the major part of  $\beta$ -like events.

The two described data cuts,  $(16.5 \pm 3.5)\%$  here and  $(412 \pm 97)\text{keV}$  from above, were quadratically added in order to form a circle, as illustrated in Diagram 4.14.

The energy-PSD-window cannot be chosen to contain an  $\alpha$  event percentage close to 100%, as on the one hand it is necessary to mainly exclude  $\beta$ -like events and on the other hand many  $\alpha$ 's even deposit only a part of their energy in the scintillator. However, this error has been accounted for, as groups of samples necessary to be compared with each other – like two samples determining a purification factor – always were analysed in the same way. So, these systematic errors can appear in absolute activities but not in relative factors.

However, like already mentioned at Diagram 4.14, this analysis erroneously includes background related and radon induced events in the window. Radon gets introduced into the scintillator whenever oxygen gets introduced – during the mentioned sample preparations. Nitrogen purging – at least for the time of 1 to 2 hours – does not reduce it completely. Further, the sample containers, teflon boxes, are capable to temporarily hold some radon gas, diffused from air into the material, and to release it later, possibly into the purified scintillator. Nevertheless, radon events can be quantified by the observation of their decay. They have to be distinguished in  $^{220}\text{Rn}$  events and  $^{222}\text{Rn}$  events. Until the nucleus  $^{210}\text{Pb}$ ,  $^{222}\text{Rn}$  causes three  $\alpha$  decays in its chain, due to the dominating  $^{222}\text{Rn}$  half-life all appearing with a decay time of 3.825 days; whereas  $^{220}\text{Rn}$  ( $t_{1/2}=55.6\text{s}$ ) quickly generates  $^{212}\text{Pb}$ , that itself generates one further alpha decay, that due to the longest half-life in this chain appears with a decay time of 10.64 hours. The energies of these  $\alpha$ 's (5.49 MeV, 6.00 MeV, 7.69 MeV in the  $^{222}\text{Rn}$  chain) are slightly different from the  $^{210}\text{Po}$  decay energy (5.30 MeV), the quenching effect however scales down these differences, and  $\alpha$ 's of higher energy can further appear in the E-PSD-

window by the mentioned peak distortion effect of the confined scintillator volume. In any case, two exponential decays with half-lives of 10.64h and 3.825d indeed succeed, concerning all low activity samples, in explaining the observed decrease of the  $\alpha$ -like activity in the E-PSD-window in the course of several days, like the example in Diagram 4.17 demonstrates. The observation of the  $^{222}\text{Rn}$  decay is a good confirmation that the applied cuts do really extract  $\alpha$  events in the right energy range from the spectra.

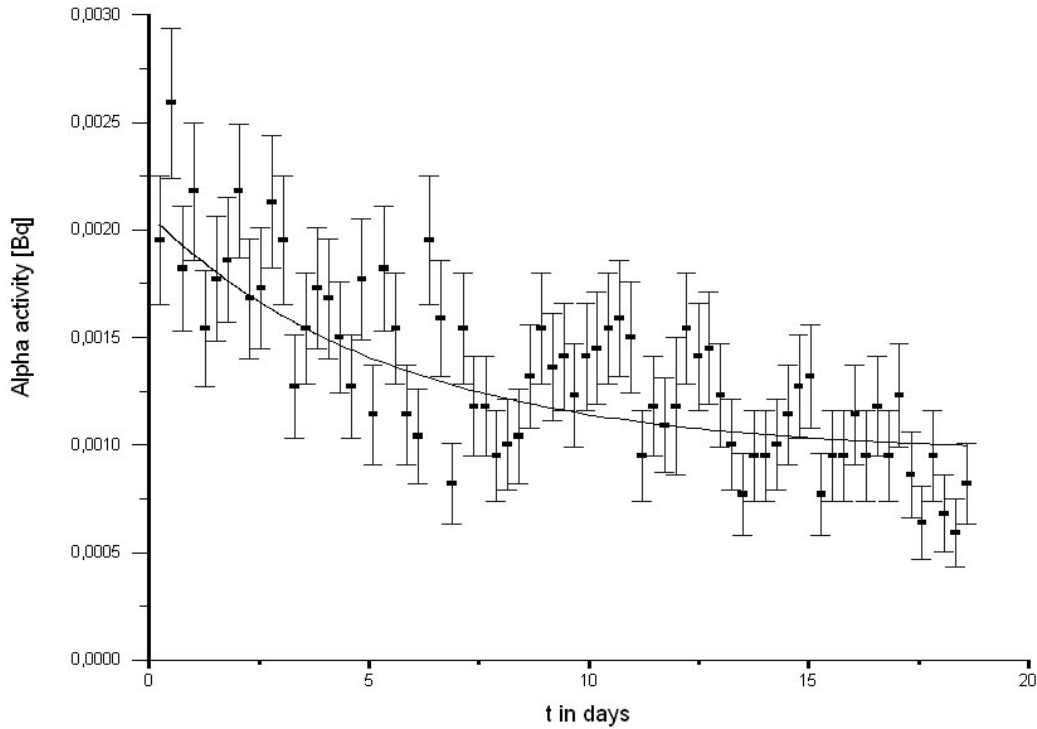


*Diagram 4.17: Radon decay fit of the  $\alpha$ -like activity in the above E-PSD-window of a scintillator sample after the silica gel batch purification. The error bars are only statistical. The  $^{220}\text{Rn}$  and  $^{222}\text{Rn}$  half lives are fixed. The fit ( $\chi^2=1.41$ ) implies a constant activity part of  $0.00096\pm 0.00006$  Bq, a  $^{222}\text{Rn}$  induced activity part of  $0.00111\pm 0.00017$  Bq and no  $^{220}\text{Rn}$  induced activity.*

The constant activity constitutes the important part of the fit result, the remained  $^{210}\text{Po}$  candidates.

A statistical subtraction of external background events, erroneously contributing to the  $\alpha$ -like events in the E-PSD-window, is even difficult with the help of some background measurements. Table 4.27 illustrates the variation of the background activity in the considered window by a factor of 4, explainable with the PSD instability and the radon presence in short time measurements. The major problem consists in the impossibility of deducing a precise number for the general background rate in arbitrary samples. An attempt is illustrated at the end of 4.2.4, in Table 4.27. Nevertheless, it is possible to use the lowest observed background value in the E-PSD-window (0.0004Bq) as lower limit for this background rate. The subtraction of this lower limit from other sample measurements leads to slightly improved upper limits for the  $^{210}\text{Po}$  activities in those samples.

The activity disregarded during the last examinations, the  $\beta$  activity of  $^{210}\text{Bi}$ , cannot be determined on such a low level. The recorded data provides two analysis possibilities, the first of which is based on a Gaussian fit of the tail-to-total ratio curve as illustrated in the plots of Diagram 4.15. The left peak, the  $\beta$ -like one, contains all background events, whose activity has to be statistically subtracted. The remaining  $\beta$  activity, due to the lower energy threshold

representing a certain part of the  $^{210}\text{Bi}$  activity, can be scaled up to the corresponding activity of a whole  $\beta$  spectra. The uncertainty arising from this method has to contain the uncertainty of the background rate, partially influenced by instabilities of the data taking system. Corresponding to the standard deviation of eight independent measurements, it amounted to 0.04 Bq.

So, it has been tried to find a second, more precise analysis method. The only remaining significance of the  $\beta$  events consists in the shape of their energy spectra. The spectra however is distorted to lower energies by the influence of the confined detection volume, a scintillator volume with a diameter of 7cm and a height of 8mm. This effect has been simulated in [Gri00]. Figure 4.18 shows the relating result, and Figure 4.19 the application of this simulated, distorted  $\beta$  curve on the contaminated scintillator sample already considered in the Diagrams 4.11 and 4.13.

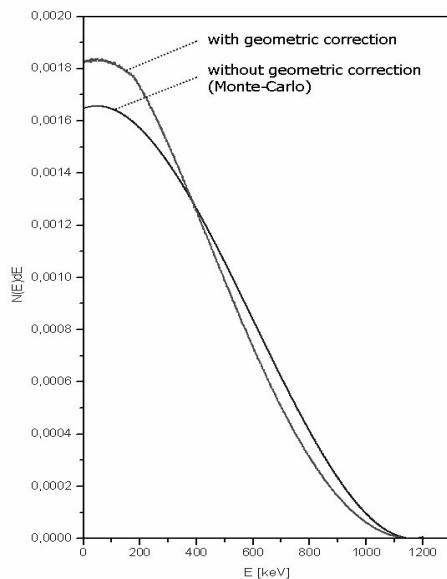


Figure 4.18:  $^{210}\text{Bi}$   $\beta$ -spectra and its distortion by the geometric properties of the sample box, obtained with a Monte-Carlo simulation [Gri00].

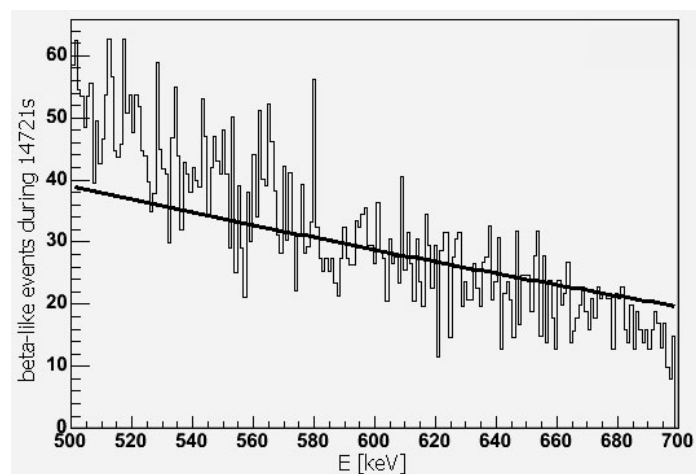


Figure 4.19: Fit of a  $\beta$ -spectra ( $^{210}\text{Bi}$ ) of a contaminated scintillator sample in the energy range from 500 to 700 keV. The gamma background, here comparatively small, is statistically subtracted. The sample is the same as in 4.11 and 4.13. The energy scale has been recalibrated with help of the  $\alpha$  peak position. The fit curve arises from the simulation shown in 4.18.

The energy range between 500 and 700 keV has been chosen in order to avoid a superposition of  $\beta$  events with both the  $\alpha$  peak and the other event group accumulated at  $\sim 1\text{MeV}$ , possibly due to cosmic muons. As the energy scaling of the sample influences the fit in a significant way, and as the energy calibration with help of the smeared out Compton edge of the  $^{137}\text{Cs}$  source causes errors in the range of  $\pm 50$  keV, all samples containing  $\beta$  activities were recalibrated using the position of the  $^{210}\text{Po}$   $\alpha$  peak – the reason, why the peak position in 4.19 differs from that in 4.11. However, as visible above, the fit still is not perfect with respect to the inclination of the curve. Remaining calibration uncertainties and further distortion effects regarding the shape of the spectra may be responsible for this. Nevertheless, the activity, scaled up to the whole  $\beta$  energy range, can be determined within a certain error, in many cases smaller than the one of the first analysis method.

Concerning pure samples, where the background rate dominates the  $\beta$ -like events, the described energy cut does not improve the sensitivity. The detection limit remains at the above value of  $\sim 0.04$  Bq.

## Germanium Detector

A further task, apart from the  $\alpha$  and  $\beta$  activity determination, consisted in the examination of  $^{210}\text{Pb}$  by a detection of the 46.5 keV gamma line, emitted in 81% of its decays. Therefore, after the photomultiplier measurement, all liquid scintillator samples were examined with a high-purity germanium detector.

The teflon boxes, containing liquid scintillator samples of 28g from the previous measurement, were completely filled with raw pseudocumene in order to guarantee a cylindrical activity distribution with respect to the positioning of the sample box in front of the germanium crystal (see Image 4.20). The distance to the crystal was approximately 1cm, whereby the absorption by the glass window ( $d=2\text{--}5\text{mm}$ ) of the sample box and the carbon window ( $d\approx 1\text{mm}$ ) of the detector slightly reduced the detection efficiency.

The high-purity germanium crystal itself, with a diameter of 7.07cm, a length of 3.02cm, and a mass of 620g, was shielded, from inside to outside, by a 5mm layer of copper, a 5cm layer of low activity lead, and a 10cm layer of normal lead. The copper shielding was particularly important with respect to the  $^{210}\text{Pb}$  detection, as it reduced the according background activity from the lead shield by a factor of  $\sim 20$ . The germanium

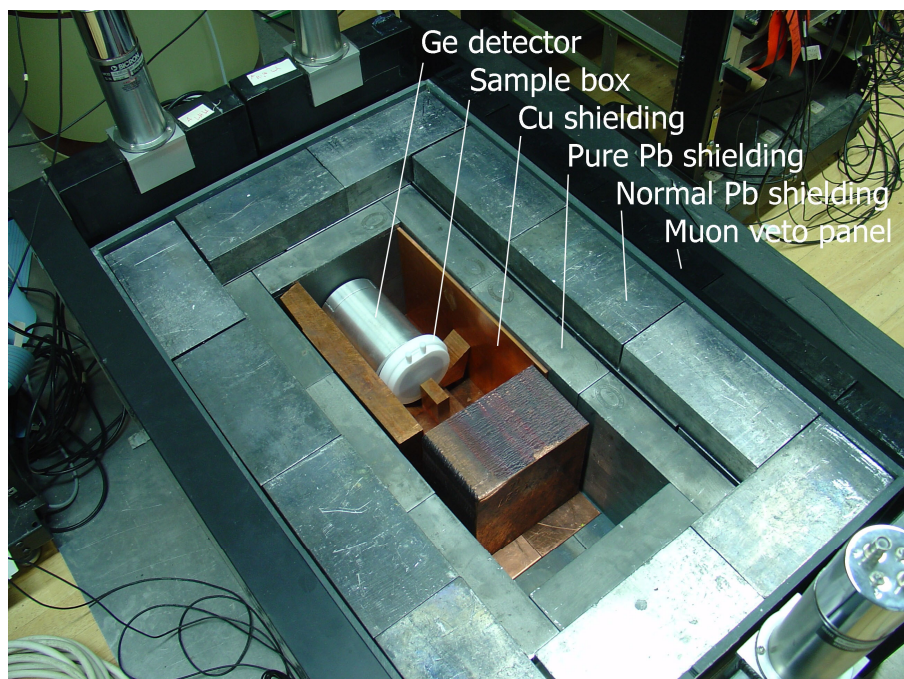


*Image 4.20: View of the germanium detector with passive shielding layers and active muon veto*

crystal was cooled with liquid nitrogen, slowly evaporating and escaping to outside, thus displacing radon in the detector volume after a certain time. The whole detector set-up was surrounded by an active muon veto, consisting of six 5cm plastic scintillator panels, which put 50ms anti-coincidence windows on muon events, recognisable by their energy deposition of about 8 MeV in the panels. A detailed detector description can be found in [Hen99].

The amplified signals were recorded by a 8192 channel ADC, and the spectra could be monitored on a computer. The linear energy calibration, once performed with the help of some different calibration sources, has remained unchanged during the whole period of measurements. The death time, below 1%, was subtracted. The Figures 4.21 and 4.22 compare a spectra of a contaminated scintillator sample with the detector background. As the resolution of the plot is not sufficient in combination with the wide energy range of the detector, the relevant part around the  $^{210}\text{Pb}$  line is enlarged, and Table 4.23 shows additional information about the most significant peaks.

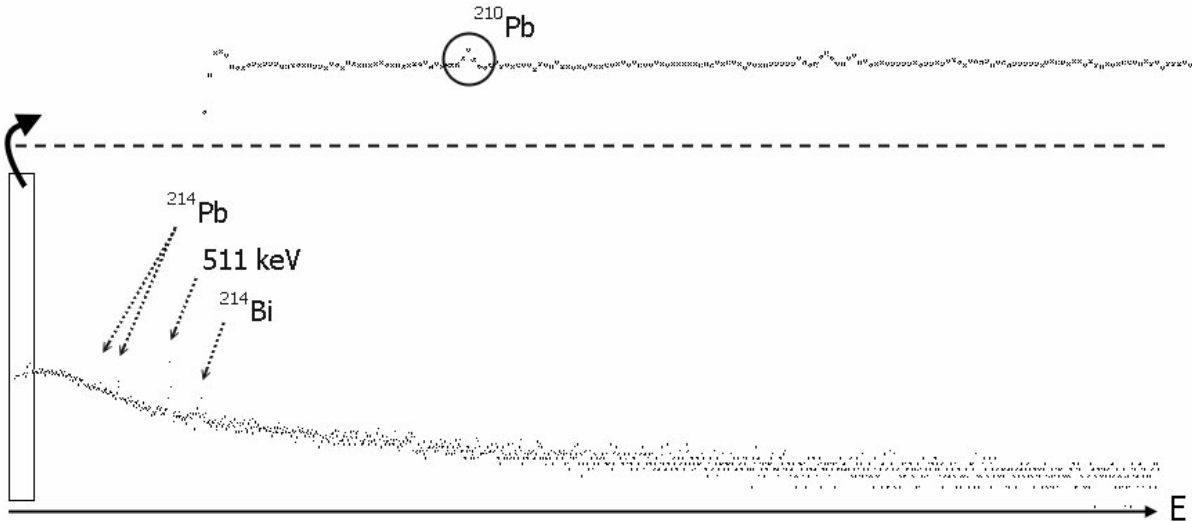


Figure 4.21: Energy spectra of a contaminated scintillator sample (prior to the batch purification test) between 30 and 3580 keV, recorded with a germanium detector during a time of 261627s. The upper curve is the focus on the marked range below.

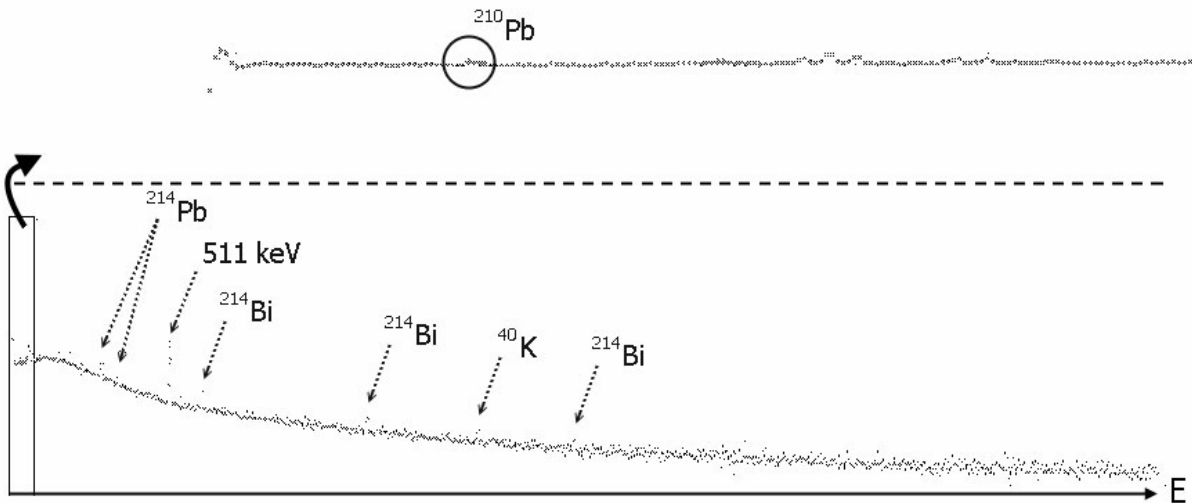


Figure 4.22: Background energy spectra of the germanium detector between 30 and 3580 keV, recorded in a time of 2167758s. The upper curve is the focus on the marked range below.

The major part of these  $\gamma$  lines is due to the isotopes  $^{214}\text{Pb}$  and  $^{214}\text{Bi}$ , generated by the  $^{222}\text{Rn}$  activity in the air. The activity of these lines, as well as the  $^{40}\text{K}$  line, does not disturb and will not be considered any more. The above plots especially show, that there is no unexpected background. The focus, however, will be turned on the intended measurement of the  $^{210}\text{Pb}$  gamma at 46.5 keV. In the detector, it normally deposited its energy in a range of three bins that by the energy calibration were related – due to a small but constant inaccuracy – to the energy interval between 44.35 and 45.65 keV (cf. Figure 4.21). The area of the  $^{210}\text{Pb}$  peak – as three data points hardly allow a Gaussian fit – was determined by an event counting in the mentioned three bins and a subtraction of the background rate in this range, averaged over 20 surrounding bins.

The  $^{210}\text{Pb}$  peak activity of the considered loaded scintillator sample – a diluted one – is one order of magnitude higher than in the background spectra (see Table 4.23), but still one

order of magnitude smaller than in an undiluted, loaded scintillator sample. This allowed a maximal experimentation range of two orders. In reality, the detection limit, i.e. the effective background for the measurements of liquid scintillator samples, arose from the observed activity in case of a sample box, full of raw pseudocumene, placed in front of the germanium crystal. This blank scenario slightly increased the background activity – to about  $2 \cdot 10^{-4}$  Bq, to some extent depending on the sample box.

Energy in keV	Isotope	Activity ( $\cdot$ eff) of contaminated scintillator sample [Bq]	Background activity
46.5	$^{210}\text{Pb}$	$(1.35 \pm 0.10)10^{-3}$	$(1.33 \pm 0.26)10^{-4}$
238.6	$^{214}\text{Pb}$	no data	$(1.4 \pm 0.3)10^{-4}$
242.0	$^{214}\text{Pb}$	no data	$(2.5 \pm 0.3)10^{-4}$
295.2	$^{214}\text{Pb}$	$(4.8 \pm 1.0)10^{-4}$	$(4.8 \pm 0.3)10^{-4}$
351.9	$^{214}\text{Pb}$	$(6.4 \pm 0.8)10^{-4}$	$(7.8 \pm 0.3)10^{-4}$
609.3	$^{214}\text{Bi}$	$(6.0 \pm 0.7)10^{-4}$	$(4.7 \pm 0.2)10^{-4}$
1120.3	$^{214}\text{Bi}$	no data	$(9.3 \pm 1.6)10^{-5}$
1460.8	$^{40}\text{K}$	$(1.8 \pm 0.4)10^{-4}$	$(1.2 \pm 0.2)10^{-4}$
1764.5	$^{214}\text{Bi}$	no data	$(5.9 \pm 1.2)10^{-5}$

*Table 4.23: Most significant  $\gamma$  peaks and their activities in a sample of the contaminated scintillator prior to the batch purification (described in 4.2.4), compared to the background activity in the germanium detector. The detector efficiency is not accounted for. The errors are at  $1\sigma$ .*

The absolute  $^{210}\text{Pb}$  activity further depends on the detection efficiency. The latter has experimentally been determined to  $\sim 1.1\%$  by a comparison of the  $^{210}\text{Pb}$  gamma peak activity with an equilibrated  $^{210}\text{Bi}$  beta activity measured in the scintillation detector. It got influenced by the  $\gamma$  branching ratio (81%), the sample geometry, the distance between sample and detector, the transmission through the glass window of the sample box, and the transmission through the carbon window of the detector. A corresponding simulation accounting for all these effects, however, implies an efficiency of  $\sim 6.4\%$ . In particular, this simulation assumes a homogeneous  $^{210}\text{Pb}$  distribution in the liquid scintillator, whereas, in reality,  $\sim 50\%$  of the  $^{210}\text{Pb}$  atoms were adsorbed on the teflon surface of the sample box (see 5.2.1). These atoms would have been farer from the detector by 1cm and, moreover, shielded by a corresponding liquid scintillator layer of the same dimension; both effects lead to a lower efficiency.

Nevertheless, as all measurements were accomplished under the same conditions, the detection efficiency does influence the results in a crucial way.

### 4.2.3. Free Enthalpy Determination

The following pages (incl. paragraphs 4.2.4, 4.2.5) describe the realisation and results of the scintillator purification experiments in the context of this thesis. They were carried out with the loaded scintillator mentioned in 4.2.1 and the apparatus illustrated in 4.2.2.

The most fundamental theoretic assumption in the context of the silica gel purification model (see chapter 4.1) consists in the adsorption equilibrium on the silica gel surface. This part of the model is examined first.

Table 4.24 shows the purification effect on 35g of loaded pseudocumene, that has been in contact for  $\sim 2$  hours with 0.16g of silica gel (grain size  $16\mu\text{m}$ , pore size  $60\text{\AA}$ , product name Kromasil, made by Eka Nobel, Sweden). In particular, the silica gel was first put into a 50ml glass vessel, then the loaded scintillator was added from a bottle. As silica gel contains

gas volume in its pores, it initially ascended to the surface of the liquid scintillator in the glass. This prevented an equilibration of the scintillator with the silica gel during the first minutes of the test, so that the loaded scintillator most probably first equilibrated with the glass surface. Therefore, the first line of Table 4.24 shows the activity of 35g of loaded scintillator, that has been in contact with a 50ml glass vessel. The systematic error of this initial scintillator activity dominates the total uncertainty and arises from two independent measurements.

During the purification process, when the silica gel had begun to take liquid scintillator in its pores and to sink to the bottom of the vessel, the impurity concentration in the scintillator decreased, and a part of the activity adsorbed on the glass surface was probably released into the scintillator. In 5.2.3, this part has been determined to  $(1.14 \pm 0.14)\%$  for Po,  $\leq 1.4\%$  for Bi and  $(1.35 \pm 0.36)\%$  for Pb with respect to the initial activities; and these activities in the first line of Table 4.24 have been corrected for this additional contribution. In general, these uncertainties arising from the impurity adsorption on glass would, if wrongly accounted for, increase the initial scintillator activity prior to the silica gel equilibration. Hence, the real silica gel purification efficiency would be higher than the measured one, so that the measurements here constitute a conservative examination of the problem.

The equilibrium between the scintillator and the silica gel, the requirement for the validity of the equation  $\Delta G = -RT \ln(k)$ , can be assumed due to the fine mixing of both substances for several minutes, while the silica gel was sinking down to the bottom of the glass vessel. During the following 2 hours, the emulsion was shaken from time to time.

	$^{210}\text{Po}$	$^{210}\text{Bi}$	$^{210}\text{Pb}$
Loaded scintillator [Bq]	$3.75 \pm 0.31$	$2.44 \pm 0.16$	$(2.46 \pm 0.17)10^{-2}$
Purified scintillator [Bq]	$0.204 \pm 0.021$	$0.172 \pm 0.026$	$(2.23 \pm 0.26)10^{-3}$
Purification factor	$18.4 \pm 2.4$	$14.2 \pm 2.3$	$11.0 \pm 1.5$
Free Enthalpy $\Delta G$ [kJ/mol]	$-21.92 \pm 0.35$	$-21.24 \pm 0.43$	$-20.57 \pm 0.37$
Former values [Gri00]	$-21.7 \pm 2.3$	$-18 \pm 5$	---
[Nie00]	$-23.4 \pm 0.4$	$-19.4 \pm 1.6$	---

*Table 4.24: Determination of the Free Enthalpy of Po, Bi and Pb for surface adsorption on silica gel. The activities are influenced by the detection efficiencies, that however vanish in the purification factors. All uncertainties are statistic and systematic. The systematic uncertainties in the contaminated scintillator activities were determined by two independent measurements. The systematic uncertainties in the purified scintillator activities were estimated to 10%, motivated by the difference between the mentioned two independent measurements of loaded samples.*

The free enthalpies of the three examined heavy metals, comparable concerning their chemical properties, result comparable as well. Above all, the adsorption capability of silica gel for Pb, not measured before, has been shown.

This time, compared to the previous experiments mentioned in Table 4.24, a minimal experimentation equipment was used, trying to avoid influences of adsorptions on other surfaces. Even the effect of the one glass vessel used was taken into account. This difference may have been responsible for the higher efficiency in [Nie00]. The activities of the purified samples clearly remained above the detection threshold, due to the selection of external

parameters. In the previous measurements, especially the  $^{210}\text{Bi}$  spectra was hardly detectable, a possible reason for the big uncertainties in those values.

#### 4.2.4. Laboratory Batch Purification Test

According to 4.1.4, the most efficient purification mode consists in a batch purification process. The verification of this prediction, i.e. a successful experimental realisation of a batch purification process, constituted the major goal of this thesis.

In particular, a comparatively high amount of liquid scintillator should be purified by a very small quantity of silica gel. The ratio of both masses should be chosen bigger than 1000, comparable to the parameters of the CTF3 tests (see 4.3). The amount of contaminated scintillator, however, was limited; the available 120g could not be infinitely diluted, as the capability of demonstrating a high purification factor decreases with the dilution of the activity. Additionally, with a look on Table 4.7, the silica gel volume was supposed to form at least five or six segments, so that the silica gel column should have some reasonable, minimum height of several cm. Within these restrictions, and with respect to the theoretical considerations in Chapter 4.1, the test parameters – the amounts of silica gel and scintillator – had to be chosen in a way to easily distinguish a high purification factor, caused by the intended segment behaviour, from a lower one in the range of the equilibrium factor. The chosen quantities of 2kg of scintillator and 1.6g of silica gel satisfied these requirements: the activity of the diluted scintillator, together with the detection limit guaranteed a sensitivity to a purification factor of  $\sim 200$ , so that the excess of a low factor around  $\sim 6$ , resulting from a general equilibrium, was possible to be unambiguously demonstrated.

The purification plant consisted of a 12 litre stainless steel vessel, supposed to contain the contaminated scintillator, teflon and stainless steel tubes leading to the purification column and a 6 litre glass vessel to collect the purified scintillator (see Picture 4.25). The purification column consisted of a stainless steel tube of 5cm in length and 10mm of inner diameter, enclosed between two VCR connectors containing nylon filter papers to confine the silica gel. The silica gel specifications were the same as in 4.2.3. Samples for activity measurements were taken with the described teflon boxes (see Figure 4.10), the amounts were controlled on a scales.

Prior to the purification, the radiopurity of the equipment was confirmed by a blank test, a measurement of an originally pure scintillator sample, that had been looped through the plant (compare first line of Table 4.26). Then, the system was loaded with contaminated scintillator, diluted to a total amount of 2010g. In particular, at that time all the system parts supposed to handle contaminated scintillator, i.e. the stainless steel vessel, and the tubes before the column, were purged with this contaminated scintillator, in order to exclude surface adsorption on steel or teflon parts as a potential source



Picture 4.25: Set-up of the laboratory batch purification test

of purification. Afterwards, the activity of the contaminated scintillator was determined and the purification process was initialised.

During the purification process, the contaminated scintillator was moved through the silica gel column with a flow rate of 0.5–1.0 g/min, applying a nitrogen pressure between 0.5 and 1.0bar. Purified scintillator samples of 28.0g were taken at the beginning of the purification (0g) and at various times during the process: after purification amounts of 74g, 232g, 722g, 852g and 1880g. The purpose consisted in recognising a possible breakthrough of the column, and in continuously controlling the purity state of the set-up. The rest of the purified scintillator – the major part of it – was collected in the 6 litre glass vessel, and its activity was determined at the end of the experiment.

The activity measurements of  $^{210}\text{Po}$  and  $^{210}\text{Pb}$  are shown in Table 4.26. The preparation and measurement of all samples was carried out applying the same procedure – as described in the previous paragraphs – in order to minimise the systematic error in the purification factor. The detection efficiencies are not necessarily considered as they influence all measurements to the same extent. The  $^{210}\text{Po}$  activity was determined by the energy and pulse shape cut described in 4.2.2; a lower background limit of 0.0004 Bq was subtracted. The activities refer to a scintillator amount of 28.0g. The limits and uncertainties are at a  $1\sigma$  level, as long as not otherwise specified.

	$^{210}\text{Po}$ activity ( $\cdot\text{eff}$ ) in Bq	$^{210}\text{Pb}$ activity ( $\cdot\text{eff}$ ) in Bq
Blank loop with raw pseudocumene	<0.0004	$(-1.2\pm 0.9)10^{-4}$
Contaminated pseudocumene	$0.26\pm 0.01$	$(9.5\pm 1.2)10^{-4}$
Purified pseudocumene after 0g	<0.0011	$(-0.7\pm 0.8)10^{-4}$
Purified pseudocumene after 74g	<0.0010	$(0.6\pm 0.8)10^{-4}$
Purified pseudocumene after 232g	<0.0017	$(-0.6\pm 0.9)10^{-4}$
Purified pseudocumene after 722g	<0.0030	no data
Purified pseudocumene after 852g	<0.0037	$(0.1\pm 1.6)10^{-4}$
Purified pseudocumene after 1880g	<0.0020	$(-0.1\pm 0.4)10^{-4}$
Purified pseudocumene, integral sample	<0.00054*	$(-0.23\pm 0.22)10^{-4}$
Purification factor	$>460 (1\sigma)^*$ $>380 (3\sigma)^*$	$>38 (1\sigma)$ $>8.9 (3\sigma)$

Table 4.26: Result of the described silica gel batch purification experiment.

With respect to the considerations above, the obtained purification factor clearly excludes an equilibrated behaviour of the whole silica gel volume – like if it would have acted as one only segment – and qualitatively confirms the column structure of the dynamic model, based on a higher number of segments as illustrated in 4.1.2. The ultra low activity of the scintillator exiting the column, expected in a column purification process before the breakthrough and illustrated by the arrows in Diagram 4.6, agrees with the lower limits between the third and

eighth line in Table 4.26. In comparison to the purification efficiencies in Table 4.7, calculated for different equilibrium times  $\tau$ , the limit  $\tau < 50$ s can be derived on a  $3\sigma$  level.

The possibility of deducing defined values instead of the upper limits marked with a (\*) in Table 4.26 is difficult with respect to the variation of the background activity in the considered E-PSD-window. Table 4.27 shows all measurements able to add a reasonable contribution in this context. It includes four independent measurements based on different samples of the same purified scintillator, collected in the described 6 litre glass vessel. Two long-time and three short-time background measurements illustrate the variation of the background activity in the E-PSD-window in different measurements. The short-time measurements in the third column are considered upper limits, as they possibly include events from radon generated background. The values of the long-time measurements in the first two columns, where a time fit of the  $^{220}\text{Rn}$  and  $^{222}\text{Rn}$  decay identifies – and helps to subtract – the radon related activity, still vary slightly, as they can further depend on the purity of the sampling boxes and the quality of the pulse shape discrimination, influenced by the optical scintillator properties. Especially a possible external contamination of the sampling boxes supports the idea of neglecting comparatively high activity values. The influence of the optical scintillator quality however, depending on former contact with oxygen, leads more or less to a certain spread of the single values, that cannot easily be accounted for.

Silica gel batch test, purified sample [Bq] (radon subtracted)	Background [Bq] (radon subtracted)	Background [Bq] (pure event counting, including radon)
$0.00109 \pm 0.00018^+$ (0.234)	$0.00047 \pm 0.00004^+$ (0.226)	$\leq 0.00174$ (0.240)
$0.00088 \pm 0.00009^+$ (0.281)	$0.00093 \pm 0.00009$ (0.314)	$\leq 0.00039$ (0.253)
$0.00096 \pm 0.00006^+$ (0.281)		$\leq 0.00079$ (0.282)
$0.00161 \pm 0.00025$ (0.308)		

*Table 4.27: Single measurements influencing the determination of the integral purification factor of the described silica gel batch purification experiment. The activities refer to the energy and pulse shape cut described in 4.2.2. The values in brackets are calibration factors, indirectly proportional to the light yield of the scintillator. The values marked with (+) are used for further calculations.*

The higher activities in the last row of the first and second column are probably enhanced due to pre-contamination or a bad optical scintillator quality and will be disregarded in the following. The three remaining measurements of the purified scintillator (+) however all agree within their errors, thus indicating a certain accuracy as well as the impossibility of reaching lower activities like in the first background measurement (+). The upper limits for the background in the third column cannot be used for a precise background subtraction, but two of them confirm a background level below the one of the purified scintillator. These considerations give some motivation to average over the three agreeing batch test measurements (+) and to subtract the low and most accurate background measurement (+) in order to obtain a more precise activity value for the purified scintillator. The optical scintillator quality cannot clearly be made responsible for the variations of the above values, as particularly the second background limit in the third column is lower than the activity of the first batch test measurement despite of a worse scintillator light yield; hence the indication for the correctness of the explained background subtraction remains. With respect to these considerations, the  $^{210}\text{Po}$  activity of the purified scintillator amounts to  $0.00048 \pm 0.00006$  Bq, implying a purification factor of  $546 \pm 71$ .

However, due to the mentioned systematically motivated variations of the background measurements, the last value cannot be considered as unambiguously settled, and the lower limits for the purification factors in the last line of Table 4.26 should still be considered the essential test result. The most important implications can even be deduced from that limit.

The purification factor concerning the  $\beta$  activity of  $^{210}\text{Bi}$  has not been considered until now, as the detection sensitivity of the set-up did not allow a determination of purification factors bigger than  $\sim 4$ . In fact, all  $\beta$  activities measured in purified scintillator samples of the batch purification test were below the detection sensitivity, so that the purification factor for  $^{210}\text{Bi}$  can be specified to  $\geq 4$ . However, this does not add new insights.

#### 4.2.5. Purification Efficiency Limitation

The theoretical model described in 4.1 allows, in dependence on the silica gel to scintillator mass ratio, unlimited purification factors. In reality, however, some limitation is probable; theoretically motivated limits on this factor can arise from additional assumptions about intrinsic radioactive contaminations in the silica gel itself or partially unadsorbable scintillator contaminants.

The first point, concerning the radiopurity of silica gel, would imply a certain concentration value as general purification limit; purification effects would just be cut off at this barrier. The limit could be determined by the equation for the equilibrium constant  $k$  in 4.1.1, with the help of the intrinsic impurity concentration in the silica gel, the free enthalpy, and the temperature. The resulting impurity concentration in the scintillator could not be crossed.

The experimental examination of such a barrier was approached in three different ways. One of them involved the method of mass spectroscopy: various samples of silica gel, even a contaminated one, were examined but the method turned out not to be sensitive enough.

In a second way, possible intrinsic impurities in silica gel were tried to be purged out by hot pseudocumene, taking advantage of the lower adsorption equilibrium constant  $k$  at higher temperatures, according to  $\Delta G = -RT \ln(k)$ . In particular, 46.6g of pseudocumene were in contact with 4.00g of silica gel for  $\sim 2$  hours at 370K in a 100ml glass vessel. The following activity measurements were carried out in the same way as described in 4.2.2. With the enthalpy values of Table 4.24, they yield the limits in the first row of Table 4.28. The second row arises from a calculation based on the  $^{210}\text{Po}$  activity only, as the detection was most sensitive to this isotope. It is motivated by the assumption of a decay equilibrium between  $^{210}\text{Pb}$ ,  $^{210}\text{Bi}$  and  $^{210}\text{Po}$  in silica gel, as the examined silica gel had been stored for at least  $3\frac{1}{2}$  years prior to the experiment.

	$^{210}\text{Po}$ concentration [g( $^{210}\text{Po}$ )/g(SiGel)]	$^{210}\text{Bi}$ concentration [g( $^{210}\text{Bi}$ )/g(SiGel)]	$^{210}\text{Pb}$ concentration [g( $^{210}\text{Pb}$ )/g(SiGel)]
values from activity measurements	$< 4.4 \cdot 10^{-17}$	$< 2.5 \cdot 10^{-16}$	$< 1.1 \cdot 10^{-13}$
calculation based on $^{210}\text{Po}$ measurement	$< 4.4 \cdot 10^{-17}$	$< 1.6 \cdot 10^{-18}$	$< 2.6 \cdot 10^{-15}$

Table 4.28: Intrinsic contamination of a pure silica gel sample with  $^{210}\text{Po}$ ,  $^{210}\text{Bi}$  and  $^{210}\text{Pb}$ , measured by a surface adsorption experiment. The limits are at  $1\sigma$ .

All these values however remain by several orders of magnitude above the values in the next paragraph (Table 4.29) and the limits derived from the CTF3 batch tests in 4.3.2.

Better contamination limits can be derived from  $^{222}\text{Rn}$  emanation measurements, described in 3.3. The emanation rate of the silica gel considered here – the same type as intended to be used for Borexino – has been measured with two amounts of 30 kg placed in two big chromatography columns in the liquid handling system Module-0 (see Chapter 3) of the Borexino experiment. In order to account for the emanation background of these measurements, the emanation rate of a stainless steel housing – the container where the considered silica gel is placed in – was separately measured and subtracted. The silica gel, two different batches of ‘Kromasil’, purchased independently of the samples examined in the laboratory experiments above, but still at Eka Nobel, Sweden, has shown an emanation rate of  $0.13 \pm 0.05$  mBq/kg (see Table 3.6). The measurements were carried out by the Max-Planck-Institut für Kernphysik, Heidelberg [Fre03]. Most probably, this emanation of  $^{222}\text{Rn}$  is due to a  $^{226}\text{Ra}$  contamination in the silica gel. In particular, a further  $^{222}\text{Rn}$  decay produces the above considered nuclei,  $^{210}\text{Pb}$ ,  $^{210}\text{Bi}$  and  $^{210}\text{Po}$ ; and it can be tried to deduce an estimation of the corresponding surface contamination in silica gel (1<sup>st</sup> row of Table 4.29). The  $^{222}\text{Rn}$  emanation rate however leads to an upper limit for the surface contamination caused by intrinsic  $^{226}\text{Ra}$ , as subsequent decays can catapult active radon daughter nuclei from the grain and pore surfaces back into the lattice, where they do not influence the adsorption equilibrium. Moreover, the decay equilibrium between  $^{222}\text{Rn}$  and  $^{210}\text{Pb}$  gets reached with a time constant of 22.3 years, implying  $^{210}\text{Pb}$  activities smaller by a factor of  $\geq 17$  in samples younger than 2 years. So far, the concentrations in the 2<sup>nd</sup> row of Table 4.29, calculated with the help of the respective free enthalpies (see Table 4.24), have to be considered upper limits; but usually the decay equilibrium between  $^{226}\text{Ra}$  and  $^{210}\text{Pb}$  is broken at the isotope  $^{222}\text{Rn}$ , so that  $^{210}\text{Pb}$  atoms adsorbed from decays of the comparatively high  $^{222}\text{Rn}$  activity in the air – as long as fresh air is able to enter the silica gel volume – could vice versa lead to higher silica gel surface contaminations.

	$^{210}\text{Po}$	$^{210}\text{Bi}$	$^{210}\text{Pb}$
concentrations in silica gel [g/g(SiGel)]	$(7.7 \pm 2.8) \cdot 10^{-22}$	$(2.8 \pm 1.0) \cdot 10^{-23}$	$(4.5 \pm 1.6) \cdot 10^{-20}$
concentrations in purified pseudocumene [g/g(PC)]	$(4.5 \pm 1.8) \cdot 10^{-25}$	$(2.2 \pm 0.9) \cdot 10^{-26}$	$(4.6 \pm 1.8) \cdot 10^{-23}$

*Table 4.29: Values for upper limits of intrinsic contamination in a pure silica gel sample, arising from intrinsic  $^{226}\text{Ra}$  contamination and measured via the emanation of  $^{222}\text{Rn}$ . The second row is calculated with the values in the first row. The errors account for systematic and statistic uncertainties.*

The best limits regarding this item here, have however been obtained with the CTF detector (see Table 4.42). The concentration limits shown there, arisen from silica gel stored for ~1 year in plastic bags, not tight against radon, are below the values of Table 4.29, thus indicating that contamination by air contact does not dominate in such samples.

A different problem of limitation, instead of considering a general purity threshold now regarding the point of a special limitation in the purification factor of silica gel, is possible as well. An examination of this problem has been carried out by an attempt of reaching the highest possible purification factor. Therefore, an undiluted amount of the contaminated scintillator, loaded at the PTB Braunschweig, was purified in three steps with 1.00g of new silica gel each time. In particular, the pseudocumene and the silica gel were brought into adsorption equilibrium during a contact time of 1–2 hours in a 50ml glass vessel. The glass vessel was exchanged for each purification step. Activity measurements, shown in the Tables

4.30 and 4.31, were carried out after the second and the third purification step, using the apparatus described in 4.2.2. The background activity caused by the sampling boxes and by radon was subtracted. All  $^{210}\text{Po}$  activities could accurately be determined with individual energy and pulse shape cuts due to excellent optical scintillator properties and a clear  $\alpha$ - $\beta$ -discrimination. The adsorption on glass and teflon surfaces was not taken into account, except for the case of the initial scintillator. The decreasing scintillator amount is explained by the scintillator molecules remaining in the silica gel at each step. The purification factors in the tables refer to the initial scintillator activity. The expected factors were calculated with the enthalpy values in Table 4.24. They are specified as lower limits in the cases they would lead to activities below the detector sensitivity.

	scintillator amount [g]	$^{210}\text{Po}$ activity ·eff in 28.0g [Bq]	obtained purification factor	expected purification factor
initial PC	35.1	2.17±0.14	-	-
after 1 <sup>st</sup> step	30.5	no data	no data	113±15
after 2 <sup>nd</sup> step	25.5	0.0097±0.0013	224±34	≥ 3000
after 3 <sup>rd</sup> step	20.9	0.0039±0.0004	558±73	≥ 3000

Table 4.30:  $^{210}\text{Po}$  purification by an adsorption equilibrium of pseudocumene and silica gel in three subsequent equilibrium steps

	scintillator amount [g]	$^{210}\text{Pb}$ activity ·eff in 28.0g [Bq]	obtained purification factor	expected purification factor
initial PC	35.1	(2.43±0.17)10 <sup>-2</sup>	-	-
after 3 <sup>rd</sup> step	20.9	(1.66±0.85)10 <sup>-4</sup>	150 <sup>+170</sup> <sub>-60</sub>	≥ 170

Table 4.31:  $^{210}\text{Pb}$  purification by an adsorption equilibrium of pseudocumene and silica gel in three subsequent equilibrium steps

As twice in the case of Po and once in the case of Pb the purification did not reach the expected efficiency, one indeed seems to observe a limitation. The purity levels reached after the batch purification test (Table 4.26), as well as the results in Table 4.28, both of better quality than the final activities reached here, exclude as cause a general purity limit due to an intrinsic silica gel contamination. However, the existence of a minor quantity of Po and Pb atoms dissolved in the scintillator in a different way would explain the observation. Complexes of heavy metal atoms with organic molecules could be formed at certain ratios, shielding the enclosed heavy metal atoms from polar forces and thus preventing them from effectively adsorbing on the silica gel surface. [Fig61] illustrates possible formations of several different complexes with polonium. Such complexes could possess an adsorption enthalpy of a lower absolute value, explaining the slight purification effect observed for  $^{210}\text{Po}$  in the third step.

The factor of the third purification step, even if being low contradicting a strict limitation in the purification factor, could theoretically be attributed to a surface adsorption effect on a glass or teflon surface. In this case, however, the supposed nature of surface adsorption should have also been observed in a normal way on the silica gel surface; hence the indication for the illustrated presumption remains.

### 4.3. Experiments with CTF3

The technique of silica gel chromatography described in this thesis has been aiming at the purification of the liquid scintillator in the Borexino experiment. As the respective scintillator amount of ~300 tons is quite large, an important step on this way consisted in the testing of purification processes at comparable dimensions with the Counting Test Facility (CTF) of Borexino, containing a scintillator amount of ~4 tons. Up to now, the last of these experiments, in a wider context already summarised in Chapter 2.4, were carried out in 2002, during the CTF3 campaign. In particular, one test of the loop purification mode (February 2002, cf. 4.3.1) and one test of the batch purification mode (June 2002, cf. 4.3.2) were performed. With respect to the idea of scaling the dimensions of the Borexino purification plant, set up with 60 kg of silica gel for 300 tons of scintillator, down to 2.4 kg of silica gel for 4 tons of CTF scintillator, the tests should simulate the envisioned process on a comparable scale. The slight difference between the factors of the mentioned scintillator and silica gel masses – 5000 for Borexino, but 1600 for CTF – arose from the technical difficulties to use a purification plant projected for the dimensions of Borexino with silica gel amounts scaled to the CTF size, 80 times smaller.

#### 4.3.1. CTF3 Loop Purification Test

Based on the principle explained in 4.1.3, the scintillator of the CTF Inner Vessel,  $\approx 3820$  kg at this time, was circulated via a silica gel column in the Module-0, the cylindrical column COL3 (see 3.1.1), loaded with 2.4 kg of ultra-pure silica gel (specifications: grain size  $10\mu\text{m}$ , pore size  $60\text{\AA}$ , product name Kromasil, company Eka Nobel, Sweden).

The motivation of this test consisted in the feasibility of such a purification process with the new Module-0 version, set up at the Borexino site during the years before. It should especially be checked whether and what kind of contamination the Module-0 plant and the silica gel column introduced into the CTF scintillator. For this purpose, the loop purification mode was chosen, as it allowed continuous CTF data taking during the purification process and thus would immediately have monitored certain problems in order to identify their cause. The activity of  $^{222}\text{Rn}$  – possibly introduced by leaks etc. – constituted an important measure in this context. The purification factor was however expected to remain comparatively small ( $\approx 4$ ) and only constituted a rough check of the free enthalpy and its transferability to large scales.

Prior to the test, a blank loop, i.e. a CTF scintillator loop excluding the silica gel column and only circulating through the Inner Vessel and stainless steel tubes (total length  $\approx 50\text{m}$ ) was accomplished in order to check whether the tubes planned to be used during the test would already have introduced unexpected contamination. This was not the case. One day after, the purification loop with the silica gel column was initialised. It ran continuously and was turned off 5.26 days later. 23820 kg of scintillator, i.e. 6.2 CTF volume cycles, were processed through the silica gel column with an average flow rate of 189 kg/h. Afterwards, the scintillator remained untouched for a month because of data taking.

#### *Data Analysis Methods*

The CTF data analysis was mainly performed by a group of the Università degli Studi di Milano. During the silica gel loop test, the CTF raw data, divided into so-called *runs*, allowed every 12 or 24 hours, with the initialisation of a new run, to analyse the previous one. This off-line analysis of the CTF falls back on energetic cuts, spatial cuts, pulse shape cuts and time coincidences. The coincidence method is, if applicable, the most effective and accurate one. Looking on pairs of events in comparatively short time windows regarding the detector

count rate ( $\sim 1\text{Bq}$  or smaller), mainly three types of scintillator contaminations can be tagged due to their decay signatures: the  $^{214}\text{Bi};^{214}\text{Po}$  coincidence in the  $^{238}\text{U}$  chain, the  $^{212}\text{Bi};^{212}\text{Po}$  coincidence in the  $^{232}\text{Th}$  chain and the  $^{85}\text{Kr}$  activity. The coincidence characteristics are summarised in Table 4.32.

		Window	Acceptance	Decay information
$^{238}\text{U}$ chain	1 <sup>st</sup> event	$\leq 3.3$ MeV	$\sim 100\%$	$\beta$ of $^{214}\text{Bi}$ ( $< 3.23\text{MeV}$ )
	2 <sup>nd</sup> event	540–950 keV	$> 99\%$	$\alpha$ of $^{214}\text{Po}$ (7.67MeV)
		3–710 $\mu\text{s}$	$\approx 95\%$	$t_{1/2} = 164 \mu\text{s}$
$^{232}\text{Th}$ chain	1 <sup>st</sup> event	0.30–2.49 MeV	87%	$\beta$ of $^{212}\text{Bi}$ ( $< 2.25\text{MeV}$ , 64%)
	2 <sup>nd</sup> event	0.75–1.05 MeV	95%	$\alpha$ of $^{212}\text{Po}$ (8.8MeV)
		$< 2 \mu\text{s}$	88%	$t_{1/2} = 0.433 \mu\text{s}$
$^{85}\text{Kr}$	1 <sup>st</sup> event	$< 241$ keV	61%	$\beta$ of $^{85}\text{Kr}$ ( $< 173\text{keV}$ , 0.4%)
	2 <sup>nd</sup> event	300–600 keV	83%	$\gamma$ of $^{85}\text{Rb}^*$ (514keV)
		$< 6 \mu\text{s}$	95%	$t_{1/2} = 1.46 \mu\text{s}$

Table 4.32: Observed coincidences and windows of the applied data analysis cuts at the beginning of the CTF3 campaign. The windows are illustrated in Diagram 4.33. The acceptance shows the activity percentage the according cut covers. The energy calibration is at  $\approx 386$  photoelectrons per MeV.

Diagram 4.33 shows the application of these cuts on the CTF scintillator during and after the silica gel loop test. The lower window (green) illustrates the  $^{85}\text{Kr}$  cut, the upper one (red) the  $^{212}\text{BiPo}$  events and the one in the middle (blue) the  $^{214}\text{BiPo}$ 's. In particular, the  $^{214}\text{BiPo}$  event window, overlapping the other two windows, gets properly distinguished by different coincidence times. In the diagram, the time is integrated. Except for radon generated contamination, the statistics normally requires a period of some weeks of data taking in order to deduce accurate activities with the described cuts.

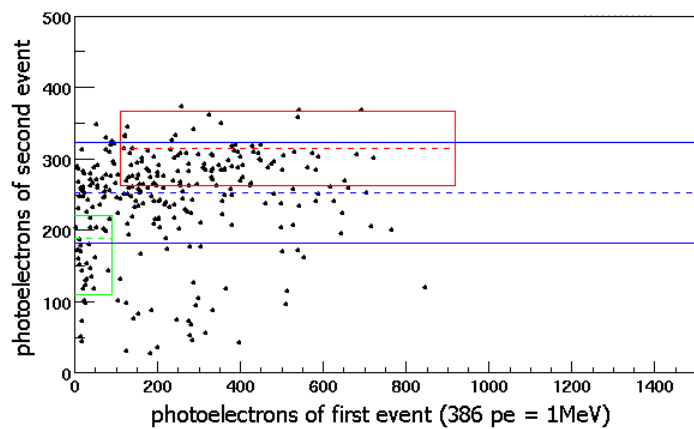


Diagram 4.33: Coincident events in 76.2 days after the silica gel loop test with CTF3 [Mil04].

### Rn contamination

As the isotopes in the U and Th chain below radon are short lived, possible  $^{222}\text{Rn}$  or  $^{220}\text{Rn}$  contaminations are well recognisable by the  $^{214}\text{BiPo}$  respectively the  $^{212}\text{BiPo}$  coincidence (see Figure 2.6). Due to their abundance, especially  $^{214}\text{BiPo}$  coincidences allowed to quickly analyse every single data run. The Figures 4.34 and 4.35 show the changes in the  $^{222}\text{Rn}$  and  $^{220}\text{Rn}$  activities, tagged by the corresponding coincidences, during the silica gel loop test and the preceding blank test. The data points illustrate activities with their statistic and systematic uncertainties during one or several runs; the run numbers are specified near the points. The width of the points corresponds to the data taking time. The two curves give possible

explanations of the data. Except for the part approaching the  $^{222}\text{Rn}$  emanation equilibrium of the silica gel column (Figure 4.34, runs 2094-2102), they are not fits, but decay or equilibration curves with fixed half lives, whose start or end points derive from the data points. The half-lives are 3.8 days in case of the  $^{222}\text{Rn}$  activity and 10.6 hours in case of the activity introduced by  $^{220}\text{Rn}$ , as this activity is shortly maintained by  $^{212}\text{Pb}$ , the most long-lived nuclei between  $^{220}\text{Rn}$  and  $^{212}\text{Bi}$ .

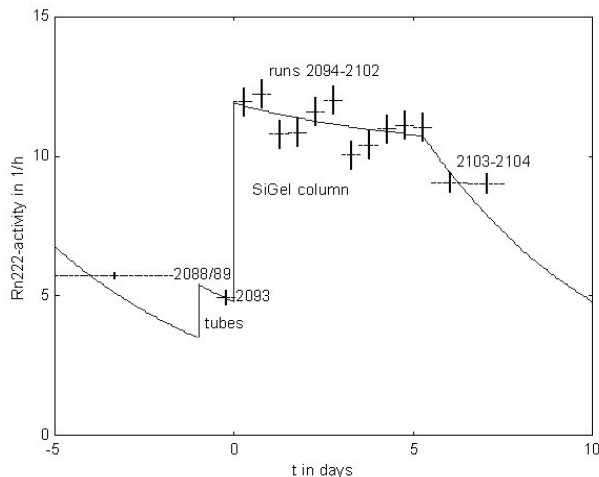


Figure 4.34:  $^{222}\text{Rn}$  activity during the silica gel loop test in CTF3 [Mon02]. The curve explains the data points in the following way: Prior to the test, the present  $^{222}\text{Rn}$  decays with  $t_{1/2}=3.8\text{d}$ . The blank loop causes an instant activity increase in the CTF, as the  $^{222}\text{Rn}$  emanated from the pipes gets introduced. Then, this  $^{222}\text{Rn}$  starts to decay. At the beginning of the purification, the  $^{222}\text{Rn}$  activity emanated by the silica gel column gets instantly introduced. Then, it starts to approach the emanation equilibrium. After the end of the test, the introduced  $^{222}\text{Rn}$  decays.

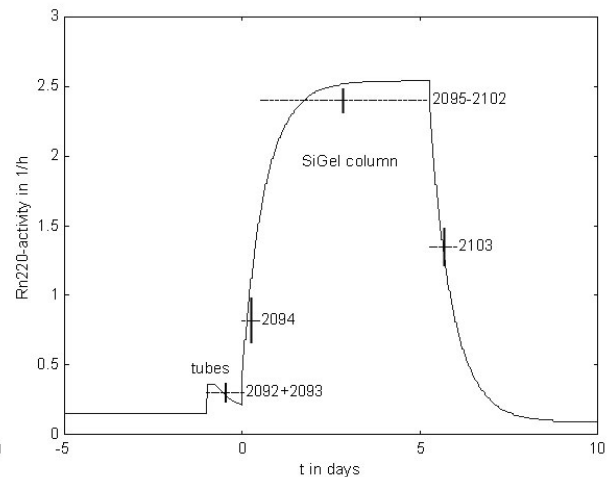


Figure 4.35:  $^{220}\text{Rn}$  activity at the silica gel loop test in CTF3 [Dan02]. The curve explains the data points in the following way: Prior to the test, the present Th daughter activity dominates the rate. The blank loop causes an instant activity increase in the CTF, as the emanated  $^{220}\text{Rn}$  of the pipes gets introduced. This activity decays with the  $^{212}\text{Pb}$  half-life. From the beginning of the purification on, the  $^{220}\text{Rn}$  activity emanated by the silica gel exits the column, gets introduced into the CTF and builds up the according daughter activity of  $^{212}\text{Pb}$ . After the end of the test, the introduced  $^{212}\text{Pb}$  decays.

The introduced amount of  $^{222}\text{Rn}$  was in the expected order of magnitude. The two instant increases lead to a determination of the emanation rates of the stainless steel pipes respectively the purification column filled with 2.4 kg of silica gel. Prior to the test, in the course of some time, these parts of the loop had emanated  $^{222}\text{Rn}$  into the liquid scintillator inside, so that the activities introduced into the CTF detector yielded the  $^{222}\text{Rn}$  emanation rates. In case of the pipes – a loop of ~50m between Module-0 and the CTF – the emanation rate amounts to  $0.9\pm 0.3$  mBq and in the case of the column to  $1.9\pm 0.3$  mBq, like already specified in Table 3.6.

The  $^{220}\text{Rn}$  emanation of the column can be quantified in a similar way, referring to the respective  $^{212}\text{BiPo}$  equilibrium built up during the five days of the test. It yields an emanation rate of  $60\pm 8$  counts/day. However, this activity is completely harmless as decaying with a half-life of 10.6 hours.

As the behaviour of the radon rates can be fully understood, the silica gel column plant in Module-0 is working properly from a technical point of view. No leaks appeared and no unexpected activity was introduced. The purification effects are specified in the following.

### <sup>232</sup>Th daughters purification

The coincidence of <sup>212</sup>BiPo, the appropriate signature to identify decays in the <sup>232</sup>Th chain according to the above paragraph, belongs to the lower part of it. Due to the short half-lives of the adjacent nuclei – even the gaseous <sup>220</sup>Rn can hardly escape in  $t_{1/2}=56\text{s}$  – the chain should be equilibrated at least until <sup>228</sup>Th ( $t_{1/2}=1.9\text{a}$ ), possibly until the original isotope <sup>232</sup>Th. The decrease of the <sup>212</sup>BiPo activity during the silica gel loop test is quantified in Table 4.36.

<sup>232</sup> Th equivalent	no radial cut	r<0.7m	r<0.5m
before [g/g]	$(5.2\pm 0.7)10^{-15}$	$(5.5\pm 1.2)10^{-15}$	$(6.8\pm 2.3)10^{-15}$
after [g/g]	$(2.3\pm 0.5)10^{-15}$	$(2.1\pm 0.8)10^{-15}$	$(1.4\pm 1.1)10^{-15}$

Table 4.36: Purification effect of the silica gel loop test in CTF3 on <sup>232</sup>Th daughters [Mil04]. The measured <sup>212</sup>BiPo activities correspond to the <sup>232</sup>Th concentrations in the table. A radial cut tries to account for surface or bulk contamination of the Inner Vessel. The radius of the CTF Inner Vessel is 1m, the spatial resolution in CTF3 was ~15cm.

The values for the different radial cuts agree all with the errors. The motivation for this analysis method however consists in a suspected surface contamination of the nylon Inner Vessel, which would be difficult – or in case of a bulk contamination even impossible – to reduce. A better activity reduction at higher distances from the vessel is slightly indicated and was later confirmed after further purification tests (compare 4.3.2, 6.3.2). The purification factor probably is in the range between 2 and 3, possibly even a little higher, and indicates the same qualitative behaviour as for the other heavy metal impurities.

### <sup>238</sup>U daughters purification

The <sup>214</sup>BiPo coincidence belongs to the <sup>238</sup>U chain. The equilibrium in this chain is broken at <sup>222</sup>Rn – able to move around during the half-life of 3.8 days – and a second time at <sup>210</sup>Pb ( $t_{1/2}=22\text{a}$ ). The problem of <sup>210</sup>Pb and its daughters, abundantly considered during this thesis, will afterwards be treated by the <sup>210</sup>Po analysis. The <sup>222</sup>Rn activity can however be observed by its decay, leading to a “decay” of the <sup>214</sup>BiPo coincidences as well. After a certain time, the observation of a constant <sup>214</sup>BiPo activity component leads to a determination of the contamination part that is due to the <sup>226</sup>Ra ( $t_{1/2}=1600\text{a}$ ), or even to further nuclei in the chain. This contamination, expressed in equivalent concentrations of <sup>238</sup>U, was reduced from  $(1.40\pm 0.34)10^{-15}$  g/g to  $(7.6\pm 1.7)10^{-16}$  g/g [Mil04]. A surface activity on the nylon vessel was not observed. The purification factor of ~2 agrees with the behaviour of other heavy metals impurities.

### <sup>85</sup>Kr activity

As Kr is a noble gas, a purification effect with silica gel is not expected. Due to its presence in the air, however, fresh silica gel contains <sup>85</sup>Kr in its air volume. In this context, the silica gel loop test increased the <sup>85</sup>Kr activity in the CTF from  $380\pm 160$  to  $750\pm 180$  counts/day [Mil04]. The analysis was performed with a radial cut at r<0.7m. <sup>85</sup>Kr can effectively be reduced by nitrogen extraction. Also, an abundant purging of the silica gel column with ultra-pure nitrogen prior to the purification avoids the contamination as shown in 4.3.2.

## $^{210}\text{Po}$ purification

As mentioned above, due to the long half-life of  $^{210}\text{Pb}$ , the activities of  $^{210}\text{Bi}$  and  $^{210}\text{Po}$  do not necessarily correspond to the  $^{214}\text{BiPo}$  activity. As no coincidence can be applied here, the analysis, among other things, takes advantage of the energy spectra and the pulse shape analysis. In particular, the data points in the Diagrams 4.38, 4.40 were obtained with a radial cut at  $r < 80\text{cm}$ , an energy cut on the window of the quenched  $^{210}\text{Po}$   $\alpha$  decay from 260 to 600 keV, a subtraction of undistinguishable radon related  $\alpha$  events, and a final  $\alpha$ - $\beta$ -discrimination. In particular, the subtraction accounts for the quenched  $\alpha$  decays of  $^{222}\text{Rn}$  (5.5 MeV) and  $^{218}\text{Po}$  (6.0 MeV), determined via the  $^{214}\text{BiPo}$  coincidence and undistinguishable from the  $^{210}\text{Po}$  decay (5.3 MeV) within the energy resolution of the photomultipliers.

The resulting  $^{210}\text{Po}$  count rate allows a single run analysis, however with comparatively large uncertainties (see Figure 4.38). The latter make it difficult to quantitatively analyse the development of the activity during the purification and to attribute a special behaviour. The model curve in Figure 4.37 has been simulated with the help of the theoretical considerations in 4.1.3, the test parameters and the experimental value for the free enthalpy of Po (Table 4.24). In particular, the used parameters are: silica gel height 0.118m, silica gel area 0.51m<sup>2</sup>, silica gel density 0.4g/cm<sup>3</sup>, CTF scintillator volume 4.33m<sup>3</sup>, scintillator flow 0.06 litres/s, scintillator density 0.885g/cm<sup>3</sup>, temperature 287K, free adsorption enthalpy -21900 J/mol, equilibrium time 5s.

The equilibrium time, the only parameter missing a quantitative determination, does not significantly change the curve, unless it gets varied in an unreasonable way.

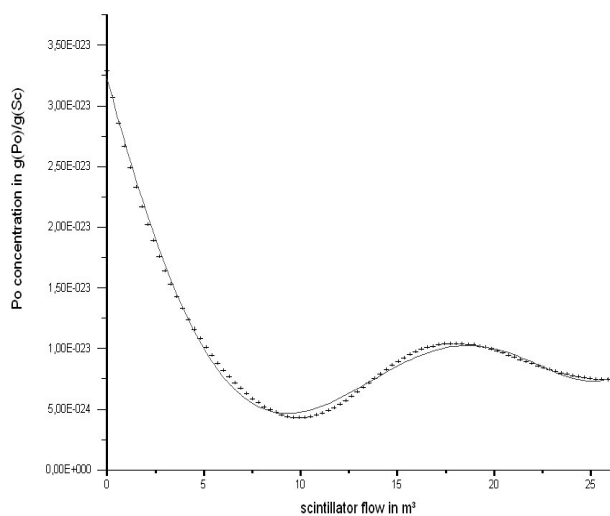


Figure 4.37: Simulation of the expected activity progression for the CTF silica gel loop test. The curve is a polynomial fit of 5<sup>th</sup> order to the simulated points.

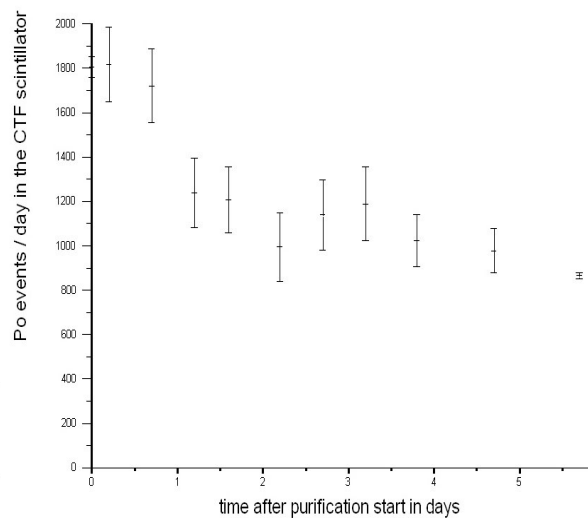


Figure 4.38:  $^{210}\text{Po}$  activity during the silica gel loop test [Mon05]. The x-axis dimension agrees with the one in the plot besides, as 5.26 d correspond to 26.9 m<sup>3</sup>.

Despite of the large data uncertainties, no reasonable parameter variation leads to an agreement of the curve in 4.37 with the data points in 4.38. Especially, the bigger purification factor in Figure 4.37 ( $\approx 4$  instead of  $\approx 2$ ) is impossible to correct within the parameter uncertainties; and even trying to vary in a wider range, the initial activity decrease would be shifted too close to the purification start and strongly disagree with the first data points.

The particular attempt of adding an extraneous activity reservoir to the loop – simulating some type of recontamination source – can partially improve the fit. With respect

to previous contacts between the CTF liquid handling system and higher contaminated scintillator samples, this would even be realistic; a possible result was presented in [Nie03]. The parameters used to generate such improved model curves however contradict to recent surface adsorption measurements on stainless steel, partially performed in the context of this thesis (compare 5.2.2 and [Leu04]).

Another idea can be derived from the fact that the data points during the purification test indeed do not explicitly sustain a breakthrough of the silica gel column. The slight, visible activity oscillation remains within the uncertainty range, and further, the last point in Figure 4.38, the first value after the test, especially well settled due to the longer, subsequent data taking period, clearly shows a lower activity than all previous points. Compared to the model, this indicates that no breakthrough has occurred during the test. As the test parameters however imply a breakthrough after  $\sim 10\text{m}^3$  of scintillator flow (see 4.37), the consideration of this presumption requires some modification of the model. In particular, the effect of a bad mixing between purified and unpurified scintillator in the CTF Inner Vessel is able to motivate such a modification

in the following way. Purified scintillator flows from the top into the spherical nylon vessel, and mainly along the central axis it replaces the scintillator exiting the vessel at the bottom. In this situation, a hydrodynamic flow pattern can form, where a big part of the purified scintillator entering the vessel crosses the same quite quickly and exits again, whereby the adjacent scintillator beside the central axis of the sphere remains more or less unmoved. Figure 4.39 shows the simulated flow pattern with the according parameters. In particular, the low flow velocity in the outer regions of the sphere would cause the discussed behaviour. In this way, several volume cycles would be necessary to perform one effective volume cycle, whereby all scintillator molecules in the nylon vessel cross the silica gel at least once. The effect expands the model curve to larger scintillator volumes. Diagram 4.40 shows a fit of the curve of Diagram 4.37, expanded by a free factor, to the CTF data points.

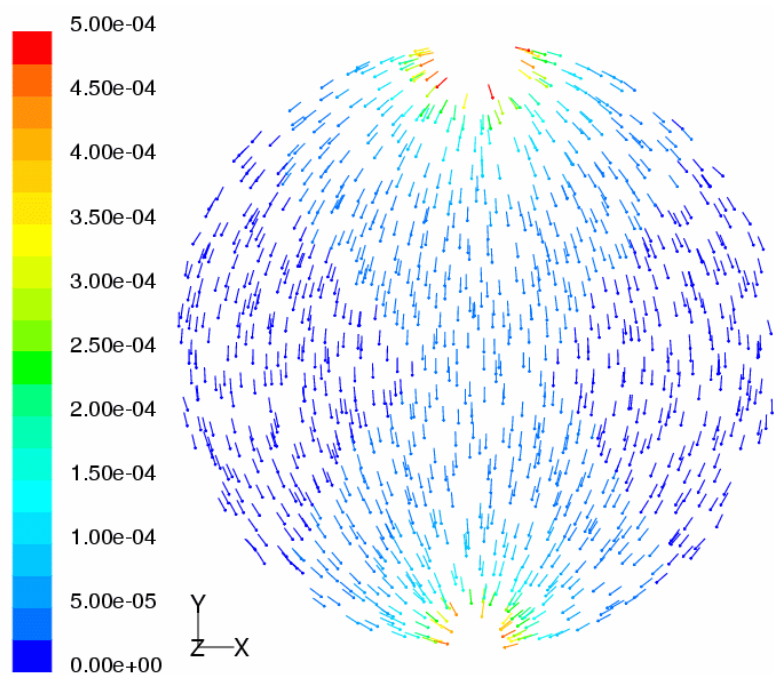


*Figure 4.39: Hydrodynamically simulated flow pattern with the CTF Inner Vessel geometry at an integral flow rate of 190 kg/h [Leu02]. The flow velocity vectors are coloured by the velocity magnitude [m/s].*

The effect expands the model curve to larger scintillator volumes. Diagram 4.40 shows a fit of the curve of Diagram 4.37, expanded by a free factor, to the CTF data points.

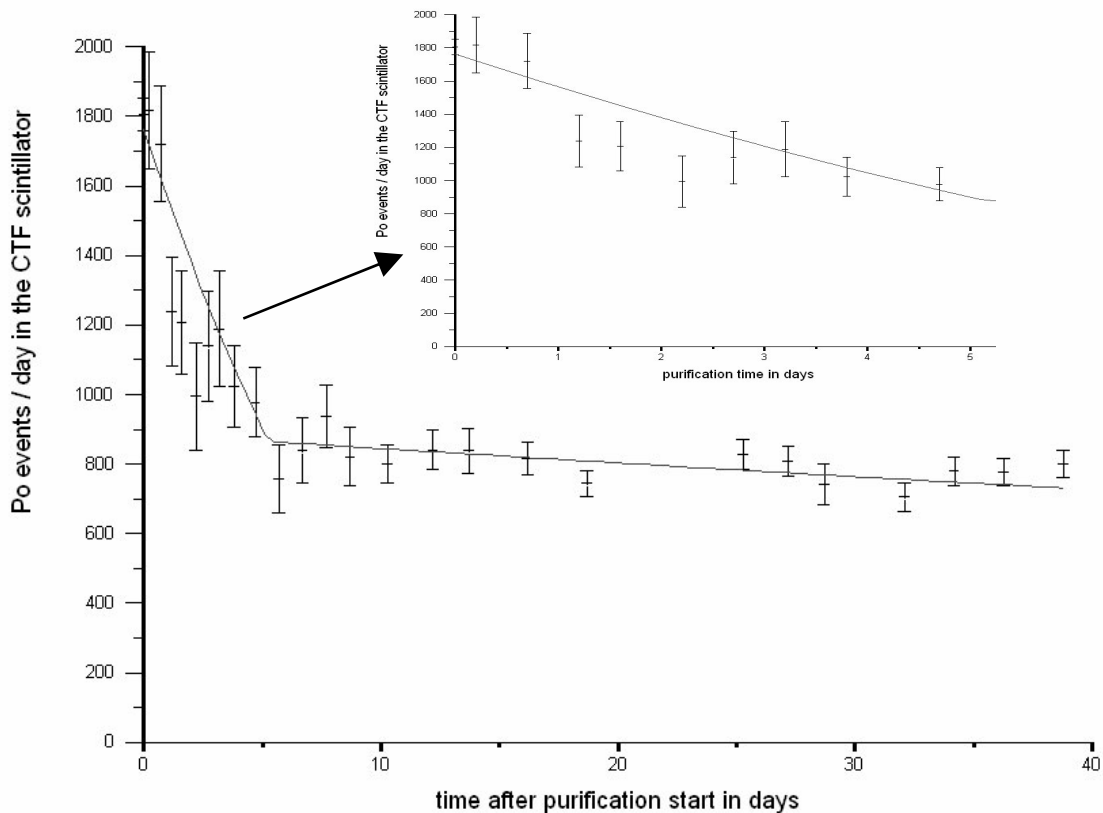


*Diagram 4.40: Fit of the CTF data points with a model curve under the assumption of bad mixing between purified and unpurified scintillator. The period after the crack corresponds to a decay of  $^{210}\text{Po}$ , fitted with help of the according half life (138d). The zoom shows the period of purification.*

Only a small initial part of the model curve gets applied on the data set. The expansion factor amounts to  $8.3 \pm 0.3$ , corresponding to the number of cycles necessary to complete one effective cycle. With each cycle, only  $\approx 12\%$  of liquid scintillator would be exchanged.

This scenario is possible but can hardly be confirmed. Even the application of hydrodynamic models is difficult, as microscopic imperfections in flow patterns can lead to macroscopic changes, due to the chaotic behaviour. Figure 4.39, difficult to interpret quantitatively because of the missing third dimension and the big velocity enhancement at the poles, indicates velocity differences of an order of magnitude at the equatorial level.

Nevertheless, the  $^{210}\text{Po}$  data deviate from the model only by a factor of 2 or less; and the purification factor ( $\approx 2$ ) of  $^{210}\text{Po}$  agrees with the factors for other heavy metal impurities considered above.

#### $^{210}\text{Bi}$ purification

As mentioned above, the  $^{210}\text{Po}$  contamination after spatial and energetic cuts gets identified by the pulse shape discrimination. This method also serves to determine the  $\beta$ -like activity part, where the  $^{210}\text{Bi}$  activity arises from after the subtraction of  $^{85}\text{Kr}$  related events. However, due to the big uncertainty in the  $^{85}\text{Kr}$  activity, the reduction of  $^{210}\text{Bi}$  during the silica gel loop test cannot be accurately determined. An unexpected activity increase nevertheless is excluded.

### 4.3.2. CTF3 Batch Purification Test

Due to its high expected purification factor (see 4.1.4), the batch purification mode is supposed to be applied on the liquid scintillator of the Borexino detector. The silica gel batch test in the CTF3 campaign should have consisted in a test of this process, scaled down to the CTF volume, like already explained at the beginning of 4.3.

In the context of this test, the CTF liquid scintillator ( $\approx 3700$  kg) was unloaded – that means replaced by deionised water – into the Module-0 tank EPS. From there, two batches of about 900 kg were purified at a flow of  $\approx 200$  kg/h into the tanks BTE and BTW, using the cylindrical silica gel column COL3 in Module-0, loaded with 2.4 kg of ultra-pure silica gel. This silica gel had been taken from the same delivery batch as the silica gel for the CTF3 loop test. After the purification of these first two tons of scintillator, the purified amount was bubbled with high-purity nitrogen for  $\sim 1$  day ( $N_2$  flow  $\sim 200$  l/min) and again loaded into the CTF Inner Vessel, temporarily leaving it in a status of half water and half scintillator. Subsequently, the remaining two tons of scintillator were purified from the tank EPS via the same silica gel into the emptied tanks BTE and BTW, bubbled with nitrogen and afterwards loaded into the CTF. So, the CTF resulted completely refilled and restarted data taking. Detailed procedures of respective liquid handling processes in general can be found in Appendix C. The following table summarises the effects on the liquid scintillator.

	Contamination before the test	Contamination after the test
$^{222}\text{Rn}$ [counts/d]	$\sim 60$	$\sim 30$
$^{232}\text{Th}$ daughters [g/g]	$(1.4 \pm 1.0) 10^{-15}$ <sup>3)</sup>	$(6.8 \pm 2.0) 10^{-16}$ <sup>3)</sup>
$^{238}\text{U}$ daughters [g/g]	$(5.60 \pm 1.46) 10^{-16}$ <sup>1)</sup>	$(5.75 \pm 0.29) 10^{-16}$ <sup>4)</sup>
$^{85}\text{Kr}$ [counts/d]	$73 \pm 73$ <sup>3)</sup>	$30 \pm 10$ <sup>3) 4)</sup>
$^{210}\text{Po}$ [counts/d]	$380 \pm 70$ <sup>2)</sup>	$980 \pm 30$ <sup>2)</sup>
$^{210}\text{Bi}$ [counts/d]	$< 120$ <sup>2)</sup>	$10 \pm 10$ <sup>2) 4)</sup>

Table 4.41: Effects of the silica gel batch test during the CTF3 campaign on the scintillator [Mil04]. The data analysis methods are described in 4.3.1.

<sup>1)</sup> Activity between the 1<sup>st</sup> and 2<sup>nd</sup> water extraction phase

<sup>2)</sup> A radial cut at  $r < 75$  cm was applied.

<sup>3)</sup> A radial cut at  $r < 70$  cm was applied.

<sup>4)</sup> Long-term measurement with  $\sim 1$  year of data taking

In most cases, the missing precision in the activities before the test makes a significant statement impossible. The decrease of the  $^{222}\text{Rn}$  activity proves an accurate accomplishment of the test, at least from a technical point of view.

The significant increase of the  $\alpha$  activity to  $\sim 1000$  counts/day however constitutes a problem, as the particular goal of the test had consisted in the reduction of  $^{210}\text{Po}$  by some factor around 10 or bigger. After the test this  $\alpha$  activity decreased to  $\sim 300$  counts/day with a “half-life” of  $\sim 40$  days which could not be attributed to any other isotope in a reasonable way. Since then, the remaining  $\alpha$  activity has decayed with the half-life of  $^{210}\text{Po}$  (138 d) and up to now has reached an order of  $\sim 10$  counts/day, comparable to the level of the constant  $^{210}\text{Bi}$  activity.

Activity decreases in CTF3 with unexplainable half-lives of comparable order were already observed during other short periods. This can be seen on the development of the internal activity before or between the CTF3 purification tests (Diagram 2.10). Such an effect can be caused by a condensation of heavy metal contaminants on microscopic water droplets,

diffusing from the shielding volume through the nylon vessel and sinking downwards. Some water would accumulate at the bottom of the Inner Vessel and make the activity of dissolved impurities disappear. In this way, strange  $\alpha$  activity half-lives do not necessarily imply the presence of a different, mysterious isotope.

One possible explanation of the activity increase consists in a recontamination of the purified scintillator by the used tanks (BTW, BTE) or stainless steel pipes. These components were partially flushed with purified scintillator prior to the test but they have been in contact with higher contaminated raw scintillator before. However, the order of the recontamination is comparatively high and surface adsorption experiments with stainless steel exclude effects in this order. In paragraph 5.2.2, the  $^{210}\text{Po}$  release from a contaminated stainless steel surface into pure scintillator amounts to  $(0.21 \pm 0.04)\%$ , and after a flushing with pure scintillator even to less than 0.033%, with respect to the scintillator activity that had contaminated the steel surface. As the surface to volume ratios of the Module-0 tanks and the experimental dimensions in 5.2.2 are of the same order, the additional  $\sim 500$  counts/day of  $^{210}\text{Po}$  would have had to be caused by a raw scintillator activity of  $>200000$  counts/day but the highest observed  $\alpha$  activity in CTF3 scintillators was at  $\sim 6000$  counts/day only.

Another possible explanation could consist in silica gel grains having leaked through the filters into the Inner Vessel, even if the grain size of  $10\mu\text{m}$  is clearly bigger than the filter pore size ( $0.05\mu\text{m}$ ). In the nylon vessel, the grains should quickly accumulate at the bottom, the  $\alpha$  activity however was observed to be homogeneously distributed after the test.

A further contamination possibility would arise from an intrinsic contamination in the silica gel. Assuming a general equilibrium of the CTF3 scintillator with the  $^{210}\text{Po}$  concentration in the silica gel, the  $^{210}\text{Po}$  activity after the CTF3 batch test would imply, according to 4.1.1 and using the enthalpy value of Table 4.24, a  $^{210}\text{Po}$  concentration in the silica gel at  $\approx 3.9 \cdot 10^{-20}$  g/g. This is by a factor of  $\approx 50$  bigger than the concentration that can be reached by the decay of the intrinsic  $^{226}\text{Ra}$  contamination in the silica gel as specified in Table 4.29. This means that the intrinsic  $^{210}\text{Po}$  contamination, in order to be able to account for the CTF3 batch test failure, would have to be due to  $^{222}\text{Rn}$  contamination of the silica gel surface by air contact. However, this  $^{210}\text{Po}$  on the silica gel surface, generated by  $^{222}\text{Rn}$ , would imply a surface contamination by  $^{210}\text{Pb}$  at the same activity level. As Pb has got a smaller free enthalpy value than Po (Table 4.24), the CTF3 scintillator should even have been contaminated more by  $^{210}\text{Pb}$  than by  $^{210}\text{Po}$ . This  $^{210}\text{Pb}$  would have generated  $^{210}\text{Bi}$  with a time constant of 5 days, which should be visible in the CTF, in particular with more than the above  $980 \pm 30$  counts/day; but since the batch test, one has never observed a  $\beta$  activity of that extent.

On the contrary, the observed  $\beta$  activity yields a new best limit for the intrinsic contamination of the silica gel. Table 4.41 quantifies the  $^{210}\text{Bi}$  activity – hence the  $^{210}\text{Pb}$  activity – to be smaller than 20 counts/day, corresponding to a concentration limit in the scintillator of  $< 2.2 \cdot 10^{-23}$  g/g. The free enthalpy of Pb in Table 4.24 together with the scintillator temperature of 287K determines the upper limit of the equilibrium constant to  $k_{\text{Pb}} < 6500$  ( $1\sigma$ ). This yields the limit for an intrinsic  $^{210}\text{Pb}$  contamination of silica gel in Table 4.42. The values  $^{210}\text{Bi}$  and  $^{210}\text{Po}$  arise from a decay equilibrium in the silica gel, assumed during the whole consideration. The values in the second row are based on the first values, assuming an adsorption equilibrium between the impurity concentrations in silica gel and in liquid scintillator. They tell to which level the heavy metal contaminations at least can be reduced.

	$^{210}\text{Po}$	$^{210}\text{Bi}$	$^{210}\text{Pb}$
concentrations in silica gel [g/g(SiGel)]	$< 5.3 \cdot 10^{-22}$	$< 1.9 \cdot 10^{-23}$	$< 3.1 \cdot 10^{-20}$
concentrations in purified pseudocumene [g/g(PC)]	$< 2.9 \cdot 10^{-25}$	$< 1.4 \cdot 10^{-26}$	$< 2.2 \cdot 10^{-23}$

*Table 4.42: Upper limits ( $1\sigma$ ) for intrinsic contamination in pure silica gel, arising from the  $^{210}\text{Pb}$  activity reached in the scintillator after the silica gel batch test in CTF3. The consideration assumes a decay equilibrium in the silica gel.*

The value for  $^{210}\text{Pb}$  especially constitutes the starting point of these calculations based on the CTF data. As these limits are by factors of 1.5–2 below the values derived from the intrinsic  $^{226}\text{Ra}$  contamination (Table 4.29), the  $^{226}\text{Ra}$  values really seem to be applicable in this context. In particular, a possible  $^{210}\text{Pb}$  contamination of silica gel arising from air contact does not dominate, although the  $^{222}\text{Rn}$  concentration in air is comparatively high ( $\sim 30\text{Bq/m}^3$ ) and the used silica gel was not packed radon-tight for more than a year.

Apart from the last considerations, the  $\alpha$  contamination in the CTF detector after the silica gel batch test finally remains unexplained. The necessity of a laboratory batch test (4.2.4) arose in this context.

#### 4.4. Conclusion

At the beginning of this chapter, a theoretic model for surface adsorption processes in silica gel chromatography columns, developed in the course of the past years, has been presented. The described experiments have tried to evaluate the validity of this model and to explore its limitations.

The measurement of the free enthalpies (Table 4.24) shows first of all that silica gel is capable to reduce Pb impurities with an efficiency comparable to Po and Bi. This is particularly important, as the isotope  $^{210}\text{Pb}$ , if not extracted, would regenerate  $^{210}\text{Bi}$  and  $^{210}\text{Po}$ . The enthalpies for Bi and Po result in the same order as former values, small deviations can be explained by different experimental procedures. In this context, the accuracy of the free enthalpy values has been improved. The agreement with former measurements, whereby similar enthalpies were reached with different experimental parameters and purification factors, confirms the applicability of the described adsorption equilibrium model (4.1.1).

The revelation among the described works consists in the success of the silica gel batch purification test on small scales. Theoretical considerations, already having predicted the batch purification as the most efficient mode (4.1.4), have been confirmed qualitatively by the reduction of a  $^{210}\text{Po}$  activity by a factor bigger than 350 on a  $3\sigma$  level (Table 4.26) with a particularly small amount of silica gel,  $\frac{1}{1200}$  the mass of the purified scintillator. A further comparison with Table 4.30 shows similar purification effects reached with 3g of silica gel after three equilibrium steps in contrast to the small amount of 0.16g of silica gel used in the batch mode. Among other things, these results reject presumptions that the failed  $^{210}\text{Po}$  purification in the CTF3 silica gel batch test could have indicated a wrong batch mode model.

In comparison, two silica gel samples from the company ‘Selecto’ with a specific surface of  $\sim 500\text{m}^2/\text{g}$  and grain sizes between 32–63 $\mu\text{m}$  and 100–200 $\mu\text{m}$ , both having lead to comparable purification efficiencies, were examined at the University of Alabama in the context of the KamLand experiment [Kee04a], [Kee04b]. Tests of the loop purification and the batch purification mode with  $^{212}\text{Pb}$  loaded scintillator lead to reduction factors of 5–7 respectively 23–30 with 10g of silica gel and  $\sim 250\text{ml}$  of liquid scintillator in total purification

times of 30 min or longer. These effects are significantly worse than the factors calculated with the model of 4.1, yielding already an equilibration factor of 96 in the loop mode, using  $T=295\text{K}$  and  $G=-20.57\text{kJ/mol}$ . The batch test particularly was accomplished with a scintillator to silica gel mass ratio of only  $\approx 25$  (compared to 1200) and reached a lower efficiency by more than one order of magnitude compared to the batch test described in 4.2.4.

With a look on the Borexino liquid scintillator ( $330\text{m}^3$ ) and the silica gel chromatography plant in Module-0, the batch purification model implies, that under conservative assumptions 120kg of silica gel – four times the volume of a Module-0 column – are required to reduce the  $^{210}\text{Pb}$  concentration of the current CTF scintillator ( $<2.2 \cdot 10^{-23} \text{ g/g}$ ) by a factor of 12. In the corresponding simulation, the conservative values  $\Delta G_{\text{Pb}}=-20.2 \text{ kJ/mol}$  and  $\tau=50\text{s}$  ( $\rightarrow 49$  segments), the technical parameters  $T=287\text{K}$  and  $\Phi=95 \text{ kg/h}$  (per column), and the geometric column dimensions (see COL1, COL2 in 3.1.1) were used. A fifth column volume, that means 150kg of silica gel in total, would yield a purification factor of 99, whereby a variation of the equilibrium constant  $\tau$  to 5s would change the two mentioned factors to 18 respectively to  $5.7 \cdot 10^5$ . According to Diagram 2.12, a reduction of  $\sim 10$  would already allow the determination of the solar  $^7\text{Be}$  neutrino rate. The desired  $^{210}\text{Pb}$  concentration in the scintillator ( $2.2 \cdot 10^{-24} \text{ g/g}$ ) however is by a factor of  $\sim 20$  below the corresponding limit arising from the intrinsic  $^{226}\text{Ra}$  contamination in silica gel,  $(4.6 \pm 1.8) \cdot 10^{-23} \text{ g/g}$  (see Table 4.29). As explained there, this can constitute a problem as the  $^{226}\text{Ra}$  contamination, decaying in the silica gel since more than three years, could already have produced too much  $^{210}\text{Pb}$ . However, only a part of the  $^{210}\text{Pb}$  atoms might have adsorbed on the silica gel surface, as the pores are small ( $60\text{\AA}$ ) and the recoil energy of the decays should catapult many decay products into the lattice, where they do not influence the adsorption equilibrium. In this context, a further  $^{210}\text{Pb}$  reduction by the Module-0 silica gel columns to the desired value is possible, but not assured. In any way, the silica gel purification – as a batch purification – has to be applied before or during the scintillator loading of Borexino, as an unloading of the Borexino detector due to big scintillator and shielding liquid volumes related to each other by buoyancy forces is excluded with respect to a reasonable time schedule.

The problems of the silica gel purification plant of Module-0 in the context of theoretical considerations have arisen from changed preconditions with respect to the projecting period three years ago. The columns were originally designed to purify  $^{210}\text{Po}$ , among other things because of a missing enthalpy determination for Pb at this time; and further, the restricting intrinsic silica gel contamination limits in Table 4.29 could only be determined with help of the already constructed purification columns.

However, as the purification behaviour of silica gel has sufficiently been understood in the context of this thesis, it allows a more accurate development of large scale silica gel chromatography systems in future experiments.

## 5. Adsorption on Surfaces

### 5.1. Motivation

Impurities do not only adsorb on silica gel, but on all surfaces. The adsorption effect on silica gel, described in the chapter before, is only that dominant because of the outstanding surface to volume ratio of silica gel. Conventional surfaces without pores, even if not able to purify effectively, can account for activity reductions by small factors  $\sim 2$ , in dependence on the surface to volume ratio. The problem, however, consists in the possibility that, after having adsorbed these impurities, they can partially be released into clean scintillator; and even if the released amount is only in the order of  $\sim 1\%$  of the original contamination, this recontamination prevents high reduction factors in purification plants.

The problem arises in the context of purification systems that need to handle purified and unpurified liquids in the same system parts. This chapter should determine the order of such recontamination effects. General experimental questions concerning presumable recontaminations in former tests (see 4.3) should be answered as well as their impact on future processes clarified. In particular, adsorption rates can influence the laboratory tests described in Chapter 4. The surface experiments were carried out on parts directly used there, so that the results give accurate information about the order of these influences.

A theoretic model will not be considered. The adsorption equilibrium and free enthalpy model of paragraph 4.1.1 could principally be applied here, the experiments however, partially even influenced by surfaces of more than one material, have not been designed for this purpose. In particular, the systematic uncertainties were difficult to quantify, as characteristics of shaking or filling processes might have had some influence on adsorption processes. They were estimated to 10%, as in one case two independent measurements of samples of the same origin roughly showed this variation.

The sizes of the adsorption surfaces and the liquid volumes will be specified, as the surface to volume ratio principally constitutes the accurate way to scale adsorption processes to other geometries.

### 5.2. Experiments

The following experiments were performed in the same laboratory with the same experimentation and detection set-up as the silica gel purification tests, described in 4.2. Loaded pseudocumene scintillator samples in small teflon boxes with glass windows were examined with a photomultiplier to their  $^{210}\text{Po}$ - $\alpha$  and  $^{210}\text{Bi}$ - $\beta$  activity respectively with a germanium detector to their  $^{210}\text{Pb}$ - $\gamma$  activity. Contaminated equipment was cleaned with acetone and diluted nitric acid.

#### 5.2.1. Adsorption on Teflon and Glass (combined)

Here, the inner side of the small teflon sample boxes themselves, together with the glass window, constituted the considered adsorption surface. It has been determined how much activity these containers adsorb from loaded scintillator and then release into clean scintillator. The contact area of teflon was  $98\text{cm}^2$ , of glass  $54\text{cm}^2$ , and the scintillator volume inside the box was  $31.7\text{cm}^3$  (28.0g). Table 5.1 shows procedures, related results and the implied percentages for the adsorbed and released activity parts. The adsorption derives from the ratio of the activity remained in the box after it had been emptied (second row) and the

initial activity (first row). The leach-off is determined by the ratio of the activity the scintillator took with it into a new box (third row) and the previous surface activity in the first box (second row).

Subsequent steps	A( <sup>210</sup> Po) ·eff. in PC [Bq]	A( <sup>210</sup> Bi) in PC [Bq]	A( <sup>210</sup> Pb) ·eff. in PC [Bq]
Loaded PC filled into clean teflon box (transfer via 50ml glass vessel)	3.71±0.31 <sup>1)</sup>	1.54±0.08 <sup>1)</sup>	(2.43±0.17)10 <sup>-2</sup> <sup>1)</sup>
2 days later: Box emptied from loaded PC and immediately refilled with clean PC	1.31±0.13 <sup>2)3)</sup>	0.76±0.08 <sup>2)</sup>	(1.27±0.14)10 <sup>-2</sup> <sup>2)</sup>
→ Adsorption:	(35±5)%	(49±6)%	(52±7)%
4 days later: PC transferred from this box to a new, clean box	0.168±0.017 <sup>2)</sup>	0.17±0.03 <sup>2)</sup>	(1.02±0.35)10 <sup>-3</sup> <sup>2)</sup>
→ Leach-off:	(12.8±1.8)%	(22±5)%	(8±3)%

*Table 5.1: Adsorption measurements on a combined teflon and glass surface. All activities refer to 28g of pseudocumene (PC). Background is subtracted. The <sup>210</sup>Pb activities contain a detection efficiency of ~1%, whereas the α efficiency arises from the discrimination by an energy and pulse shape cut. β's from <sup>210</sup>Bi were fitted between 600 and 800 keV. The uncertainties arise from a quadratic addition of the statistic error and the systematic error, whereby the latter is <sup>1)</sup> determined by two independent measurements <sup>2)</sup> estimated to 10%. The value at <sup>3)</sup> arises from the calculation 2·(0.74Bq−0.168Bq)+0.168Bq, as the measured α activity (0.74Bq) minus the α activity dissolved in PC (0.168Bq, see table) stays here all on the box surface, causing a detection efficiency of 50%.*

The adsorption and leach-off percentages of the three different heavy metals agree in their order. This is not surprising, as the free adsorption enthalpies, determined with silica gel in Table 4.24, and describing the same physical process, also show similar values. That gives a rough confirmation of the similar adsorption behaviour of Po, Bi and Pb in a general way.

With respect to the glass surface measurements in 5.2.3, a similar amount of activity adsorbs on teflon and glass, whereas the leach-off mostly seems to be due to the teflon surface.

As these measurements were carried out with the same sample boxes serving for all laboratory measurements of this thesis, they mainly helped to develop a feeling for contaminations and to test detection and analysis methods. The accuracy of the applied equipment cleaning procedures, using first acetone and then diluted nitric acid at 10% and 60°C in an ultrasonic bath for ~20min, was shown in this context.

## 5.2.2. Adsorption on Stainless Steel

In these tests, the adsorption and leach-off with a stainless steel part of ~50cm<sup>2</sup> surface – a ¾ inch VCR connector – were checked. The procedures and results are summarised in Table 5.2. The adsorption percentage is calculated by the difference between the values in the first two rows in ratio to the first row values. Both leach-off percentages refer here, in contrast to the normal definition, to the initial pseudocumene activities instead of the steel surface activities, as the latter, with a look on the adsorption percentages, could not be determined.

Subsequent steps	A( <sup>210</sup> Po) ·eff. in PC [Bq]	A( <sup>210</sup> Bi) in PC [Bq]	A( <sup>210</sup> Pb) ·eff. in PC [Bq]
Loaded PC filled into clean teflon box (transfer via 50ml glass vessel)	2.27±0.27	1.60±0.26	(2.32±0.24)10 <sup>-2</sup>
Steel part thrown into 28.2g of loaded PC and taken out after 20min	2.07±0.23	1.49±0.15	(2.55±0.30)10 <sup>-2</sup>
→ <i>Adsorption</i> :	(9±16)%	(7±19)%	(-10±17)%
Same steel part (now contaminated) in 28.6g of clean PC for 2 hours	(4.8±0.8)10 <sup>-3</sup>	< 0.04 (1σ)	(0.7±0.7)10 <sup>-4</sup>
→ <i>Leach-off</i> :	(0.21±0.04)%	< 3.0%	(0.3±0.3)%
Same steel part purged in 100g of clean PC, then in contact with 36.7g of new clean PC for 2 hours	< 6.5·10 <sup>-4</sup> (3σ)	< 0.04 (1σ)	no data
→ <i>Leach-off after purging</i> :	< 0.033%	< 3.0%	

Table 5.2: Adsorption measurements on a stainless steel surface. All activities refer to 28g of pseudocumene (PC). Background is subtracted. The <sup>210</sup>Pb activities contain a detection efficiency of ~1%, whereas the α efficiency arises from the discrimination by an energy and pulse shape cut. β's from <sup>210</sup>Bi were fitted between 600 and 800 keV. The uncertainties arise from a quadratic addition of the statistic error and a systematic error estimated to 10%.

With a look on the table, the systematic uncertainty does not allow a quantitative determination of the adsorption effect on stainless steel. The limits show, that stainless steel adsorbs significantly less than teflon and glass. The leach-off in the first step after the presumable contamination of the steel surface is even smaller.

Here, it was particularly examined whether this small, released activity could have been due to loaded scintillator adhered to the steel part, while that was taken out of the liquid: the steel part afterwards lost ~0.2g of weight while the adhered, loaded scintillator on its surface was drying, corresponding to ~0.7% of the initial amount. This is ~3 times higher compared to the leach-off percentages and can easily be responsible for them, assumed that pseudocumene evaporates and the heavy metal atoms stay slightly bound on the steel surface. The upper limit after the second leach-off, showing that purging with pseudocumene, at least for one time, is an effective possibility, could have taken away this slightly bound activity. Whether there exists a strongly bound part that was not released, could not be clarified.

On the other hand, measurements in [Leu04] show that a stainless steel surface of 32m<sup>2</sup>, having been exposed to 1 litre of contaminated pseudocumene for several months, releases (4.1±0.8)% of <sup>210</sup>Pb during a one-day soak in clean pseudocumene. Due to the different exposure times (20 min ↔ 5 months), a comparison with the test here is difficult but would imply an <sup>210</sup>Pb adsorption on stainless steel of (7±7)%, consistent with the according value (-10±17)% in Table 5.2.

As shown in 5.2.1 and Table 4.24, it can be observed, that the adsorption and leach-off behaviour of Po, Bi and Pb causes effects in the same order.

In any way, the leach-off effect from stainless steel into pseudocumene, examined in this paragraph, amounts to an order that is too low to attribute possible recontamination problems during the CTF3 silica gel tests to contaminated surfaces of stainless steel tubes and tanks. A quantitative estimation can be found in 4.3.2.

### 5.2.3. Adsorption on Glass

Here, the adsorption and leach-off on a Duran glass vessel with a volume of 50cm<sup>3</sup> were examined. 40cm<sup>3</sup> of liquid scintillator covered a glass surface of ~60cm<sup>2</sup>. The procedures and results are summarised in Table 5.3. The adsorption percentage is determined by the difference between the values in the first two rows in ratio to the first row values. The leach-off percentage refers to the surface activity, again the difference between the first two rows.

Subsequent steps	A( <sup>210</sup> Po) ·eff. in PC [Bq]	A( <sup>210</sup> Bi) in PC [Bq]	A( <sup>210</sup> Pb) ·eff. in PC [Bq]
Loaded PC	3.67±0.39 <sup>2)</sup>	3.95±0.40 <sup>2)</sup>	(4.25±0.47)10 <sup>-2</sup> <sup>2)</sup>
Loaded PC after contact (5 min) with a 50ml glass vessel	2.17±0.14 <sup>1)</sup>	1.54±0.08 <sup>1)</sup>	(2.43±0.17)10 <sup>-2</sup> <sup>1)</sup>
→ <i>Adsorption:</i>	(41±12)%	(61±12)%	(43±13)%
Clean PC in contact for 2h with the above glass vessel	(2.49±0.26)10 <sup>-2</sup> <sup>2)</sup>	< 2·10 <sup>-2</sup> (1σ)	(3.27±0.84)10 <sup>-4</sup> <sup>2)</sup>
→ <i>Leach-off:</i>	(1.7±0.5)%	< 1.0%	(1.8±0.7)%

*Table 5.3: Adsorption measurements on a glass surface. All activities refer to 28g of pseudocumene (PC). Background is subtracted. The <sup>210</sup>Pb activities contain a detection efficiency of ~1%, whereas the α efficiency arises from the discrimination by an energy and pulse shape cut. β's from <sup>210</sup>Bi were fitted between 600 and 800 keV. The uncertainties arise from a quadratic addition of the statistic error and the systematic error, whereby the latter is <sup>1)</sup> determined by two independent measurements <sup>2)</sup> estimated to 10%.*

As the measurements of 5.2.1 and 5.2.2 show, the adsorption and leach-off effect for the considered heavy metals ranges in the same order. The leach-off from glass is significantly lower than from teflon; these measurements here even imply that the major part of the leach-off observed in 5.2.1 must have been caused by the teflon surface.

The loaded scintillator amount, which remained adhered to the glass surface, after the vessel had been emptied, could be specified to ~0.1g. This corresponds to ~1.5·10<sup>-3</sup> Bq for <sup>210</sup>Po, ~2.2·10<sup>-3</sup> Bq for <sup>210</sup>Bi and ~2.4·10<sup>-5</sup> Bq for <sup>210</sup>Pb. The released activities into clean PC (Table 5.3) however are higher by an order of magnitude, so that they can clearly be attributed to a leach-off effect from the glass surface.

As the above measurements were carried out with the type of glass vessel, where liquid scintillator and silica gel were equilibrated in for the determination of the free enthalpies in paragraph 4.2.3, these results serve in an accurate way to account for the leach-off effect that might have influenced the silica gel purification equilibrium. In particular, the above values imply that the loaded pseudocumene activity in the glass vessel gets increased by (1.14±0.14)% for Po, <1.4% for Bi and (1.35±0.36)% for Pb due to a leach-off effect during the purification process.

## 6. Water Extraction

Like silica gel chromatography, treated in the chapter before, water extraction is a purification method reducing impurities in organic liquids. The availability of ultra-pure water by deionisation and distillation plants makes it an easily applicable method based on a reproducible substance. This constitutes the main advantage compared to silica gel chromatography, where the exchange of used silica gel in order to reach further purification is much more expensive.

Water extraction is one of the purification methods considered for the solar neutrino experiment Borexino and other low counting rate scintillation experiments. At the Borexino site, a water extraction plant has been set up by Princeton University. Some tests with the CTF detector were performed and are described in the following.

### 6.1. Realisation Possibilities

As most impurities are of polar nature, they prefer to dissolve in polar liquids like water. As soon as water comes in contact with an unpolar liquid scintillator, a big part of polar scintillator contaminants dissolve in water. The efficiency of this process improves with a higher contact time and a better mixing quality between the two liquid phases. Either an optimal mixing – such as a big number of liquid bubbles causing a huge contact area – or an infinite contact time leads to a complete equilibration of the impurity concentrations in both liquids. This equilibrium depends on the impurity solubilities in both liquids, varying with different pH values. It can be described with an unknown equilibrium constant, in comparison to the silica gel chromatography model (see 4.1.1). This constant, however, remained undetermined by the performed tests due to problems in the comprehension of the results. The purification efficiency further depends on the water purity and the mass ratio of water and scintillator.

The realisation in the easiest case requires a clean tank where a liquid scintillator is brought in contact with a similar amount of ultra-pure water. A pump can serve to mix both phases by circulating water from the tank outlet to the inlet, thus accelerating the equilibration. After some time the water – concentrated with polar impurities – can be removed from the bottom of the tank. This procedure corresponds to one equilibrium stage and can be repeated as often as practicable. It can be easily applied in Module-0 (see C.8) and was tested during the CTF1 campaign. A purification of bigger scintillator amounts like 300 tons however is hardly feasible in batches of  $\sim 1\text{m}^3$ . Therefore, a continuously running water extraction plant ('Purification Skid', PS) with a counter current flow column has been set up at the Borexino experiment, as described in 6.2. Its advantage mainly consists in the feasibility of a loop purification mode under the avoidance of a quality decrease in the purifying water, the purity of which can be maintained at a constant level by an on-line water distillation loop. This principle makes the plant an excellent possibility of purifying the scintillator of an already loaded Borexino detector.

### 6.2. The Borexino Water Extraction Plant

Diagram 6.1 outlines the equipment of the 'Purification Skid', a distillation and water extraction plant at the Borexino site. The intended scintillator flow is at 1000 kg/h.

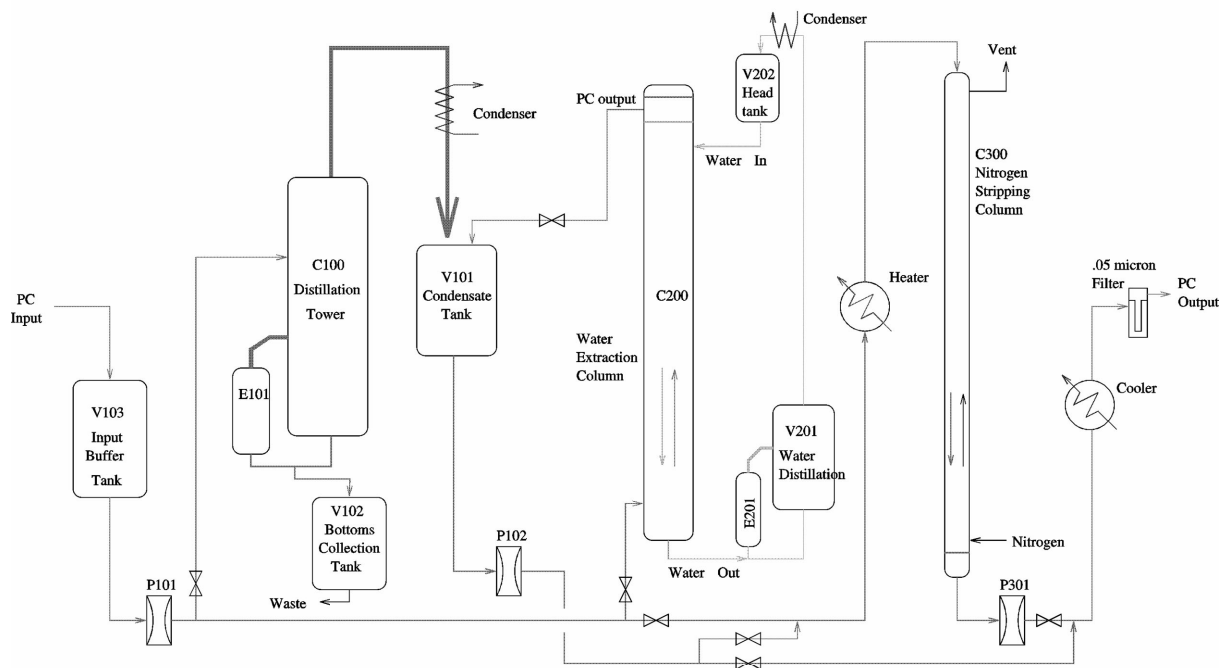


Diagram 6.1: Block Diagram of the Purification Skid at Borexino site [For03]

The unpurified liquid scintillator can temporarily be stored in tank V103, from where it enters the distillation unit or the water extraction column. The latter is designed as a counter current flow column, where ultra-pure water and scintillator contemporaneously flow in opposite directions. Unpurified scintillator enters at the bottom and moves upwards due to its buoyancy in water; it is supposed to become the purer, the longer it is in contact with the pure water that moves downwards. In this way, the purest water, entering at the top of the column, is always in contact with the purest scintillator, thus optimising the purification efficiency. The stainless steel column itself contains some packing material in order to reduce the flow velocity inside the column and to provide a better mixing. According to simulations by the manufacturing company KMPS, this package improves the contact time from ~5s to 20–30s, leading to 2–5 equilibrium stages for perfect water quality. This would increase an equilibrium efficiency of 40%, regarding one stage, to a total efficiency between 64 and 92% for the whole column.

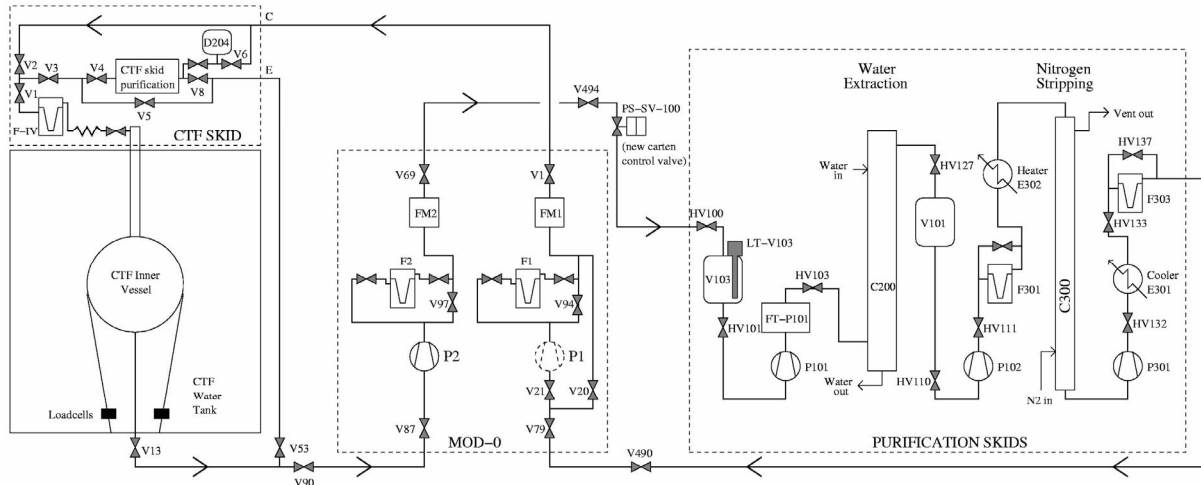
Deionised water is supplied by the water plant in hall C. The ‘Purification Skid’ comprises an own water distillation unit, able to handle a continuous water flow of 200 kg/h. On the one hand, the water can be further distilled here in order to reduce initial  $R_n$ ,  $K_r$  and heavy metal concentrations before it gets used in the extraction process. On the other hand, the plant envisions a continuous water distillation loop during the extraction of the scintillator in order to maintain the purity of the water. This continuous distillation should avoid the necessity of exchanging the water and allow an uninterrupted purification.

The extracted scintillator exiting the water extraction column can be stripped with ultra-pure nitrogen ( $HPN_2$  or  $LAK N_2$ ), optionally including a heater and a cooler, because nitrogen extraction should be more efficient at higher temperatures. The temperature of the liquid scintillator can be particularly adjusted here.

## 6.3. Experiments with CTF3

### 6.3.1. Test Set-up

Two water extraction tests with the CTF scintillator were carried out from March to May 2002. The CTF scintillator was looped through the CTF Inner Vessel, the Module-0, the water extraction (C200) and nitrogen stripping (C300) units in the Purification Skid.



- Notes:
- 1) Flow is controlled by adjusting the feed rate from V103 so that FM1 and FM2 have the same flow. The feed rate is controlled by FT-P101 and the pump P101. The rate of scintillator make-up (i.e. the losses) are monitored via the V103 level probe.
  - 2) The inner vessel volume is monitored with the IV loadcells. Also regular visual checks will be made using the cameras.
  - 3) System can stop automatically by the DCS, for example on loadcell changes or changed make-up rate. The pump P2 and all the skid pumps are stopped, and valve PS-SV-100 is closed to prevent gravitational flow through P2.
  - 4) In MOD-0 the pump P1 is bypassed through V20.
  - 5) Valves V490, V494 and PS-SV-100 are located in BBE. Valves V13, V53, and V90 are located at the bottom of the CTF water tank.

Richard Ford March 9th 2002

*Diagram 6.2: Equipment and flow path for the CTF3 water extraction testing [For03]*

Diagram 6.2 shows the respective scintillator flow path. Module-0 served as liquid handling system for the CTF Inner Vessel, controlling the flow rates (flow meters FM1, FM2) into and out of the Inner Vessel, whereas the purification was performed inside the Purification Skid. The scintillator was filtered twice in the loop (F301, F303). The three pumps inside the Purification Skid (P101, P102, P301) were controlled via a digital control system (DCS), continuously supplied with parameters from load cells, level sensors (LT), temperature sensors and flow meters (FM, FT). As the loop involved columns and tanks with variable in- and outflow, the most delicate task consisted in the coordination of these flow rates in order to maintain the volume of the CTF Inner Vessel.

Principally, on-line data could have been taken during the whole test, but the need of observing the status of the Inner Vessel, mostly at the beginning of the test, prevented this intention. The lights inside the CTF detector were turned on from time to time in order to take pictures of the Inner Vessel with an inserted digital camera. This prevented the photomultipliers from having been switched on constantly. It turned out that the Inner Vessel had been shrinking during the whole test. The nitrogen stripping might have decreased the water concentration in the liquid scintillator, drying the nylon vessel and reducing its flexibility.

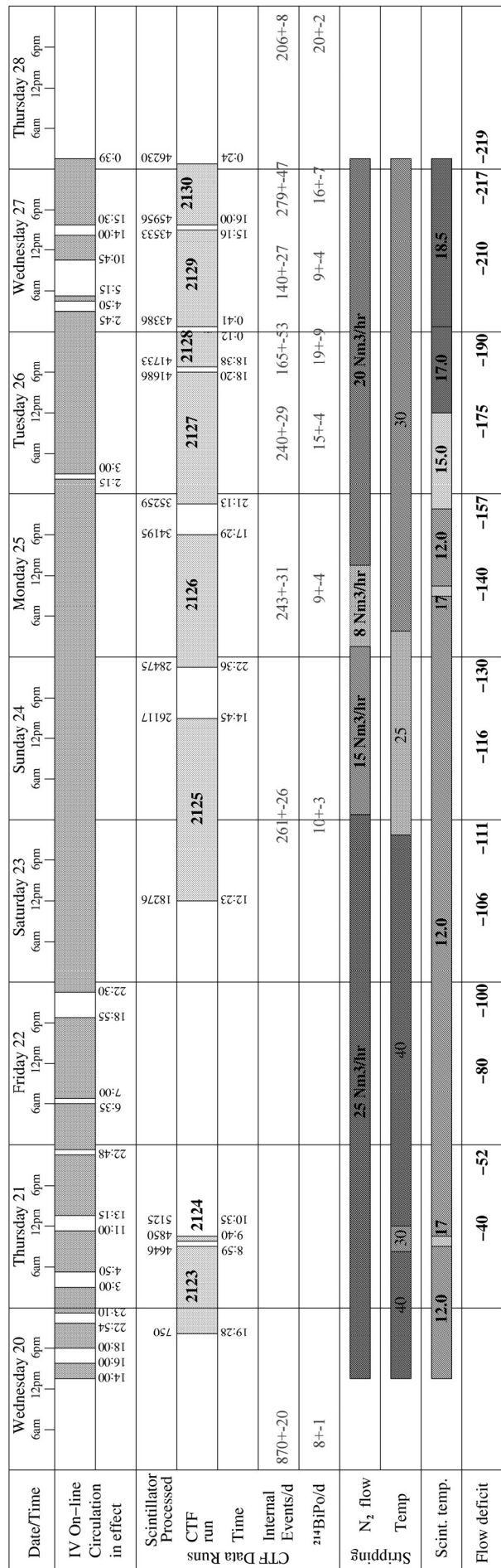
### 6.3.2. First Test Phase

A first test, performed in March 2002, comprised 13 Inner Vessel volume cycles during 8 days at a scintillator flow rate of 300 kg/h. One volume cycle corresponded to  $\approx 3900$  kg of scintillator, as besides the Inner Vessel volume  $\sim 200$  kg of scintillator were required to load the water extraction plant. During the first 3 days, the purification was sometimes interrupted because of technical problems. Due to the Inner Vessel safety concerns mentioned above, continuous data was taken from the 4<sup>th</sup> day on, after 5 volume cycles. Diagram 6.3 shows a detailed test progression together with on-line data results and other important parameters. The activity during the runs 2125 to 2130 illustrates, that most of the total purification effect had already been achieved at the beginning, after 5 volume cycles or less.

In the second half of the test, the variation of some system parameters was checked. A slight increase of the scintillator temperature did not improve the purification. As expected, lower nitrogen flow and temperature seemed to worsen the stripping efficiency, as an increase in the  $^{222}\text{Rn}$  events ( $^{214}\text{BiPo}$  coincidences) during the runs 2127 and 2128 shows.

The  $^{222}\text{Rn}$  related activity during the whole test however remained low enough to confirm a proper accomplishment from the technical point of view.

*Diagram 6.3: Progression of the first CTF3 water extraction test [For03]. The processed scintillator [kg] and the data runs in dependence on the time are shown, together with the interruptions. The data were analysed with a radial fit in the energy window between 250 and 600 keV [Cad02b]. The data runs 2123 and 2124 could not be analysed due to hardware problems. The internal events include radon related activity, that however is comparatively low. The flow deficit [kg] in the last line should balance the shrinking of the nylon vessel.*



	Princeton group analysis			Milano group analysis		
	before	after		before	during run 2125-2130	after
Internal $\alpha, \beta$ events, $^{222}\text{Rn}$ subtracted	855 $\pm$ 20	155 $\pm$ 15		913 $\pm$ 20	244 $\pm$ 21	175 $\pm$ 11
Internal $\alpha$ 's, $^{222}\text{Rn}$ subtracted	715 $\pm$ 50	115 $\pm$ 35		570 $\pm$ 50 <sup>1)</sup>	no data	120 $\pm$ 40 <sup>1)</sup>
Internal $\beta$ 's, $^{222}\text{Rn}$ subtracted	135 $\pm$ 50	40 $\pm$ 35		230 $\pm$ 70 <sup>1)</sup>	no data	40 $\pm$ 30 <sup>1)</sup>
Superficial $\alpha, \beta$ events	930 $\pm$ 20	893 $\pm$ 12		1068 $\pm$ 21	1052 $\pm$ 8	1010 $\pm$ 15

Table 6.4: Number of events per day before and after the first CTF3 water extraction test.

Data marked with <sup>1)</sup> result from pure event counting after a radial cut of  $r < 70\text{cm}$  and an energetic cut of 260–600 keV. All other internal event numbers were obtained with a radial fit in an energy window between 250 and 600 keV. The Princeton analysis results were taken from [Cad02b] and the Milano analysis results from [Mil04].

With a look on Table 6.4, the total purification factor regarding the internal events,  $^{222}\text{Rn}$  subtracted, moves between 5 and 6. The  $\alpha$ - $\beta$ -discrimination shows, that this factor is mostly due to a purification of  $^{210}\text{Po}$   $\alpha$ 's. Even if the big uncertainties in the  $\beta$  activity prevent a precise specification of the  $^{210}\text{Bi}$  purification factor, the data here indicate a reduction with a similar efficiency. The superficial events seem to decrease slightly, probably due to an adsorption equilibrium between the superficial events and the internal events. The small decrease however indicates that this equilibrium only refers to a small part of superficial activity. A big part of the impurities is probably bound more strongly to the nylon vessel or even enclosed in there. The number of superficial events during the purification period (1052/d) further indicates that the superficial events might have been washed off continuously or at the end of the test, in any case not at the time when most of the internal activity was reduced. However, the decrease of the superficial events is not able to account for the missing purification efficiency during the last 8 volume cycles. Even wash-off effects from other liquid handling system surfaces in these dimensions are improbable – in comparison to the silica gel batch test (4.3.2) – as the leach-off from stainless steel surfaces (5.2.2) is quite low,  $\leq 0.2\%$  of the raw scintillator activity.

Two possible suspicions able to explain the purification behaviour consist in the quality of the water and in the formation of hydrodynamic loops inside the CTF Inner Vessel after some time preventing further effective mixing of purified and unpurified scintillator. Both items will be clarified in 6.3.3.

	event identification	before purification	after purification
$^{238}\text{U}$ daughters	$^{214}\text{BiPo}$ coincidence	3.1 $\pm$ 0.7 d <sup>-1</sup> (7.6 $\pm$ 1.7)10 <sup>-16</sup> g/g	2.3 $\pm$ 0.6 d <sup>-1</sup> (5.6 $\pm$ 1.5)10 <sup>-16</sup> g/g
$^{232}\text{Th}$ daughters	$^{212}\text{BiPo}$ coincidence, radial cut at $r < 0.7\text{m}$	1.7 $\pm$ 0.6 d <sup>-1</sup> (2.1 $\pm$ 0.8)10 <sup>-15</sup> g/g	0.81 $\pm$ 0.41 d <sup>-1</sup> (9.8 $\pm$ 5.0)10 <sup>-16</sup> g/g
$^{85}\text{Kr}$	coincident $\gamma$ of $^{85}\text{Rb}^*$ , radial cut at $r < 0.7\text{m}$	750 $\pm$ 180 d <sup>-1</sup>	52 $\pm$ 52 d <sup>-1</sup>

Table 6.5: Purification results for U, Th and Kr related events [Mil04]. The different coincidence cuts are illustrated in Table 4.32.

Apart from  $\alpha$  and  $\beta$  activities, some contaminants, shown in Table 6.5, can be discriminated by coincidences.

The Kr reduction shows a good nitrogen stripping efficiency.  $^{238}\text{U}$  daughters – probably corresponding to the concentration of  $^{226}\text{Ra}$ , the next long lived nucleus the  $^{214}\text{BiPo}$  coincidence – were reduced by a factor  $\sim 1.5$ , a bit less than the efficiency of the silica gel loop test, however achieved at a lower level.  $^{232}\text{Th}$  daughters were reduced by a factor of  $\sim 2$ , as in the silica gel loop test.

During the purification loop, an increased  $^{212}\text{BiPo}$  coincidence rate of  $29 \pm 3 \text{ d}^{-1}$  was observed, which however decayed quickly after the test. This activity probably is, as during the silica gel loop test, due to an emanation of  $^{220}\text{Rn}$  out of the liquid handling equipment.

### 6.3.3. Second Test Phase

Although the purification results of the first test phase are encouraging, the event rate reached at the end is still too high. A second water extraction test with the CTF was carried out in May 2002 in order to examine how to reach further progress. Between the two phases, the activity in the CTF scintillator had been influenced by an exchange of 440 kg of scintillator with a raw pseudocumene batch of higher activity (see 3<sup>rd</sup> row in Table 2.9).

One of the suspicions that could have prevented further purification during the first phase, consisted in the formation of special hydrodynamic flow patterns in the CTF Inner Vessel, possibly induced by the continuous scintillator flow. Figure 6.6 shows a hydrodynamic simulation with the respective test parameters. While a big part of the liquid scintillator flows straight through the vessel, loops form in the outer parts of the sphere. The mixing between the loops and the straight flow was calculated to  $\approx 15\%$ , so that several volume cycles would be necessary to pass each scintillator molecule at least once through the purification plant. As already explained in 4.3.1, this would increase the time constant of

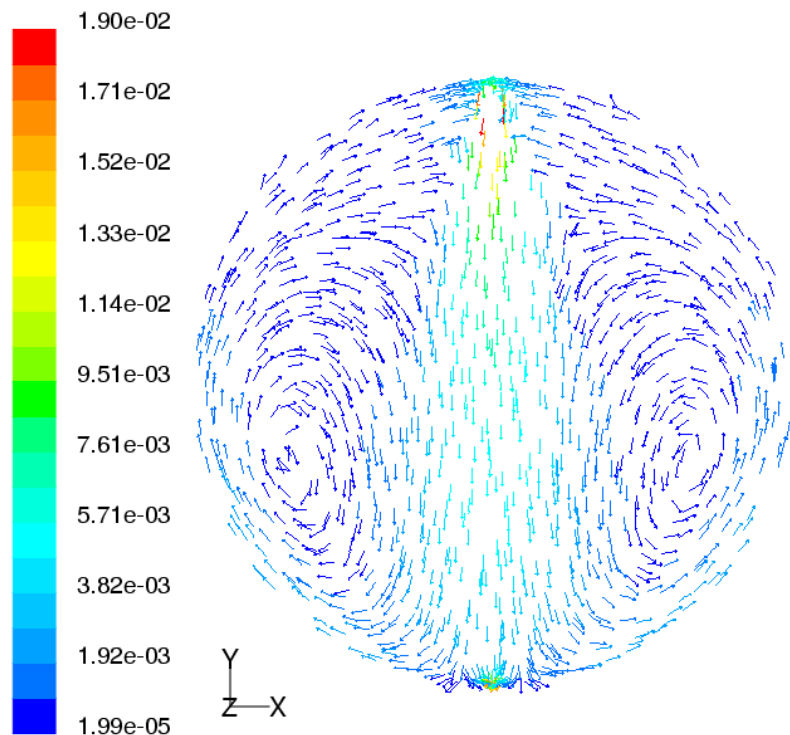


Figure 6.6: Hydrodynamically simulated flow pattern with the CTF Inner Vessel geometry at an integral flow rate of 300 kg/h [Leu02]. The flow velocity vectors are coloured by the velocity magnitude [m/s].

the purification development. In fact, as the loops take some time to form, this could explain the initial purification effect and the later failure. Hence, during the first six days of the second test phase a stop-and-go purification mode was tried, turning the purification loop on and off several times. Even the duration of the different purification runs and breaks was varied. The values in the first seven rows of Table 6.7 show the result.

Date	Purification Processed scintillator	Data acquisition			
		Data runs	Internal events	Internal $\alpha$ 's	Internal $\beta$ 's
	before purification	2157- -2160	<b>382±47</b>	329±40	58±16
8.5.02	started 17:00, stopped 22:30 1700 kg processed	2161	<b>278±53</b>	236±58	41±32
9.5.02	started 11:30, stopped 23:05 2594 kg processed	2162	<b>355±51</b>	281±59	67±43
10.5.02	started 10:30, stopped 20:30 2796 kg processed	2163 2164	<b>227±26</b> <b>306±35</b>	190±24 213±37	38±11 90±31
13.5.02	started 13:00, stopped 16:40 started 18:20, stopped 21:30 2183 kg processed	2165	<b>288±44</b>	240±41	48±18
14.5.02	started 10:45, stopped 13:32 started 16:45, stopped 18:25 started 21:15, stopped 22:40 1700 kg processed	2167 2168 2169	<b>272±44</b> <b>255±29</b> <b>190±25</b>	224±45 197±26 172±23	55±29 59±15 20±10
17.5.02	started 10:00, stopped 13:05 started 14:05, stopped 17:10 started 18:30, stopped 20:45 2604 kg processed	2170 2171 2172	<b>215±17</b> <b>232±37</b> <b>186±25</b>	166±16 200±35 168±27	48±8 34±15 18±13
22.5.02	<i>Use of acid water (0.2% HNO<sub>3</sub>)</i> started 10:45, stopped 14:50 started 15:40, stopped 18:45 started 19:40, stopped 21:45 2773 kg processed	2173	<b>222±40</b>	182±40	37±22
23.5.02	<i>Use of acid water (0.2% HNO<sub>3</sub>)</i> started 9:45, stopped 12:30 started 13:30, stopped 16:00 started 16:50, stopped 18:20 started 18:50, stopped 20:45 2550 kg processed	2175 2176 2177 2178 2179	<b>230±19</b> <b>257±23</b> <b>216±21</b> <b>209±19</b> <b>238±21</b>	188±18 209±21 165±18 201±18 211±19	43±8 47±9 51±10 8±4 26±7

*Table 6.7: Purification steps and data analysis during the second CTF3 water extraction phase [For03]. The data runs in each row show the obtained activity after all the purification steps of the specified day, not the activities between the single steps. The data was analysed by pure event counting between 260 and 600 keV with a radial cut of  $r < 70\text{cm}$  [Mil04]. <sup>222</sup>Rn related events were subtracted. The nitrogen stripping was performed with a nitrogen flow of 25m<sup>3</sup>/h and at a temperature of 35–40°C. One volume cycle corresponded to ≈3900kg of scintillator.*

The data do not show any further purification effect. Compared to the value before purification, the number of events decreases slightly, but the limitation observed during the first test phase (see 6.3.2) gets confirmed. The hydrodynamic model can be excluded as source of the problem.

Another possible explanation concerns the quality of the water used for the extraction. In fact, the stagnation during the first test phase after the initial purification could have arisen from an equilibrated impurity concentration in the water, with the water distillation loop not being efficient. In this case, the exchanged water of the second phase should already have

improved the situation, however it did not. The further possibility of the fresh, deionised water already being too strongly contaminated was faced by the attempt of using acid water, loaded with nitric acid at a concentration of 0.2%. The acid had been sparged with ultra-pure nitrogen and its purity checked with mass spectroscopy for U and Th. The pH change in the water should have shifted the extraction equilibrium to higher heavy metal concentrations in water and lower ones in the scintillator, resulting in a further purification below the level of phase one,  $\sim 100 \alpha$  events per day. However, with a look at the last two rows of Table 6.7, this could neither be achieved.

A remaining possible explanation of the barrier at  $\sim 100$  counts/day can arise from a general limitation in the water extraction purification factor for the considered heavy metals in pseudocumene scintillator, as illustrated for silica gel in 4.2.5 at Table 4.30. In fact, the initial, raw scintillator – referring to the loading of CTF3 in November 2001 – had contained an  $\alpha$  activity around  $\sim 2000$  counts/day, some smaller batches with up to even  $\sim 6000$  counts/day had meanwhile been added (see Table 2.9), and the nylon vessel surface activity around  $\sim 1000$  counts/day had additionally been introduced. In this context, the total reduction during the CTF3 campaign reached a factor between 10 and 40, and this factor constitutes a lower limit regarding possible higher pseudocumene contaminations during fabrication and delivery. As the respective limitation in the silica gel efficiency for Po in pseudocumene seems to be in the order of  $\sim 500$  (Table 4.26), the limitation of water extraction could also differ by an order of magnitude and, matching with the factor illustrated above, account for the observed barrier at 100 counts/day. The reason of the limitation could consist in the formation of polonium complexes with organic molecules [Fig61], shielding the polar nature of the impurities.

Apart from these considerations, the following table shows the purification effect on Th daughters and  $^{85}\text{Kr}$ .

	event identification	before purification	after purification
$^{232}\text{Th}$ daughters	$^{212}\text{BiPo}$ coincidence, radial cut at $r < 0.7\text{m}$	$2.2 \pm 1.3 \text{ d}^{-1}$ $(2.7 \pm 1.6) 10^{-15} \text{ g/g}$	$1.2 \pm 0.9 \text{ d}^{-1}$ $(1.4 \pm 1.0) 10^{-15} \text{ g/g}$
$^{85}\text{Kr}$	coincident $\gamma$ of $^{85}\text{Rb}^*$ , radial cut at $r < 0.7\text{m}$	$110 \pm 110 \text{ d}^{-1}$	$73 \pm 73 \text{ d}^{-1}$

Table 6.8: Purification results for Th and Kr related events [Mil04]. The different coincidence cuts are illustrated in Table 4.32.

The uncertainties are however too big to deduce significant changes. Probably, there is no change with respect to the values obtained during the first water extraction phase (6.3.2). The U daughter analysis was impossible, as the decay of the  $^{214}\text{BiPo}$  rate did not approach a constant level until the next CTF3 test.

The emanation of  $^{220}\text{Rn}$  amounted to  $7.3 \pm 1.7$  counts/day during the second water extraction phase.

## Conclusion

The discovery of neutrino oscillations by the gallium solar neutrino experiments as well as by SuperKamiokande, SNO, and KamLand during the past years has led to a different situation for the Borexino experiment, mainly projected to aim at the measurement of solar  $^7\text{Be}$  neutrino oscillations. Beyond this, Borexino provides an excellent possibility for the detection of anti-neutrinos from supernova, solar and geological sources. A precise measurement of the solar  $^7\text{Be}$  neutrino rate will still significantly contribute to astrophysical questions. Further ideas for a utilisation of the CTF detector, as the  $\beta\beta 0\nu$  search with the described CAMEO and  $^{150}\text{Nd}$  projects, have arisen.

On the basis of the CTF3 campaign results, of particular precision after two years of data taking, the status of the Borexino experiment has been reevaluated regarding the background remained in the liquid scintillator. The presence of the isotope  $^{210}\text{Pb}$  together with its daughters seems to constitute the major background in the energy range from 250 to 800 keV. This has to be further reduced by a factor of  $\sim 10$  in order to achieve a signal-to-background ratio in the order of  $\sim 1$ , and to allow an extraction of the solar  $^7\text{Be}$  neutrino signal from the Borexino scintillator background spectra.

Within this frame, the completion of the Borexino detector remains an important task, in which the radiopurity of the liquid scintillator constitutes the most crucial question. A liquid handling and purification system, the so-called Module-0, aiming at the purification of the Borexino scintillator by the technique of silica gel chromatography, has been developed and installed at the Laboratori Nazionali del Gran Sasso, Italy, during the past years. Its purity has successfully been checked by radon emanation measurements and particulate counting tests. First purification tests on scales of some tons were carried out together with the CTF detector and have demonstrated a proper installation of the system. However, an interruption of these tests by jurisdiction has led to the necessity of continuing the purification tests on small scales.

In the subsequent laboratory tests, the capability of the installed purification plant in Module-0 should be checked and respective procedures drawn up. Basic elements have been developed to a model and a computer simulation, predicting efficiencies for two different purification modes. The more efficient one, the batch purification mode, has been qualitatively confirmed by an experimental test on small scales, showing an excellent efficiency at a silica gel to scintillator mass ratio down to  $1/1200$ . Further important parameters of the model like adsorption enthalpies of ultra-pure silica gel for heavy metal impurities have been determined more precisely with respect to previous works. Possible limitations in the purification efficiency were examined and indications for two different kinds of limitations have been derived.

Together with these experimental results, the model suggests the necessity of increasing the silica gel amount in the Borexino related purification plant Module-0 by a factor of 2 with respect to the previous design, in order to reach a sufficient sensitivity to extract the solar  $^7\text{Be}$  neutrino signal from the background spectra of the Borexino scintillator. Possible problems arising from purification limitations could not definitively be clarified.

The Borexino experiment disposes of two further scintillator purification possibilities, a water extraction plant and a distillation plant. The functionality and purification efficiency of the water extraction plant has been demonstrated in two tests with the CTF detector, reducing the  $^{210}\text{Po}$  concentration in the liquid scintillator to  $\sim 2 \cdot 10^{-24}$  g/g. The distillation plant could not be tested with the CTF detector until now, but some laboratory tests performed by a related group indicate better purification efficiency with respect to the water extraction plant.

# Appendices

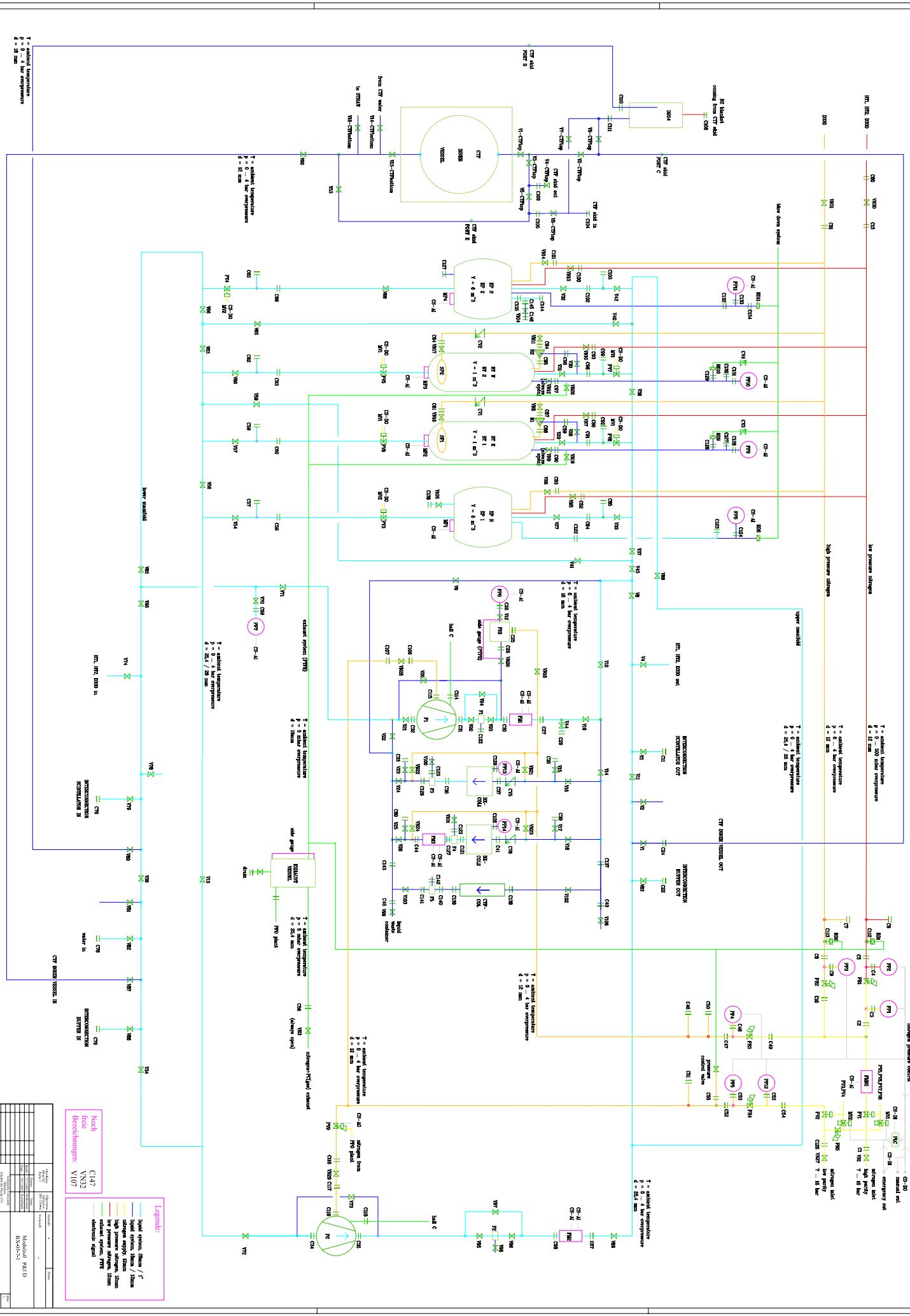
## A. Piping & Instrumentation Drawing of Module-0 and the CTF Inner Vessel

### *Legend:*

EP	EP Tank
BT	Buffer Tank
P	Pump
PH	Pressure head
F	Filter
COL	Purification column
SP	Sparger
N	Nozzle
FM	Flow meter
MP	Load cell
PP	Pressure probe
PR	Pressure reducer
RD	Rupture disk
PV	Pneumatic valve
CV	Check valve
V	Valve in liquid system
VN	Valve in nitrogen system
MV	Magnetic valve
C	VCR connector
CS	Digital Control System
AI	Analogue input
DI	Digital input
AO	Analogue output
DO	Digital output

light blue line	liquid pipe, diameter 1 inch (25.4 mm) or 28 mm
dark blue line	liquid pipe, diameter 12 mm or 18 mm
yellow line	nitrogen supply line, 0–16 bar, diameter 12mm
orange line	high pressure nitrogen system, 0–4 bar, diameter 12mm
red line	low pressure nitrogen system, diameter 12mm
green line	exhaust system
grey line	electric signal

The P&ID follows on the next page.



**Legend:**

- Liquid system, Steam / T
- High pressure nitrogen
- Low pressure nitrogen
- Emergency outlet
- High pressure nitrogen
- Low pressure nitrogen
- Emergency outlet

**Legend:**

- Blue: Liquid system, Steam / T
- Green: High pressure nitrogen
- Yellow: Low pressure nitrogen
- Red: Emergency outlet

**Legend:**

- Blue: Liquid system, Steam / T
- Green: High pressure nitrogen
- Yellow: Low pressure nitrogen
- Red: Emergency outlet

Item	Symbol	Description
PI 101	Circle with '101'	Pressure indicator
TI 101	Circle with '101'	Temperature indicator
VI 101	Circle with '101'	Valve indicator
CI 101	Circle with '101'	Control indicator
SI 101	Circle with '101'	Signal indicator
LI 101	Circle with '101'	Level indicator
MI 101	Circle with '101'	Moment indicator
DI 101	Circle with '101'	Display indicator
AI 101	Circle with '101'	Alarm indicator
BI 101	Circle with '101'	Block indicator
FI 101	Circle with '101'	Flow indicator
SI 101	Circle with '101'	Signal indicator
LI 101	Circle with '101'	Level indicator
MI 101	Circle with '101'	Moment indicator
DI 101	Circle with '101'	Display indicator
AI 101	Circle with '101'	Alarm indicator
BI 101	Circle with '101'	Block indicator
FI 101	Circle with '101'	Flow indicator

## B. Scintillator Solvents

	PC	PXE
Technical Term	1,2,4-Trimethylbenzene	Phenyl-o-xylene
Physical State	Liquid	Liquid
Colour	Clear, Colourless	Clear, Colourless
Odour	Sweet, Aromatic	Aromatic
Molecular Formula	C <sub>9</sub> H <sub>12</sub>	C <sub>16</sub> H <sub>18</sub>
Molecular Weight	120	210
Chemical Family	Aromatic Hydrocarbon	Aromatic Hydrocarbon
pH Value	Neutral	Neutral
Melting Point	-43°C	no data
Pour Point	no data	-48°C
Boiling Point	169°C	295°C
Flash Point	43°C (Tag Closed Cup)	145°C (P-M Closed Cup)
Explosion Limits	0.9 to 6.4 %	no data
Auto-Ignition Temperature	500°C	375°C
Vapour Pressure at 25°C	260 Pa	1.3 Pa
Vapour Density (Air = 1)	4.15	7.3
Density	0.88 g/cm <sup>3</sup>	0.99 g/cm <sup>3</sup>
Viscosity at 20°C	0.8 cP	20 cP
Refractive Index	1.505	1.565

*Physical and chemical properties of PC and PXE*

## C. Operation Procedures of Module-0

This section contains descriptions and instructions how to carry out standard fluid operations, envisioned for persons operating Module-0.

### C.I. Operation of Module-0 Safety Valves

At the beginning of any process in Module-0, the status of the Module-0 safety valves (PV1-8) has to be checked. It can be looked up on the DCS. If the status is 'closed', Module-0 cannot be operated. In order to recover the system, the cause has to be checked by looking at the LED's below the load cell displays inside BBE:

- The green light labelled "Power" has to be on. If not, check the switch on the back side of the device and the fuses No. 3 and 4 in the fuse box on the wall behind the silica gel columns. If it is impossible to turn on the power by this switch, the problem might be caused by an electric power black-out. In this case contact the operational manager of Borexino.
- The red light at the label "Handsteu." indicates a manual closure by the switch below. Open by turning the switch to the mid position "auf".
- The red light at the label "Gasmangel" indicates a closure because of erroneous pressure conditions in the system. Look at the device near the nitrogen panel to identify the alarm cause indicated by its LED's and the pressure controllers PP1-5, PP12. In case of an overpressure in a part of the system (PP2-5) restore first the proper pressure conditions and then press the "Reset"-button. In case of lack of regular nitrogen pressure (PP12), the safety valves cannot be operated, as they are pneumatic valves to be supplied with 7 bar overpressure at least. Then, stop every further process in Module-0 and contact the operational manager. In case of lack of high-purity nitrogen pressure (PP1) only the activities using high-purity nitrogen are impossible. Decide if you can proceed without high-purity nitrogen, otherwise contact the operational manager. In general, when the nitrogen pressure is reestablished, the safety valves can be reopened by pressing "Reset" and turning the switch below the load cell displays to the left position.
- The red light at the label "Zentrale Steuerung" indicates a closure caused by the DCS. Use a DCS workstation to log in, switch to the DCS Module-0 page and open the safety valves. If you are not authorised to enter the DSC, ask the operational manager.
- A closed status in spite of all red lights turned off might be caused by the 'Emergency out' button outside the BBE at its front door. Check the status of this button and pull it out to reopen.

Note: Opening the safety valves will immediately cause a pressure increase in the nitrogen supply lines to ~10 bar. Therefore, it is important to check the system status first, mainly the pressure regulators PR1-4 on the nitrogen panel. In case of doubt close them by turning counter-clockwise.

### C.II. Transferring of Liquids

This paragraph, basic knowledge for accomplishing more complicated processes as described afterwards, contains a general description how to move liquids between the different tanks of Module-0.

- Check the capacity of the input tank (EPN, EPS, BTE, BTW). The levels are monitored by the load cells (MP1, MP4, MP2, MP3), the proper calibration is available on the DCS (EP tank values too high by factors  $\approx 1.2$ , BT tank values too high by factors 5–6). The uncertainty of these values is below 10%. Be aware of the density difference between water and scintillator, as load cells measure the mass instead of the volume.
- Check the status of the nitrogen system and the safety valves (C.1).
- Watch the nitrogen pressure in the input tank by looking on the respective pressure probe (PP8, PP11, PP9 or PP10) in order not to exceed the tank specification during the filling process. If needed, release some pressure via a ventilation valve on BTE or BTW (VN19 or VN20), or leave open the ventilation line during the process. Further, you can connect tank blankets via the nitrogen system, using the valves VN5, VN6, VN7, VN8, VN10, VN11, VN13, VN14. In any case, pay attention that the valve VN3 (outside BBE) is open during the ventilation process.
- Note that the tanks EPN and EPS do not have own ventilation lines. For a respective ventilation, nitrogen has to pass through BTE or BTW. Therefore, connect the respective EP and BT blankets. Meanwhile, pay attention not to exceed the BT's pressure specification, particularly open always the BT ventilation valve before connecting the EP blanket.
- Configure the nitrogen blanket of the output tank to avoid a vacuum: Supply continuously with high-purity nitrogen, using the valves PR1, VN5, VN7, VN10, VN13 or PR2, VN6, VN8, VN11, VN14 respectively. Watch the pressure on PP2 or PP3.
- Look for the liquid flow path without opening all required valves immediately. Pass through a flow meter (FM1, FM2) if possible; this provides a more reliable control of the flowing liquid amount than the load cells. The flow meter uncertainty is below 2%.
- Insert a filter (F1, F2) if desired. Pay attention to the medium the cartridge has been used with before (compare description in 3.2.1).
- Open the flow path to the input tank. You can avoid a back flow by using the top inlet.
- Open the bottom valve of the output tank at last. Pay attention, because the liquid possibly starts to flow at this time. A pump – if not supplied – does not block a flow in forward direction.
- Start the pump (P1, P2) if necessary. Regulate the power by the nitrogen supply via the valves PR4, VN28 or PR4, VN29, EV3, while looking at the pressure on PP5. EV3 has to be operated via the DCS. The liquid flow can additionally be regulated by using the bypass valve V20 or V73.
- To end the process, stop the pump, close all valves, and regulate the tank blankets via the nitrogen system.
- Emergency shutdown: Press the 'Emergency out' button. If possible, close V19 or V69 in case of a flow through FM1 or FM2.

### C.III. Mixing of Scintillator

The liquid scintillator normally consists of a solvent (PC or PXE) and a wavelength shifter (PPO in case of PC) in form of a white powder. Since the CTF3 period, the so-called Master Solution, a concentrated solution of this powder, has been prepared outside Module-0. Therefore, this paragraph contains only a description how to mix Master Solution with scintillator solvent.

- Move the solvent into a Module-0 tank (EPN, EPS, BTE or BTW).

- Add an appropriate amount of Master Solution to the solvent in the respective tank. If the amount is small, consider the volume of pipes, pump, and filter along the flow path. Compare the flow meter and the load cell values.
- Circulate the mixture in the tank via P1 or P2, until a homogeneous concentration is obtained. A time in the range of one hour should be enough.
- The density of the solution monitored on the flow meter provides a good indication for the wavelength shifter concentration (experience values during period CTF3:  $\rho_{PC} \approx 0.882 \text{ kg/l}$ ,  $\rho_{Sc} \approx 0.885 \text{ kg/l}$ ,  $\rho_{PPO} \approx 1.06 \text{ kg/l}$ ). If needed, take a sample to accomplish a more precise measurement.
- Emergency shutdown: Press the 'Emergency out' button.

#### C.IV. Volumetric Loading of the CTF Inner Vessel

As Module-0 serves as liquid handling system of the CTF Inner Vessel, it necessarily has to perform every scintillator exchange concerning this detector. The idea of a *volumetric scintillator loading* of the CTF requires the Inner Vessel to be completely filled with liquid – either with water only, or with water and scintillator. The loading process consists in a loop exchanging liquid between the CTF Inner Vessel and a Module-0 tank that both do not contain any gas volume, but only water and scintillator. Water and scintillator separate because of their density difference, hence, the lower part of the loop contains only water, and the upper part only scintillator. The circulation is maintained by a pump, volumetrically exchanging water in the Inner Vessel with scintillator in the Module-0 tank (EPN, EPS, BTE or BTW), here called filling tank (FT). In particular, scintillator enters the Inner Vessel from the top, and a corresponding volume of water exits at the bottom. As the total volume in the loop is maintained during the process, the danger of breaking the Inner Vessel is comparatively small; however, an Inner Vessel expert should be present during the whole operation. Using an EP tank as FT, the Inner Vessel can be loaded all at once, whereas the volume of a Buffer tank allows to only exchange a part of the Inner Vessel volume. The loading procedure is the following:

- The CTF-IV, filled with water, is not completely inflated.
- The FT has to be filled completely; mainly scintillator and possibly some ultra-pure water should be inside. During this process, the nitrogen blanket has to be removed except small, non-removable amounts in the range of some litres remaining in flange volumes. In any case, the overpressure has to be removed.
- If the FT is BTE/BTW, close either C126/C129 with a blind VCR gasket, or close VN9/VN12. Closing C126/C129 is advantageous, as in this case the pressure probes PP9/PP10 remain connected.
- The recommended flow path is: CTF Inner Vessel - V13CTFbottom - V90 - V87 - ... - P1/P2 - FM1/FM2 - ... - FT bottom - FT top - ... - V1 - V2CTFtop - V1CTFtop - CTF Inner Vessel. Note that some valves are outside Module-0. Most Module-0 valves depend on the FT and the pump. The pump is supposed to move liquid towards the bottom inlet of the FT in order to provide maximum safety for the Inner Vessel.
- All lines used should be filled with scintillator or water. No overpressure should be left.
- Open all valves.
- Turn on the pump and adjust the pressure supply to 4 bar. Possibly, the pump does not even start at a lower pressure. The major part of the pressure gets consumed by the flow resistance.
- During the circulation, the overpressure in the FT may reach about 2 bar.

- The recommended flow rate is 400 kg/h. The flow can be controlled by adjusting the pump bypass valve (V20/V73).
- Stop the operation, before water would exit from the top of the FT. As soon as the Inner Vessel is loaded completely, scintillator starts to pass through the flow meter, recognisable by a density change.
- To stop the process, first stop the pump, and then close all valves.
- Reconnect the FT to the nitrogen system, and reset its nitrogen blanket by removing about 100 kg of liquid. If the FT is BTE/BTW, reopen C126/C129 or VN9/VN12 respectively.
- Emergency shutdown: Press the 'Emergency out' button, and close V87 and V1. Then, isolate the CTF Inner Vessel by closing V13CTFbottom and V1CTFtop.

### C.V. Volumetric Unloading of the CTF Inner Vessel

The principle of *volumetric unloading* of the CTF Inner Vessel corresponds completely to the loading process described in C.4. As the only difference, the Inner Vessel here is filled with scintillator and the filling tank (FT) with ultra-pure water. The liquids in both reservoirs will be exchanged by a loop. See section C.4 for more details. The unloading procedure is the following:

- The CTF-IV, filled with liquid scintillator, is not completely inflated.
- The FT has to be filled completely; mainly ultra-pure water and possibly some scintillator should be inside. During this process, the nitrogen blanket has to be removed except small, non-removable amounts in the range of some litres remaining in flange volumes. In any case, the overpressure has to be removed.
- If the FT is BTE/BTW, close either C126/C129 with a blind VCR gasket, or close VN9/VN12. Closing C126/C129 is advantageous, as in this case the pressure probes PP9/PP10 remain connected.
- The recommended flow path is: CTF Inner Vessel - V1CTFtop - V2CTFtop - V1 - ... - P1/P2 - FM1/FM2 - ... - FT top - FT bottom - ... - V87 - V90 - V13CTFbottom - CTF Inner Vessel. Note that not all valves are inside Module-0. Note that some valves are outside Module-0. Most Module-0 valves depend on the FT and the pump. The pump is supposed to move liquid towards the bottom inlet of the FT in order to provide maximum safety for the Inner Vessel.
- All lines used should be filled with scintillator or water. No overpressure should be left.
- Open all valves.
- Turn on the pump and adjust the pressure supply to 4 bar. Possibly, the pump does not even start at a lower pressure. The major part of the pressure gets consumed by the flow resistance.
- During the circulation, the overpressure in the FT may reach about 2 bar.
- The recommended flow rate is 300 kg/h. The flow can be controlled by adjusting the pump bypass valve (V20/V73).
- Stop the operation, before scintillator would exit from the top of the FT. As soon as the Inner Vessel is loaded completely, water starts to pass through the flow meter, recognisable by a density change.
- To stop the process, first stop the pump, and then close all valves.
- Reconnect the FT to the nitrogen system, and reset its nitrogen blanket by removing about 100 kg of liquid. If the FT is BTE/BTW, reopen C126/C129 or VN9/VN12 respectively.

- Emergency shutdown: Press the 'Emergency out' button, and close V87 and V1. Then, isolate the CTF Inner Vessel by closing V13CTFbottom and V1CTFtop.

## C.VI. Silica Gel Chromatography

The process of scintillator purification by silica gel chromatography, the major motivation for the construction of Module-0, requires a certain number of preparation steps. First, the column has to be filled with ultra-pure silica gel and a nitrogen blanket of ~0.3 bar. The filter after the column should be furnished with a clean cartridge. The silica gel should be flushed with HPN<sub>2</sub> to avoid radon or krypton contamination. The purification process should be initialised in the following way:

- All lines before the column have to be filled with scintillator or scintillator solvent; especially water has to be prevented from entering the silica gel column. Use V106 to flush these lines.
- Nitrogen is able to pass through the silica gel. However, try to avoid a big gas volume in the column, because nitrogen blocks the teflon filter after the column. Therefore, the column should be filled with scintillator; nitrogen can escape via a slightly opened VCR connector on the top of the column. While doing this, keep partially open the bypass valve of the pump and pay attention not to exceed 2.5 bar. The gas at the bottom of the column cannot be removed in this way.
- Before the purification process, the silica gel column and the filter should be flushed with scintillator or scintillator solvent. This can be done by “purifying” via the silica gel column into a waste container, V99 can be used to exit Module-0. Flush about 10 times the volume of the filter housing. If the filter contains gas, it might take several minutes until the scintillator will start to flow continuously.
- In order to avoid a back flow, initialise the scintillator flow through the silica gel column in the following way: First, apply some overpressure to the top inlet of the column. Therefore, open the flow path to the pump, adjust the pump pressure to 2–3 bar, but keep open the pump bypass valve (V20) partially such that the pump is running smoothly. Then, open the top column valve (V16, V18 or V102), and after that, open the bottom column valve (V24, V26, V103). Looking at the respective points of this procedure, open the whole flow path. You can adjust the pressure on the silica gel column by the pump pressure and the pump bypass valve; it should not exceed 2.5 bar.
- Watch the flow through the column on the flow meter. Probably, there is some gas left in the column, hence, the filter after the column might block. However, keep on applying a normal constant pressure to the column, as the nitrogen will slowly pass through the filter; it can take about an hour. Apart from this, adjust the flow by the bypass valve V20. The recommended flow rate is between 100 and 200 litres per hour.
- Once the purification loop is running, it is recommended to set up respective DCS alarms concerning flow meters and pressure probes, depending on the desired system parameters.
- To shut down the operation, first stop the pump by closing VN28. Then, close the top column valve, and wait until the pressure in the column has relaxed. Finally, close the bottom column valve and all other valves.
- Emergency shutdown: Push the 'Emergency out' button. Close V19 if possible. Then, isolate the Inner Vessel if involved.

### *Silica Gel Loop Purification*

During a silica gel loop purification process, the scintillator is circulated between a reservoir – this can be a tank or the Inner Vessel of CTF or Borexino – and a silica gel column. Initialise the purification, as explained above. The following points are of further importance:

- A standard circulation path is: CTF/Borexino Inner Vessel - V87/V79 - V39 - V86 - V71 - V21 - P1 - V94 - FM1 - V19 - V14 - V16/V18/V102 – Silica Gel Column - V24/V26/V103 - V9 - V8 - V11 - V1/V3 - CTF/Borexino Inner Vessel.
- To set up a purification loop with CTF or Borexino, always keep contact with the CTF/Borexino responsible.
- For a purification loop with the CTF, the pump supply pressure has to be adjusted around 4 bar, as the resistance of the lines to the CTF Inner Vessel additionally contributes.

Optionally, nitrogen extraction in BTE/BTW can be included by involving the second pump P2, according to the procedure for *Continuous Mode* described in C.7. However, in this case, the cleanliness level of BTE/BTW can affect the purification. Another possibility, the on-line nitrogen extraction, is made available by the Purification Skid, accessible via the Interconnection System.

### *Silica Gel Batch Purification*

In a batch purification process, the scintillator is moved from a reservoir via a silica gel column to another reservoir. Even if this purification method is the most effective one, the purity level of the second reservoir can influence the scintillator purity significantly. Recontamination by tank and pipe surfaces has to be avoided. The silica gel column should be prepared as described above. A possible flow path, in case of purifying from the tank EPS into the tank BTE, is:

- EPS - V68 - PV4 - V85 - V71 - V21 - P1 - V94 - V19 - V14 - V102 - V103 - V9 - V43 - V37 - PV8 - V29 - BTE

From the beginning on, nitrogen extraction in the BT tanks can be applied, either in continuous or in batch mode. Both procedures are described in section C.7.

In order to use a minimum of liquid handling equipment, it can be advantageous to purify the scintillator and to simultaneously load it into the CTF or Borexino Inner Vessel. This is possible from any Module-0 tank, via the pump P1 and a silica gel column. However, in this case, the radon emanated out of the silica gel is completely introduced into the detector.

## C.VII. Nitrogen Extraction

The method of nitrogen extraction is envisioned for reducing gaseous contaminants in liquids. In particular, the two BT tanks of Module-0 are equipped with spargers (SP1, SP2), two stainless steel spirals placed in the bottom of these tanks and supplied with high-purity nitrogen. The level of the liquid to be purified has to notably exceed the height of the spiral, guaranteed from a volume of ~200 litres. On the other hand, the liquid volume should not exceed 1200 litres in order not to block the nitrogen ventilation. The purification efficiency scales with the nitrogen flow, monitored on a flow meter (FMN2) in the nitrogen supply line.

Nitrogen extraction can also be applied during a tank loading or unloading process. The spargers can be operated in the following way:

- Check VN3 to be open. It is located between the BBE and the wall of hall C at a height of about 5 meters, and are accessible via the corridors along the wall of hall C.
- Open the ventilation valve VN19/VN20 to the exhaust vessel.
- Supply the sparger SP1/SP2 with  $\text{HPN}_2$  via VN16/VN17. Regulate the supply pressure with the regulator PR2, looking on the manometer PP3 and the flow meter FMN2.
- Stop the nitrogen flow when desired, and close the ventilation valve VN19/VN20. An extraction time in the range of one day should be enough.
- Emergency shutdown: Press the 'Emergency out' button.

### *Continuous Mode*

Continuous extraction may be necessary to process liquid amounts bigger than the Module-0 tank capacities. In the following, two possibilities providing a continuous liquid flow through BTE/BTW are described. Note that the purification factor scales with the extraction time, and is thus influenced by the average liquid flow.

On the one hand, a continuous flow through the extraction tank can be established by feeding via the top inlet and draining via the bottom inlet, using two different pumps operating at the same flow. The load cell value of the tank can be used to maintain the level. A problem affecting the purification may consist in the continuous mixing between purified and unpurified liquid inside the BT tank. It hardly can be estimated how the purity of the exiting liquid is influenced, depending on the liquid and nitrogen flow rates and the turbulences in the tank.

On the other hand, the following procedure avoids this problem:

- At the beginning, BTE and BTW have to be empty.
- Turn on the nitrogen flow in BTE and BTW by opening VN19, VN20, VN3, VN16, VN17, PR2. Keep it open always. Later, when the tanks are full, readjust the pressure.
- Start to fill BTE (V29) from the liquid reservoir by using the pump P1 and FM1. Keep a constant flow, 200kg/h are recommended. If needed, later adjust the supply pressure by using VN28 in order not to influence the supply of the pump P2.
- Keep always open the valves V29, V31, V36, V57, V60.
- When the BTE load cell (MP2) exceeds 1050 kg, turn to filling BTW by opening PV7 and closing PV8.
- Continue the nitrogen extraction in the filled tank BTE for some hours, then drain BTE via the pump P2 and FM2 in order to have it available as soon as BTW will be filled. Estimate when to start the tank unloading, considering the level of BTW (MP3) and the flow rates in FM1 and FM2. It is recommended to start the unloading process of BTE at a BTW level of ~800 kg.
- Therefore, open PV6 and drain BTE via P2 to the desired destination. Open VN29 and PV9 completely. Try to reach a high flow at ~1000 kg/h by increasing the pressure on PP5 with PR4. Readjust the flow in P1 by operating VN28.
- When BTE is empty, turn off P2 by closing PV9. Then, close PV6.
- When the BTW load cell (MP3) exceeds 1050 kg, turn again to filling BTE by opening PV8 and closing PV7.
- Continue the nitrogen extraction in the filled tank BTW for some hours, then empty BTW via P2 and FM2 in order to have it available as soon as BTW will be filled. It is

recommended to start the unloading process of BTW at a BTE level of 800 kg. Therefore, open PV5 and PV9. Watch the flow rates on FM1 and FM2.

- Repeat this procedure cyclically.
- All valves to be operated during the cyclical repetition of the procedure can be controlled by the DCS. It is recommended to automate this procedure with a respective software on the DCS, using the system values of the load cells and flow meters. The software should include alarms and a shutdown routine.
- Emergency shutdown: Press the 'Emergency out' button. If possible, close V19.

### C.VIII. Water Extraction

Principally, the Purification Skid is envisioned to perform water extraction processes with large liquid scintillator volumes in continuous mode. Module-0 is able to perform water extraction in batch mode only, and with comparatively small amounts, limited by its tank sizes. The spargers and spray nozzles in the BT tanks help to improve the contact between scintillator and water. The following procedure can be applied:

- Transfer a scintillator batch to BTE/BTW.
- Open the ventilation of BTE/BTW (VN19/VN20). Check VN3 to be open.
- Add ultra-pure, deionised water from the water plant (V82) via the spray nozzle (N1/N2, V28/V30) into BTE/BTW. In particular, mix the water in N1/N2 with high-purity nitrogen (via VN8/VN11).
- To mix water and scintillator, create turbulences by using the spargers SP1/SP2.
- Wait for a separation of the two phases.
- Remove the water via the bottom outlet (V57/V60) and dispose it via V99 to the liquid waste tank. Pay attention to the level of the waste tank.
- Flush the lines used with ultra-pure water and repeat the procedure until a satisfactory result is obtained.
- Emergency shutdown: Press the 'Emergency out' button. Close V82 and V99.

### C.IX. Liquid Supply to the Skid on the CTF Tank

The skid on the CTF tank – capable of treating comparatively small amounts of liquids – contains a water extraction unit, a nitrogen stripper, and a distillation unit. In future, this system possibly will perform pre-purification steps. It has to be supplied with liquid via Module-0. The tank D204 (volume ~100 litres) in the skid, able to receive liquid from Module-0 via V1 and C111, is supposed to decouple the liquid flow supplied by the Module-0 pump (via V1 and V6CTFtop) and the liquid consumption by the skid internal process (via V7CTFtop and C104). In particular, if the Module-0 pump moves liquid to the skid with a higher flow rate than needed, the excess can escape via C111 into D204, then overflows via C110, and finally can be returned to the supply point of the Module-0 pump via V80. Apart from that, the purified liquid can contemporarily return from the skid to Module-0 via C109, V5CTFtop, V53 and V87.

#### D. Recommended Alarm Set Points in Module-0

Instrument	Description	Alarm Set Point	Alarm Mode
MP1	Load cell EPN	6500 kg	upper limit
MP2	Load cell BTE	1050 kg	upper limit
MP3	Load cell BTW	1050 kg	upper limit
MP4	Load cell EPS	6500 kg	upper limit
PP8	Pressure EPN	3.0 bar	upper limit
PP8	Pressure EPN	0.0 bar	lower limit
PP9	Pressure BTE	0.35 bar	upper limit
PP9	Pressure BTE	0.0 bar	lower limit
PP10	Pressure BTW	0.35 bar	upper limit
PP10	Pressure BTW	0.0 bar	lower limit
PP11	Pressure EPS	3.0 bar	upper limit
PP11	Pressure EPS	0.0 bar	lower limit
PP6	Pressure head	4.0 bar	upper limit
PP7	Pressure lower manifold	4.0 bar	upper limit
PP13	Pressure Column 1	2.5 bar	upper limit
PP13	Pressure Column 1	0.0 bar	lower limit
PP14	Pressure Column 2	2.5 bar	upper limit
PP14	Pressure Column 2	0.0 bar	lower limit
O <sub>2</sub>	Oxygen monitor	19.0 %	lower limit
FM1	Flow Pump 1	variable	variable
FM1DEN	Density Pump 1	variable	variable
FM2	Flow Pump 2	variable	variable
FM2DEN	Density Pump 2	variable	variable
FM3	Flow Column 2	variable	variable
FM3DEN	Density Column 2	variable	variable
N <sub>2</sub>	Status safety valves	closed	---
PV5	BTW bottom valve	variable	---
PV6	BTE bottom valve	variable	---
PV7	BTW top valve	variable	---
PV8	BTE top valve	variable	---

*Recommended alarms for the Module-0 page of the digital control system (DCS)*

Instrument	Description	Alarm Set Point	Alarm Mode
PP1	HPN <sub>2</sub> supply	3.5 bar	lower limit
PP12	RN <sub>2</sub> supply	7.0 bar	lower limit
PP2	Low pressure HPN <sub>2</sub>	0.4 bar	upper limit
PP3	High pressure HPN <sub>2</sub>	3.5 bar	upper limit
PP4	RN <sub>2</sub> pump supply	4.0 bar	upper limit
PP5	HPN <sub>2</sub> for columns	2.5 bar	upper limit

*Recommended alarms at the Module-0 nitrogen panel*

# Tables & Diagrams

- Diagram 1.1: Neutrino flux on the earth from different sources [Kos92]  
Diagram 1.2: The pp-cycle reactions of the helium fusion in the sun, together with the emitted neutrinos  
Table 1.3: Energy and flux of solar neutrinos according to [Bah01]  
Diagram 1.4: Solar neutrino spectrum and according uncertainties, compared to the thresholds of some neutrino experiments [Bah04]  
Diagram 1.5:  $\nu_e$  survival possibility for different neutrino energies and different oscillation parameters (LMA-I, -0, -D) [Mir04a]  
Diagram 1.6: Graphics of the SNO Phase I result (1999-2001) [Rob03]  
Diagram 1.7: Comparison of KamLand with the solar neutrino experiments' data (mainly SNO) in the  $(\nu_e, \nu_\mu)$  oscillation parameter space [Gra04]
- Diagram 2.1: Recoil electron spectra caused by the  $^7\text{Be}$  solar neutrino line at 862keV.  
Diagram 2.2: Calculated anti-neutrino spectra for Borexino [Ian04a]  
Diagram 2.3: The Borexino area in hall C of the LNGS, Assergi, Italy  
Diagram 2.4: Configuration of the Borexino detector  
Table 2.5: Scintillator purity requirements for Borexino corresponding to a background rate of  $1\text{d}^{-1}$  from 250-800 keV in 100 tons of scintillator [Nef96]  
Figure 2.6: Decay chains of  $^{232}\text{Th}$  and  $^{238}\text{U}$   
Table 2.7: Background caused by muon-induced radioactive nuclei [Goe01]  
Image 2.8: Interior of the CTF detector  
Table 2.9: Batches of raw PC measured during the CTF3 period.  
Diagram 2.10: Activity between 250 and 800 keV in the CTF detector during the CTF3 campaign [Mil04]  
Diagram 2.11: Simulated energy spectra in Borexino after 1000 days:  $^{210}\text{Bi}$ - $\beta$ 's with  $500\text{d}^{-1}$  +  $^7\text{Be}$ - $\nu$ 's with  $33\text{d}^{-1}$   
Diagram 2.12: Simulated energy spectra in Borexino after 1000 days:  $^{210}\text{Bi}$ - $\beta$ 's with  $50\text{d}^{-1}$  +  $^7\text{Be}$ - $\nu$ 's with  $33\text{d}^{-1}$
- Figure 3.1: Big Building East in Hall C, LNGS  
Figure 3.2: Block Diagram showing the main equipment of Module-0  
Figure 3.3: Sketch of the Interconnection System, providing the connections between Module-0 and other important liquid handling components of Borexino  
Picture 3.4: View of the Module-0 equipment from the entrance door, May 2003  
Figure 3.5:  $^{222}\text{Rn}$  activity progression caused by emanation  
Table 3.6:  $^{222}\text{Rn}$  emanation measurements with Module-0 equipment  
Diagrams 3.7: Particulate counting in Module-0 water samples  
Table 3.8: Particulate concentrations in water samples taken in Module-0, together with reference values of the US Military Standard 1246
- Figure 4.1: Surface of silica gel  
Table 4.2: Some characteristics of the silica gel 'Kromasil' from Eka Nobel, Sweden, for different pore sizes

- Diagram 4.3: Impurity adsorption on the silica gel surface in a sectional view of a silica gel grain and its pores
- Figure 4.4: Segment model of a silica gel column
- Diagram 4.5: Qualitative development of the impurity concentration with the mass of processed liquid scintillator
- Diagram 4.6: Impurity concentration in the purified scintillator when leaving the column; simulated with the parameters of the batch test described in 4.2.4 and with  $\tau=10\text{s}$
- Table 4.7: Purification factors for different equilibrium time constants and segment numbers in the case of the batch purification experiment of paragraph 4.2.4
- Diagram 4.8: Purification progression of loop mode and batch mode in comparison
- Diagram 4.9: Sketch of the set-up used for the contamination of pseudocumene with radon at the PTB Braunschweig
- Figure 4.10: PMT looking on liquid scintillator in a teflon sample box
- Figure 4.11: Energy spectra of a contaminated scintillator sample
- Figure 4.12: Energy spectra of a purified scintillator sample
- Diagram 4.13: Energy-PSD spectra of a contaminated scintillator sample
- Diagram 4.14: Energy-PSD spectra of a purified scintillator sample
- Diagram 4.15: Plots of the event number over the tail-to-total ratio of five contaminated scintillator samples and a purified one, the latter arising from the scintillator after the batch purification test
- Table 4.16: Tail-to-total ratios of pulse shape discrimination analyses at different energy calibration factors with respect to the plots in 4.15
- Diagram 4.17: Radon decay fit of the  $\alpha$ -like activity in the E-PSD-window of a scintillator sample after the silica gel batch purification
- Figure 4.18:  $^{210}\text{Bi}$   $\beta$ -spectra and its distortion by the geometric properties of the sample box, obtained with a Monte-Carlo simulation [Gri00]
- Figure 4.19: Fit of a  $\beta$ -spectra ( $^{210}\text{Bi}$ ) of a contaminated scintillator sample in the energy range from 500 to 700 keV
- Image 4.20: View of the germanium detector with passive shielding layers and active muon veto
- Figure 4.21: Energy spectra of a contaminated scintillator sample (prior to the batch purification test) between 30 and 3580 keV, recorded with a germanium detector
- Figure 4.22: Background energy spectra of the germanium detector between 30 and 3580 keV
- Table 4.23: Most significant  $\gamma$  peaks and their activities in a sample of the contaminated scintillator prior to the batch purification (described in 4.2.4), compared to the background activity in the germanium detector
- Table 4.24: Determination of the Free Enthalpy of Po, Bi and Pb for surface adsorption on silica gel
- Picture 4.25: Set-up of the laboratory batch purification test
- Table 4.26: Result of the laboratory silica gel batch purification experiment
- Table 4.27: Single measurements influencing the determination of the integral purification factor of the laboratory silica gel batch purification experiment
- Table 4.28: Intrinsic contamination of a pure silica gel sample with  $^{210}\text{Po}$ ,  $^{210}\text{Bi}$  and  $^{210}\text{Pb}$ , measured by a surface adsorption experiment
- Table 4.29: Orientation for the upper limit of the intrinsic contamination in a pure silica gel sample, arising from intrinsic  $^{226}\text{Ra}$  contamination and measured via the emanation of  $^{222}\text{Rn}$  [Fre03]

- Table 4.30:  $^{210}\text{Po}$  purification by an adsorption equilibrium of pseudocumene and silica gel in three subsequent equilibrium steps
- Table 4.31:  $^{210}\text{Pb}$  purification by an adsorption equilibrium of pseudocumene and silica gel in three subsequent equilibrium steps
- Table 4.32: Observed coincidences and windows of the applied data analysis cuts at the beginning of the CTF3 campaign
- Diagram 4.33: Coincident events in 76.2 days after the silica gel loop test with CTF3 [Mil04]
- Figure 4.34:  $^{222}\text{Rn}$  activity during the silica gel loop test in CTF3 [Mon02]
- Figure 4.35:  $^{220}\text{Rn}$  activity at the silica gel loop test in CTF3 [Dan02]
- Table 4.36: Purification effect of the silica gel loop test in CTF3 on  $^{232}\text{Th}$  daughters [Mil04]
- Figure 4.37: Simulation of the expected activity progression for the CTF silica gel loop test
- Figure 4.38:  $^{210}\text{Po}$  activity during the silica gel loop test [Mon05]
- Figure 4.39: Hydrodynamically simulated flow pattern for the silica gel loop test in CTF3 [Leu02]
- Diagram 4.40: Fit of the CTF data points with a model curve under the assumption of bad mixing between purified and unpurified scintillator
- Table 4.41: Effects of the silica gel batch test during the CTF3 campaign on the scintillator [Mil04].
- Table 4.42: Upper limits for intrinsic contamination in pure silica gel, arising from the  $^{210}\text{Pb}$  activity reached in the scintillator after the silica gel batch test in CTF3
- 
- Table 5.1: Adsorption measurements on a combined teflon and glass surface
- Table 5.2: Adsorption measurements on a stainless steel surface
- Table 5.3: Adsorption measurements on a glass surface
- 
- Diagram 6.1: Block Diagram of the Purification Skid at Borexino site [For03]
- Diagram 6.2: Equipment and flow path for the CTF3 water extraction testing [For03]
- Diagram 6.3: Progression of the first CTF3 water extraction test [For03]
- Table 6.4: Number of events per day before and after the first CTF3 water extraction test.
- Table 6.5: Purification results for U, Th and Kr related events [Mil04]
- Figure 6.6: Hydrodynamically simulated flow pattern for the CTF3 water extraction testing
- Table 6.7: Purification steps and data analysis during the second CTF3 water extraction phase [For03]
- Table 6.8: Purification results for Th and Kr related events [Mil04]



# Bibliography

- [Ali98a] G. Alimonti et al., *A large-scale low-background liquid scintillation detector: The Counting Test Facility at Gran Sasso*, Nucl. Instrum. Meth. **A406** (1998), 411-426
- [Ali98b] G. Alimonti et al., *Ultra-low background measurements in a large volume underground detector*, Astroparticle Physics **8** (1998), 141-157
- [Alt04] G. Altarelli, CERN, Geneva, Switzerland: Conference talk at Neutrino 2004, Paris, France
- [Apo03] M. Apollonio et al., *Search for neutrino oscillations on a long base-line at the Chooz nuclear power station*, arXiv:hep-ex/0301017v1, Jan 13, 2003
- [Ara04] T. Araki et al., arXiv:hep-ex/0406035, June 13, 2004, submitted to Phys. Rev. Lett.
- [Bah89] J.N. Bahcall, *Neutrino Astrophysics*, Cambridge University Press, 1989
- [Bah01] J.N. Bahcall, S. Basu, M.H. Pinsonneault, *Solar Models: current epoch and time dependencies, neutrinos, and helioseismological properties*, Astrophysical Journal **555** (2001), 990-1012
- [Bah04] J. Bahcall, C. Pena-Garay, *Solar Models and Solar Neutrino Oscillations*, New Journal of Physics **6** (2004) 63
- [Bal96] M. Balata et al., *The water purification system for the low background counting test facility of the Borexino experiment at Gran Sasso*, Nucl. Instr. Meth. **A370** (1996) 605
- [Bea99] J.F. Beacom, *Neutrinos from the Next Galactic Supernova*, arXiv:hep-ph/9909231, (1999)
- [Bel00] G. Bellini et al., *High sensitivity  $2\beta$  decay study of  $^{116}\text{Cd}$  and  $^{100}\text{Mo}$  with the Borexino counting test facility (CAMEO project)*, Eur. Phys. J. **C19** (2001) 43-55; arXiv:nucl-ex/0007012, July 11, 2000
- [BOR02] Borexino Collaboration, *Science and technology of Borexino: a real-time detector for low energy solar neutrinos*, Astroparticle Physics **16** (2002) 205-234
- [BOR03a] Borexino Collaboration, *Study of neutrino electromagnetic properties with the prototype of the Borexino detector*, Physics Letters B **563** (2003) 35-47
- [BOR03b] Borexino Collaboration, *New experimental limits on heavy neutrino mixing in  $^8\text{B}$ -decay obtained with the Borexino Counting Test Facility*, JETP Letters **78** (5) 261-266
- [BOR04] Borexino Collaboration, *Constraints on the solar electron anti-neutrino flux obtained with the Borexino prototype*, July 9, 2004, to be submitted
- [BOR04b] Borexino Collaboration, *Phenylxylethane (PXE): a high-density, high-flashpoint organic liquid scintillator for applications in low-energy particle and astrophysics experiments*, NIM A (2004), arXiv:physics/0408032
- [Bur03] C.P. Burgess et al., *Cornering Solar Radiative-Zone Fluctuations with KamLAND and SNO salt*, arXiv:hep-ph/0310366v1, Oct 31, 2003
- [Cad02a] L. Cadonati, F.P. Calaprice, M.C. Chen, *Supernova Neutrino Detection in Borexino*, Astroparticle Physics **16** (2002) 361-372
- [Cad02b] L. Cadonati, Data analysis group for Borexino (2002), Princeton University, USA, world wide web, <http://borex.princeton.edu/tshutt98/ctf3Analisi/Ctf3Laura.html> (restricted area)
- [Cat04] C.M. Cattadori, Laboratori Nazionali del Gran Sasso, Assergi, Italy: Conference talk at Neutrino 2004, Paris, France

- [Dan02] D. D'Angelo, Technische Universität München, Germany, private communication (2002)
- [Dav98] R. Davis et al., *Measurements of the solar electron neutrino flux with the Homestake chlorine detector*, *Astrophysical Journal* **496** (1998), 505-526
- [DCh04] Double-Chooz Collaboration, *Letter of Intent for Double-CHOOZ: a Search for the Mixing Angle  $\theta_{13}$* , arXiv:hep-ex/0405032, May 14, 2004
- [Egu04] K. Eguchi et al. (KamLAND collaboration), *Phys.Rev.Lett.* **92**, 071301 (2004)
- [Fae98] A. Faessler, F. Simkovic, *J. Phys.* **G24**, 2139 (1998)
- [Fig61] P.E. Figgins, *The Radiochemistry of Polonium*, NAS-NS 3037, Mound Laboratory Miamisburg, Ohio, USA, (1961)
- [Fre03] B. Freudiger, *Untersuchungen zu den radioaktiven Edelgasnukliden als Untergrundquelle im Sonnenneutrino-detektor Borexino*, Dissertation, Universität Heidelberg, Germany, (2003)
- [For03] R. Ford, LNGS Assergi, Italy, private communication (2003)
- [Gav01] V.N. Gavrin, *Solar neutrino results from SAGE*, *Nucl. Phys. B (Proc. Suppl.)* **91** (2001), 36-43
- [Goe01] M. Göger-Neff, *Development of a Liquid Scintillator and of Data Analysis Methods for Borexino*, Dissertation, Technische Universität München, Germany, (2001)
- [Gol97] T. Goldbrunner, *Messung niedrigster Aktivitäten für das solare Neutrinoexperiment Borexino*, Dissertation, Technische Universität München (1997), Germany
- [Gos04] S. Goswami, Harish-Chandra Research Institute, Allahabad, India: Conference talk at Neutrino 2004, Paris, France
- [Gra04] G. Gratta, Stanford University, USA: Conference talk at Neutrino 2004, Paris, France
- [Gri00] C. Grieb, *Untersuchungen zur Szintillatorreinigung mit Kieselgel, Studien zum Untergrund und Vakuum-Neutrinooszillationen in Borexino*, Diploma thesis, Technische Universität München, Germany, (2000)
- [Gro00] D.E. Groom et al. (Particle Data Group), *The number of light neutrino types from Collider Experiments*, *Eur. Phys. Jour.* **C15**, 1 (2000)
- [Har97] F.X. Hartmann, *Results for preparations of the low-level scintillator in Borexino*, Proc. 4<sup>th</sup> Int. Sol. Neutrino Conf., Heidelberg, Germany, (1997)
- [Har99] F.X. Hartmann, private communication (1999)
- [Her92] J.M. Herndon, *Naturwissenschaft*, **79**, 7, (1992)
- [Heu00] G. Heusser et al.,
- [Hen99] R. von Hentig, *Spurenanalyse primordialer Radionuklide für das solare Neutrinoexperiment Borexino*, Dissertation, Technische Universität München, Germany, (1999)
- [Ian04a] Aldo Ianni, Oleg Smirnov, *Search for electron anti-neutrinos with the CTF3*, Borexino internal report, April 18, 2004
- [Ian04b] Aldo Ianni, LNGS Assergi, Italy, private communication (2004)
- [Jun04] Ch. K. Jung, Neutrino 2004, 14-19 June 2004, Collège de France, Paris, <http://neutrino2004.in2p3.fr/slides/thursday/jung.pdf>
- [Kee04a] G. Keefer, *Results from  $^{212}\text{Pb}$  Reduction Experiments*, University of Alabama, USA (2004)
- [Kee04b] G. Keefer,  *$^{212}\text{Pb}$  Purification Analysis Update*, University of Alabama, USA, talk at Kamland Collaboration Meeting, March 11-13, 2004
- [Kim93] C.W. Kim, A. Pevsner, *Neutrinos in Physics and Astrophysics*, Harwood Academic Publishers, Chur etc., 1993
- [Kla04] H.V. Klapdor-Kleingrothaus et al., *PLB* 586 (2004) 198-212

- [Kos92] M. Koshiba, Phys. Rep. **220** (1992), 229
- [Leu02] M. Leung, Princeton University, USA, private communication (2002)
- [Leu04] M. Leung, *<sup>210</sup>Pb Binding on Stainless Steel and Implications for Borexino*, Borexino Internal Report, Princeton University, USA, Sep. 30, 2004
- [Mas82] Mason, Moore, *Principles of Geochemistry*, 4<sup>th</sup> edition, John Wiley & Sons, New York (1982)
- [Mil04] Università degli Studi di Milano, Italy, Borexino data analysis group (2004), world wide web, <http://pcdavide.mi.infn.it/protected/analysis.html> (restricted area)
- [Mir04a] O.G. Miranda, M.A. Tórtola, J.W.F. Valle, *Are solar neutrino oscillations robust ?*, arXiv:hep-ph/0406280, June 28, 2004
- [Mir04b] O.G. Miranda et al., *Constraining the neutrino magnetic moment with anti-neutrinos from the sun*, arXiv:hep-ph/0311014 (2004)
- [Mon02] M.E. Monzani, Università degli Studi di Milano, Italy, private communication (2002)
- [Mon05] M.E. Monzani, *Characterization and Calibration of the Borexino Detector for Solar and Supernova Neutrinos*, Dissertation, Università degli Studi di Milano, Italy (2005)
- [Nak04] M. Nakahata, Kamioka Observatory, ICRR, University of Tokyo, Japan: Conference talk at Neutrino 2004, Paris, France
- [Nef96] M. Neff, *Untersuchungen zum Untergrund durch Radioaktivität und kosmische Strahlung für das solare Neutrinoexperiment Borexino*, Diploma thesis, Technische Universität München, Germany, (1996)
- [Nie00] L. Niedermeier, *Untersuchungen zur Reinheit von Szintillatorkomponenten im Rahmen des solaren Neutrinoexperimentes Borexino*, Diploma thesis, Technische Universität München, Germany, (2000)
- [Nie03] L. Niedermeier et al., *Scintillator Purification by Silica Gel Chromatography in the context of Low Counting Rate Experiments*, Astroparticle, Particle and space physics, detectors and medical physics applications: Proceedings of the 8<sup>th</sup> Conference (2003), available at <http://www.e15.physik.tu-muenchen.de/borexino/como-paper.pdf>
- [Obe03a] L. Oberauer et al., *Light Concentrators for Borexino and CTF*, arXiv:physics/0310076 (2003)
- [Obe03b] L. Oberauer, TU München, *A large liquid scintillator detector for low energy neutrino astronomy*, at NOVE 2003 Conference in Venice, Italy (2003)
- [Ohl00] T. Ohlsson, H. Snellman, *Three flavor neutrino oscillations in matter*, Journal of Mathematical Physics, **41**(5) (2000), 2768-2788
- [Rob03] R.G.H. Robertson, University of Washington, USA: Conference talk at TAUP 2003, Seattle, USA
- [Rot02] A. Rotunno, *Oscillazione di antineutrini da reattore su grandi distanze: prospettive di soluzione al problema dei neutrini solari*, University of Bari, Italy (2002)
- [Sch00] S. Schönert, Max-Planck-Institut für Kernphysik, Heidelberg, Germany, private communication (2000)
- [Schm97] N. Schmitz, *Neutrino Physik*, Teubner Verlag Stuttgart, 1997
- [Sim02] H. Simgen, Max-Planck-Institut für Kernphysik, Heidelberg, Germany, private communication (2002)
- [SK02] The Super-Kamiokande Collaboration, *Determination of Solar Neutrino Oscillation Parameters using 1496 Days of Super-Kamiokande-I Data*, Phys. Lett. **B539** (2002) 179-187

- [SK04] The Super-Kamiokande Collaboration, *Evidence for an oscillatory signature in atmospheric neutrino oscillation*, arXiv:hep-ex/0404034v1, April 24, 2004
- [SNO04] SNO Collaboration, *Measurement of the Total Active  $^8\text{B}$  Solar Neutrino Flux at the Sudbury Neutrino Observatory with Enhanced Neutral Current Sensivity*, Physical Review Letters **92(18)** (2004)
- [Sta90] A. Staudt, K. Muto, H.V. Klapdor-Kleingrothaus, Europhys. Lett. **13**, 31 (1990)
- [Ung79] K.K.Unger, "porous silica, its properties and use as support in column liquid chromatographie", Journal of Chromatographie Library, Vol.16 (1979)
- [Woj96] M. Wojcik, *Environmental  $^{222}\text{Rn}$  as a background source in the solar neutrino experiment GALLEX*, Report No. 1729/PH, Cracow, Poland, 1996
- [Zuz02] G. Zuzel,  *$^{226}\text{Ra}$  in the nylon scintillator vessel as a background source in the solar neutrino experiment Borexino*, Dissertation, Jagellonian University, Cracow, Poland, 2002
- [Zuz04] G. Zuzel, D. Franco, *Measurements of Ar/Kr and  $^{222}\text{Rn}$  concentrations in the LAK nitrogen in a real test for the Borexino experiment*, Internal Report, Max-Planck-Institut für Kernphysik, Heidelberg, Germany, (2004)

# Acknowledgement

Ich danke Ihnen, Herr Prof. v. Feilitzsch, für die Überlassung des Themas und der damit verbundenen Aufgaben am Gran Sasso. Am meisten schätzte ich die große Gestaltungsfreiheit und Verantwortung, die Sie mir bereits zu Anfang der Arbeit zugestanden.

Ich danke Dir, Lothar, für die ständige Unterstützung als Ansprechpunkt während der gesamten Arbeit. Die gemeinsame Zeit am Gran Sasso mit den zahlreichen Abendessen hat mir sehr gefallen!

Ich danke Euch, Christian, Christian, Jean und Davide sehr herzlich für die gute Freundschaft während der letzten fünf Jahre und für alle gemeinsamen Unternehmungen während dieser Zeit, die mich teilweise sehr weit geführt haben! Vielen Dank auch im Zusammenhang mit den WG's am Gran Sasso und in Eching.

Ich danke Euch, Teresa, Kathrin und Michael W. für den netten Kontakt und die neuerlichen Initiativen in der Gruppe, seitdem Ihr da seid.

Ich danke Euch, Tobi und Marianne, für Eure Freundschaft und die Hilfe bei Computerproblemen während der letzten Jahre.

Dir, Gunther, danke ich für das Vertrauen und die Übertragung der Zuständigkeit für das Modul-0 am Gran Sasso sowie für die unersetzliche Mithilfe bei der Planung der Silikagelsäulen.

Ich danke Dir, Walter, für die wertvolle Unterstützung meiner eine osteuropäische Stadt betreffenden Zukunftsplanung.

Ich danke Euch allen, Michi Stark, Wolfgang Rau, Marco Razeti, Hesti Wulandari, Doreen Wernicke, Michi Huber, Thomas Jagemann, Wolfgang Westphal, Jan König, Chiara Coppi, Christian Hollerith sowie allen weiteren Kollegen während der vergangenen Jahre für den gemeinsamen Weg am Institut und die gelegentlichen Unternehmungen.

Ich danke Ihnen, Herr Prof. Nolte und Ihrer Gruppe, Herbert Reithmeier, Vitali Lazarev, Georg Rugel und anderen für die angenehme Zusammenarbeit beim Übungsbetrieb sowie bei sonstigen Dingen.

Ich danke Dir, Eckhard, für Deine gute Laune und Deine Bemühungen in Verbindung mit dem Versuch, meiner Arbeit zu einem weiteren Kapitel zu verhelfen.

Ich danke Euch, Beatrice und Alexandra, für die Hilfe bei allen bürokratischen Dingen trotz meiner bescheidenen Fortschritte auf diesem Gebiet. Ein weiteres herzliches Dankeschön Dir, Beatrice, für die Mühe beim Korrekturlesen.

Ich danke Euch, Norbert und Harry, für das freundschaftliche Verhältnis sowie die unschätzbare Hilfe bei allen elektrotechnischen und feinmechanischen Problemen, von denen das Modul-0 einen schier unerschöpflichen Vorrat zu beherbergen schien. Insbesondere danke ich Euch, wie auch Erich, Thomas und Werner, für die Arbeitsausflüge zum Gran Sasso. In diesem Zusammenhang auch vielen Dank an die Leute der Zentralwerkstatt, wo die Gehäuse der Silikagelsäulen gefertigt wurden, deren Gewicht bis heute ein Rätsel geblieben ist.

Inoltre, e soprattutto, vorrei mandare un grande bacio a tutti i cari amici – troppo numerosi per menzionarli tutti – la cui conoscenza ho fatto al Gran Sasso, dove ho passato quasi metà del dottorato. Grazie dell'aiuto sotterraneo a tutti gli altri "tecnici", specialmente della ottima cooperazione per tutto quello che riguardava il Modulo Zero, come lo sfortunato batch-test, la grande pulizia prima dell'incidente, il collegamento al sistema di controllo, agli altri sistemi, i lavori per la impermeabilizzazione del pavimento nel BBE, etc. Grazie per tutte le partite di calcio alla TV e soprattutto dal vivo, tutte le serate all'Aquila e Paganica con tutte le pizze, gli amari e le genziane, tutti gli ospiti in casa nostra che ci hanno fatto compagnia e che hanno contribuito alle spese, e tutti i caffè che abbiamo preso al bar dei laboratori.

I'd like to thank you, Richard, for the great cooperation, the sixth chapter of my thesis and the alternative weekly meetings in the Irish pubs of L'Aquila. In the context of the water extraction chapter, I like to thank the Borexino group of the Princeton University, who has set up the corresponding plant.

I'd also like to thank the data analysis groups in Milan and Princeton, as they provided precious data analyses for various tests illustrated in my thesis.

Herzlichen Dank Dir, Burkhard, für die gemeinsame Zeit in der Wohnung sowie die reibungslose Zusammenarbeit und Flexibilität bei den Radonmessungen. In diesem Zusammenhang auch ein herzliches Dankeschön an alle vom MPIK Heidelberg!

Ich möchte auch Dir, Caren, sehr herzlich danken für die netten Gespräche und die Einladung nach Virginia, die mir zwei sehr schöne Wochen bescherte, an denen auch Christian Grieb maßgeblich beteiligt war.

I thank the whole Borexino Collaboration for the time we have spent together on this experiment.

Vielen Dank an Anja Honig und die übrigen Leute von der PTB Braunschweig, ohne deren Einverständnis und tatkräftige Mithilfe bei der Radonbeladung eines Flüssigszintillators große Teile meiner Arbeit nicht möglich gewesen wären.

Vielen Dank an Theo Hertrich, Karl-Heinz Schuhbeck, Stefan Schönert, Frank Hartmann, Marianne Göger sowie Caren und Tanja Hagner, die in den vorhergehenden Jahren dazu beigetragen haben, das Module-0 bzw. eine seiner zahlreichen, vergangenen Versionen dem näherzubringen, was letztendlich daraus geworden ist.

Ich möchte mich bei der Technischen Universität München sowie der Marie Curie Fellow Association für die beiden Stipendien bedanken, die mit Blick auf die finanzielle Komponente meiner Doktorarbeit den Weg geebnet haben. In diesem Zusammenhang ebenfalls vielen Dank an die DFG und das MLL.

Letztendlich möchte ich Euch, meine Eltern, für die moralische und finanzielle Unterstützung über die gesamte Dauer der Arbeit hinweg herzlichst danken.